

Variationally consistent inertia templates for speed-up and customization in explicit dynamics

Anne-Kathrin Schäuble

variational basis

functional inertia patch test

displacement

velocity

three-field formulation

linear momentum

reciprocal mass

d'Alembert forces

inverse mass matrix

time step size

Gershgorin theorem

efficient time step estimate

mass scaling

free parameters

multi-parameter template

desired properties

tuning

quasi static highly nonlinear phenomena

lumped mass matrix short-term dynamics

penalty contact

Variationally Consistent Inertia Templates for Speed-up and Customization in Explicit Dynamics

by

Anne-Kathrin Schäuble

Bericht Nr. 69

Institut für Baustatik und Baudynamik der Universität Stuttgart

Professor Dr.-Ing. habil. M. Bischoff

2019



© Anne-Kathrin Schäuble

Berichte können bezogen werden über:
Institut für Baustatik und Baudynamik
Universität Stuttgart
Pfaffenwaldring 7
70550 Stuttgart

Tel.: 0711 - 685 66123
Fax: 0711 - 685 66130
E-Mail: sekretariat@ibb.uni-stuttgart.de
<http://www.ibb.uni-stuttgart.de/>

Alle Rechte, insbesondere das der Übersetzung in andere Sprachen, vorbehalten. Ohne Genehmigung des Autors ist es nicht gestattet, diesen Bericht ganz oder teilweise auf photomechanischem, elektronischem oder sonstigem Wege zu kommerziellen Zwecken zu vervielfältigen.

D 93 - Dissertation an der Universität Stuttgart
ISBN 978-3-00-062288-5

Variationally Consistent Inertia Templates for Speed-up and Customization in Explicit Dynamics

Von der Fakultät Bau- und Umweltingenieurwissenschaften
der Universität Stuttgart zur Erlangung der Würde eines
Doktor-Ingenieurs (Dr.-Ing.) genehmigte Abhandlung

vorgelegt von

Anne-Kathrin Schäuble

aus Waldshut-Tiengen

Hauptberichter: Prof. Dr.-Ing. habil. Manfred Bischoff, Stuttgart

Mitberichter: Prof. Dr.-Ing. habil. Detlef Kuhl, Kassel

Prof. José A. González Pérez, Sevilla

Tag der mündlichen Prüfung: 08. Februar 2019

Institut für Baustatik und Baudynamik der Universität Stuttgart

2019

Kurzfassung

Die vorliegende Arbeit beschäftigt sich mit neuartigen Berechnungsmethoden für die Computersimulation dynamischer Probleme mit expliziten Zeitintegrationsverfahren. Dynamische Simulationen sind immer dann erforderlich, wenn die Belastung im zu simulierenden System oder Prozess zügig aufgebracht wird und Trägheitskräfte nicht vernachlässigt werden können. Explizite Methoden kommen aufgrund der kleinen, kostengünstigen Zeitschritte und nichtexistierender Konvergenzprobleme im Bereich der Kurzzeitdynamik, sowie für quasi-statische, aber hoch nichtlineare Probleme zum Einsatz. Klassische Anwendungsfelder sind zum Beispiel die Simulation des Zusammenstoßens zweier Autos, der Aufprall eines Mobiltelefons auf den Boden oder die Simulation eines Tiefziehprozesses eines Blechteils.

In der Vergangenheit wurden verschiedene Anstrengungen unternommen um die Effizienz expliziter dynamischer Berechnungen zu steigern. Eine gängige Methode ist die Massenskalierung. Hierbei wird durch eine Manipulation der Massenmatrix die maximale Eigenfrequenz reduziert, welche umgekehrt proportional zum kritischen Zeitschritt ist. Somit erlaubt die Massenskalierung größere Zeitschritte. Diese Manipulation erfolgt oft nur für einzelne kleine oder besonders steife Elemente, die den Zeitschritt des gesamten Modells begrenzen. In den letzten Jahren wurden viele Vorschläge gemacht um den ursprünglichen, konventionellen Ansatz der Massenskalierung zu verbessern: Statt die diagonale Struktur der Massenmatrix zu erhalten und nur Masse auf der Diagonalen hinzuzufügen, wurde im Rahmen der selektiven algebraischen Massenskalierung vorgeschlagen, Masse auf der Diagonalen hinzuzufügen und gleichzeitig auf der Nebendiagonalen zu subtrahieren um so zumindest die Masse und die translatorische Trägheit zu erhalten. Um Massenmatrizen, die einen größeren kritischen Zeitschritt erlauben, nicht nur durch algebraische Manipulationen, sondern basierend auf einer fundierten theoretischen Herleitung zu erhalten, wurden variationell selektive Massenskalierungsmethoden vorgeschlagen. Zuletzt wurden, um die Lösung eines linearen Gleichungssystems für nichtdiagonale Massenmatrizen zu umgehen, sogenannte reziproke Massenmatrizen eingeführt, die im Folgenden noch näher erläutert werden.

Die in dieser Arbeit behandelten neuartigen Berechnungsmethoden zielen sowohl auf eine Erhöhung der Genauigkeit, als auch auf eine Reduktion des Rechenaufwands ab. Die Basis für die Entwicklung stellen variationell konsistente Trägheitsschablonen dar. Unter dem Begriff der Trägheitsschablonen verbergen sich sowohl alternative Massenmatrizen zu den gewöhnlich verwendeten diagonalen Massenmatrizen, als auch neuartige reziproke Massenmatrizen. Reziproke Massenmatrizen sind direkt aus der variationellen Formulierung resultierende, dünnbesetzte, assemblierbare, inverse Massenmatrizen, die eine triviale Lösung der Beschleunigung aus dem zweiten Newtonschen Gesetz erlauben. Die Konstruktion der Trägheitsmatrizen erfolgt auf der Basis eines variationellen Prinzips. Der Ausgangspunkt für die Formulierung ist das Hamiltonsche Prinzip, welches durch die Einführung dreier unabhängiger Felder, der Verschiebung, der Geschwindigkeit und des Impulses, erweitert wird. Die variationelle Formulierung, und damit die

resultierenden Trägheitsmatrizen, weisen freie Parameter auf, die eine benutzerspezifische Anpassung der Eigenschaften der Matrizen erlauben. So kann zum Beispiel gezielt eine Reduktion der maximalen Eigenfrequenz im Sinne der Massenskalierung, oder eine Verbesserung der Genauigkeit und Konvergenzeigenschaften für niedrige Frequenzen erfolgen.

Der Schwerpunkt der Arbeit liegt auf den folgenden Aspekten: Erstens wird die variationelle Konsistenz der reziproken Massenmatrizen im Speziellen für Materialien mit variabler Dichteverteilung und die damit verbundenen Mindestanforderungen an die Ansatzräume diskutiert. Zweitens geht es um die systematische Verwendung der Methodik nicht nur zur Vergrößerung der Zeitschrittweite, aber auch zur gezielten Generierung von Trägheitsmatrizen für benutzerspezifische Interessen, wie z.B. einer verbesserten Genauigkeit für niedere Frequenzen. Drittens zielt die Arbeit auf die Weiterentwicklung reziproker Massen ab, um sie für praktische Anwendungen verwendbar zu machen. Dabei stehen die Bereitstellung eines effizienten Zeitschrittschätzers, die Weiterentwicklung der Methode für eine Vielzahl von Elementtypen und die Behandlung von Kontakt im Vordergrund. In den folgenden Abschnitten werden die Schwerpunkte der Arbeit näher erläutert.

Die für die Anwendung der Massenskalierung vorgeschlagenen variationell skalierten Massen- und reziproken Massenmatrizen werden in einem gemeinsamen Rahmen als sogenannte variationell konsistente Trägheitsschablonen vorgestellt. Diese werden dann nicht nur zur Effizienzsteigerung, wie es das Ziel der Massenskalierung ist, eingesetzt, sondern können auch gezielt für verschiedene Benutzerinteressen angepasst werden. Entscheidend ist hierbei die Auswahl des geeigneten Ansatzraumes für die Geschwindigkeit. Verschiedene mögliche Ansatzräume können im Rahmen einer Mehrparameterschablone kombiniert werden. Die Anpassung der freien Schablonenparameter erfolgt mithilfe einer systematischen, analytischen Dispersionsanalyse im räumlichen Gebiet. Je nach Wahl der Parameter können dann sowohl Trägheitsmatrizen mit deutlich vergrößertem Zeitschritt gegenüber dem der diagonalen Masse konstruiert werden, sowie Trägheitsmatrizen mit höherer Genauigkeit für niedere Moden als es die konsistente Massenmatrix liefern kann.

Ein weiterer Aspekt der Arbeit ist die Weiterentwicklung und systematische Untersuchung der reziproken Massenmatrizen, um sie für ein breiteres Anwendungsgebiet zugänglich zu machen. In vorangegangenen Arbeiten wurden reziproke Massenmatrizen zunächst nur für Simplex-Elemente, homogene Materialien und kleine Verformungen untersucht. Dabei wurde beobachtet, dass sich die bestehende Formulierung nicht einfach auf Materialien mit heterogener Dichteverteilung erweitern lässt, beziehungsweise die Ergebnisse unbefriedigend sind. Die Ursache liegt in der Auswahl der Impulsansatzfunktionen. Für die Impulsansatzfunktionen werden zu den Verschiebungsansatzfunktionen biorthogonale Funktionen gewählt, da dies eine Eliminierung der Impulsfreiheitsgrade erlaubt, ohne dabei auf globalem Niveau eine Matrixinversion durchführen zu müssen. Während biorthogonale Funktionen aus der Literatur, wie sie für Mortar-Kontakt verwendet

werden, die Elementgeometrie, nicht aber die Massenverteilung des Elements (und benachbarter Elemente) berücksichtigen, muss bei der Konstruktion der biorthogonalen Funktionen für reziproke Massenmatrizen die Dichte in der Konstruktion berücksichtigt werden. Die Konsistenz der Formulierung für verschiedene Dichteverteilungen kann mithilfe von einfachen Trägheits-Element-Patch-Tests bestätigt werden. Neben der Berücksichtigung verschiedener Dichteverteilungen im Element wird auch die Auswahl der Ansatzräume für verschiedene Elementtypen und Ausgangsgeometrien diskutiert und getestet um so die variationelle Konsistenz der Formulierung sicherzustellen. Auch die Berücksichtigung von Randbedingungen und Multi-point constraints wird diskutiert.

Desweiteren wird ein konservativer Zeitschrittschätzers für reziproke Massenmatrizen vorgeschlagen. Nur wenn es eine effiziente Möglichkeit gibt, den kritischen Zeitschritt und damit zulässige Zeitschrittweiten für die Berechnung mit reziproken Massenmatrizen zu bestimmen, können die Möglichkeiten der neuen Methoden voll ausgeschöpft werden. Während für konsistente und diagonale Massenmatrizen elementweise Zeitschrittschätzer eine effiziente Methode zur Bestimmung des kritischen Zeitschritts darstellen, können für reziproke Massenmatrizen keine konservativen elementweisen Zeitschrittschätzer entwickelt werden. Diese Tatsache wird ausführlich erläutert und anschließend wird eine Erweiterung des knotenweisen Zeitschrittschätzers basierend auf dem Gershgorin-Kreis-Theorem für reziproke Massenmatrizen und Penalty-Kontakt vorgeschlagen.

Während in der gesamten Arbeit kleine Verifikationsbeispiele die gewonnenen Erkenntnisse illustrieren, wird am Ende der Arbeit durch größere Beispiele nochmals auf den möglichen Effizienz- und Genauigkeitsgewinn der vorgestellten Methoden eingegangen. Einen Ausblick auf geometrisch und materiell nichtlineare Probleme ermöglicht schlussendlich das letzte Beispiel dieser Arbeit.

Abstract

The present work deals with innovative numerical methods for the computer simulation of dynamic problems with explicit time integration. Dynamic simulations are always required if inertia forces cannot be neglected, because the process to be simulated involves large accelerations, for instance due to quickly applied loads or instability phenomena. The characteristics of explicit time integration methods are their small but cheap time steps. Additionally, there exist no convergence problems. Therefore, explicit methods are used in the field of short-term dynamics, as well as for quasi-static but highly nonlinear problems. Classical fields of application are for example the simulation of the collision of cars, the impact of a mobile phone on the floor or the simulation of a deep-drawing process of a sheet metal part.

In the past, various methods have been proposed to improve the efficiency of explicit dynamic calculations. A common technique is mass scaling. By a manipulation of the mass matrix the maximum eigenfrequency is reduced. Since the maximum eigenfrequency is reversely proportional to the critical time step, mass scaling allows larger time steps. This manipulation is often only applied to individual small or particularly stiff elements that limit the time step of the entire model. In the recent years, many approaches have been proposed to improve the original idea of conventional mass scaling: instead of preserving the diagonal structure of the mass matrix and adding mass on the diagonal only, algebraic selective mass scaling was suggested, which adds mass on the diagonal and at the same time subtracts mass on the off-diagonal in order to preserve total mass and translational inertia. Recently, in order to create mass matrices with larger critical time step not only by algebraic manipulations but based on a sound theoretical derivation variationally based, selective mass scaling approaches were proposed. Finally, with the aim to avoid the solution of a linear system of equations for non-diagonal mass matrices, reciprocal mass matrices were proposed which will be described in more detail in the following.

The innovative computational methods discussed in this work aim to increase accuracy as well as reduce the calculation effort for explicit dynamics. The basis for the development are variationally consistent inertia templates. The term ‘inertia template’ covers both alternatives to the commonly used diagonal mass matrices and novel reciprocal mass matrices. Reciprocal mass matrices result directly from the variational formulation and are sparse, assemblable, inverse mass matrices, which allow a trivial computation of the acceleration from Newton’s second law. The starting point for the derivation is Hamilton’s principle, which is modified by the introduction of three independent fields, namely the displacement, velocity and linear momentum. The resulting inertia matrices contain free parameters that allow a customization for desired properties. Possible customization goals are for example a significant reduction of the maximum eigenfrequency, as it is the goal for mass scaling, or an improvement of the accuracy and convergence behaviour for low frequencies.

The present work focuses on the following issues: First, variational consistency of reciprocal mass matrices is examined, especially for non-homogeneous density distributions and the therewith associated minimum requirements on the ansatz spaces. Second, the approach is systematically exploited not only to increase the critical time step but also to customize the inertia template for specific needs, like improved low-frequency accuracy. Third, the work aims at further development and investigation of reciprocal mass matrices to increase their usability for practical applications. The focus is therefore on the development of an efficient time step estimate, the further development of the method for a wide range of finite element types and the treatment of contact. In the following, the mentioned aspects are further explained.

The variationally scaled mass matrix and variationally scaled reciprocal mass matrix are presented within a unified framework, which is called a variationally consistent inertia template. This template is then not only used to obtain improved efficiency, as it is the aim for mass scaling, but it can be adjusted for user-specific customization goals. The decisive factor is the selection of suitable ansatz spaces for the velocity. Various ansatz spaces are combined within the framework of a multi-parametric template. The free template parameters are then adjusted using a systematic, analytical grid dispersion analysis. Depending on the choice of parameters, both inertia matrices with significantly larger time step with respect to the diagonal mass matrix are constructed and inertia matrices with higher accuracy than the consistent mass matrix for the low frequency range can be provided.

Another important aspect of the work is the further development and investigation of the reciprocal mass matrix to make it valuable for a wider range of applications. In the past, the reciprocal mass matrix was developed only for simplex elements, homogeneous materials and small deformations. Within the present work it is observed that the original formulation is not simply applicable for materials with heterogeneous density distribution, or at least the results are unsatisfactory. The reason is the choice of the linear momentum ansatz functions. In order to allow elimination of the linear momentum degrees of freedom from the formulation without matrix inversion on the global level, biorthogonal ansatz functions need to be used. Standard biorthogonal functions from literature, as they are used for mortar contact formulations, take the element geometry into account but not the mass distribution of the element (and neighboring elements). However, for the construction of the biorthogonal basis for reciprocal mass matrices the density distribution of the element needs to be taken into account. The consistency of the formulation for different density distributions can be confirmed by simple inertia element patch tests. Besides the consideration of different density distributions in the element, the appropriate choice of ansatz spaces for different finite element types and initial geometries to ensure the variational consistency of the formulation is discussed and tested. Furthermore, consideration of Dirichlet boundary conditions and multi-point constraints for reciprocal mass matrices is discussed.

At last, a conservative time step estimate for reciprocal mass matrices is proposed. Only if there is an efficient way to determine the critical time step and thus choose an

allowable time step for the calculation with reciprocal mass matrices, the possibilities of the novel method can be fully exploited. While for consistent and diagonal mass matrices elemental time step estimates are efficient and conservative for determining the critical time step, for reciprocal mass matrices, unfortunately, no conservative element-wise time step estimate can be developed. This fact is explained in detail and subsequently, an extension of the nodal time step estimate based on Gershgorin's theorem is proposed for reciprocal mass matrices and penalty contact.

While throughout the whole work small verification examples illustrate the obtained findings, the potential of the presented methods for improved efficiency and accuracy is illustrated by numerical examples at the end of the thesis. An outlook to geometrically and materially nonlinear problems is provided with the final example.

Danksagung

Die vorliegende Arbeit entstand während meiner Zeit als wissenschaftliche Mitarbeiterin am Institut für Baustatik und Baudynamik der Universität Stuttgart. Zunächst danke ich Herrn Prof. Dr.-Ing. habil. Manfred Bischoff für die Ermöglichung und Betreuung meiner Doktorarbeit. Die fachlichen Gespräche mit ihm haben immer wieder ganz neue Fragen und Gedanken aufgeworfen und die Arbeit damit bereichert. Neben der fachlichen Unterstützung danke ich ihm vor allem für die menschliche Größe und den selbstlosen Einsatz mit dem er sich für die Interessen des Instituts und für seine Mitarbeiter stark macht. Immer, aber besonders in den schwierigen Zeiten meiner Promotion, hatte ich seine vollste Unterstützung und sein Vertrauen, ohne welches diese Arbeit nicht zum Abschluss gekommen wäre. Des Weiteren bedanke ich mich bei Herrn Prof. Dr.-Ing. habil. Detlef Kuhl und Herrn Prof. José A. Gonzalez für die Übernahme des Mitberichts und die schnelle Anfertigung der Gutachten. Die in dieser Arbeit dokumentierten Forschungsergebnisse wurden durch die Deutsche Forschungsgemeinschaft (DFG) - Projektnummer BI 722-10/1 gefördert. Dieser finanziellen Unterstützung gebührt ebenfalls großer Dank!

Mein größter Dank aber gilt meinem engsten Begleiter, fachlichen Betreuer und unbezahlbaren Freund Anton, von dem ich fachlich unglaublich viel gelernt habe und der mir immer mit Rat und Tat zur Seite stand und steht. Seine fachliche Unterstützung, vor allem aber sein mentaler Beistand, seine aufbauenden Worte, seine unendliche Geduld und Kreativität mit mir und meinen Sorgen haben es überhaupt erst möglich gemacht, dass ich heute diese Zeilen schreibe. DANKE!

Des Weiteren danke ich allen Mitarbeitern des Instituts, die mich in der Zeit begleitet haben und immer ein offenes Ohr für Diskussionen und Sinnfragen hatten. Danke für die gemeinsamen Mittagessen, Konferenzen, Eistreffen, Frühstücke, Ausflüge und Forschungstage. Auch möchte ich mich herzlich bei meinen Freunden und meiner Familie bedanken, die immer für mich da sind und mich unterstützt und in schwierigen Zeiten aufgebaut haben!

Stuttgart, im Februar 2019

Anne Schäuble

Contents

List of Figures	xiii
List of Tables	xvii
Abbreviations and nomenclature	xix
1 Introduction	1
1.1 Motivation and goal of the work	1
1.2 Structure of the work	5
2 State of the art	7
2.1 Basic continuum mechanics	7
2.1.1 Motion	7
2.1.2 Deformation and strain measures	9
2.1.3 Stress measures and constitutive equations	9
2.1.4 Conservation equations	11
2.1.5 Equilibrium equation	13
2.1.6 The strong form of the initial boundary value problem (IBVP)	13
2.1.7 The virtual work principle as weak form	15
2.1.8 Hamilton's principle	16
2.2 Discretization in space	18
2.2.1 Semi-discretization with the consistent mass matrix (CMM)	18
2.2.2 Mass diagonalization	20
2.3 Discretization in time	21
2.3.1 Central difference method (CDM)	22
2.3.2 Critical time step estimates	23
2.3.3 Energy balance	28
2.4 Mass scaling methods	29
2.4.1 Conventional mass scaling (CMS)	30

2.4.2	Algebraic selective mass scaling (ASMS)	31
2.4.3	Variational selective mass scaling (VSMS)	34
2.5	Reciprocal mass matrix approaches	36
2.5.1	Inverse mass matrix by approximation	37
2.5.2	Variational selective reciprocal mass scaling (VSRMS) for simplex elements with constant density	38
2.5.3	Reciprocal mass matrices without dual basis	39
2.6	Finite element templates	40
3	Variationally consistent reciprocal mass matrices	43
3.1	Basic ideas of the direct assembly of reciprocal mass matrices	43
3.2	Variational formulation	45
3.2.1	The $\mathbf{u-v-p}$ -formulation	45
3.2.2	A remark on the $\mathbf{u-v-v}_p$ -formulation	48
3.3	Discretization in space	49
3.3.1	The general inertia template	49
3.3.2	Variationally scaled consistent mass matrices (VSMS)	51
3.3.3	Variationally scaled consistent inverse mass matrices (VSRMS)	52
3.4	Requirements on the ansatz spaces for consistency for constant density	53
3.4.1	Spaces for displacements	53
3.4.2	Spaces for velocities	54
3.4.3	Spaces for linear momenta	54
3.5	Limitations of the formulation	55
3.5.1	Verification example for constant density in 1-D	56
3.5.2	Falsification example for non-constant density	58
3.6	Improved ansatz spaces for linear momenta	59
3.6.1	Generalized construction procedure	59
3.6.2	Validation for different density distributions in 1-D	60
3.6.3	Verification for various density distributions for a 2-D serendipity element	65
3.7	Treatment of boundary conditions and MPCs	67
3.7.1	Homogeneous Dirichlet boundary conditions	67
3.7.2	Multi-point constraints	69
3.8	A brief summary of Chapter 3	70
4	Inertia customization	71
4.1	Choice of ansatz spaces for speed-up and accuracy	72
4.2	Multi-parametric template	73
4.3	Systematic tuning by grid dispersion analysis (GDA) in 1-D	75
4.3.1	Grid dispersion analysis for reciprocal mass matrices	77

4.3.2	Tuning towards optimal low-frequency accuracy	80
4.3.3	Tuning towards speed-up	83
4.3.4	Evaluation of stability	85
4.3.5	Recovery of existing mass matrices from literature	86
4.4	Grid dispersion analysis (GDA) in 2-D	87
4.5	A brief summary of Chapter 4	92
5	Time-step estimates for reciprocal mass matrices and penalty contact	95
5.1	Requirements on the novel estimate and limitations of existing ones	96
5.2	Nodal time step estimate for reciprocal mass matrices	98
5.2.1	Time step estimates for problems without contact	99
5.2.2	Time step estimates for problems with penalty contact	101
5.2.3	Rearrangements for improved efficiency	105
5.3	A brief summary of Chapter 5	108
6	Numerical examples	111
6.1	Linear transient analysis of a 3-D cantilever beam	112
6.2	Eigenfrequency analysis of a 2-D tapered structure	117
6.3	Linear transient analysis of a tapered structure under an abrupt load	120
6.4	Eigenvalue analysis and convergence study of a two-material 2-D tapered structure	121
6.5	Time step estimation for a 2-D problem with penalty contact and highly distorted mesh	123
6.6	Transient analysis of a cantilever, taking material/geometric nonlinearities into account	128
6.7	A brief summary of Chapter 6	135
7	Summary and Future Work	139
7.1	Summary	139
7.2	Future Work	141
	References	145
	Appendix	159
A	Dispersion relation for standard mass matrices for an infinite, uniform 2-D B-spline discretization	159
A.1	Consistent mass matrix (CMM)	159
A.2	Lumped mass matrix (LMM)	160
B	Reduced integrated Q1 element with stiffness/viscous hourglass control	162

List of Figures

1.1	Possible application fields for numerical simulations: car crash (left), simulation of a nitinol stent (middle) and simulation of the folding process of a beverage package (right). PSO (2006) (CC BY-SA 3.0), BONSIGNORE (2017) (CC BY 2.0), ROBERTSSON ET AL. (2018).	2
2.1	Deformation of a body, reference and current configuration.	8
2.2	Typical dispersion graph for consistent (CMM) and lumped mass matrix (LMM), here for a 1-D linear finite element.	21
2.3	Visualization of the central difference time discretization method.	23
2.4	Gershgorin's circles of matrix \mathbf{A}^* from eq. (2.69).	27
2.5	Schematic illustration of the idea of mass scaling using a one-degree-of-freedom system.	29
2.6	Qualitative illustration of the ratio of the scaled to the original eigenfrequency versus the mode number for conventional mass scaling (left) and selective mass scaling (right).	32
3.1	Assembly of two linear finite elements with identical material properties.	44
3.2	Tonti diagram of the proposed formulation.	48
3.3	Shape functions for two linear finite elements of constant density.	57
3.4	Assembly of two linear finite elements with constant, but different density.	58
3.5	Shape functions for the $\mathbf{u-v-p}$ -formulation for two linear finite elements of piecewise constant (left), linear (middle) and quadratic (right) density distribution with $\bar{\alpha} = \bar{\beta} = \bar{\gamma} = 1$.	63
3.6	Patch consisting of three serendipity finite elements.	66
3.7	Result of patch test C, where a uniform external body load is applied. The result is a rigid body movement with uniform acceleration.	67
3.8	Linear momentum ansatz function in the boundary element without modification (left) and with modification (right) in the boundary element of a quadratic B-spline patch.	68

4.1	Result of patch test C, where a uniform external body load is applied. Since the result is not a rigid body motion, the patch test is not passed.	75
4.2	Schematic illustration of a wave packet with and without dispersion.	76
4.3	Representative patch and element (marked by dashed and dotted lines) considered in the grid dispersion analysis.	78
4.4	Dispersion graph for the consistent (CMM), the lumped mass matrix (LMM) and the reciprocal mass matrix (RMM, all scaling factors are set to zero) for an infinite 1-D quadratic B-spline patch.	80
4.5	Analytical grid dispersion curves for different mass and reciprocal mass matrices for optimized low-frequency accuracy for an infinite 1-D quadratic B-spline patch.	82
4.6	Analytical dispersion curves for the variationally scaled mass matrix (VSMS) for various choices of the free parameters for an infinite 1-D quadratic B-spline patch.	83
4.7	Analytical dispersion curves for the variationally scaled reciprocal mass matrix (VSRMS) for various choices of the free parameters for an infinite 1-D quadratic B-spline patch.	84
4.8	Analytical grid dispersion curves for different mass matrices for optimized low-frequency accuracy for an infinite 1-D quadratic B-spline patch.	87
4.9	Plane wave propagating through a mesh under the angle of inclination θ	88
4.10	Dispersion relation for a 2-D quadratic B-spline patch for the variationally scaled mass (VSMS, left) and reciprocal mass matrix (VSRMS, right).	91
4.11	Dispersion error for different inclination angles θ for a 2-D quadratic B-spline patch for the variationally scaled mass matrix (VSMS) of the dilatation branch (left) and the shear branch (right).	93
4.12	Dispersion error for different inclination angles θ for a 2-D quadratic B-spline patch for the variationally scaled reciprocal mass matrix (VSRMS) of the dilatation branch (left) and the shear branch (right).	94
5.1	Problem setup for the example of the 1-D linear truss with regular and irregular mesh.	100
5.2	Visualization of the data required for row-wise (left) and column-wise (right) estimates for penalty contact.	103
5.3	Problem setup for the example of the 1-D linear truss in contact with a rigid wall.	104
5.4	1-D linear truss in contact with a rigid wall, ratio between estimated and reference time step in dependence of the penalty scale factor for different nodal estimates with the reciprocal mass matrix (VSRMS, $C_{21} = 0.99$).	105

5.5	1-D linear truss in contact with a rigid wall, ratio between estimated and reference time step in dependence of the penalty scale factor for different assumptions on the row-wise estimate with the reciprocal mass matrix (VSRMS, $C_{21} = 0.99$).	108
6.1	Setup of the 3-D-cantilever beam problem, bending load case.	112
6.2	Tip displacement history for different variationally scaled mass matrices (VSMS) for the bending load case.	113
6.3	Tip displacement history for the variationally scaled mass matrix (VSMS) in comparison with the algebraically scaled mass matrix (ASMS) for the bending load case.	114
6.4	Tip displacement history for the variationally scaled reciprocal mass matrix (VSRMS) for the bending load case.	114
6.5	Setup of the 3D-cantilever beam problem, longitudinal load case.	115
6.6	Tip displacement history for the variationally scaled mass matrix (VSMS) in comparison with the algebraically scaled mass matrix (ASMS) for the longitudinal load case	115
6.7	Tip displacement history for the variationally scaled reciprocal mass matrix (VSRMS) for the longitudinal load case.	116
6.8	Setup of the 2-D tapered structure (similar to NAFEMS FV32 benchmark). The mesh is created by quadratic NURBS.	118
6.9	Relation between scaled and reference eigenfrequency versus mode number.	118
6.10	Relation between scaled and reference eigenfrequency versus mode number for the reciprocal mass matrix (VSRMS) with small perturbations of the free parameters C_{21} (left) and C_{24} (right), respectively.	119
6.11	Displacement history at the upper right node for different mass matrices.	120
6.12	Relative error in the displacement at the upper right node with respect to the reference solution for different mass and reciprocal mass matrices	121
6.13	Setup of the FV32 NAFEMS benchmark, modelled with two different material densities. The mesh is created by quadratic NURBS.	122
6.14	Convergence plot for a two-material problem for the original (left) and novel (right) formulation.	123
6.15	Setup for the example of a Q1 highly distorted mesh with penalty contact.	124
6.16	Contour plot of the nodal time step for $f_{si} = 10.0$ for the row-wise Gershgorin estimate, interpolated from the nodal values for visualization.	125
6.17	Ratio between estimated and reference time step in dependence of the penalty scale factor for different nodal estimates for the reciprocal mass matrix (VSRMS, left) and for the lumped mass matrix (LMM, right) for a highly distorted mesh.	126

6.18	Ratio between estimated and reference time step in dependence of the penalty scale factor for different assumptions on the row-wise estimate for the reciprocal mass matrix (VSRMS, left) and for the lumped mass matrix (LMM, right) for a highly distorted mesh.	127
6.19	Critical time step in dependence of the penalty scale factor for different estimates for the reciprocal mass matrix and for the lumped mass matrix.	128
6.20	Setup of the nonlinear cantilever beam problem.	129
6.21	Energy history for the variationally scaled reciprocal mass matrix (VSRMS).	131
6.22	Tip displacement history for different methods for a moderate speed-up. .	132
6.23	Tip displacement history for the algebraically scaled mass matrix (ASMS) for moderate to large speed-ups.	132
6.24	Tip displacement history for the variationally scaled mass matrix with constant velocity ansatz functions (VSMS, const.) for moderate to large speed-ups.	133
6.25	Tip displacement history for the variationally scaled mass matrix with linear velocity ansatz functions (VSMS, lin.) for moderate to large speed-ups.	134
6.26	Energy history for the variationally scaled mass matrix (VSMS, lin.) with high speed-up (573 steps).	135
B.1	Dispersion relation for a 2-D quadratic B-spline patch for CMM (left) and LMM (right).	160
B.2	Dispersion error for the consistent mass matrix (CMM) for different inclination angles θ for the dilatation branch (left) and the shear branch (right) for a 2-D quadratic B-spline patch.	161
B.3	Dispersion error for the lumped mass matrix (LMM) for different inclination angles θ for the dilatation branch (left) and the shear branch (right) for a 2-D quadratic B-spline patch.	161

List of Tables

3.1	Check of mass preservation for different choices of $\bar{\alpha}$, $\bar{\beta}$, and $\bar{\gamma}$ for a constant, linear and quadratic spatial distribution of the density.	61
4.1	Choice of free parameters for optimal low-frequency accuracy for the 1-D quadratic and cubic B-Spline patch.	81
4.2	Dispersion relation for different mass matrices for free parameters (if present), chosen according to Table 4.1.	82
4.3	Dispersion relation for different algebraic mass matrices for a 1-D quadratic and cubic B-Spline patch.	86
4.4	Dispersion relation of the dilatation branch for different mass and inverse mass matrices for $\theta = 0$ for a 2-D quadratic B-spline patch.	90
4.5	Dispersion relation of the shear branch for different mass and inverse mass matrices for $\theta = 0$ for a 2-D quadratic B-spline patch.	90
5.1	Comparison of the maximum eigenfrequency for different eigenvalue problems.	98
5.2	Comparison of different nodal time step estimates for the variationally scaled reciprocal mass matrix (VSRMS) for regular and irregular meshes.	101
5.3	Results for different nodal time steps for different penalty stiffnesses ε_i for a 1-D linear truss in contact with a rigid wall with the reciprocal mass matrix (VSRMS, $C_{21} = 0.99$).	104
5.4	Results for different assumptions on the row-wise Gershgorin time step estimate for different penalty stiffnesses ε_i for a 1-D linear truss in contact with a rigid wall with the reciprocal mass matrix (VSRMS, $C_{21} = 0.99$).	108
6.1	Comparison of the critical time step for linear and quadratic 1-D discretizations with lumped and reciprocal mass matrix ($C_{21} = 0.99$). The distance between nodes is h , c is the wave speed.	117

6.2	Comparison of the first eigenfrequencies (in s^{-1}) for a two-material problem. The relative error is given in brackets.	122
6.3	Results for different nodal time step estimates for a highly distorted Q1 mesh for various penalty stiffnesses ε_i with the reciprocal mass matrix (VSRMS, $C_{21} = 0.99$).	125
6.4	Results for different assumptions on the row-wise Gershgorin estimate for a highly distorted Q1 mesh for various penalty stiffnesses ε_i with the reciprocal mass matrix (VSRMS, $C_{21} = 0.99$)	127
6.5	Time step size and condition number for different inertia matrices.	130
6.6	Required time interval for the mass update for the variationally scaled mass matrix with linear velocity ansatz space (VSMS,lin.).	134

Abbreviations and nomenclature

Abbreviations

ANS	assumed natural strain
ASMS	algebraic selective mass scaling
CAD	computer aided design
CDM	central difference method
CMM	consistent mass matrix
CMS	conventional mass scaling
EAS	enhanced assumed strain
FDA	full dispersion analysis
FEM	finite element method
FEA	finite element analysis
FLOPS	floating point operations per second
GDA	grid dispersion analysis
HHT	Hilber-Hughes-Taylor
HRZ	Hinton-Rock-Zienkiewicz
IBVP	initial boundary value problem
IGA	isogeometric analysis
LMM	lumped mass matrix
MPC	multi-point constraint
NURBS	non-uniform rational B-splines
PVP	Parametrized variational principle
RMM	reciprocal mass matrix
SMS	selective mass scaling
VSMS	variationally selective mass scaling
VSRRMS	variationally selective reciprocal mass scaling

Mathematic notations

$(\bullet)^{-1}$	inverse of (\bullet)
$\dot{(\bullet)}$	material time derivative of (\bullet)
$\ddot{(\bullet)}$	second material time derivative of (\bullet)
$(\bullet)^T$	transposed of (\bullet)
$(\bullet)^{-T}$	transposed of the inverse of (\bullet)
$(\bullet)^{23T}$	transposed of the second and third component of a symmetric fourth order tensor (\bullet)
$\det(\bullet)$	determinant of (\bullet)
$\text{Div}(\bullet)$	divergence of (\bullet) w.r.t. the reference configuration
$\frac{d(\bullet)}{d(\bullet)}$	total derivative
$\frac{\partial(\bullet)}{\partial(\bullet)}$	partial derivative
$\delta(\bullet)$	variation of (\bullet)
$\text{Grad}(\bullet)$	gradient of (\bullet) w.r.t. the reference configuration
$\ln(\bullet)$	natural logarithm of (\bullet)
$\Re(\bullet)$	real part of (\bullet)
$\Im(\bullet)$	imaginary part of (\bullet)
$\text{tr}(\bullet)$	trace of (\bullet)
$(\bullet \otimes \bullet)$	dyadic product of \bullet and \bullet
$\mathcal{O}(\bullet)$	Big O notation, grows not faster than (\bullet)
$\mathcal{F}(\bullet)$	operator returning indices of non-zero entries of a sparse vector
$\ (\bullet)\ _1$	L1 norm of the vector (\bullet)
$\square_{i,:}$	row-extraction operator to extract row i
\cup_e	assembly operator, assembly over all elements e
\cup	union
\cap	intersection
\emptyset	empty set
\forall	for all
\in	element of

Latin letters

A	area
-----------	------

A_j	contact face area of element j
a_1, a_2	Rayleigh damping parameters
\mathbf{a}	acceleration vector of a material point
$\mathbf{a}^{\text{ave}}, \mathbf{a}^{\text{diff}}$	average/difference acceleration vector in a solid shell finite element
$\mathbf{a}^{\text{up}}, \mathbf{a}^{\text{low}}$	upper/lower acceleration vector in a solid shell finite element
\mathbf{A}	global dimensionless projection matrix
\mathbf{A}_∞	global dimensionless projection matrix of an infinite patch
\mathbf{a}_e	dimensionless projection matrix of element e
\mathbf{A}^*	exemplary square matrix
$\hat{\mathbf{b}}$	prescribed body acceleration
$\bar{\mathbf{B}}$	strain-displacement operator
\mathbf{B}	global weighted projection matrix
\mathbf{b}_e	weighted projection matrix of element e
C_1, C_2, C_3	inertia scaling parameters
$C_{2\alpha}$	inertia template parameters for the scaled reciprocal mass matrix with different choices of Ψ_α
$C_{3\alpha}$	inertia template parameters for the scaled mass matrix with different choices of Ψ_α
c	wave speed in 1-D
c_0	wave speed (phase velocity) in 1-D continuum
c_d	dilatation phase velocity in 2-D
c_s	shear phase velocity in 2-D
c_{d0}	dilatation phase velocity in 2-D continuum
c_{s0}	shear phase velocity in 2-D continuum
c_j	parameter in the construction of the dual basis
$\bar{\mathbf{C}}$	right Cauchy-Green tensor
\mathbf{C}	reciprocal mass matrix
\mathbf{C}°	scaled reciprocal mass matrix
\mathbf{c}_e°	scaled reciprocal mass matrix of element e
\mathbf{c}_e	reciprocal mass matrix of element e
\mathbf{C}_∞°	scaled reciprocal mass matrix of an infinite patch
\mathbf{C}_∞	reciprocal mass matrix of an infinite patch
$\mathbf{C}^{\text{mic},1}$	inverse mass matrix from first order approximation
$\mathbf{C}^{\text{mic},2}$	inverse mass matrix from second order approximation

\mathcal{C}	damping matrix
\mathbb{C}	set of complex numbers
$\overset{4}{\mathbf{C}}$	fourth-order material tensor
\mathbf{D}	elastic modulus (in Voigt notation)
E	elastic modulus
$e(z)$	center of Gershgorin's circle \bar{S}_i in the complex plane
\mathcal{E}^3	Euclidean space
$\mathbf{e}_1, \mathbf{e}_2, \mathbf{e}_3$	normalized basis vectors of the Cartesian coordinate system
\mathbf{E}	Green-Lagrangean strain tensor
\mathbf{F}	deformation gradient
\mathbf{F}^{tot}	total force vector
$\mathbf{F}_n^{\text{tot}}$	total force vector at time step n
$\mathbf{F}^{\text{int}}, \mathbf{F}^{\text{ext}}$	global internal/external force vector
$\mathbf{F}_n^{\text{int}}, \mathbf{F}_n^{\text{ext}}$	global internal/external force vector at time step n
\mathbf{F}^{damp}	global damping force vector
$\mathbf{f}_e^{\text{int}}, \mathbf{f}_e^{\text{ext}}$	internal/external force vector of element e
\mathbf{F}^{cont}	global contact force vector
$\mathbf{F}_n^{\text{cont}}, \mathbf{F}_n^{\text{cont}}$	global contact force vector at time step n
f_{si}	scale factor for the interface stiffness
\mathbf{g}_0	vector of constraint offsets
\mathbf{g}_{N0j}	initial normal gap at contact constraint j
\mathbf{g}_{Nj}	normal gap at contact constraint j
\mathbf{G}	constraint matrix of a multi-point constraint
\mathbf{G}_i	constraint vector of contact constraint i
$H(\mathbf{u})$	Hamiltonian
H_e°	Hamiltonian with modified kinetic energy of element e
H_{iso}	isotropic hardening modulus
H_{kin}	kinematic hardening modulus
\mathbf{I}	second-order identity tensor or identity matrix
k	stiffness of a 1-dof system (in Chapter 2)
k	wave number (in Chapter 4)
\mathbf{k}	wave vector
K_j	bulk modulus of element j
\mathbf{K}^{P}	penalty stiffness matrix (assembled from all active contacts)
\mathbf{K}_i^{P}	penalty stiffness matrix of contact constraint i

$k_{p,i}^{\text{scal}}$	scalar value of the penalty stiffness at degree of freedom i
\mathbf{K}	stiffness matrix
\mathbf{k}_e	stiffness matrix of element e
\mathbf{K}_∞	stiffness matrix of an infinite patch
\mathbf{K}_b	basic stiffness matrix
\mathbf{K}_h	higher-order stiffness matrix
l	length
l_c	characteristic element length
l_{mic}	micro-inertia length scale
\mathbf{L}	differential operator
\mathcal{L}	lower triangular matrix of the Cholesky decomposition of \mathbf{C}°
m	mass of a 1-dof system
m_e	mass of element e
m°	scaled mass of a 1-dof system
\mathbf{M}	consistent mass matrix
\mathbf{m}_e	consistent mass matrix of element e
\mathbf{M}^D	diagonal mass matrix
\mathbf{m}_e^D	diagonal mass matrix of element e
\mathbf{M}^{inv}	inverse of the diagonal mass matrix
\mathbf{M}°	scaled mass matrix
\mathbf{m}_e°	scaled mass matrix of element e
\mathbf{M}_∞°	scaled mass matrix of an infinite patch
\mathbf{M}^m	micro-inertia mass matrix
\mathbf{m}_e^m	micro-inertia mass matrix of element e
\mathbf{M}_x	first sub-matrix of a tensor-product structure
\mathbf{M}_y	second sub-matrix of a tensor-product structure
$\mathbf{m}_e^{\text{ave}}, \mathbf{m}_e^{\text{diff}}$	average/difference mass matrix of solid shell finite element e
\mathbf{m}_e^*	metric of element e
n_{dof}	matrix size
n_n	number of nodes
n_c	number of constrained degrees of freedom
$n_{\text{max}}^{\text{iter}}$	maximum number of iterations in the eigenvalue estimate
\mathbf{n}	outer normal vector
\mathbf{N}	displacement ansatz function matrix
N_i	i^{th} displacement ansatz function

P	mechanical power
P_i	Legendre polynomial of i^{th} order
p	characteristic polynomial
\mathbf{p}	linear momentum of a material point
\mathbf{p}^h	approximated linear momentum
\mathcal{P}	material point
\mathbf{P}	discrete linear momentum
\mathbf{P}_e	discrete elemental linear momentum
\mathbf{P}_n	discrete linear momentum at time step n
$\hat{\mathbf{P}}$	amplitude of the plane wave ansatz in 2-D for the linear momentum
\hat{P}	amplitude of the plane wave ansatz in 1-D for the linear momentum
r	radius of Gershgorin's circle
\mathcal{S}	sum (used in the construction of the algebraically scaled mass matrix)
S	speed-up in terms of the computational time
\mathbf{S}	second Piola-Kirchhoff stress
$\bar{S}_i(e(z), r)$	Gershgorin's circle with center $e(z)$ and radius r
t	time
Δt	time step size
Δt_{crit}	critical time step size
$\Delta t_{\text{crit,ref}}$	reference critical time step size
$\Delta t_{\text{crit}}^{\circ}$	critical time step size of a system with mass scaling
$\Delta t_{\text{crit}}^{\text{row-wise, pen}}$	critical time step for the reciprocal mass matrix obtained with the row-wise Gershgorin estimate with penalty contact
$\Delta t_{\text{crit}}^{\text{row-wise}}$	critical time step for the reciprocal mass matrix obtained with the row-wise Gershgorin estimate
$\Delta t_{\text{crit}}^{\text{col-wise, pen}}$	critical time step for the reciprocal mass matrix obtained with the column-wise Gershgorin estimate with penalty contact
$\Delta t_{\text{crit}}^{\text{col-wise}}$	critical time step for the reciprocal mass matrix obtained with the column-wise Gershgorin estimate
$\Delta t_{\text{crit}}^{\text{symm, pen}}$	critical time step for the reciprocal mass matrix obtained with the symmetric Gershgorin estimate with penalty contact
$\Delta t_{\text{crit}}^{\text{symm}}$	critical time step for the reciprocal mass matrix obtained with the symmetric Gershgorin estimate

$\Delta t_{\text{crit}}^{\text{glob. it.}}$	critical time step for the reciprocal mass matrix obtained with the global iterative estimate
$\Delta t_{\text{crit}}^{\text{rw. + trngl., pen}}$	critical time step for the reciprocal mass matrix obtained with the row-wise Gersghorin estimate for penalty contact, with triangle inequality
$\Delta t_{\text{crit}}^{\text{rw. + trngl. + pen., pen}}$..	critical time step for the reciprocal mass matrix obtained with the row-wise Gersghorin estimate for penalty contact, with triangle inequality and assumption on the penalty stiffness
Δt_{SMS}	time step size for computation with lumped mass matrix
Δt_{LMM}	time step size for computation with scaled mass matrix
t_0	initial time of the considered time interval
t_{end}	final time of the considered time interval
t_n	time at time step n
\mathbf{t}	traction at an arbitrary cutting plane
$\hat{\mathbf{t}}$	prescribed traction
T_{LMM}	computation time of a simulation with lumped mass matrix
T_{SMS}	computation time of a simulation with selectively scaled mass matrix
T_0	computation time for initialization
$T_{\Delta t}$	computation time for one time step
T_{ele}	computation time for element processing
T_{solver}	computation time for solving a linear system of equations
\mathbf{T}	Cauchy stress
$\bar{\mathbf{T}}$	global support
$\bar{\mathbf{t}}_e$	local support of element e
$\bar{t}_{e,i}$	local support of degree of freedom i of element e
\mathbf{u}	displacement of a material point
$\dot{\mathbf{u}}$	velocity of a material point
$\ddot{\mathbf{u}}$	acceleration of a material point
$\hat{\mathbf{u}}$	prescribed displacement
\mathbf{u}_0	initial displacement
\mathbf{u}^h	approximated displacement
$\ddot{\mathbf{u}}^h$	approximated acceleration
\mathbf{P}_∞	discrete linear momentum of an infinite patch
$\Delta \mathbf{U}$	displacement increment

\mathbf{U}	discrete displacement
\mathbf{U}_∞	discrete displacement of an infinite patch
\mathbf{U}_n	discrete displacement at time step n
\hat{U}	amplitude of the plane wave ansatz in 1-D for the displacement
$\hat{\mathbf{U}}$	amplitude of the plane wave ansatz in 2-D for the displacement
$\dot{\mathbf{U}}$	discrete velocity
$\dot{\mathbf{U}}_n$	discrete velocity at time step n
$\dot{\mathbf{U}}_d$	velocity at degrees of freedom with velocity boundary condition
$\dot{\hat{\mathbf{U}}}_d$	prescribed discrete velocity at degrees of freedom with velocity boundary condition
\mathbf{U}_0	discrete initial displacement
$\dot{\mathbf{U}}_0$	discrete initial velocity
$\ddot{\mathbf{U}}$	discrete acceleration
$\ddot{\mathbf{U}}_n$	discrete acceleration at time step n
\mathbf{U}_e	discrete elemental displacement
$\ddot{\mathbf{U}}_e$	discrete elemental acceleration
V_j	volume of element j
\mathbf{v}	velocity of a material point
\mathbf{v}_p	mass-specific linear momentum of a material point
\mathbf{v}_0	initial velocity
\mathbf{v}^h	approximated velocity
\mathbf{V}_e	discrete elemental velocity
W_{kin}	kinetic energy
W_{kin}°	modified kinetic energy
W_{kin}^n	kinetic energy at time step n
$w_{\text{int}}(\mathbf{E})$	strain energy function
W_{int}	internal energy
W_{int}^n	internal energy at time step n
W_{ext}	external energy
W_{ext}^n	external energy at time step n
W_{damp}	damping energy
W_{damp}^n	damping energy at time step n
W_{cont}	contact energy
W_{cont}^n	contact energy at time step n

\mathbf{W}	global dimensionless projection matrix
\mathbf{w}_e	dimensionless projection matrix of element e
x	coordinate
\mathbf{x}	position vector of a material point in the current configuration
\mathbf{X}	position vector of a material point in the reference configuration
\mathbf{Y}	global mass matrix on the space \mathbf{V}
\mathbf{y}_e	mass matrix on the space \mathbf{V} of element e
\mathbf{Z}	global vector of the discrete reaction forces
z	complex number

Greek letters

α	parameter for conventional mass scaling
β	parameter for algebraic selective mass scaling
$\bar{\alpha}, \bar{\beta}, \bar{\gamma}, \bar{\delta}$	parameters for the construction of the dual basis
Γ_0, Γ	boundary surface in reference/current configuration
Γ_u	boundary surface with Dirichlet boundary condition
Γ_σ	boundary surface with Neumann boundary condition
$\Gamma_{\sigma e}$	element boundary surface with Neumann boundary condition
δ_{ij}	Kronecker symbol
$\boldsymbol{\varepsilon}$	linearized or engineering strain (in Voigt notation)
ε_i	penalty stiffness at contact constraint i
ϵ	convergence tolerance
η	local coordinate
θ	inclination angle of a plane wave
κ	dimensionless wave number
$\boldsymbol{\varkappa}$	mass-specific linear momentum ansatz function matrix
λ	first Lamé parameter
λ_{\max}	maximum eigenvalue of the system
λ_{\max}^E	maximum of all elemental eigenvalues
λ_i	i^{th} eigenvalue of the system
λ_i^e	i^{th} eigenvalue of the element e
λ_{\max}^i	estimate for the maximum eigenvalue in iteration i of the iterative eigenvalue estimate

λ°	added mass
λ_e°	added mass of element e
$\tilde{\lambda}^\circ$	added inverse mass
Λ	diagonal matrix with eigenvalue λ_i on the i^{th} diagonal entry
μ	second Lamé parameter
ν	Poisson's ratio
ξ	local coordinate
ρ_0, ρ	density in reference/current configuration
ρ_i	arbitrary coefficients to construct a density distribution
σ_{PK1}	first Piola-Kirchhoff stress tensor
σ	linearized stress (in Voigt notation)
σ_y	yield stress
$\sigma_\infty, \sigma_{\text{exp}}$	hardening parameters
ϕ	placement function
ϕ_i	i^{th} eigenvector of the system
ϕ_i^e	i^{th} eigenvector of element e
ϕ_i^{L}	i^{th} left eigenvector of the system
$\phi_i^{\text{L},e}$	i^{th} left eigenvector of element e
ϕ^0	initial eigenvector in the iterative eigenvalue estimate
ϕ^i	eigenvector of iteration i in the iterative eigenvalue estimate
φ_i	i^{th} eigenvector of the symmetric system after Cholesky decomposition
Φ	matrix containing all eigenvectors ϕ_i
χ	linear momentum ansatz function matrix
χ_i	i^{th} linear momentum ansatz function
$\hat{\chi}$	intermediate matrix for computing the linear momentum ansatz function matrix, before scaling with the local and global support
$\tilde{\chi}$	intermediate matrix for computing the linear momentum ansatz function matrix, before scaling with the global support
$\tilde{\chi}_{\text{mod}}$	intermediate matrix for computing the linear momentum ansatz function matrix, before scaling with the global support, modified due to Dirichlet boundary conditions
Ψ_i^{xD}	velocity ansatz function matrix for the x-dimensional case with constant ($i = 1$), rigid-body motion ($i = 2$), decoupled up to linear ($i = 3$) or complete up to linear ($i = 4$) ansatz space

Ψ	velocity ansatz function matrix
ψ^0	initial vector in the iterative eigenvalue estimate
ψ^i	vector of iteration i in the iterative eigenvalue estimate
Ω_0, Ω	domain of a body in the reference/current configuration
Ω_e	element domain
Ω	dimensionless circular frequency of a plane wave (in the GDA in Chapter 4)
ω	circular frequency of a plane wave (in the GDA in Chapter 4)
ω	eigenfrequency of a 1-dof system
ω°	scaled eigenfrequency of a 1-dof system
ω_i	i^{th} eigenfrequency of the system
ω_i^e	i^{th} eigenfrequency of the element e
ω_{\max}	maximum eigenfrequency of the system
$\omega_{\max}^{\text{LMM}}$	maximum eigenfrequency of the system for the lumped mass matrix
$\omega_{\max}^{\text{LMM,pen}}$	maximum eigenfrequency of the system for the lumped mass matrix with penalty contact
$\omega_{\max}^{\text{row-wise}}$	maximum eigenfrequency for the reciprocal mass matrix with the row-wise Gershgorin estimate
$\omega_{\max}^{\text{col-wise}}$	maximum eigenfrequency for the reciprocal mass matrix with the column-wise Gershgorin estimate
$\omega_{\max}^{\text{symm}}$	maximum eigenfrequency for the reciprocal mass matrix with the symmetric Gershgorin estimate

1

Introduction

The present work deals with the development of variationally consistent inertia templates for speed-up and customization in explicit dynamics. Before the title and therewith the goals of this thesis are explained in more detail, a short introduction to the topic is provided and the topic is classified in the field of numerical computations for structural mechanics. Finally, this first chapter closes with an explanation of the structure of the present work.

1.1 Motivation and goal of the work

Numerical computations are used in many engineering disciplines, for example in mechanical and automotive engineering, in civil engineering, as well as in medical engineering or packaging industry, to mention only a few. The purpose of numerical computations is to better understand and optimize processes or products. Simulations often replace measurements in the early development stage and thus help to save time and money in the development process. They are used in areas where the effects of failure are serious and of significant importance, such as when modelling the collision of cars, the stability failure of shell structures or when simulating medical products and surgeries, see Figure 1.1 (left and middle).

These days, simulations are also used to model processes in detail which seem to have only small impact on the customer but may provide a decisive competitive advantage for a company over their competitors. Examples from the packaging industry are the simulation of the opening process of a beverage package to optimize the sealing cap (CONFALONIERI ET AL. 2018) or the simulation of the folding process of a beverage package (ROBERTSSON ET AL. 2018) as illustrated in Figure 1.1 (right). Especially due to improved computer capacities and the urge to increase efficiency and digitize

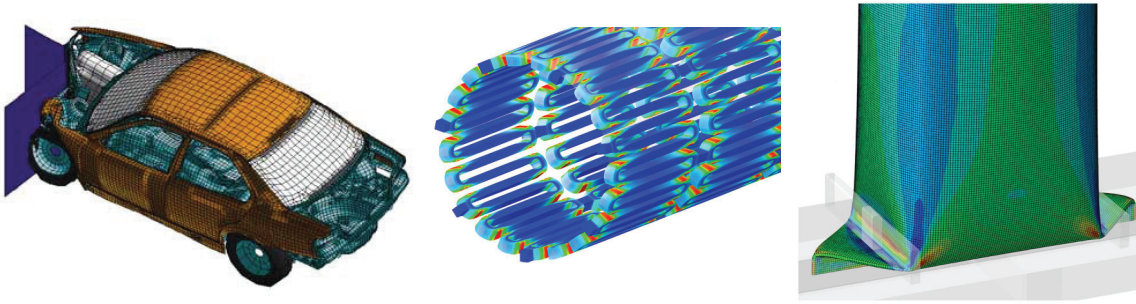


Figure 1.1: Possible application fields for numerical simulations: car crash (left), simulation of a nitinol stent (middle) and simulation of the folding process of a beverage package (right). PSO (2006) (CC BY-SA 3.0), BONSIGNORE (2017) (CC BY 2.0), ROBERTSSON ET AL. (2018).

processes, numerical calculations have become more and more important in the recent decades and will probably become even more important in the future.

The most important numerical computational method in structural mechanics is the finite element method (FEM), where the domain is divided into elements of simple shape, whose deformation is easy to describe. The finite element method was developed in the 1960's and it was initially applied to structural problems. Later, it was understood that the same method can be applied to any problem described by partial differential equations, where the analytical solution is often difficult or impossible to obtain. Apart from structural mechanics, the finite element method is for example used in acoustics, thermal analyses or coupled problems like electromagnetics, piezoelectrics or fluid-structure interaction problems.

The present work focuses on structural mechanical problems, where inertia effects can not be neglected, i.e. structural dynamics. In order to solve a problem in structural dynamics, the finite element method is usually applied first to discretize in space and obtain the semi-discrete equation of motion. Then, a solution in the time or frequency domain is carried out. In the present work, explicit time discretization with the central difference method is used, which is applied for example in car crash, deep drawing or drop test simulations to robustly model highly nonlinear processes. The advantage of the explicit time discretization algorithm over the implicit one is that no iterative solution of the balance equation on the global level is necessary. However, the method allows only small time steps due to its conditional stability.

In the past, many methodological ideas to speed-up explicit dynamic finite element analyses were suggested. One idea is for example to increase the efficiency directly by using more efficient finite element formulations, i.e. the computational effort for the internal force computation is reduced. This is for example the case for one-point integrated

4-node quadrilateral and 8-node hexahedral solid finite elements with hourglass stabilization of FLANAGAN AND BELYTSCHKO (1984) and BELYTSCHKO AND BINDEMAN (1991). For these reduced integrated elements, the reduction of the computational effort is proportional to the number of saved integration points. Additionally to the fact that the one-point integrated elements are very efficient, they are locking-free. Therefore, they provide a more accurate solution with a coarse mesh than standard finite element formulations for many problems. Thus, alternatively to focusing on more efficient finite element formulations, more accurate finite element formulations can as well be of interest to speed-up explicit analyses. Recently, a locking-free finite element for explicit dynamics based on the method of incompatible modes was for example proposed by MATTERN ET AL. (2015).

A third approach to speed-up explicit analysis, which as well manipulates the finite element formulation, is mass scaling. A modification of the mass matrix allows an increase of the stable time step size and therefore less time steps are needed for the simulation. The original implementation of this idea is conventional mass scaling, where by a simple artificial increase of the density the allowable time step is increased. On one side, this method preserves the diagonal structure of the mass matrix. On the other side, the increase of the density influences all eigenfrequencies equally and therefore the method is to be applied only locally to the few small or stiff elements which limit the time step.

The idea of conventional mass scaling was further developed in the form of algebraic selective mass scaling approaches for solid as well as for shell finite elements. In the approach of selective mass scaling, not all eigenfrequencies of the system or the element are equally decreased, but only selective modes are altered (cf. COCCHETTI ET AL. (2013, 2015); CONFALONIERI ET AL. (2015); OLOVSSON ET AL. (2005, 2004)). Since not all modes always participate in the transient solution, the relevant – usually low-frequency modes – are kept unaltered, whereas the high-frequency modes are influenced by the mass scaling parameter.

In the present work, variationally consistent inertia templates for speed-up and customization in explicit dynamics are provided. According to the title, three different aspects are included:

- The work is based on a variational formulation.
- Both mass matrices and reciprocal (i.e. inverse) mass matrices are considered.
- The proposed method does not only aim for a substantial speed-up with respect to the usual diagonal mass matrix but it can also be used for customization (i.e. tuning for specific needs like optimal low-frequency accuracy).

These three aspects are further explained in the following.

Both this work and the prior work of TKACHUK (2013) make use of a variational formulation based on Hamilton’s principle with three independent unknowns: the displacement, the velocity and the linear momentum. Presupposing a correct choice of ansatz spaces – which will also be an important topic of this work – consistency is guaranteed and consequently the inertia patch test (cf. TKACHUK (2013)) is successfully passed.

The earlier mentioned selective mass scaling approaches provided an alternative to the commonly used lumped mass matrix. However, the obtained mass matrix is non-diagonal. Therefore, a linear system of equations has to be solved in every time step. In this work, both alternative mass matrices as well as so-called reciprocal mass matrices are considered. The latter were first proposed by TKACHUK AND BISCHOFF (2015) for simplex elements in a variational setup. The basic idea of the reciprocal mass matrix is to directly construct an inverse mass matrix so that the nodal accelerations are easily obtained from the total force vector without the need of solving a linear system of equations. Since both mass and reciprocal mass matrices result from the same formulation, they are united in the terminology ‘inertia matrices’. (Similarly, the terms ‘inertia templates’ or ‘inertia scaling’ are used herein instead of ‘mass scaling’ or ‘mass templates’ to emphasize that both mass matrices and reciprocal mass matrices are considered.)

While in the context of mass scaling the goal is to obtain a significant speed-up with respect to the lumped mass matrix, the developed inertia template can not only be tuned for large speed-up, but also systematically for other customization goals. A systematic tuning of the introduced free parameters (which justify the term ‘template’) allows for example a more accurate solution than it can be obtained with the consistent mass matrix, by tuning the template to a higher-order accurate mass or reciprocal mass matrix.

The present work focuses especially on three aspects of variationally consistent inertia templates for solid finite elements: First, the existing variational formulation is critically examined and its appropriate ansatz spaces, especially for inhomogeneous density distributions, are discussed. Second, the idea of customization is applied to tune the obtained template for specific needs. Third, an appropriate time step estimate for reciprocal mass matrices is proposed.

In the following, the objectives of the present work are further examined and formulated in form of questions which are to be answered:

- The variationally consistent reciprocal mass matrices were initially only proposed for simplex elements by TKACHUK AND BISCHOFF (2015), i.e. for 2-node rods, 3-node triangles and 4-node tetrahedrons in 1-D to 3-D. Is it possible to extend

the idea of directly constructed variationally consistent reciprocal mass matrices to a wide range of solid elements? Which speed-up can be obtained?

- In combination with heterogeneous media surprisingly bad results were observed with the initially proposed reciprocal mass matrices by TKACHUK AND BISCHOFF (2015). Even consistency was observed to be violated. Does a consistent formulation with improved performance with respect to the existing formulation for heterogeneous media exist?
- In previous works, the variationally constructed mass and inverse mass matrices were only used in the context of mass scaling to increase the critical time step and to allow computations with larger time steps. Is there a systematic way to choose optimal ansatz spaces for a specific customization goal? Apart from maximum speed-up customization goals could be higher-order low-frequency accuracy or improved dispersion behaviour. Which requirements do the ansatz spaces have to meet to guarantee stability?
- To date, the maximum eigenfrequency to determine the critical time step is obtained from the eigenvalue problem on the global level, e.g. by the forward iteration method. This provides an accurate, but very expensive estimate. Is there a conservative and efficient alternative on the local level to determine the critical time step for reciprocal mass matrices?

1.2 Structure of the work

The present work is structured as follows: In Chapter 2 the basics to understand this work are reviewed. This includes a review of basic continuum mechanics, the spatial discretization by the finite element method and the temporal discretization by the central difference method. In this work, the semi-discrete equation of motion is derived based on Hamilton's principle. The equivalence with the standard approach, where the semi-discrete equation is derived from the virtual work principle, is shown. The chapter closes with a summary of existing work in the field of inertia scaling and finite element templates, which form the basis of the developments presented in the following chapters. In Chapter 3 the variational framework for the inertia templates is presented. The chapter concentrates mainly on reciprocal mass matrices, since many aspects have no influence on the variationally scaled mass matrices, but are crucial for the reciprocal ones. The focus in this chapter is on the appropriate choice of ansatz functions to guarantee consistency and stability for non-constant density and the generalization of the construction for non-simplex solid finite elements. The findings are verified by

inertia patch tests. While Chapter 3 focuses on the minimal requirements for consistency, Chapter 4 aims to provide a framework that allows tuning of the proposed mass and inverse mass matrices for specific needs. The core element for this purpose is a novel multi-parametric template, allowing the systematic investigation of various ansatz spaces for spatial discretization. A possible customization goal is for example the tuning towards optimal low-frequency accuracy. The customization is performed by analytical grid dispersion analyses in 1-D and 2-D by the example of B-spline finite elements. In Chapter 5 a novel, local time step estimate for reciprocal mass matrices is proposed. In Chapter 6 the advances made in this work are supported by numerical examples. First, the customization power of the proposed multi-parametric template is shown. Second, a two-material example is considered to illustrate the improvements that were made by the modifications in the ansatz spaces. Third, the conservativeness and efficiency of the novel local time step estimate is confirmed by the example of a highly distorted mesh in 2-D with penalty contact. The last example shows the applicability of the proposed method in the nonlinear regime. In Chapter 7 a summary is given and future perspectives for possible research are outlined.

State of the art

In this chapter the basics to understand the present work are summarized. This includes a short summary of the basic continuum mechanics, spatial discretization by the finite element method and discretization in time by the central difference method, as well as a summary of the preliminary work in the field of inertia scaling and templates.

For further reading on continuum mechanics, the books of HOLZAPFEL (2010) and WRIGGERS (2001) are suggested. Details on finite element fundamentals can for example be found in BELYTSCHKO ET AL. (2014) and in ZIENKIEWICZ AND TAYLOR (2006). Algorithmic details are comprehensively described in the book of BATHE (1982) on finite element procedures. Variational principles in dynamics, which are the starting point for inertia templates, are for example described in WASHIZU (1982) and MURA ET AL. (1992). For further reading on (mass) templates the papers of FELIPPA ET AL. (2015) and FELIPPA (2004) are recommended as a good starting point.

2.1 Basic continuum mechanics

Even though most of the methodical developments presented in this work can be explained equally well in a linear and a nonlinear setting, the description is started from the more general case of nonlinear continuum mechanics. Later, simplifications are introduced wherever used.

2.1.1 Motion

The deformation and motion of a continuous body, which can generally be a solid or a fluid, is described by distinguishing between its reference and current configuration as shown in Figure 2.1. The continuous body consists of material points \mathcal{P} , which have at

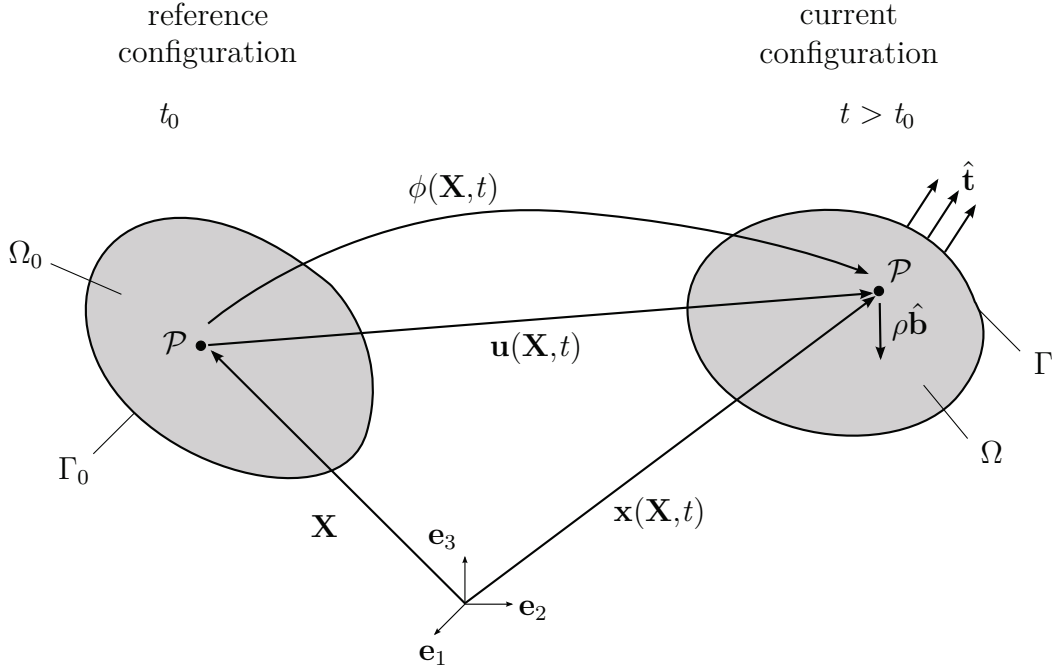


Figure 2.1: Deformation of a body, reference and current configuration.

any time t a unique position in the Euclidean point space \mathcal{E}^3 with the current position

$$\mathbf{x} = \phi(\mathbf{X}, t), \quad (2.1)$$

where \mathbf{x} is the spatial or Eulerian coordinate and ϕ is the placement function mapping from the reference to the current configuration. Herein, as it is usually the case in solid mechanics, a Lagrangian description is used, i.e. the independent variable is the material coordinate \mathbf{X} and all quantities are expressed in dependence of the material coordinate \mathbf{X} and time t . The displacement \mathbf{u} of a material point is expressed by the difference of the current and the reference position with

$$\mathbf{u}(\mathbf{X}, t) = \mathbf{x}(\mathbf{X}, t) - \mathbf{X}. \quad (2.2)$$

The velocity \mathbf{v} and the acceleration \mathbf{a} are expressed by

$$\mathbf{v}(\mathbf{X}, t) = \frac{\partial \mathbf{u}(\mathbf{X}, t)}{\partial t} = \dot{\mathbf{u}}, \quad (2.3)$$

$$\mathbf{a}(\mathbf{X}, t) = \frac{\partial \mathbf{v}(\mathbf{X}, t)}{\partial t} = \dot{\mathbf{v}}. \quad (2.4)$$

Here, the time derivative is taken with \mathbf{X} held constant, also referred to as the material time derivative.

2.1.2 Deformation and strain measures

In nonlinear continuum mechanics the deformation of a body is described by the deformation gradient

$$\mathbf{F}(\mathbf{X}, t) = \frac{\partial \mathbf{x}(\mathbf{X}, t)}{\partial \mathbf{X}} = \text{Grad } \mathbf{x} = \mathbf{I} + \text{Grad } \mathbf{u}, \quad (2.5)$$

where $\text{Grad}(\cdot)$ is the differential operator with respect to the reference configuration with $\text{Grad}(\cdot) = \frac{\partial(\cdot)}{\partial \mathbf{X}}$. \mathbf{I} is the second-order identity tensor. With the help of the deformation gradient \mathbf{F} the mapping of an infinitesimal material fiber $d\mathbf{X}$ in the initial configuration to its position $d\mathbf{x}$ in the current configuration is described by linear mapping with

$$d\mathbf{x} = \mathbf{F} d\mathbf{X}. \quad (2.6)$$

In order to measure the straining many different strain measures exist. One is the Green-Lagrangian strain

$$\begin{aligned} \mathbf{E} &= \frac{1}{2} (\bar{\mathbf{C}} - \mathbf{I}) = \frac{1}{2} (\mathbf{F}^T \mathbf{F} - \mathbf{I}) = \frac{1}{2} ((\mathbf{I} + \text{Grad } \mathbf{u})^T (\mathbf{I} + \text{Grad } \mathbf{u}) - \mathbf{I}) \\ &= \frac{1}{2} (\text{Grad}^T \mathbf{u} + \text{Grad } \mathbf{u} + \text{Grad}^T \mathbf{u} \text{Grad } \mathbf{u}). \end{aligned} \quad (2.7)$$

$\bar{\mathbf{C}}$ is the right Cauchy-Green tensor. Linearization of the Green-Lagrangian strain \mathbf{E} (as well as any other strain) results in the linearized (or engineering) strain

$$\boldsymbol{\varepsilon} = \frac{1}{2} (\text{Grad}^T \mathbf{u} + \text{Grad } \mathbf{u}). \quad (2.8)$$

The engineering strain $\boldsymbol{\varepsilon}$ is inappropriate for large deformations, since large rigid body rotations result in nonzero strains. For large displacements and rotations but small strains usually the Green-Lagrangian strain measure \mathbf{E} is used. In case of large strains the logarithmic strain provides reasonable results.

2.1.3 Stress measures and constitutive equations

The true, physical stresses are measured by the Cauchy stresses \mathbf{T} , which are related to the current (deformed) configuration. They are related to the traction \mathbf{t} acting on an arbitrary cutting surface by Cauchy's theorem with

$$\mathbf{t}(\mathbf{X}, \mathbf{n}, t) = \mathbf{T}(\mathbf{X}, t) \mathbf{n}, \quad (2.9)$$

where \mathbf{n} is the outer normal of the cutting surface. Through a covariant pull-back to the reference configuration, the second Piola-Kirchhoff stress \mathbf{S} is obtained resulting in

$$\mathbf{S} = (\det \mathbf{F})\mathbf{F}^{-1}\mathbf{T}\mathbf{F}^{-T}, \quad (2.10)$$

i.e. the second Piola-Kirchhoff stresses are fully related to the reference configuration.

Saint Venant-Kirchhoff material model

The most simple material law relating the energetically conjugate Green-Lagrangian strain \mathbf{E} and the second Piola-Kirchhoff stress \mathbf{S} is the Saint Venant-Kirchhoff material model with

$$\mathbf{S} = \overset{4}{\mathbf{C}}\mathbf{E}, \quad (2.11)$$

where $\overset{4}{\mathbf{C}}$ is the fourth-order material tensor. Eq. (2.11) describes a hyperelastic material, valid in the small strain regime only. Hyperelastic material laws are derived from a potential, thus the material tensor can be derived from the strain energy function $w_{\text{int}}(\mathbf{E})$ with

$$\overset{4}{\mathbf{C}} = \frac{\partial^2 w_{\text{int}}(\mathbf{E})}{\partial \mathbf{E} \partial \mathbf{E}} \quad \text{where} \quad w_{\text{int}}(\mathbf{E}) = \frac{1}{2} \mathbf{E} \cdot \mathbf{S}, \quad (2.12)$$

with $(\bullet) \cdot (\bullet)$ being the scalar product of two tensors. For isotropic linear elastic material behavior the material tensor is

$$\overset{4}{\mathbf{C}} = 2\mu(\mathbf{I} \otimes \mathbf{I})^{\overset{23}{T}} + \lambda(\mathbf{I} \otimes \mathbf{I}), \quad (2.13)$$

where $(\bullet)^{\overset{23}{T}}$ is the transposition of the second and third component of the symmetric fourth order tensor $(\mathbf{I} \otimes \mathbf{I})$ resulting from the diadic product of the second order identity tensor \mathbf{I} with itself. The material parameters μ and λ are the Lamé parameters. They are related to the elastic modulus E and Poisson's ratio ν through

$$\lambda = \frac{\nu E}{(1 + \nu)(1 - 2\nu)}, \quad (2.14)$$

$$\mu = \frac{E}{2(1 + \nu)}. \quad (2.15)$$

In a geometrically linear setting, where only small rotations occur, the Saint Venant-Kirchhoff material law reduces to Hooke's law relating the linearized strain $\boldsymbol{\varepsilon}$ to the

linearized stress $\boldsymbol{\sigma}$ by the elastic modulus \mathbf{D} with

$$\boldsymbol{\sigma} = \mathbf{D}\boldsymbol{\varepsilon} \quad (2.16)$$

in Voigt notation.

Neo-Hookean material model

For large strains, elastic material behavior can be described by the Neo-Hookean material model. The Neo-Hookean material model is as well a hyperelastic material model. The strain energy function of a compressible, isotropic Neo-Hookean material is

$$w_{\text{int}}(\mathbf{E}) = \frac{1}{2}\mu \left(\text{tr}(\bar{\mathbf{C}}) - 3 \right) - \mu \ln(\det \mathbf{F}) + \frac{1}{2}\lambda \left(\ln(\det \mathbf{F}) \right)^2, \quad (2.17)$$

where the determinant of the deformation gradient and the right Cauchy-Green tensor are related through

$$\det(\mathbf{F}) = (\det(\bar{\mathbf{C}}))^{\frac{1}{2}} \quad (2.18)$$

and the right Cauchy-Green tensor and the Green-Lagrangian strain are related through eq. (2.7). The latter relation allows a transformation of the partial derivative with respect to the Green-Lagrangian strain to a partial derivative with respect to the right Cauchy-Green tensor by

$$\frac{\partial \bullet}{\partial \mathbf{E}} = 2 \frac{\partial \bullet}{\partial \bar{\mathbf{C}}}. \quad (2.19)$$

Thus, the stress-strain relation is obtained by

$$\begin{aligned} \mathbf{S} &= \frac{\partial w_{\text{int}}(\mathbf{E})}{\partial \mathbf{E}} = 2 \frac{\partial w_{\text{int}}(\bar{\mathbf{C}})}{\partial \bar{\mathbf{C}}} = \mu(\mathbf{I} - \bar{\mathbf{C}}^{-1}) + \lambda \ln(\det(\bar{\mathbf{C}}))^{\frac{1}{2}} \bar{\mathbf{C}}^{-1} \\ &= \mu \left(\mathbf{I} - (\mathbf{F}^T \mathbf{F})^{-1} \right) + \lambda \ln(\det \mathbf{F}) (\mathbf{F}^T \mathbf{F})^{-1}. \end{aligned} \quad (2.20)$$

All hyperelastic materials (in contrast to hypoelastic materials) share the property that they are path-independent, reversible and nondissipative.

2.1.4 Conservation equations

The conservation (or balance) laws state that specific quantities must be preserved in closed physical systems. Later, we will see that these equations may be violated in the

discrete setting, e.g. for conventional mass scaling, where the density is altered and thus the mass is increased for numerical reasons. The conservation equations stated in the following may also serve as an a priori condition for the development of inertia templates. The equations stated in the following are formulated in the local form in the Lagrangian description.

Conservation of mass

The balance of mass states that in a closed system the mass of a body is constant during deformation, i.e.

$$\rho(\mathbf{X},t) \det \mathbf{F}(\mathbf{X},t) = \rho_0(\mathbf{X}), \quad (2.21)$$

where ρ_0 is the initial density $\rho(\mathbf{X},0)$.

Conservation of linear momentum

The balance of linear momentum states that the temporal change of the linear momentum is equal to the sum of all the forces acting on the body, i.e.

$$\rho_0 \frac{\partial \mathbf{v}(\mathbf{X},t)}{\partial t} = \text{Div} \boldsymbol{\sigma}_{\text{PKI}} + \rho_0 \hat{\mathbf{b}}, \quad (2.22)$$

where $\boldsymbol{\sigma}_{\text{PKI}}$ is the first Piola-Kirchhoff stress tensor and $\rho_0 \hat{\mathbf{b}}$ is the body load. $\text{Div}(\cdot)$ is the divergence operator with respect to the reference configuration.

Conservation of angular momentum

The balance of angular momentum states that the temporal change of the angular momentum is equal to the sum of all the moments of all forces acting on the body. From this law results the symmetry of the second Piola-Kirchhoff stress $\mathbf{S} = \mathbf{S}^T$ and the Cauchy stress tensor with $\mathbf{T} = \mathbf{T}^T$. Note that the first Piola-Kirchhoff stress tensor is not symmetric, i.e. $\boldsymbol{\sigma}_{\text{PKI}} \neq \boldsymbol{\sigma}_{\text{PKI}}^T$.

Conservation of mechanical energy

The balance of energy, or herein simplified to the balance of mechanical energy for isothermal processes, is a direct consequence from the momentum balance, stating that

the temporal change of the kinetic and the internal energy W_{kin} and W_{int} is equal to the sum of the mechanical power P resulting from external forces.

$$\frac{d}{dt}(W_{\text{kin}} + W_{\text{int}}) = P, \quad (2.23)$$

with

$$W_{\text{kin}} = \int_{\Omega_0} \frac{1}{2} \rho_0 \mathbf{v}^T \mathbf{v} \, d\Omega_0, \quad (2.24)$$

$$W_{\text{int}} = \int_{\Omega_0} w_{\text{int}}(\mathbf{E}) \, d\Omega_0, \quad (2.25)$$

$$P = \int_{\Omega_0} \rho_0 \hat{\mathbf{b}}^T \mathbf{v} \, d\Omega_0 + \int_{\Gamma_0} \hat{\mathbf{t}}^T \mathbf{v} \, d\Gamma_0. \quad (2.26)$$

The integration is carried out over the reference domain Ω_0 and its boundary Γ_0 .

2.1.5 Equilibrium equation

In applications where the load is applied slowly and inertia effects are negligible, the momentum eq. (2.22) reduces to the equilibrium equation

$$\text{Div } \boldsymbol{\sigma}_{\text{PK1}} + \rho_0 \hat{\mathbf{b}} = \mathbf{0}, \quad (2.27)$$

describing a static, time-independent problem. Eq. (2.27) describes an elliptic problem, whereas eq. (2.22) describes a hyperbolic problem.

If inertia and damping effects are negligible, but a time dependency, e.g. of the loading, is present, the problem is called quasi-static. Within the present work, dynamic problems are considered.

2.1.6 The strong form of the initial boundary value problem (IBVP)

In order to completely describe a dynamic problem, additionally to the kinematic equation, the constitutive equation and the equation of linear momentum, the initial and boundary conditions are required. They complete the so-called initial boundary value problem (IBVP). At the boundary either the displacement or the traction is prescribed

with $\hat{\mathbf{u}}$ and $\hat{\mathbf{t}}$ on Γ_u and Γ_σ , respectively, with

$$\begin{aligned} \mathbf{u}(\mathbf{X}, t) &= \hat{\mathbf{u}} && \text{on } \Gamma_u, \\ \mathbf{T}(\mathbf{X}, t)\mathbf{n} &= \hat{\mathbf{t}} && \text{on } \Gamma_\sigma. \end{aligned} \quad (2.28)$$

For the boundary Γ_0 it holds:

$$\Gamma_u \cap \Gamma_\sigma = \emptyset, \quad \Gamma_u \cup \Gamma_\sigma = \Gamma_0. \quad (2.29)$$

Since eq. (2.22) is a differential equation of second order in time, two initial conditions are required. The displacement and velocity at time $t = t_0$ are prescribed by

$$\mathbf{u}(\mathbf{X}, t_0) = \mathbf{u}_0(\mathbf{X}), \quad (2.30)$$

$$\dot{\mathbf{u}}(\mathbf{X}, t_0) = \mathbf{v}_0(\mathbf{X}). \quad (2.31)$$

For nonlinear elasto-dynamics in the small strain regime, the strong form of the IBVP can then be summarized for a time interval $(t_0, t_{\text{end}}]$ to

$$\left\{ \begin{array}{ll} \rho_0 \ddot{\mathbf{u}} = \text{Div } \boldsymbol{\sigma}_{\text{PK1}} + \rho_0 \hat{\mathbf{b}} & \text{in } (t_0, t_{\text{end}}] \times \Omega_0 \\ \mathbf{E} = \frac{1}{2} (\mathbf{F}^T \mathbf{F} - \mathbf{I}) \text{ with } \mathbf{F} = \mathbf{I} + \text{Grad } \mathbf{u} & \text{in } (t_0, t_{\text{end}}] \times \Omega_0 \\ \mathbf{S} = \overset{4}{\mathbf{C}} \mathbf{E} & \text{in } (t_0, t_{\text{end}}] \times \Omega_0 \\ \mathbf{u}(\mathbf{X}, t) = \hat{\mathbf{u}} & \text{in } (t_0, t_{\text{end}}] \times \Gamma_u \\ \mathbf{T}(\mathbf{X}, t)\mathbf{n} = \hat{\mathbf{t}} & \text{in } (t_0, t_{\text{end}}] \times \Gamma_\sigma \\ \mathbf{u}(\mathbf{X}, 0) = \mathbf{u}_0(\mathbf{X}) & \text{in } \Omega_0 \\ \dot{\mathbf{u}}(\mathbf{X}, 0) = \mathbf{v}_0(\mathbf{X}) & \text{in } \Omega_0. \end{array} \right. \quad (2.32)$$

In eq. (2.32) the Green-Lagrangian strain measure and the Saint Venant-Kirchhoff material model are used. For linear elasto-dynamics, the strong form of the IBVP reduces to

$$\left\{ \begin{array}{ll} \rho \ddot{\mathbf{u}} = \mathbf{L}^T \boldsymbol{\sigma}(\mathbf{u}) + \rho \hat{\mathbf{b}} & \text{in } (t_0, t_{\text{end}}] \times \Omega \\ \boldsymbol{\varepsilon} = \mathbf{L} \mathbf{u} & \text{in } (t_0, t_{\text{end}}] \times \Omega \\ \boldsymbol{\sigma} = \mathbf{D} \boldsymbol{\varepsilon} & \text{in } (t_0, t_{\text{end}}] \times \Omega \\ \mathbf{u} = \hat{\mathbf{u}} & \text{in } (t_0, t_{\text{end}}] \times \Gamma_u \\ \boldsymbol{\sigma} \mathbf{n} = \hat{\mathbf{t}} & \text{in } (t_0, t_{\text{end}}] \times \Gamma_\sigma \\ \mathbf{u}(\cdot, t_0) = \mathbf{u}_0 & \text{in } \Omega \\ \dot{\mathbf{u}}(\cdot, t_0) = \mathbf{v}_0 & \text{in } \Omega, \end{array} \right. \quad (2.33)$$

where \mathbf{L} is the differential operator of the problem. For small strains, no distinction between different strain and stress measures or density in reference and current configuration is required.

Since it is not of importance for the derivation of the variationally consistent inertia templates, whether a linear or nonlinear setting is considered, in the following derivations a linear setting is used for simplicity. Later in the present work, necessary modifications for a general nonlinear setup are discussed. A possible reason for necessary modifications is that the proposed inertia templates can depend on the position and the position has to be updated in case of large rotations.

2.1.7 The virtual work principle as weak form

For the spatial discretization by the finite element method a weak form of the IBVP is needed. The weak form can be obtained by the method of weighted residuals. To obtain the weak form, the linear momentum equation and the force boundary condition are satisfied in a weak sense. The kinematic equation, the material law and the displacement boundary condition are subsidiary conditions and satisfied in a strong sense. According to the method of weighted residuals, the equations to be satisfied in a weak sense are to be multiplied with a test function $\delta \mathbf{u}^T$ and integrated over the domain Ω (or the boundary Γ),

$$\int_{\Omega} \delta \mathbf{u}^T (\rho \ddot{\mathbf{u}} - \mathbf{L}^T \boldsymbol{\sigma} - \rho \hat{\mathbf{b}}) d\Omega - \int_{\Gamma_{\sigma}} \delta \mathbf{u}^T (\hat{\mathbf{t}} - \boldsymbol{\sigma} \mathbf{n}) d\Gamma_{\sigma} = 0. \quad (2.34)$$

Integration by parts in space yields

$$- \int_{\Omega} \delta \mathbf{u}^T \mathbf{L}^T \boldsymbol{\sigma} d\Omega = \int_{\Omega} (\delta \mathbf{u}^T \mathbf{L}^T) \boldsymbol{\sigma} d\Omega - \int_{\Gamma_{\sigma}} \delta \mathbf{u}^T (\boldsymbol{\sigma} \mathbf{n}) d\Gamma_{\sigma}. \quad (2.35)$$

Inserting the right-hand side of eq. (2.35) into eq. (2.34) results in the weak form

$$\int_{\Omega} \rho \delta \mathbf{u}^T \ddot{\mathbf{u}} d\Omega + \int_{\Omega} (\delta \mathbf{u}^T \mathbf{L}^T) \boldsymbol{\sigma} d\Omega - \int_{\Omega} \rho \delta \mathbf{u}^T \hat{\mathbf{b}} d\Omega - \int_{\Gamma_{\sigma}} \delta \mathbf{u}^T \hat{\mathbf{t}} d\Gamma_{\sigma} = 0. \quad (2.36)$$

The individual virtual work terms can be named as the virtual kinetic energy δW_{kin} , the virtual internal energy δW_{int} and the virtual external energy δW_{ext} with

$$\delta W_{\text{kin}} = \int_{\Omega} \rho \delta \mathbf{u}^T \ddot{\mathbf{u}} \, d\Omega, \quad (2.37)$$

$$\delta W_{\text{int}} = \int_{\Omega} (\delta \mathbf{u}^T \mathbf{L}^T) \boldsymbol{\sigma} \, d\Omega, \quad (2.38)$$

$$\delta W_{\text{ext}} = - \int_{\Omega} \rho \delta \mathbf{u}^T \hat{\mathbf{b}} \, d\Omega - \int_{\Gamma_{\sigma}} \delta \mathbf{u}^T \hat{\mathbf{t}} \, d\Gamma_{\sigma}. \quad (2.39)$$

The virtual work principle can then be written as

$$\delta W_{\text{kin}} + \delta W_{\text{int}} + \delta W_{\text{ext}} = 0 \quad (2.40)$$

and can be used as starting point for the discretization in space to obtain the semi-discrete equation of motion.

Note that only one independent field, namely the displacement \mathbf{u} is used here. Alternative variational principles as starting point for the finite element discretization are the Hellinger-Reissner principle with independent displacements \mathbf{u} and stresses $\boldsymbol{\sigma}$ and the Hu-Washizu principle with independent displacements \mathbf{u} , stresses $\boldsymbol{\sigma}$ and strains $\boldsymbol{\varepsilon}$. While standard displacement-based finite elements result from the virtual work principle, the Hellinger-Reissner principle and the Hu-Washizu principle are the basis for hybrid stress and enhanced assumed strain (EAS) finite elements, respectively. These alternative multi-field variational principles result in a modified stiffness matrix or more generally speaking in a modified internal force vector, avoiding artificial stiffening phenomena (locking).

The main focus of this work is to propose variationally consistent inertia templates. Therefore, the kinetic energy term needs to be modified. This modification is possible in a more elegant way by starting not from the strong form and applying the method of weighted residuals but starting from Hamilton's principle, where the kinetic energy is directly included. Both ways of derivation are equivalent, the latter one is described next.

2.1.8 Hamilton's principle

Hamilton's principle of elasto-dynamics (see e.g. MURA ET AL. (1992)), also called the principle of stationary action, states that the integral of the difference between the

kinetic and potential energy over time is stationary, i.e.

$$H(\mathbf{u}) = \int_{t_0}^{t_{\text{end}}} (W_{\text{kin}} - (W_{\text{int}} + W_{\text{ext}})) dt \rightarrow \text{stat.} \quad (2.41)$$

when the initial and end values of \mathbf{u} are prescribed. Therein, the kinetic energy W_{kin} and the potential energy, which consists of the sum of the internal energy W_{int} and the external energy W_{ext} , are defined by

$$W_{\text{kin}} = \frac{1}{2} \int_{\Omega} \rho \dot{\mathbf{u}}^T \dot{\mathbf{u}} d\Omega, \quad (2.42)$$

$$W_{\text{int}} = \frac{1}{2} \int_{\Omega} \boldsymbol{\varepsilon}^T \mathbf{D} \boldsymbol{\varepsilon} d\Omega, \quad (2.43)$$

$$W_{\text{ext}} = - \int_{\Omega} \rho \mathbf{u}^T \hat{\mathbf{b}} d\Omega - \int_{\Gamma_{\sigma}} \mathbf{u}^T \hat{\mathbf{t}} d\Gamma_{\sigma}. \quad (2.44)$$

Note that a single-field functional in \mathbf{u} is used¹. To satisfy eq. (2.41), the first variation must be zero, i.e.

$$\begin{aligned} \delta H = & \int_{t_0}^{t_{\text{end}}} \left(\int_{\Omega} \rho \delta \dot{\mathbf{u}}^T \dot{\mathbf{u}} d\Omega \right) dt \\ & - \int_{t_0}^{t_{\text{end}}} \left(\int_{\Omega} \delta \boldsymbol{\varepsilon}^T \mathbf{D} \boldsymbol{\varepsilon} d\Omega - \int_{\Omega} \rho \delta \mathbf{u}^T \hat{\mathbf{b}} d\Omega - \int_{\Gamma_{\sigma}} \delta \mathbf{u}^T \hat{\mathbf{t}} d\Gamma_{\sigma} \right) dt = 0. \end{aligned} \quad (2.45)$$

For the first term of eq. (2.45) integration by parts in time is used with

$$\int_{t_0}^{t_{\text{end}}} \left(\int_{\Omega} \rho \delta \dot{\mathbf{u}}^T \dot{\mathbf{u}} d\Omega \right) dt = - \int_{t_0}^{t_{\text{end}}} \left(\int_{\Omega} \rho \delta \mathbf{u}^T \ddot{\mathbf{u}} d\Omega \right) dt, \quad (2.46)$$

where $\delta \mathbf{u} = \mathbf{0}$ at time $t = t_0$ and $t = t_{\text{end}}$ ensures vanishing of the boundary term. With the right-hand side of eq. (2.46), the material equation and the kinematic equation the

¹In WASHIZU (1982) the single-field functional is called least (or stationary) action principle, whereas the two field functional with displacement and linear momentum is called Hamilton's principle. Herein, the naming is used according to MURA ET AL. (1992).

weak form

$$\begin{aligned} \delta H = & - \int_{t_0}^{t_{\text{end}}} \left(\int_{\Omega} \rho \delta \mathbf{u}^T \ddot{\mathbf{u}} \, d\Omega \right) dt \\ & - \int_{t_0}^{t_{\text{end}}} \left(\int_{\Omega} (\delta \mathbf{u}^T \mathbf{L}^T) \boldsymbol{\sigma} \, d\Omega - \int_{\Omega} \rho \delta \mathbf{u}^T \hat{\mathbf{b}} \, d\Omega - \int_{\Gamma_{\sigma}} \delta \mathbf{u}^T \hat{\mathbf{t}} \, d\Gamma_{\sigma} \right) dt = 0 \end{aligned} \quad (2.47)$$

is obtained, which is weak both in time and in space. Localization in time would yield again the weak form given in eq. (2.36).

Note that the first variation of Hamilton's principle can as well be used as starting point for the derivation of one- or two-field continuous or discontinuous Galerkin time discretization methods, cf. e.g. CANNAROZZI AND MANCUSO (1995).

2.2 Discretization in space

In the following, the weak form of eq. (2.47) is discretized in space. Since the formulation is a standard one-field formulation with only one independent unknown, namely the displacement \mathbf{u} , discretization results in the standard equation of motion. In the first section, discretization resulting in a sparse, but non-diagonal, consistent mass matrix is considered. In the second section, different diagonalization techniques to obtain a diagonally lumped mass matrix for explicit dynamics are reviewed.

2.2.1 Semi-discretization with the consistent mass matrix (CMM)

Discretization of the weak form (eq. (2.47)) in space by the finite element method with Bubnov-Galerkin finite elements is considered. The displacement and its first variation are discretized by

$$\mathbf{u}(\mathbf{X}, t) \approx \mathbf{u}^h(\mathbf{X}, t) = \mathbf{N}(\mathbf{X}) \mathbf{U}_e(t), \quad (2.48)$$

$$\delta \mathbf{u}(\mathbf{X}, t) \approx \delta \mathbf{u}^h(\mathbf{X}, t) = \mathbf{N}(\mathbf{X}) \delta \mathbf{U}_e(t), \quad (2.49)$$

where \mathbf{N} are the displacement ansatz functions and $\mathbf{U}_e(t)$ are the discrete displacements on the element level. Similarly, it holds for the acceleration

$$\ddot{\mathbf{u}}(\mathbf{X}, t) \approx \ddot{\mathbf{u}}^h(\mathbf{X}, t) = \mathbf{N}(\mathbf{X}) \ddot{\mathbf{U}}_e(t). \quad (2.50)$$

Introducing the discretization (2.49), (2.50) into the first variation of Hamilton's principle (2.47) results in

$$\begin{aligned} \delta H_e = & - \int_{t_0}^{t_{\text{end}}} \left(\delta \mathbf{U}_e^T \int_{\Omega_e} \rho \mathbf{N}^T \mathbf{N} \, d\Omega_e \dot{\mathbf{U}}_e \right) dt \\ & - \int_{t_0}^{t_{\text{end}}} \left(\delta \mathbf{U}_e^T \left(\int_{\Omega_e} (\mathbf{N}^T \mathbf{L}^T) \boldsymbol{\sigma} \, d\Omega_e - \int_{\Omega_e} \rho \mathbf{N}^T \hat{\mathbf{b}} \, d\Omega_e - \int_{\Gamma_{\sigma e}} \mathbf{N}^T \hat{\mathbf{t}} \, d\Gamma_{\sigma e} \right) \right) dt \end{aligned} \quad (2.51)$$

on the element level. Next, the standard consistent mass matrix

$$\mathbf{M} = \bigcup_e \mathbf{m}_e = \bigcup_e \left(\int_{\Omega_e} \rho \mathbf{N}^T \mathbf{N} \, d\Omega_e \right) \quad (2.52)$$

can be defined, where \bigcup_e is the assembly operator for vectors and matrices. The characteristics of the element mass matrix \mathbf{m}_e are its matrix symmetry, physical symmetry, positivity and conservation of mass. The consistent mass matrix additionally preserves angular momentum, but this is an optional property for mass matrices which is for example not fulfilled by the row-sum lumped mass matrix (FELIPPA (2013a)). Additionally to the consistent mass matrix, the internal and external force vector are introduced with

$$\mathbf{F}^{\text{int}} = \bigcup_e \mathbf{f}_e^{\text{int}} = \bigcup_e \left(\int_{\Omega_e} (\mathbf{N}^T \mathbf{L}^T) \boldsymbol{\sigma} \, d\Omega_e \right), \quad (2.53)$$

$$\mathbf{F}^{\text{ext}} = \bigcup_e \mathbf{f}_e^{\text{ext}} = \bigcup_e \left(\int_{\Omega_e} \rho \mathbf{N}^T \hat{\mathbf{b}} \, d\Omega_e + \int_{\Gamma_{\sigma e}} \mathbf{N}^T \hat{\mathbf{t}} \, d\Gamma_{\sigma e} \right). \quad (2.54)$$

Then, the semi-discrete equation of motion is obtained on the global level with

$$\mathbf{M} \ddot{\mathbf{U}} = \mathbf{F}^{\text{ext}} - \mathbf{F}^{\text{int}}. \quad (2.55)$$

In explicit dynamics, the stiffness matrix is usually not required. Only in linear structural dynamics, the internal force \mathbf{F}^{int} may be computed with

$$\mathbf{F}^{\text{int}} = \mathbf{K} \mathbf{U}, \quad (2.56)$$

where \mathbf{K} is the stiffness matrix with

$$\mathbf{K} = \bigcup_e \mathbf{k}_e = \bigcup_e \left(\int_{\Omega_e} \bar{\mathbf{B}}^T \mathbf{D} \bar{\mathbf{B}} \, d\Omega_e \right). \quad (2.57)$$

Therein, $\bar{\mathbf{B}}$ is the strain-displacement operator with $\bar{\mathbf{B}} = \mathbf{L}\mathbf{N}$. For the estimate of the critical time step information from the stiffness matrix may be required as well, see Section 2.3.2.

Up to now, damping effects are ignored in eq. (2.55) as standard Hamilton's principle is valid only for conservative systems. In the presence of damping, an additional force

$$\mathbf{F}^{\text{damp}} = \mathbf{C}\dot{\mathbf{U}} \quad (2.58)$$

appears on the left hand side. The damping matrix \mathbf{C} is symmetric and positive definite or semi-definite. The Rayleigh damping model with

$$\mathbf{C} = a_1\mathbf{M} + a_2\mathbf{K}, \quad (2.59)$$

where a_1 and a_2 are free parameters, can be used. Damping may reduce the critical time step size as shown for example in BELYTSCHKO ET AL. (2014).

Likewise, contact is neglected in eq. (2.55). It will be later taken into consideration in Chapter 5.

2.2.2 Mass diagonalization

For explicit dynamics, a diagonal (or lumped) mass matrix is favored for trivial solution of eq. (2.55). The most common procedures to obtain a diagonal mass matrix \mathbf{M}^{D} are row-sum lumping and Hinton-Rock-Zienkiewicz lumping (see HINTON ET AL. (1976)).

To obtain a row-sum lumped mass, the row-sum of each row of the mass matrix is built, i.e. the diagonal entry of the i^{th} row of the mass matrix is obtained by

$$M_i^{\text{D}} = \sum_{j=1}^{n_{\text{dof}}} M_{ij} \quad (2.60)$$

for solid finite elements, with n_{dof} being the matrix size. For higher order finite elements like the 8-node serendipity, the 8-node triangle or the 10-node tetrahedral element this procedure may result in negative or zero mass on the diagonal, which is unphysical.

Then, the Hinton-Rock-Zienkiewicz lumping scheme is used. The procedure can for example be found in FELIPPA (2013b). It is somehow cumbersome, but easy to be implemented and the main advantage is that this procedure is applicable to any finite element type where a consistent mass matrix exists and the mass is guaranteed to be nonnegative. For further details on diagonally lumped mass matrices it is referred to the textbooks of BELYTSCHKO AND HUGHES (1983) and COOK ET AL. (1989).

Alternative lumping procedures are for example the Lobatto mass lumping (FRIED AND MALKUS (1975), used in spectral finite elements), or mass lumping through mass orthogonality by a specific choice of shape functions (used for spline functions e.g. in SCHUMAKER (2007)). Recently, a rigorous but cumbersome lumping scheme based on the integration of manifolds for higher-order elements has been presented in YANG ET AL. (2017).

The main advantage of the diagonally lumped mass matrix is that it saves computational cost because of the trivial solution of the equation of motion and the reduced storage cost. Additionally, it results in a smaller maximum eigenfrequency and thus in a larger allowable time step than the consistent mass matrix for the same finite element mesh size. This is illustrated by the typical dispersion graph in Figure 2.2 of a lumped mass matrix (LMM) and a consistent mass matrix (CMM) discretization. In a dispersion

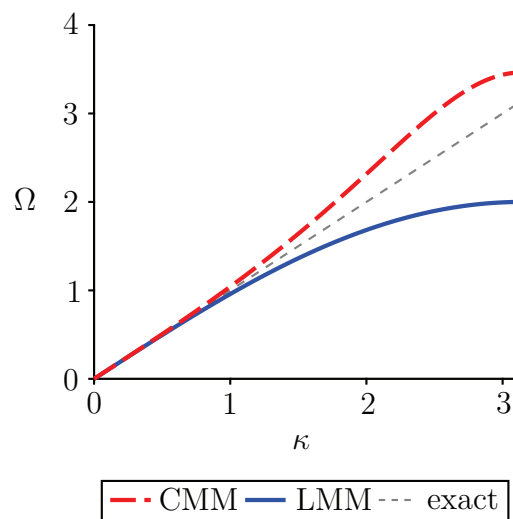


Figure 2.2: Typical dispersion graph for consistent (CMM) and lumped mass matrix (LMM), here for a 1-D linear finite element.

graph the dimensionless angular frequency Ω is plotted versus the dimensionless wave number κ . The wave number is inversely proportional to the wave length. For large wave numbers (i.e. small wave lengths = short waves) the frequency is significantly smaller for LMM than for CMM, allowing significantly larger time steps.

2.3 Discretization in time

Various different algorithms are available to solve the semi-discrete equation of motion given in eq. (2.55) in time. A good overview of existing algorithms is found in BELYTSCHKO AND HUGHES (1983), Chapter 9 of HUGHES (2000) or HULBERT (2017).

The different time discretization algorithms mainly vary in their stability, accuracy, dispersion and dissipation behavior. For classification it can for example be distinguished between explicit and implicit methods, where the central difference method (CDM) and the Newmark method (NEWMARK (1959)) with the trapezoidal rule are the most common explicit and implicit algorithms, respectively. Other prominent methods are for example the HHT- α method (HILBER ET AL. (1977)), Runge-Kutta methods, one- and two-field continuous and discontinuous Galerkin methods (e.g. FRIED (1969), JOHNSON ET AL. (1984) and recently e.g. GLEIM AND KUHL (2013)) and weighted residual methods in time (e.g. ARGYRIS AND SCHARPF (1969)). Note that implicit algorithms, which work well for linear structural dynamics, like the Newmark method may fail in nonlinear structural dynamics. Then, special algorithmic tricks for energy decay or additional energy- or momentum-preserving conditions need to be considered, see e.g. the work of Simo and Tarnow or Kuhl and coworkers (SIMO AND TARNOW (1992), SIMO AND TARNOW (1994), KUHL AND RAMM (1996, 1999), KUHL AND CRISFIELD (1999) among others).

Herein, the focus is on explicit integration schemes which are able to solve highly nonlinear and non-smooth problems efficiently. For explicit schemes no iterative solution of the balance equation on the global level is necessary and they are therefore more robust than implicit schemes. Their application is for example in car crash or deep drawing simulations. In the present work, the central difference method (CDM) is used and described in Section 2.3.1. A drawback of the explicit schemes is that the time step size is limited by a critical time step. Existing time step estimates are discussed in Section 2.3.2. To control that no energy is lost throughout simulation, the energy balance is checked regularly. The required equations are given in Section 2.3.3.

2.3.1 Central difference method (CDM)

The most common explicit time discretization scheme is the central difference method. For both the update of the displacement as well as of the velocity the central difference approximation is used, introducing an error of second order. The displacements are computed at the full time steps, whereas the velocities are computed at the half time steps. This is illustrated in Figure 2.3. Often, the update of the velocities is split into a first and second partial update to obtain the velocities at the full time steps as well. The time discretization scheme for the central difference method with lumped mass is given in the following as provided in BELYTSCHKO ET AL. (2014). Alternatively, the central difference method can be obtained as a special case of the a-form of the Newmark method as described in HUGHES (2000). The algorithm according to BELYTSCHKO ET AL. (2014) reads as follows:

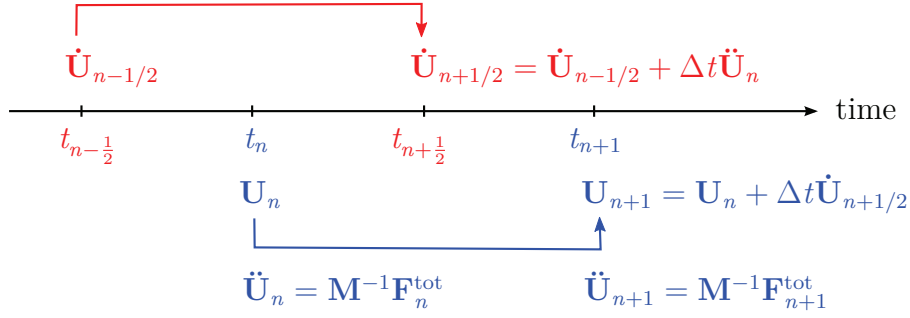


Figure 2.3: Visualization of the central difference time discretization method.

1. Initialization $n = 0$, $t = t_0$, $\mathbf{U} = \mathbf{U}_0$, $\dot{\mathbf{U}} = \dot{\mathbf{U}}_0$,
compute lumped mass \mathbf{M}
2. Get force $\mathbf{F}_n^{\text{tot}} = \mathbf{F}_n^{\text{ext}} - \mathbf{F}_n^{\text{int}}$
3. Compute accelerations $\ddot{\mathbf{U}}_n = \mathbf{M}^{-1} \mathbf{F}_n^{\text{tot}}$
4. Time update: $t_{n+1} = t_n + \Delta t$
5. First partial update of nodal velocities: $\dot{\mathbf{U}}_{n+1/2} = \dot{\mathbf{U}}_n + \frac{\Delta t}{2} \ddot{\mathbf{U}}_n$
6. Enforce velocity boundary conditions: $\dot{\mathbf{U}}_d = \dot{\hat{\mathbf{U}}}_d$
7. Update nodal displacements $\mathbf{U}_{n+1} = \mathbf{U}_n + \Delta t \dot{\mathbf{U}}_{n+1/2}$
8. Get force $\mathbf{F}_{n+1}^{\text{tot}} = \mathbf{F}_{n+1}^{\text{ext}} - \mathbf{F}_{n+1}^{\text{int}}$
9. Compute acceleration $\ddot{\mathbf{U}}_{n+1} = \mathbf{M}^{-1} \mathbf{F}_{n+1}^{\text{tot}}$
10. Second partial update of nodal velocities: $\dot{\mathbf{U}}_{n+1} = \dot{\mathbf{U}}_{n+1/2} + \frac{\Delta t}{2} \ddot{\mathbf{U}}_{n+1}$
11. Check energy balance at time step $n + 1$ according to Section 2.3.3
12. Update time step counter $n = n + 1$
13. Output; if simulation is not complete, go to 4.

Necessary modifications on the time discretization in case of non-diagonal or reciprocal mass matrices are discussed in Sections 2.4.3 and 2.5.2, respectively.

2.3.2 Critical time step estimates

For the central difference method, the time step Δt is limited by the critical time step Δt_{crit} through the stability criterion

$$\Delta t < \Delta t_{\text{crit}} = \frac{2}{\omega_{\text{max}}}, \quad (2.61)$$

where ω_{max} is the maximum eigenfrequency. Since a new, efficient time step estimate for reciprocal mass matrices is proposed in Chapter 5 of this work, existing time step estimates for lumped and consistent mass matrices are shortly reviewed. Existing estimates

to determine the critical time step Δt_{crit} can be categorized into two groups, namely global and local time step estimates – depending on whether they use information from the global or local level. Local information may either be information from the element level, like a characteristic length of the element, or nodal information, i.e. from the degree-of-freedom level, like the associated mass or stiffness.

Global time step estimates

Global time step estimates determine the maximum eigenfrequency of the global generalized eigenvalue problem

$$(\mathbf{K} - \lambda_i \mathbf{M})\phi_i = \mathbf{0} \quad \text{with} \quad \lambda_i = \omega_i^2. \quad (2.62)$$

The solution is usually carried out iteratively since the roots of a characteristic polynomial p of order n_{dof} , where n_{dof} is the size of the matrices \mathbf{K} and \mathbf{M} , are to be determined. The characteristic polynomial is

$$p(\lambda_i) = \det(\mathbf{K} - \lambda_i \mathbf{M}) = 0. \quad (2.63)$$

The iterative solution schemes can be classified as vector iteration methods, transformation methods and polynomial iteration techniques (cf. BATHE (1982)). Vector iteration methods operate directly upon eq. (2.62). Examples for vector iteration methods are the inverse iteration method, which determines the lowest eigenvector (and eigenfrequency), or the forward iteration method, which determines the largest one. Eigenvectors in between the smallest and the largest one can be obtained by shifting as it is proposed in the Rayleigh quotient iteration method. Transformation methods make use of the spectral decomposition property

$$\Phi^T \mathbf{K} \Phi = \Lambda, \quad (2.64)$$

$$\Phi^T \mathbf{M} \Phi = \mathbf{I}, \quad (2.65)$$

where Φ is a matrix of all eigenvectors ϕ_i and Λ is a diagonal matrix with the eigenvalues λ_i on the diagonal. The eigenvectors are normalized with respect to the mass matrix in eq. (2.64) and (2.65). Examples of transformation methods are for example the (generalized) Jacobi method, the Householder-QR-inverse-iteration method or the Arnoldi or Lanczos method. These methods are based on a transformation of the matrices into a tridiagonal or Hessenberg-form which then allows a simpler determination of the eigenvectors. While vector iteration methods solve for a single eigenvalue or eigenvector, transformation methods solve for all eigenvalues at once. Polynomial iteration techniques, like the explicit polynomial iteration method, calculate the roots

of the characteristic polynomial (2.63) directly. However, small errors in the coefficients of the polynomial may lead to large errors in the eigenvalues.

Since only the largest eigenvalue is required to determine the critical time step for explicit analysis, usage of the forward iteration method seems to be self-evident. The sequence of this very simple global eigenvalue estimate is given in the following according to BATHE (1982).

1. Initialize the eigenvector ϕ^0 e.g. by random numbers in the range $[-1..1]$, initialize the estimate of the maximum eigenvalue with $\lambda_{\max}^0 = 1e-12$, assign the maximum number of iterations n_{\max}^{iter} , assign a convergence tolerance ϵ and initialize the counter $i = 0$
2. Compute $\psi^0 = \mathbf{K}\phi^0$
3. Update the eigenvector by solving $\mathbf{M}\phi^{i+1} = \psi^i$
4. Compute $\psi^{i+1} = \mathbf{K}\phi^{i+1}$
5. Compute the estimate of the maximum eigenvalue $\lambda_{\max}^{i+1} = \frac{(\phi^{i+1})^T \psi^{i+1}}{(\phi^{i+1})^T \psi^i}$
6. If $|\lambda_{\max}^{i+1}/\lambda_{\max}^i - 1| > \epsilon$ and $i < n_{\max}^{\text{iter}}$ increase the counter i by 1 and go to step 3.
7. Finish.

With increasing i , λ_{\max}^{i+1} converges to the maximum eigenvalue λ_{\max} and ϕ^i to the corresponding eigenvector ϕ_{\max} .

This algorithm is used in this work for a global time step estimate if computational efficiency is not of importance. The algorithm is also easily adaptable to reciprocal mass matrices by modification of step 3. Then, instead of a linear system of equations only a sparse matrix-vector multiplication is to be performed in each iteration.

Element-based estimates

Existing element-based local estimates for lumped and consistent mass matrices make use of the element eigenvalue inequality by FRIED (1972), which states that the global eigenvalue λ is bounded by the element eigenvalues λ_i^e ,

$$|\lambda_{\max}| \leq |\lambda_{\max}^E| \quad \text{where} \quad \lambda_{\max}^E = \max_{i,e} \lambda_i^e = \left(\max_{i,e} \omega_i^e \right)^2. \quad (2.66)$$

The maximum element eigenfrequencies are usually obtained by simple formulas, e.g. based on geometric considerations (as used in LS-DYNA, HALLQUIST (2006)) through

the Courant-Friedrichs-Lewy-criterion (COURANT ET AL. (1928)) with

$$\max_{i,e} \omega_i^e = \frac{c}{l_c}. \quad (2.67)$$

Here, c is the characteristic wave speed and l_c is the characteristic length of the element. The characteristic length varies from element type to element type and also depends on the mass matrix in use. An overview of various elemental estimates can for example be found in BELYTSCHKO ET AL. (2014). Alternatively, an estimate of the maximum eigenfrequency can be obtained by considering the strain-displacement operator as proposed by FLANAGAN AND BELYTSCHKO (1984).

Since elemental estimates are not of interest for reciprocal mass matrices (the reason is explained in Section 5.1), they are not further elaborated herein.

Node-based estimates

Alternative local time step estimates are node-based estimates. The existing one found in literature is based on Gershgorin's theorem², given in GERŠGORIN (1931). Gershgorin's theorem states that all eigenvalues of a square matrix $\mathbf{A}^* \in \mathbb{C}^{n_{\text{dof}} \times n_{\text{dof}}}$ are found inside so-called Gershgorin's circles. For a given square matrix, the Gershgorin's circles that belong to the i^{th} diagonal entry A_{ii}^* of the matrix are defined by

$$\begin{aligned} \bar{S}_i(A_{ii}^*, \sum_{j=1, j \neq i}^{n_{\text{dof}}} |A_{ij}^*|), i = 1..n_{\text{dof}} \text{ (row-wise)} \quad \text{and} \\ \bar{S}_i(A_{ii}^*, \sum_{j=1, j \neq i}^{n_{\text{dof}}} |A_{ji}^*|), i = 1..n_{\text{dof}} \text{ (column-wise)}, \end{aligned} \quad (2.68)$$

where $\bar{S}(e(z), r)$ defines a circle with center $e(z)$ and radius r in the complex plane. Gershgorin's circles are thus obtained by simple algebraic computations and can be used as a computational cheap upper bound for the maximum eigenvalue. For illustration, the Gershgorin's circles of an exemplary square matrix

$$\mathbf{A}^* = \begin{bmatrix} 2 & 1 & 0.5 \\ 0.2 & 5 & 0.7 \\ 1 & 0 & 6 \end{bmatrix} \quad (2.69)$$

²Although the Soviet-Belarusian mathematician's name is Geršgorin, the English spelling is usually used to name Gershgorin's theorem in English literature.

are determined. The exact eigenvalues of \mathbf{A}^* are $\lambda_1 = 1.869$, $\lambda_2 = 4.873$ and $\lambda_3 = 6.258$. According to eq. (2.68) the Gershgorin's circles are

$$\bar{S}(2.0,1.5), \quad \bar{S}(5.0,0.9), \quad \bar{S}(6.0,1.0), \quad (2.70)$$

$$\bar{S}(2.0,1.2), \quad \bar{S}(5.0,1.0), \quad \bar{S}(6.0,1.2). \quad (2.71)$$

Eq. (2.70) describes all row-wise obtained circles, eq. (2.71) describes all column-wise obtained ones. The circles are illustrated in Figure 2.4. As expected, all eigenvalues

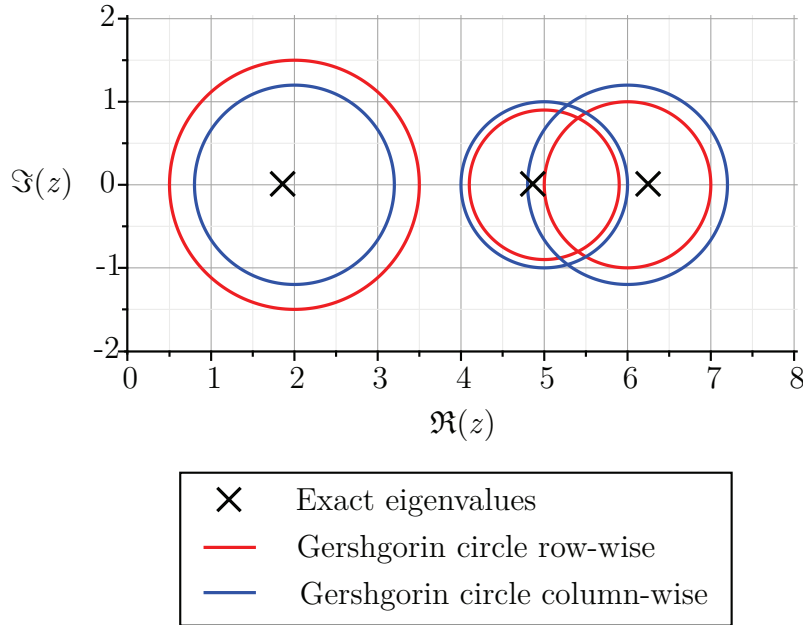


Figure 2.4: Gershgorin's circles of matrix \mathbf{A}^* from eq. (2.69).

lie inside Gershgorin's circles. For the matrix \mathbf{A}^* , all eigenvalues are real and thus all centers of the Gershgorin's circles lie on the real axis. From the maximum abscissa, the upper bound for the maximum eigenvalue is determined: For the matrix \mathbf{A}^* , the largest eigenvalue has to be smaller than 7.2. Since the exact largest eigenvalue is 6.258, the result of the estimate is conservative, as expected. If now the generalized eigenvalue problem from eq. (2.62) is considered, a transformation to a standard eigenvalue problem is required to apply Gershgorin's theorem (\mathbf{A}^* then corresponds to $\mathbf{M}^{-1}\mathbf{K}$). For diagonally lumped mass matrices, each entry of the matrix \mathbf{A}^* is computed by

$$A_{ij}^* = \frac{K_{ij}}{M_i^D}, \quad (2.72)$$

where M_i^D is the lumped mass at degree of freedom i . Inserting this equation into the definition of Gershgorin's circle results in a row-wise estimate of the maximum

eigenfrequency

$$\omega_{\max}^{\text{LMM}} = \max_i \sqrt{\frac{\sum_{j=1}^{n_{\text{dof}}} |K_{ij}|}{M_i^{\text{D}}}}. \quad (2.73)$$

Alternatively, a column-wise estimate could be proposed with

$$\omega_{\max}^{\text{LMM,column-wise}} = \max_i \sqrt{\sum_{j=1}^{n_{\text{dof}}} \frac{|K_{ij}|}{M_i^{\text{D}}}}. \quad (2.74)$$

However, while the row-wise estimate requires $n-1$ additions and 1 division to obtain one Gershgorin's circle, the column-wise estimate requires $n-1$ additions and n divisions. Therefore, a column-wise estimate requires approximately twice as much operations and a row-wise estimate is thus preferred.

In case of penalty contact the row-wise estimate can be supplemented by the absolute row sum $k_{p,i}^{\text{scal}}$ at degree of freedom i of the penalty stiffness matrix (see BELYTSCHKO AND NEAL (1991)) with

$$\omega_{\max}^{\text{LMM,pen}} = \max_i \sqrt{\frac{\sum_{j=1}^n |K_{ij}| + k_{p,i}^{\text{scal}}}{M_i^{\text{D}}}}. \quad (2.75)$$

Details on penalty contact and further development of the time step estimate from eq. (2.75) to reciprocal mass matrices are presented in Chapter 5.

2.3.3 Energy balance

To control that energy is preserved during simulation, the history of the kinetic, internal, external and dissipative energy due to damping is observed. The sum of the kinetic, internal and dissipative energy should be equal to the external and contact energy,

$$W_{\text{kin}} + W_{\text{int}} - W_{\text{ext}} + W_{\text{damp}} - W_{\text{cont}} \stackrel{!}{=} 0. \quad (2.76)$$

The energy is computed incrementally during simulation with

$$W_{\text{int}}^{n+1} = W_{\text{int}}^n + \frac{1}{2} \Delta \mathbf{U}^T (\mathbf{F}_n^{\text{int}} + \mathbf{F}_{n+1}^{\text{int}}), \quad (2.77)$$

$$W_{\text{ext}}^{n+1} = W_{\text{ext}}^n + \frac{1}{2} \Delta \mathbf{U}^T (\mathbf{F}_n^{\text{ext}} + \mathbf{F}_{n+1}^{\text{ext}}), \quad (2.78)$$

$$W_{\text{damp}}^{n+1} = W_{\text{damp}}^n + \frac{1}{2} \Delta \mathbf{U}^T \mathbf{C} (\dot{\mathbf{U}}_n + \dot{\mathbf{U}}_{n+1}), \quad (2.79)$$

$$W_{\text{kin}}^{n+1} = \frac{1}{2} (\dot{\mathbf{U}}_{n+1})^T \mathbf{M} \dot{\mathbf{U}}_{n+1}, \quad (2.80)$$

$$W_{\text{cont}}^{n+1} = W_{\text{cont}}^n + \frac{1}{2} \Delta \mathbf{U}^T (\mathbf{F}_n^{\text{cont}} + \mathbf{F}_{n+1}^{\text{cont}}), \quad (2.81)$$

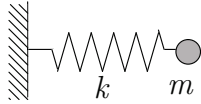
where n is the time increment number and $\Delta \mathbf{U} = \mathbf{U}_{n+1} - \mathbf{U}_n$. In case reduced integrated finite elements with hourglass stabilization are used, the hourglass energy needs to be observed as well. The stabilization parameters should be chosen so that the hourglass energy stays below 5% of the total energy of the system.

2.4 Mass scaling methods

The goal of mass scaling is to speed-up explicit dynamic finite element analyses, i.e. to obtain reliable results at significantly smaller computational costs than with the lumped mass matrix.

The idea of mass scaling can already be understood from a one-degree-of-freedom system as shown in Figure 2.5 consisting of a point mass m and a spring k . To allow larger time

original system



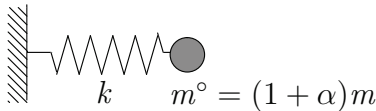
eigenfrequency

$$\omega = \sqrt{\frac{k}{m}}$$

increase of critical time step

$$\frac{\Delta t_{\text{crit}}^{\circ}}{\Delta t_{\text{crit}}} = \frac{\omega}{\omega^{\circ}} = \sqrt{1 + \alpha}$$

mass-scaled system



eigenfrequency

$$\omega^{\circ} = \sqrt{\frac{k}{m^{\circ}}}$$

Figure 2.5: Schematic illustration of the idea of mass scaling using a one-degree-of-freedom system.

steps the critical time step size needs to be enlarged. According to eq. (2.61) the critical time step size is inversely proportional to the eigenfrequency, i.e. to increase the critical time step, the eigenfrequency needs to be decreased. Therefore, either the mass has to

be increased or the stiffness has to be reduced. To leave at least the static properties unchanged, an increase of the mass is introduced by the factor α . This results in an increase of the critical time step size by the factor $\sqrt{1 + \alpha}$.

All mass scaling approaches for explicit dynamic finite element analyses introduce a manipulation on the mass matrix. The scaled mass \mathbf{M}° is constructed by the standard mass matrix \mathbf{M} , which is either the lumped or consistent mass matrix, and an artificially added mass $\boldsymbol{\lambda}^\circ$ with

$$\mathbf{M}^\circ = \mathbf{M} + \boldsymbol{\lambda}^\circ. \quad (2.82)$$

According to TKACHUK AND BISCHOFF (2014) mass scaling methods can be classified in local and global approaches, manipulating either the global or element-wise mass matrix. All mass scaling methods known by the author can be defined both on the element level or on the global level. In general, an element-wise construction is preferred since it allows different amounts of artificially added mass for various elements.

In the following, a short overview of existing mass scaling methods is given.

2.4.1 Conventional mass scaling (CMS)

Conventional mass scaling for explicit finite element analysis (described e.g. in BELYTSCHKO ET AL. (2014)) works similarly to mass scaling for a one-degree-of-freedom system. Mass scaling is applied on the element level. Artificial mass is added only to the diagonal terms of an element lumped mass matrix, i.e. the modified element mass matrix is

$$\mathbf{m}_e^\circ = (1 + \alpha)\mathbf{m}_e^D. \quad (2.83)$$

The factor α is called mass scaling parameter.

The main advantage of the approach is that the diagonal structure of the mass matrix is preserved, i.e. computational cost per time step is unaffected. Additionally, the approach is easily applicable to any element type. Recently, conventional mass scaling was applied to isogeometric Reissner-Mindlin shell elements by HARTMANN AND BENSON (2014). The main disadvantage of conventional mass scaling is that the element inertia is increased and the eigenfrequency of all modes is equally decreased by the factor

$$\frac{\omega^\circ}{\omega} = \frac{1}{\sqrt{1 + \alpha}} \quad (2.84)$$

as illustrated in Figure 2.6 (left). This means that both the structurally relevant low-frequency modes as well as the irrelevant high-frequency modes are affected. Therefore, this method needs to be applied very carefully. It is mainly used where the addition of nonphysical mass has no influence on the result. This is the case in quasi-static simulations where the kinetic energy is relatively small compared to the internal energy. Then conventional mass scaling may be used in a large area of the model. A second field of application are models with large variety of the finite element size. Then artificial mass can be added to a few very small or stiff elements like spotweld beams in areas where the altered inertia does not have a significant influence.

2.4.2 Algebraic selective mass scaling (ASMS)

An advancement to conventional mass scaling are algebraic selective mass scaling methods. The term ‘selective’ indicates that only selective modes are influenced by the approach. The earliest attempt of selective mass scaling is found in MACEK AND AUBERT (1995). Therein, in the work of OLOVSSON ET AL. (2005) and also in the work of GROSSEHOLZ ET AL. (2015) stiffness-proportional mass scaling is suggested. It is selective since only non-rigid body modes are scaled. Additionally, the order and the shape of the eigenmodes are preserved. But since the stiffness may change throughout a geometrically non-linear simulation, this approach was not further pursued. In OLOVSSON ET AL. (2004) a stiffness-independent selective mass scaling approach is suggested, where rigid body translational accelerations are filtered and excluded from conventional mass scaling. In OLOVSSON ET AL. (2005) a generalization of the earlier work is proposed, allowing an algebraic construction of the artificially altered mass. This paper focuses on an 8-node hexahedral solid element. The construction procedure for the artificially added mass λ° can be generalized for any solid element with translational degrees of freedom with n_n nodes.

1. For each coordinate direction the degrees of freedom are selected that contribute to the motion in that direction.
2. The consistent mass matrix entries belonging to the translational degree of freedom subset are added up to obtain the sum \mathcal{S} .
3. The diagonal entry of the added mass λ_e° is $\frac{(1+\beta)\mathcal{S}}{n_n}$.
4. The off-diagonal entry of the added mass λ_e° is $-\frac{\beta\mathcal{S}}{n_n(n_n-1)}$.
5. Steps 2 to 4 are repeated for all coordinate directions.

This construction procedure preserves the translational rigid body motion. More visually, the algebraically scaled elemental mass \mathbf{m}_e° can be constructed from the normalized elemental eigenvectors ϕ_i^e for which the inertia is to be preserved with

$$\mathbf{m}_e^\circ = \mathbf{m}_e^D + \boldsymbol{\lambda}_e^\circ \quad \text{with} \quad \boldsymbol{\lambda}_e^\circ = \frac{\beta m_e}{(n_n - 1)} (\mathbf{I} - \sum_i (\phi_i^e)^T \phi_i^e), \quad (2.85)$$

where m_e is the elemental mass and β is the mass scaling parameter. Eq. (2.85) can be used to construct an algebraically scaled mass, preserving translational rigid body motions only as well as an algebraically scaled mass, preserving both translational and rotational rigid body motions.

The advantage of the selective mass scaling approach is that only selected modes are influenced. This is visualized schematically in Figure 2.6 (right) where the ratio between

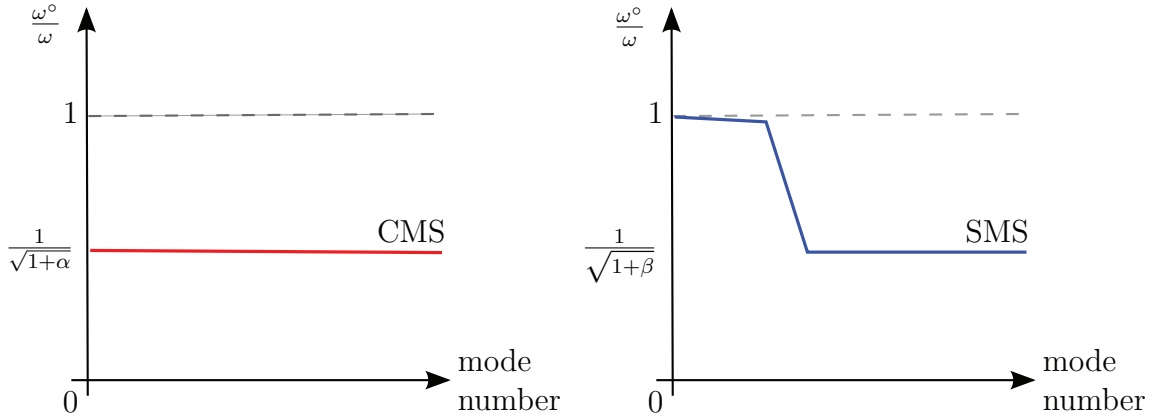


Figure 2.6: Qualitative illustration of the ratio of the scaled to the original eigenfrequency versus the mode number for conventional mass scaling (left) and selective mass scaling (right).

the scaled eigenfrequency and the unaltered eigenfrequency is plotted versus the mode number. One disadvantage of selective mass scaling is that the method is not easy to be generalized for NURBS and higher order FEM. A second, and the main, disadvantage is that the mass matrix is no longer diagonal. Therefore, a solution of a linear system of equations is required at every time step. OLOVSSON AND SIMONSSON (2006) suggested to use the conjugate gradient method as an iterative solution procedure to solve the linear system of equations with a non-diagonal mass matrix at every time step. This approach additionally allows to use a non-constant mass matrix efficiently (e.g. in case of element erosion or for adaptivity). However, in the case of high scaling factors, which result in a bad conditioning of the matrix, direct solvers may be advantageous. Additionally to the drawback of a linear system of equations which is to be solved, many standard routines in a finite element code like for contact treatment or multi-point constraints, are designed for lumped mass matrices and have to be revised for non-diagonal mass

matrices. To date algebraic selective mass scaling from OLOVSSON ET AL. (2005) is available in LS-DYNA and RADIOSS. In ABAQUS/Explicit (2016) only conventional mass scaling is implemented.

Algebraic selective mass scaling approaches for solid-shell finite elements can be found in COCCHETTI ET AL. (2013). For thin-walled structures the thickness h is the limiting characteristic length for the critical time step. Therefore, selective mass scaling is used to add artificial inertia in thickness direction. From the accelerations at the upper and lower surface of the element \mathbf{a}^{up} and \mathbf{a}^{low} , respectively, the average accelerations \mathbf{a}^{ave} , governing the rigid body motion of the element, and the difference accelerations \mathbf{a}^{diff} , governing the higher order modes, are obtained by linear transformation with

$$\mathbf{a}^{\text{ave}} = \frac{\mathbf{a}^{\text{up}} + \mathbf{a}^{\text{low}}}{2}, \quad (2.86)$$

$$\mathbf{a}^{\text{diff}} = \frac{\mathbf{a}^{\text{up}} - \mathbf{a}^{\text{low}}}{2}. \quad (2.87)$$

Then, mass scaling is only applied to the mass associated with the difference degrees of freedom, leaving the mass of the average degrees of freedom (and therefore the rigid body modes) unaltered leading to the scaled mass matrix on the element level

$$\mathbf{m}_e^{\circ} = \begin{bmatrix} \mathbf{m}_e^{\text{ave}} & \mathbf{0} \\ \mathbf{0} & \alpha \mathbf{m}_e^{\text{diff}} \end{bmatrix}, \quad (2.88)$$

where α is the mass scaling parameter. Off-diagonal terms are neglected in eq. (2.88) preserving the diagonal structure of the lumped mass matrix. The algebraic selective mass scaling approach of COCCHETTI ET AL. (2013) is further used in the work of PAGANI ET AL. (2014) for a different type of solid-shell element. In COCCHETTI ET AL. (2015) and CONFALONIERI ET AL. (2015) the approach is extended to distorted elements and layered shells, respectively.

Another selective mass scaling approach to selectively scale the volumetric modes in nearly incompressible materials is presented in YE ET AL. (2017) with application to biological tissues. Therein, shear and volumetric eigenmodes are separated and mass scaling is applied to the volumetric modes only. Last, a selective scaling of the element mass to influence the critical time step is used in MATTERN ET AL. (2015) in the context of incompatible mode finite elements for explicit dynamics. Therein, the incompatible degrees of freedom to reduce artificial stiffness effects (locking) are not eliminated by static condensation but treated as regular unknowns. An artificial mass is associated with these additional degrees of freedom and the time step is regulated by scaling the artificial density $\tilde{\rho}$.

2.4.3 Variational selective mass scaling (VSMS)

In the thesis of TKACHUK (2013), a variational formulation based on Hamilton's principle was proposed, providing the basis for both singular mass matrices and selectively scaled mass matrices. The singular mass matrices allow to significantly reduce spurious oscillations of the contact force in implicit contact problems. The selectively scaled mass matrices allow for substantial speed-up in explicit dynamics, but the mass matrix is no longer obtained from algebraic manipulations. Instead, it is obtained from a sound variational basis, guaranteeing consistency by construction, provided that proper ansatz spaces are chosen. The parametric Hamilton's principle proposed first in TKACHUK AND BISCHOFF (2013) is a three-field functional with independent displacement \mathbf{u} , velocity \mathbf{v} and linear momentum \mathbf{p} with three free parameters C_1 , C_2 , C_3 serving as scaling factors. It results from standard Hamilton's principle (eq. (2.41)) where the kinetic energy W_{kin} is replaced by a modified kinetic energy W_{kin}° with

$$W_{\text{kin}}^\circ(\dot{\mathbf{u}}, \mathbf{v}, \mathbf{p}, C_1, C_2, C_3) = \frac{1}{2} \int_{\Omega} \rho \dot{\mathbf{u}}^2 \, d\Omega + \int_{\Omega} \left(\frac{C_1}{2\rho} (\rho \dot{\mathbf{u}} - \mathbf{p})^2 + \frac{C_2}{2\rho} (\rho \mathbf{v} - \mathbf{p})^2 + \frac{C_3 \rho}{2} (\mathbf{v} - \dot{\mathbf{u}})^2 \right) \, d\Omega. \quad (2.89)$$

For variational selective mass scaling the parameters C_1 and C_2 are set to $C_1 = 0$ and $C_2 = 0$. C_3 is kept as free mass scaling parameter. This parameter choice reduces the formulation to a two-field formulation with the independent variables \mathbf{u} and \mathbf{v} . Derivation details are discussed in Chapter 3. Both the consistent mass matrix as well as the algebraically scaled mass matrix can be recovered from the variational form. Due to the two-field formulation and various possible ansatz spaces for discretization of \mathbf{u} and \mathbf{v} the variational scheme is more powerful than the algebraic one.

A different parameter choice results in reciprocal mass matrices, see Section 2.5.2.

Modified central difference scheme for non-diagonal mass matrices

For non-diagonal mass matrices the time discretization scheme provided in Section 2.3.1 is still valid, with the only difference that the lumped mass matrix \mathbf{M} is replaced by the non-diagonal mass matrix \mathbf{M}° . Thus, in step 3. and 9. the accelerations $\ddot{\mathbf{U}}_n$ are obtained from solving the linear system of equation $\mathbf{M}^\circ \ddot{\mathbf{U}}_n = \mathbf{F}_n^{\text{tot}}$ and similarly for the accelerations at t_{n+1} . Also the check of the energy balance gets a little more expensive since the kinetic energy $W_{n+1}^{\text{kin}} = \frac{1}{2} (\dot{\mathbf{U}}_{n+1})^T \mathbf{M}^\circ \dot{\mathbf{U}}_{n+1}$ is obtained from two sparse matrix-vector products instead of two scalar products.

Estimate of speed-up for non-diagonal mass matrices

Selectively scaled mass matrices allow computation with a larger time step ($\Delta t_{\text{SMS}} > \Delta t_{\text{LMM}}$), but due to the non-diagonal structure of the mass matrix each time step is more expensive. The final speed-up, i.e. the ratio between the computation time of a simulation with lumped mass T_{LMM} and with scaled mass T_{SMS} , was analyzed in BORRVALL (2011) and TKACHUK (2013) and is explained in the following in more details. The computation time is composed of the time for initialization T_0 and the time for one time step $T_{\Delta t}$ times the number of time steps. The number of time steps results from the quotient of the total simulation time t_{end} and the time step size Δt . The speed-up S is thus computed with

$$S = \frac{T_{\text{LMM}}}{T_{\text{SMS}}} = \frac{T_{\Delta t, \text{LMM}} \frac{t_{\text{end}}}{\Delta t_{\text{LMM}}} + T_{0, \text{LMM}}}{T_{\Delta t, \text{SMS}} \frac{t_{\text{end}}}{\Delta t_{\text{SMS}}} + T_{0, \text{SMS}}} \approx \frac{T_{\Delta t, \text{LMM}} \Delta t_{\text{SMS}}}{T_{\Delta t, \text{SMS}} \Delta t_{\text{LMM}}}. \quad (2.90)$$

In the last part of eq. (2.90), the time for initialization is neglected as one-time cost. The computation time for one time step consists mainly of the element processing time T_{ele} , i.e. the time for the internal force computation. For the non-diagonal mass matrix, a linear system of equation has to be solved in each time step to obtain the accelerations. This overhead is identified as T_{solver} . The computation time for one time step with lumped and selectively scaled mass is thus

$$T_{\Delta t, \text{LMM}} = T_{\text{ele}} \quad (2.91)$$

$$T_{\Delta t, \text{SMS}} = T_{\text{ele}} + T_{\text{solver}}. \quad (2.92)$$

Finally, the speed-up S then results in

$$S = \frac{T_{\text{LMM}}}{T_{\text{SMS}}} \approx \frac{T_{\text{ele}} \Delta t_{\text{SMS}}}{(T_{\text{ele}} + T_{\text{solver}}) \Delta t_{\text{LMM}}} \quad (2.93)$$

as proposed in TKACHUK (2013). Thus, the speed-up for selectively scaled mass matrices in comparison to lumped mass matrices results not only from the ratio of the time steps but also from the overhead in the solver due to the non-diagonal structure of the scaled mass matrix.

Note that the physical speed-up S in terms of the computation time can only be measured in a highly efficient explicit code. In the present C++-based finite element code NumPro, where the methods presented herein are implemented, the element processing time is significantly larger than in any commercial explicit code. However, the computational time for the solution of a linear system of equations is competitive with commercial codes since efficient solvers and external libraries are used. The reason for the higher element processing time is that the code is developed for both implicit and explicit anal-

yses and therefore the data structures can not be optimized towards top-performance in the explicit mode. Moreover, the code serves as research tool for doctoral students and therefore readability is of higher importance than efficiency of implementation.

Therefore, throughout this work the speed-up is evaluated in terms of the ratio of the time step size of the scaled mass matrix and the lumped mass matrix rather than measuring computational time. Additionally, the condition number of the mass matrix can be provided as a measure for the number of iterations in an iterative solver for linear systems of equations.

2.5 Reciprocal mass matrix approaches

All mass scaling approaches presented in Section 2.4 introduce a scaled mass \mathbf{M}° in the semi-discrete equation of motion

$$\mathbf{M}^\circ \ddot{\mathbf{U}} = \mathbf{F}^{\text{ext}} - \mathbf{F}^{\text{int}}. \quad (2.94)$$

Conventional mass scaling keeps the diagonal structure of the mass matrix, but significantly influences the element inertia. Algebraic selective mass scaling by OLOVSSON ET AL. (2005) and variational mass scaling by TKACHUK AND BISCHOFF (2013) partly preserves the inertia, but results in a non-diagonal mass matrix. COCCHETTI ET AL. (2013) propose a selective mass scaling approach for solid-shells, where the mass matrix is lumped by neglecting the off-diagonal terms. GAO AND CALO (2014) suggest for mass matrices with tensor-product structure of the form $(\mathbf{M}_x \otimes \mathbf{M}_y)$, like for regular isogeometric finite elements, to exploit the special property $(\mathbf{M}_x \otimes \mathbf{M}_y)^{-1} = \mathbf{M}_x^{-1} \otimes \mathbf{M}_y^{-1}$. Then, a fast solution is obtained by recursively applying a series of one-dimensional mass matrices. For more complex geometries, where a coupling term occurs in the integral, the factorization is not possible. In this case, the obtained inverse without coupling term is used as a preconditioner in the conjugate gradient method to obtain a fast iterative solution.

Alternatively, since one is not interested in the mass matrix, but only in the accelerations, a reciprocal (or inverse) mass matrix \mathbf{C}° can be directly constructed so that the semi-discrete equation of motion

$$\ddot{\mathbf{U}} = \mathbf{C}^\circ (\mathbf{F}^{\text{ext}} - \mathbf{F}^{\text{int}}) \quad (2.95)$$

is used instead. For a computationally efficient solution the reciprocal mass matrix should be sparse, i.e. with the same fill-in as the consistent mass matrix or less. For a sufficiently accurate solution the reciprocal mass matrix should provide at least the

same convergence rate as the lumped mass matrix for the lowest eigenfrequencies. Additionally, the matrix should be positive definite and symmetric. Existing approaches for the direct construction of an inverse mass matrix are discussed in the following.

2.5.1 Inverse mass matrix by approximation

In the work of LOMBARDO AND ASKES (2013) a non-diagonal mass matrix for explicit dynamics is developed, subsequently an approximation of the inverse of this mass matrix is introduced.

The mass matrix is developed in the context of a continuum theory taking micro-inertia into account. The effect of the incorporated micro-inertia is that dispersion effects occurring in micro-structured materials can be modelled. The strong form of dynamic equilibrium with micro-inertia in 1-D and 2-D read

$$1\text{-D: } \rho(\ddot{u}_x - l_{\text{mic}}^2 \ddot{u}_{x,xx}) = E u_{x,xx} \quad (2.96)$$

$$2\text{-D: } \begin{cases} \rho(\ddot{u}_x - l_{\text{mic}}^2 (\ddot{u}_{x,xx} + \ddot{u}_{x,yy})) & = (\lambda + \mu)(u_{x,xx} + u_{y,xy}) + \mu(u_{x,xx} + u_{x,yy}) \\ \rho(\ddot{u}_y - l_{\text{mic}}^2 (\ddot{u}_{y,xx} + \ddot{u}_{y,yy})) & = (\lambda + \mu)(u_{y,yy} + u_{x,xy}) + \mu(u_{y,xx} + u_{y,yy}) \end{cases} \quad (2.97)$$

with l_{mic} being the micro-inertia length scale. The resulting finite element formulation is identical to standard continuum elasticity, only the mass matrix is altered. The standard mass matrix is replaced by the mass matrix with micro-inertia $\mathbf{M}^D + \mathbf{M}^m$. \mathbf{M}^D is the standard lumped mass matrix and \mathbf{M}^m is the non-diagonal micro-inertia modification matrix. \mathbf{M}^m is obtained by assembly of the element micro-inertia matrix

$$\mathbf{m}_e^m = \int_{\Omega_e} \rho l_{\text{mic}}^2 \nabla \mathbf{N}^T \nabla \mathbf{N} \, d\Omega_e, \quad (2.98)$$

with $\nabla \mathbf{N}$ being the standard gradient operator. In 1-D, $\nabla \mathbf{N} = \bar{\mathbf{B}}$ with $\bar{\mathbf{B}}$ being the strain-displacement operator, which was already introduced earlier.

Since mass lumping of $\mathbf{M}^D + \mathbf{M}^m$ would simply erase the micro-inertia terms, the inverse of the mass matrix is approximated by a directly constructed inverse, resulting from Neumann expansion. The inverse mass matrix follows either from the first order approximation with

$$\mathbf{C}^{\text{mic},1} = \mathbf{M}^{\text{inv}} - \mathbf{M}^{\text{inv}} \mathbf{M}^m \mathbf{M}^{\text{inv}} \quad (2.99)$$

or from the second order approximation with

$$\mathbf{C}^{\text{mic},2} = \mathbf{M}^{\text{inv}} - \mathbf{M}^{\text{inv}}\mathbf{M}^{\text{m}}\mathbf{M}^{\text{inv}} + \mathbf{M}^{\text{inv}}\mathbf{M}^{\text{m}}\mathbf{M}^{\text{inv}}\mathbf{M}^{\text{m}}\mathbf{M}^{\text{inv}}, \quad (2.100)$$

where \mathbf{M}^{inv} is the inverse of the standard lumped mass matrix.

Note that eq. (2.99) and (2.100) work only on the global level. An approximation on the local level and subsequent assembly are not allowed due to the non-additivity of inverse matrices. The variational framework introduces a special trick to allow the assembly, see Section 3.1 and the following.

Alternative approaches to obtain an approximation of the inverse mass matrix were recently proposed by WU AND QIU (2009), CHAN AND EVANS (2018) and HANUKAH AND GIVLI (2018). While WU AND QIU (2009) propose an iterative approach to obtain the inverse mass matrix, HANUKAH AND GIVLI (2018) suggests a new numerical quadrature scheme.

2.5.2 Variational selective reciprocal mass scaling (VSRMS) for simplex elements with constant density

The modified Hamilton's principle proposed in TKACHUK (2013) can not only be used to derive variationally scaled mass matrices, but with a specific choice of scaling parameters and a specific choice of ansatz functions, variationally consistent reciprocal (=inverse) mass matrices can be constructed directly. The derivation proposed in TKACHUK AND BISCHOFF (2015) uses the modified kinetic energy from eq. (2.89), the parameters C_1 , C_2 and C_3 are set to $C_1 = -1$ and $C_3 = 0$, C_2 is kept as free parameter. Elimination of the velocity ansatz functions on the element level by static condensation and employment of the biorthogonality condition between the linear momentum and displacement shape functions yields the equation of motion

$$\begin{cases} \dot{\mathbf{P}} = \mathbf{F}^{\text{ext}} - \mathbf{F}^{\text{int}} \\ \dot{\mathbf{U}} = \mathbf{C}^\circ \mathbf{P}, \end{cases} \quad (2.101)$$

with the displacement \mathbf{U} , the linear momentum \mathbf{P} and the variationally selectively scaled reciprocal mass matrix \mathbf{C}° . A similar system of equation (with independent displacement and velocity) results from the algebraically constructed dispersion correction by KRENK (2001). Insertion of the second equation into the first one ((2.101)₂ into (2.101)₁) results in the standard equation of motion for reciprocal mass matrices (see eq. (2.95)).

Within the present work, improvements, enhancements and further analysis of the formulation by TKACHUK AND BISCHOFF (2015) are discussed. In the initial work of

TKACHUK AND BISCHOFF (2015), only simplex elements were considered, where the construction of the biorthogonal shape functions is unique. In Chapter 3, the construction for non-simplex elements is discussed. In the presence of Dirichlet boundary conditions modifications on the biorthogonal basis are necessary to retain a purely explicit scheme. This modification is also not unique for non-simplex elements and is discussed in Section 3.7.1 (for non-simplex elements). The formulation proposed in TKACHUK AND BISCHOFF (2015) provides satisfactory results only for problems with homogeneous material. An improved formulation for problems with non-constant density is proposed in SCHAEUBLE ET AL. (2017) in form of a $\mathbf{u}\text{-}\mathbf{v}\text{-}\mathbf{v}_p$ -formulation, where the third independent field is a mass-specific linear momentum (or velocity, defined in dependence of the linear momentum field). Later, the author understood that the crucial step for preserving the mass in case of non-constant density is not the choice of primary variables but the resulting construction of the biorthogonal basis. Therefore, both the $\mathbf{u}\text{-}\mathbf{v}\text{-}\mathbf{v}_p$ - and the $\mathbf{u}\text{-}\mathbf{v}\text{-}\mathbf{p}$ -formulation can be used, their equivalence is discussed in Section 3.2.2. Appropriate ansatz spaces for inhomogeneous media are discussed in Section 3.6.

The standard time discretization scheme for lumped mass matrices given in Section 2.3.1 needs to be adjusted for reciprocal mass matrices. In step 1, both the variationally scaled reciprocal mass matrix \mathbf{C}° and the lumped mass matrix \mathbf{M}^D are computed. In steps 3 and 9 the accelerations $\ddot{\mathbf{U}}_n$ are obtained from the relatively cheap sparse matrix-vector multiplication $\ddot{\mathbf{U}}_n = \mathbf{C}^\circ \mathbf{F}_n^{\text{tot}}$ and similarly for the accelerations at t_{n+1} . To save costs in the check of the energy balance, the kinetic energy is approximated with the lumped mass matrix to $W_{\text{kin}}^{n+1} = \frac{1}{2}(\dot{\mathbf{U}}_{n+1})^T \mathbf{M}^D \dot{\mathbf{U}}_{n+1}$. Alternatively, the kinetic energy could be computed from the reciprocal mass matrix and the linear momentum with $W_{\text{kin}}^{n+1} = \frac{1}{2}(\dot{\mathbf{P}}_{n+1})^T \mathbf{C}^\circ \dot{\mathbf{P}}_{n+1}$. If one is not interested in the exact energy balance or reaction forces, the linear momentum \mathbf{P} does not need to be computed, i.e. the necessary modifications in the control routine of a finite element program (i.e. on the global level outside of the element formulation) are very small. While for mass scaling the free parameters can be arbitrarily increased to enlarge the allowable time step (of course with decreasing accuracy and with unacceptable accuracy at some point), the increase of the allowable time step for reciprocal mass matrices is limited by stability issues.

2.5.3 Reciprocal mass matrices without dual basis

Two main disadvantages of the variationally selectively scaled reciprocal mass matrix are the following: First, biorthogonal bases need to be found for the construction and second, modifications are necessary in presence of displacement boundary conditions. Both of these disadvantages are addressed in the paper of GONZÁLEZ ET AL. (2018a).

Therein, the inverse mass matrix is constructed by usage of the standard elemental mass matrices, i.e. the lumped and the consistent mass matrix. In this way, biorthogonal spaces are omitted. The boundary conditions are employed by the method of localized Lagrange multipliers.

Recently, the application to isogeometric analysis is considered in GONZÁLEZ ET AL. (2018b).

2.6 Finite element templates

In the previous two sections, the focus was mainly on inertia scaling for explicit dynamics, i.e. the aim of the proposed mass or inverse mass matrices was a significant increase of the critical time step. All the scaled mass and inverse mass matrices presented therein had free parameters in their formulation and can therefore be called templates.

In general, a finite element template is defined as an algebraic form carrying free parameters. These free parameters occur in the stiffness or mass matrix formulation, or can even be introduced in the kinetic energy term included earlier in the derivation (resulting then as well in a parametrization of the inertia term, i.e. in a parametrized mass or inverse mass matrix). The free parameters can be customized to particular needs. In the context of inertia scaling the free parameters of the scaled mass and inverse mass matrices are mainly chosen for high speed-up. Within the present work, the proposed variationally consistent inertia templates are not only to be tuned for speed-up, but also for other customization goals, like optimal low frequency accuracy.

According to FELIPPA (2004), templates can be classified by their parametrization technique. One distinguishes matrix-weighted parametrization, spectral parametrization and entry-weighted parametrization. Also combinations of these parametrization techniques are possible, resulting in so-called multilevel parametrization.

The advantage of templates are that specific conditions may be satisfied a priori, for example stability or consistency of the stiffness matrix or non-negativity or linear momentum preservation of the mass matrix. Templates allow the construction of a set of mass or stiffness matrices at once, but only one template has to be coded. This saves a lot of implementation effort. Standard matrices, like the consistent or lumped mass matrix, can be obtained as special instances of the mass template. A disadvantage is that implementation of a template is more complicated than implementation of a standard finite element. Often, a symbolic analysis is required to determine optimal free parameters for a specific customization goal.

Originally, templates were mainly proposed for stiffness matrices to construct high-performance finite elements with the aim of achieving sufficient accuracy with a relatively coarse mesh. BERGAN AND HANSSEN (1975) suggested to derive the coefficients of the stiffness matrix by a direct algebraic approach, i.e. directly from linear constraint equations guaranteeing convergence, performing a so-called individual element test. Subsequently, a simplified approach to derive the stiffness matrix, the free formulation was proposed by BERGAN (1980) and BERGAN AND NYGÅRD (1984). Herein, the stiffness matrix is composed of a basic and a higher-order stiffness matrix with

$$\mathbf{K} = \mathbf{K}_b + \mathbf{K}_h. \quad (2.102)$$

The basic stiffness matrix \mathbf{K}_b guarantees consistency whereas the higher-order stiffness matrix \mathbf{K}_h guarantees stability (rank sufficiency). The second term can also be adjusted for optimal accuracy. The matrix \mathbf{K}_h is orthogonal to rigid body motions and constant strain states to leave these basic modes unaltered. Based on the free formulation BERGAN AND FELIPPA (1985) proposed the first rank-sufficient triangular membrane element with drilling degrees of freedom. It can be understood as the first paper in the direction of templates by Carlos Felippa, many more followed. As a second root of templates, the ANDES (assumed natural deviatoric strain) formulation (FELIPPA AND MILITELLO (1992)) can be seen, which was a further development of the assumed natural strain(ANS) formulation. While in the free formulation the higher-order stiffness is displacement-based, the deviatoric part of the assumed strains is used in the ANDES element.

To provide a general formulation that contains most of the proposed templates, Felippa proposed general parametrized variational principles for elasticity (and electromagnetics) in FELIPPA (1994). A parametrized variational principle (PVP) is a functional with free parameters. The Euler-Lagrange equation and natural boundary conditions are independent of these parameters. Both single-field and multi-field parameterized variational principles exist, the standard principles like the Hellinger-Reissner principle, the Hu-Washizu principle and the total potential energy functional can be obtained as special instances of the PVP.

To obtain optimal results in structural dynamics, the mass and stiffness matrix need to be adjusted to each other resulting in so-called mass-stiffness templates as proposed by FELIPPA (2001a, b). Therein, high performance Euler-Bernoulli beam elements for vibration and buckling analysis are proposed. Highly optimized mass-stiffness templates tend to become sensitive to mesh distortion or material inhomogeneity. Therefore, often only the mass matrix is adjusted for a given stiffness matrix and a specific customization goal (see for example the tutorial paper of FELIPPA ET AL. (2015)). Possible customiza-

tion goals are optimal low frequency accuracy of the acoustic branch, a constant optical branch or angular momentum preservation.

Independent from the ideas of templates, several alternative mass matrices with improved properties were reported. The first non-standard mass matrix was proposed by MACNEAL (1970) who suggested to use an average of the consistent and lumped mass matrix. BELYTSCHKO AND MULLEN (1978) studied this suggestion by Fourier analysis, a customization technique that is used also in Chapter 4 to customize the proposed inertia templates. KRIEG AND KEY (1973) proposed that the time discretization scheme need to be chosen with respect to the spatial discretization to obtain optimal results. This idea is used in the full dispersion analysis (FDA), see e.g. KOLMAN ET AL. (2016).

Inspired from the work of Felippa on PVPs, a parametrized variational formulation based on Hamilton's principle was proposed by TKACHUK (2013). The initial aim was to find a variational basis for the earlier proposed algebraic mass scaling methods.

Variationally consistent reciprocal mass matrices

In this chapter the variational formulation and the appropriate choice of ansatz spaces for consistent inertia templates are discussed. Although the presented formulation is valid for both mass and reciprocal mass matrices, the focus herein is on reciprocal mass matrices. The reason is that the advancements discussed in this chapter have only an influence on reciprocal mass matrices, whereas the formulation for variationally consistent mass matrices (as presented in TKACHUK AND BISCHOFF (2013)) remains unaffected. In the first section the basic ideas of the direct construction of reciprocal mass matrices are demonstrated by simple thought experiments. In the second section the variational formulation is presented in its original form (cf. TKACHUK AND BISCHOFF (2015)) and the requirements on the ansatz spaces for a variationally consistent formulation for constant density are discussed. In the subsequent section the limitation of the formulation for material with non-constant density is shown and improved ansatz spaces are proposed. The choice of ansatz spaces is verified by simple checks for mass preservation for different density distributions and inertia patch tests. The chapter closes with the discussion of the treatment of boundary conditions and multi-point constraints for general solid finite elements with reciprocal mass matrices.

3.1 Basic ideas of the direct assembly of reciprocal mass matrices

In general, reciprocal, i.e. inverse mass matrices may not be simply assembled from the element level. This fact can be visualized by the following thought-experiment: The assembly of two linear one-dimensional finite elements is considered. The geometric and

3 Variationally consistent reciprocal mass matrices

material properties are given in Figure 3.1. The (lumped) mass matrix on the element level and the inverse of it are

$$\mathbf{m}_e = \begin{bmatrix} 2500 & 0 \\ 0 & 2500 \end{bmatrix}, \quad \mathbf{m}_e^{-1} = \begin{bmatrix} \frac{1}{2500} & 0 \\ 0 & \frac{1}{2500} \end{bmatrix}, \quad (3.1)$$

respectively. While the mass matrix on the global level is obtained from assembly of the element mass matrices, i.e. the global mass matrix is

$$\mathbf{M} = \bigcup_e \mathbf{m}_e = \begin{bmatrix} 2500 & 0 & 0 \\ 0 & 5000 & 0 \\ 0 & 0 & 2500 \end{bmatrix}, \quad (3.2)$$

the inverse of the global mass matrix may not be simply obtained by assembly, i.e.

$$\mathbf{M}^{-1} = \begin{bmatrix} \frac{1}{2500} & 0 & 0 \\ 0 & \frac{1}{5000} & 0 \\ 0 & 0 & \frac{1}{2500} \end{bmatrix} \neq \bigcup_e (\mathbf{m}_e^{-1}) = \begin{bmatrix} \frac{1}{2500} & 0 & 0 \\ 0 & \frac{2}{2500} & 0 \\ 0 & 0 & \frac{1}{2500} \end{bmatrix}. \quad (3.3)$$

This observation is not very astonishing and equivalent to the fact that the reciprocal of a sum of numbers is not equivalent to the sum of the reciprocals of these numbers.

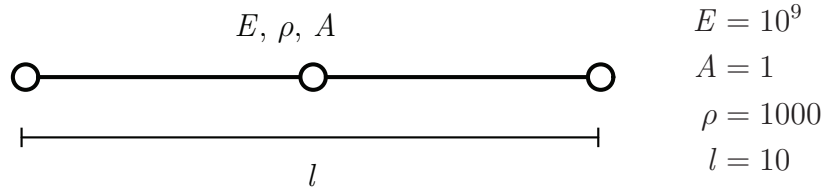


Figure 3.1: Assembly of two linear finite elements with identical material properties.

Continuing the thought-experiment, an appropriate element inverse mass matrix \mathbf{c}_e for the left and right element would be

$$\mathbf{c}_1 = \begin{bmatrix} \frac{1}{2500} & 0 \\ 0 & \frac{1}{10000} \end{bmatrix}, \quad \mathbf{c}_2 = \begin{bmatrix} \frac{1}{10000} & 0 \\ 0 & \frac{1}{2500} \end{bmatrix}, \quad (3.4)$$

which would result in the correct inverse of the system mass matrix by assembly. Here, the division of the reciprocal mass at the common degree of freedom is unique, due to the symmetry condition. These algebraically constructed inverse mass matrices on the element level show that the element inverse mass matrices of a single element and

an assembled element are not the same, compare \mathbf{m}_e^{-1} with \mathbf{c}_1 or \mathbf{c}_2 . The reason is that an appropriate element inverse mass matrix for assembly needs to know about its connectivity.

The algebraically constructed element inverse mass matrix \mathbf{c}_e can also be obtained from the inverted element mass matrix \mathbf{m}_e^{-1} by pre- and post-multiplying it with a diagonal (unitless) transformation matrix \mathbf{a}_e , i.e.

$$\mathbf{c}_1 = \mathbf{a}_1 \mathbf{m}_1^{-1} \mathbf{a}_1, \quad \text{with} \quad \mathbf{a}_1 = \begin{bmatrix} 1 & 0 \\ 0 & 1/2 \end{bmatrix}, \quad (3.5)$$

$$\mathbf{c}_2 = \mathbf{a}_2 \mathbf{m}_2^{-1} \mathbf{a}_2, \quad \text{with} \quad \mathbf{a}_2 = \begin{bmatrix} 1/2 & 0 \\ 0 & 1 \end{bmatrix}. \quad (3.6)$$

Only after transformation, the inverted element mass matrix may be assembled, and results in a global inverse mass matrix which preserves mass.

In this thought-experiment it was visualized that an inverse mass matrix may not be simply obtained from assembly of the inverted element matrices. In the following, a variational framework is presented which results in a template of consistent mass and reciprocal mass matrices. These sparse matrices are obtained directly by assembly from the element level. The pre- and post-multiplication to allow the assembly as described in eq. (3.5) and (3.6) for algebraic matrices results directly from the variational framework.

3.2 Variational formulation

In this section the variational formulation is given in form of the **u-v-p**-formulation (cf. TKACHUK AND BISCHOFF (2015)). A remark on the alternative **u-v-v_p**-formulation and their relation is provided subsequently.

3.2.1 The u-v-p-formulation

For the derivation of the variationally consistent inertia templates, the formulation of the kinetic energy is enriched by additional terms, where independent variables for the displacement \mathbf{u} , the velocity \mathbf{v} and the (volume specific) linear momentum \mathbf{p} are introduced. These three independent fields are linked through free parameters. These

free parameters C_1 , C_2 and C_3 can later be used for inertia scaling and customization. The modified kinetic energy thus reads

$$W_{\text{kin}}^{\circ}(\dot{\mathbf{u}}, \mathbf{v}, \mathbf{p}, C_1, C_2, C_3) = \frac{1}{2} \int_{\Omega} \rho \dot{\mathbf{u}}^2 \, d\Omega + \int_{\Omega} \left(\frac{C_1}{2\rho} (\rho \dot{\mathbf{u}} - \mathbf{p})^2 + \frac{C_2}{2\rho} (\rho \mathbf{v} - \mathbf{p})^2 + \frac{C_3 \rho}{2} (\mathbf{v} - \dot{\mathbf{u}})^2 \right) d\Omega. \quad (3.7)$$

To make the independent variables better visible, the modified kinetic energy (3.7) can as well be written in matrix template form with

$$W_{\text{kin}}^{\circ} = \frac{1}{2} \int_{\Omega} \begin{bmatrix} \rho \dot{\mathbf{u}} \\ \rho \mathbf{v} \\ \mathbf{p} \end{bmatrix}^T \begin{bmatrix} (1 + C_1 + C_3) \mathbf{I} & -C_3 \mathbf{I} & -C_1 \mathbf{I} \\ -C_3 \mathbf{I} & (C_2 + C_3) \mathbf{I} & -C_2 \mathbf{I} \\ -C_1 \mathbf{I} & -C_2 \mathbf{I} & (C_1 + C_2) \mathbf{I} \end{bmatrix} \begin{bmatrix} \dot{\mathbf{u}} \\ \mathbf{v} \\ \rho^{-1} \mathbf{p} \end{bmatrix} d\Omega. \quad (3.8)$$

This modified kinetic energy is then introduced into standard Hamilton's principle from eq. (2.41) leading to a modified Hamilton's principle

$$H^{\circ} = \int_{t_0}^{t_{\text{end}}} (W_{\text{kin}}^{\circ} - (W_{\text{int}} + W_{\text{ext}})) \, dt \rightarrow \text{stat}. \quad (3.9)$$

This formulation is also denoted as penalized Hamilton's principle in [TKACHUK \(2013\)](#). With all free parameters set to zero, the original form of Hamilton's principle can be recovered. To satisfy the stationarity of the principle, the first variation of modified Hamilton's principle must be zero, i.e.

$$\begin{aligned} \delta H^{\circ} = & \int_{t_0}^{t_{\text{end}}} \left(\int_{\Omega} \delta \dot{\mathbf{u}}^T ((1 + C_1 + C_3) \rho \dot{\mathbf{u}} - C_3 \rho \mathbf{v} - C_1 \mathbf{p}) \, d\Omega \right) dt \\ & + \int_{t_0}^{t_{\text{end}}} \left(\int_{\Omega} \delta \mathbf{v}^T (-C_3 \rho \dot{\mathbf{u}} + (C_2 + C_3) \rho \mathbf{v} - C_2 \mathbf{p}) \, d\Omega \right) dt \\ & + \int_{t_0}^{t_{\text{end}}} \left(\int_{\Omega} \delta \mathbf{p}^T (-C_1 \dot{\mathbf{u}} - C_2 \mathbf{v} + (C_1 + C_2) \rho^{-1} \mathbf{p}) \, d\Omega \right) dt \\ & - \int_{t_0}^{t_{\text{end}}} \left(\int_{\Omega} \delta \boldsymbol{\varepsilon}^T \mathbf{D} \boldsymbol{\varepsilon} \, d\Omega - \int_{\Omega} \rho \delta \mathbf{u}^T \hat{\mathbf{b}} \, d\Omega - \int_{\Gamma_{\sigma}} \delta \mathbf{u}^T \hat{\mathbf{t}} \, d\Gamma_{\sigma} \right) dt = 0. \end{aligned} \quad (3.10)$$

To remove the first derivative from the test function $\delta \dot{\mathbf{u}}$, the first term of eq. (3.10) is integrated by parts in time yielding

$$\begin{aligned}
 & \int_{t_0}^{t_{\text{end}}} \left(\int_{\Omega} \delta \dot{\mathbf{u}}^T \left((1 + C_1 + C_3) \rho \dot{\mathbf{u}} - C_3 \rho \mathbf{v} - C_1 \mathbf{p} \right) d\Omega \right) dt \\
 = & - \int_{t_0}^{t_{\text{end}}} \left(\int_{\Omega} \delta \mathbf{u}^T \left((1 + C_1 + C_3) \rho \ddot{\mathbf{u}} - C_3 \rho \dot{\mathbf{v}} - C_1 \dot{\mathbf{p}} \right) d\Omega \right) dt \\
 & + \left(\int_{\Omega} \delta \mathbf{u}^T \left((1 + C_1 + C_3) \rho \dot{\mathbf{u}} - C_3 \rho \mathbf{v} - C_1 \mathbf{p} \right) d\Omega \right) \Big|_{t_0}^{t_{\text{end}}}.
 \end{aligned} \tag{3.11}$$

Assuming that the variation $\delta \mathbf{u}$ is zero at the time interval boundaries $t = 0$ and $t = t_{\text{end}}$, the last term vanishes. The weak form, which provides the basis for the discretization in space, is thus

$$\begin{aligned}
 \delta H^\circ = & - \int_{t_0}^{t_{\text{end}}} \left(\int_{\Omega} \delta \mathbf{u}^T \left((1 + C_1 + C_3) \rho \ddot{\mathbf{u}} - C_3 \rho \dot{\mathbf{v}} - C_1 \dot{\mathbf{p}} \right) d\Omega \right) dt \\
 & + \int_{t_0}^{t_{\text{end}}} \left(\int_{\Omega} \delta \mathbf{v}^T \left(-C_3 \rho \dot{\mathbf{u}} + (C_2 + C_3) \rho \mathbf{v} - C_2 \mathbf{p} \right) d\Omega \right) dt \\
 & + \int_{t_0}^{t_{\text{end}}} \left(\int_{\Omega} \delta \mathbf{p}^T \left(-C_1 \dot{\mathbf{u}} - C_2 \mathbf{v} + (C_1 + C_2) \rho^{-1} \mathbf{p} \right) d\Omega \right) dt \\
 & - \int_{t_0}^{t_{\text{end}}} \left(\int_{\Omega} \delta \boldsymbol{\varepsilon}^T \mathbf{D} \boldsymbol{\varepsilon} d\Omega - \int_{\Omega} \rho \delta \mathbf{u}^T \hat{\mathbf{b}} d\Omega - \int_{\Gamma_\sigma} \delta \mathbf{u}^T \hat{\mathbf{t}} d\Gamma_\sigma \right) dt = 0.
 \end{aligned} \tag{3.12}$$

From eq. (3.12), the Euler-Lagrange equations

$$\begin{cases}
 \rho(1 + C_1 + C_3) \ddot{\mathbf{u}} - \rho C_3 \dot{\mathbf{v}} - C_1 \dot{\mathbf{p}} = \mathbf{L}^T \boldsymbol{\sigma} + \hat{\mathbf{b}} \\
 -C_3 \rho \dot{\mathbf{u}} + (C_2 + C_3) \rho \mathbf{v} - C_2 \mathbf{p} = \mathbf{0} \\
 -C_1 \rho \dot{\mathbf{u}} - C_2 \rho \mathbf{v} + (C_1 + C_2) \mathbf{p} = \mathbf{0}
 \end{cases} \tag{3.13}$$

can be recovered. The three-field formulation described herein can be represented by the Tonti diagram, which is illustrated in Figure 3.2. The independent fields are highlighted in the Figure by bold boxes.

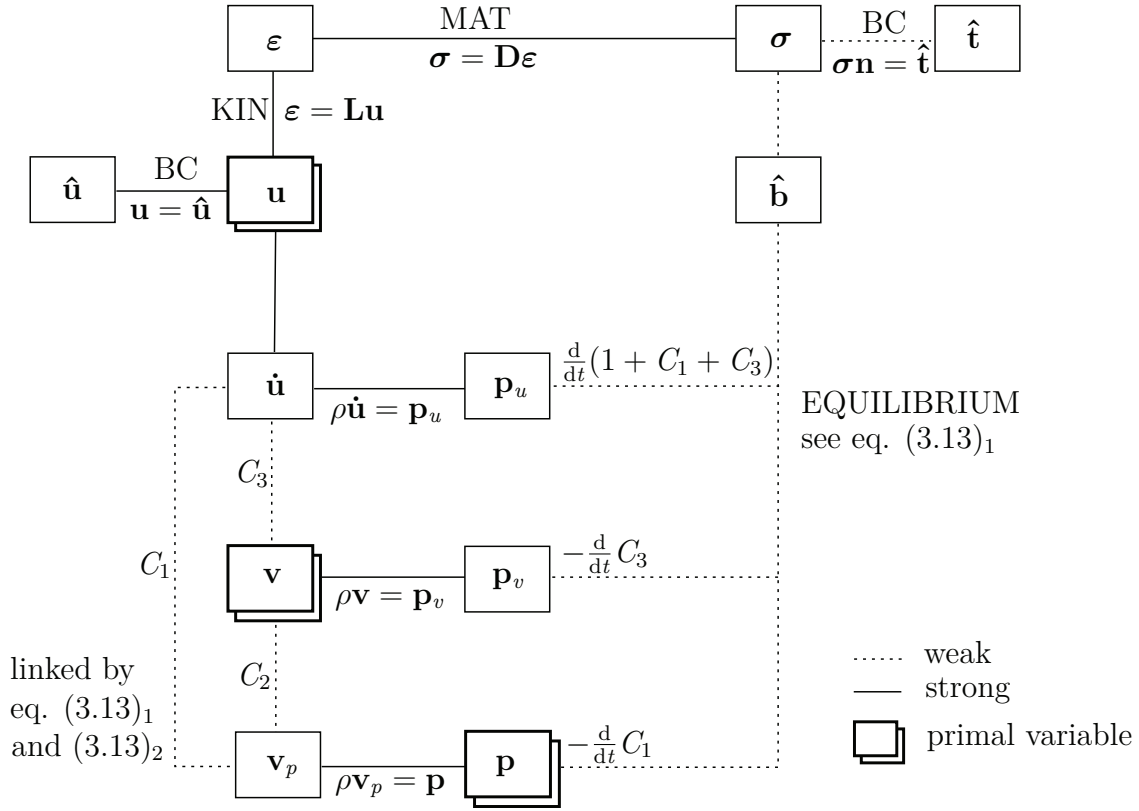


Figure 3.2: Tonti diagram of the proposed formulation.

3.2.2 A remark on the \mathbf{u} - \mathbf{v} - \mathbf{v}_p -formulation

In the previous section, the displacement \mathbf{u} , the velocity \mathbf{v} and the (volume specific) linear momentum \mathbf{p} were used as independent variables, like it was done in the original work of TKACHUK (2013) and in the first paper on variationally scaled reciprocal mass matrices by TKACHUK AND BISCHOFF (2015). Note that the mass-specific linear momentum \mathbf{v}_p can as well be used as third independent variable instead of the volume-specific linear momentum \mathbf{p} . This approach is realized in SCHAEUBLE ET AL. (2017). In general, the reparametrization $\mathbf{p} = \rho\mathbf{v}_p$ has no influence on the result; only the choice of ansatz functions associated with it improved the performance for non-constant density, as shown in SCHAEUBLE ET AL. (2017). Therefore, the reparametrization is not required and the \mathbf{u} - \mathbf{v} - \mathbf{v}_p -formulation can today be understood as a development vehicle to the formulation presented herein. Herein, the original \mathbf{u} - \mathbf{v} - \mathbf{p} -formulation is used in the following and the construction of the ansatz functions is corrected to obtain the same results as in SCHAEUBLE ET AL. (2017) and improved results compared to TKACHUK AND BISCHOFF (2015) for non-constant density. Details on the choice of linear momentum ansatz functions are provided in Sections 3.4 and 3.6.

3.3 Discretization in space

In this section the discretization in space of the variational formulation is introduced. First, a general inertia template is derived. Then, specific parameter choices lead to the variationally scaled mass and reciprocal mass matrices.

3.3.1 The general inertia template

Independent ansatz functions for displacement, velocity and volume-specific linear momentum are used, without specifying the shape functions in detail.

Discretization of the weak form in space is carried out using Bubnov-Galerkin finite elements with

$$\begin{aligned} \mathbf{u}^h(\mathbf{X}, t) &= \mathbf{N}(\mathbf{X})\mathbf{U}_e(t), & \mathbf{v}^h(\mathbf{X}, t) &= \mathbf{\Psi}(\mathbf{X})\mathbf{V}_e(t), & \mathbf{p}^h(\mathbf{X}, t) &= \chi(\mathbf{X})\mathbf{P}_e(t), \\ \delta\mathbf{u}^h(\mathbf{X}, t) &= \mathbf{N}(\mathbf{X})\delta\mathbf{U}_e(t), & \delta\mathbf{v}^h(\mathbf{X}, t) &= \mathbf{\Psi}(\mathbf{X})\delta\mathbf{V}_e(t), & \delta\mathbf{p}^h(\mathbf{X}, t) &= \chi(\mathbf{X})\delta\mathbf{P}_e(t). \end{aligned} \quad (3.14)$$

The continuous displacement \mathbf{u} , the velocity \mathbf{v} and the linear momentum \mathbf{p} (or approximated \mathbf{u}^h , \mathbf{v}^h and \mathbf{p}^h) have dimensions m, m/s and (kg m/s)/m³, respectively. The discretized displacement \mathbf{U}_e , the velocity \mathbf{V}_e and the linear momentum \mathbf{P}_e have the dimensions m, m/s and kg m/s, respectively. Therefore, while the displacement and velocity ansatz functions \mathbf{N} and $\mathbf{\Psi}$ are dimensionless, the linear momentum ansatz functions χ have the dimension 1/m³.

Insertion of the discretization from eq. (3.14) into the weak form of eq. (3.12) leads to the discretized form of modified Hamilton's principle on the element level with

$$\begin{aligned} \delta H_e^o &= - \int_{t_0}^{t_{\text{end}}} \left(\delta\mathbf{U}_e^T \int_{\Omega_e} \mathbf{N}^T ((1 + C_1 + C_3)\rho\mathbf{N}\dot{\mathbf{U}}_e - C_3\rho\mathbf{\Psi}\dot{\mathbf{V}}_e - C_1\chi\dot{\mathbf{P}}_e) d\Omega_e \right) dt \\ &+ \int_{t_0}^{t_{\text{end}}} \left(\delta\mathbf{V}_e^T \int_{\Omega_e} \mathbf{\Psi}^T (-C_3\rho\mathbf{N}\dot{\mathbf{U}}_e + (C_2 + C_3)\rho\mathbf{\Psi}\mathbf{V}_e - C_2\chi\mathbf{P}_e) d\Omega_e \right) dt \\ &+ \int_{t_0}^{t_{\text{end}}} \left(\delta\mathbf{P}_e^T \int_{\Omega_e} \chi^T (-C_1\rho\mathbf{N}\dot{\mathbf{U}}_e - C_2\rho\mathbf{\Psi}\mathbf{V}_e + (C_1 + C_2)\chi\mathbf{P}_e) d\Omega_e \right) dt \\ &- \int_{t_0}^{t_{\text{end}}} \left(\delta\mathbf{U}_e^T \int_{\Omega_e} (\mathbf{N}^T \mathbf{L}^T) \boldsymbol{\sigma} d\Omega_e - \int_{\Omega_e} \rho \mathbf{N}^T \hat{\mathbf{b}} d\Omega_e - \int_{\Gamma_{\sigma e}} \mathbf{N}^T \hat{\mathbf{t}} d\Gamma_{\sigma e} \right) dt. \end{aligned} \quad (3.15)$$

Beside the internal and external force vector \mathbf{F}^{int} and \mathbf{F}^{ext} and the standard consistent mass matrix \mathbf{M} , which were already introduced in Section 2.2, the following matrices

are introduced:

$$\mathbf{B} = \bigcup_e \mathbf{b}_e = \bigcup_e \left(\int_{\Omega_e} \rho \mathbf{N}^T \Psi \, d\Omega_e \right), \quad (3.16)$$

$$\mathbf{Y} = \bigcup_e \mathbf{y}_e = \bigcup_e \left(\int_{\Omega_e} \rho \Psi^T \Psi \, d\Omega_e \right), \quad \mathbf{A} = \bigcup_e \mathbf{a}_e = \bigcup_e \left(\int_{\Omega_e} \mathbf{N}^T \chi \, d\Omega_e \right), \quad (3.17)$$

$$\mathbf{C} = \bigcup_e \mathbf{c}_e = \bigcup_e \left(\int_{\Omega_e} \rho^{-1} \chi^T \chi \, d\Omega_e \right), \quad \mathbf{W} = \bigcup_e \mathbf{w}_e = \bigcup_e \left(\int_{\Omega_e} \chi^T \Psi \, d\Omega_e \right). \quad (3.18)$$

The matrix \mathbf{Y} can be interpreted as a mass matrix on the space \mathbf{V} and \mathbf{C} is the reciprocal mass matrix (RMM). Therefore, \mathbf{Y} has dimension kg, the reciprocal mass matrix has dimension kg^{-1} and is square and positive definite by construction. \mathbf{B} is a weighted projection matrix between the discrete spaces \mathbf{U} and \mathbf{V} with dimension kg. \mathbf{A} and \mathbf{W} are dimensionless projections of the discrete spaces \mathbf{U} onto \mathbf{P} and \mathbf{P} onto \mathbf{V} , respectively.

With these matrices at hand and the independence of the variations $\delta \mathbf{U}_e$, $\delta \mathbf{V}_e$ and $\delta \mathbf{P}_e$, the semi-discrete equation of motion on the global level

$$\left\{ \begin{array}{l} (1 + C_1 + C_3) \mathbf{M} \ddot{\mathbf{U}} - C_3 \mathbf{B} \dot{\mathbf{V}} - C_1 \mathbf{A} \dot{\mathbf{P}} = \mathbf{F}^{\text{ext}} - \mathbf{F}^{\text{int}} \\ -C_3 \mathbf{B}^T \dot{\mathbf{U}} + (C_2 + C_3) \mathbf{Y} \mathbf{V} = C_2 \mathbf{W}^T \mathbf{P} \\ -C_1 \mathbf{A}^T \dot{\mathbf{U}} = (-C_1 - C_2) \mathbf{C} \mathbf{P} + C_2 \mathbf{W} \mathbf{V} \end{array} \right. \quad (3.19)$$

is obtained. In presence of displacement boundary conditions, the system of equations is reduced and additional reaction forces need to be taken into account. The consideration of boundary conditions is discussed in Section 3.7.1 for reciprocal mass matrices.

In the following, two special cases of the general template are considered by specific parameter choices. The first choice leads to the variationally scaled consistent mass matrices presented first in TKACHUK AND BISCHOFF (2013). The second choice leads to the variationally scaled reciprocal mass matrix presented first in TKACHUK AND BISCHOFF (2015).

Note that even though the chapter is named ‘Variationally consistent reciprocal mass matrices’ the variationally scaled consistent mass matrices are described next for completeness, before the variationally scaled reciprocal mass matrices are described. Both will be used in Chapter 4 for inertia customization.

3.3.2 Variationally scaled consistent mass matrices (VSMS)

With $C_1 = 0$, $C_2 = 0$ and C_3 kept as free parameters, variationally scaled consistent mass matrices are considered. This parameter choice reduces the variational formulation to a two-field formulation with the independent variables \mathbf{u} and \mathbf{v} . The modified kinetic energy herein is thus

$$W_{\text{kin}}^\circ(\dot{\mathbf{u}}, \mathbf{v}, C_3) = \frac{1}{2} \int_{\Omega} \rho \dot{\mathbf{u}}^2 d\Omega + \frac{1}{2} \int_{\Omega} C_3 \rho (\mathbf{v} - \dot{\mathbf{u}})^2 d\Omega. \quad (3.20)$$

The semi-discrete equation of motion is

$$\begin{cases} (1 + C_3)\mathbf{M}\ddot{\mathbf{U}} - C_3\mathbf{B}\dot{\mathbf{V}} = \mathbf{F}^{\text{ext}} - \mathbf{F}^{\text{int}} \\ \mathbf{B}^T\dot{\mathbf{U}} = \mathbf{Y}\mathbf{V}. \end{cases} \quad (3.21)$$

In case of element-wise ansatz functions for Ψ , the variable \mathbf{V} can be eliminated from the system of equations above by static condensation as proposed in HUGHES ET AL. (1976). This yields the equation of motion

$$\mathbf{M}^\circ \ddot{\mathbf{U}} = \mathbf{F}^{\text{ext}} - \mathbf{F}^{\text{int}}. \quad (3.22)$$

\mathbf{M}° is the variationally scaled mass matrix (VSMS) with

$$\mathbf{M}^\circ = \mathbf{M} + \boldsymbol{\lambda}^\circ \quad (3.23)$$

with the augmented mass

$$\boldsymbol{\lambda}^\circ = C_3(\mathbf{M} - \mathbf{B}\mathbf{Y}^{-1}\mathbf{B}^T). \quad (3.24)$$

The augmented mass $\boldsymbol{\lambda}^\circ$ can be computed on the element level, so that the matrix inversion \mathbf{y}_e^{-1} is computationally cheap. The free parameter C_3 can be chosen uniformly for the whole geometry or varied from element to element. Especially for practical applications a non-uniform choice of the free parameters throughout the geometry may be used. It allows individual free parameters for each element depending on the element geometry and material properties to influence the elemental critical time step.

3.3.3 Variationally scaled consistent inverse mass matrices (VSRMS)

A second instance of the template from eq. (3.19) is obtained with $C_1 = -1$, $C_3 = 0$ and C_2 kept as free parameter. The modified kinetic energy is thus

$$W_{\text{kin}}^\circ(\dot{\mathbf{u}}, \mathbf{v}, \mathbf{p}, C_2) = -\frac{1}{2} \int_{\Omega} \rho^{-1} \mathbf{p}^2 \, d\Omega + \int_{\Omega} \dot{\mathbf{u}}^T \mathbf{p} \, d\Omega + \frac{C_2}{2\rho} \int_{\Omega} (\rho \mathbf{v} - \mathbf{p})^2 \, d\Omega, \quad (3.25)$$

leading to the semi-discrete equation of motion

$$\begin{cases} \mathbf{A}\dot{\mathbf{P}} = \mathbf{F}^{\text{ext}} - \mathbf{F}^{\text{int}} \\ \mathbf{A}^T \dot{\mathbf{U}} = (1 - C_2)\mathbf{C}\mathbf{P} + C_2\mathbf{W}\mathbf{V} \\ \mathbf{Y}\mathbf{V} = \mathbf{W}^T \mathbf{P}. \end{cases} \quad (3.26)$$

The variable \mathbf{V} can again be eliminated from the system of equations above by static condensation, yielding the equation of motion

$$\begin{cases} \mathbf{A}\dot{\mathbf{P}} = \mathbf{F}^{\text{ext}} - \mathbf{F}^{\text{int}} \\ \mathbf{A}^T \dot{\mathbf{U}} = \mathbf{C}^\circ \mathbf{P}. \end{cases} \quad (3.27)$$

The directly constructed variationally scaled reciprocal mass matrix (VSRMS) is

$$\mathbf{C}^\circ = \mathbf{C} + \tilde{\boldsymbol{\lambda}}^\circ \quad (3.28)$$

with the augmented reciprocal mass

$$\tilde{\boldsymbol{\lambda}}^\circ = C_2(\mathbf{W}\mathbf{Y}^{-1}\mathbf{W}^T - \mathbf{C}). \quad (3.29)$$

Again, the augmented reciprocal mass $\tilde{\boldsymbol{\lambda}}^\circ$ can be computed on the element level. Thus, a matrix inversion \mathbf{y}_e^{-1} is only required on the element level. The system of equations given in (3.27) can be solved explicitly only if the projection matrix \mathbf{A} is diagonal. This is achieved by taking the basis of the momentum ansatz functions $\boldsymbol{\chi}$ to be biorthogonal to the displacement shape functions. The specific choice of ansatz functions for \mathbf{N} , $\boldsymbol{\Psi}$ and $\boldsymbol{\chi}$ in eq. (3.14) is discussed in the following section.

Explicit codes usually treat the equation of motion as one second order differential equation. To fit this pattern the momentum can be further eliminated leading to the equation of motion in the form

$$\dot{\mathbf{U}} = \mathbf{A}^{-T} \mathbf{C}^\circ \mathbf{A}^{-1} (\mathbf{F}^{\text{ext}} - \mathbf{F}^{\text{int}}). \quad (3.30)$$

Provided we use a biorthogonal basis for discretization of the linear momentum \mathbf{p} , the projection matrix \mathbf{A} has diagonal structure and thus, the accelerations are obtained trivially without matrix inversion and without the solution of a linear system of equations on the global level.

3.4 Requirements on the ansatz spaces for consistency for constant density

In this section, the required ansatz spaces for a consistent formulation with constant density are provided. Appropriate ansatz spaces for all independent fields, namely the displacement, the velocity and the linear momentum are to be discussed.

3.4.1 Spaces for displacements

For the approximation of the displacements in space standard shape functions are used. The required continuity of the shape functions depends on the highest spatial derivative in the weak form, called the variational index. Since only solid elements are considered herein, the variational index for the displacement \mathbf{u} is always 1, requiring at least C^0 -continuity between elements.

To date, the following element types have been analyzed for variational mass and reciprocal mass matrices: In the initial work of variational mass matrices of TKACHUK AND BISCHOFF (2013), Q1 and Hex8 finite elements were considered. In the dissertation of TKACHUK (2013), various linear and quadratic element types were studied. In SCHÄUBLE ET AL. (2014) the focus was on higher order elements. Different ansatz spaces were analyzed by the multi-parametric template described in Section 4.2. In the initial work for reciprocal mass matrices of TKACHUK AND BISCHOFF (2015) only simplex elements in form of a 1-D 2-node rod element, a 2-D three-node triangle element and a 3-D four-node tetrahedral element were considered. In SCHAEUBLE ET AL. (2017), the focus was on B-spline- and NURBS-based continuum finite elements in 1-D and 2-D. Herein, the formulation of reciprocal mass matrices is generalized for a wide range of solid finite elements. In this work, additionally to the elements mentioned above, for example standard Lagrange finite elements, like 2-D 4-node standard and reduced integrated Q1 elements, 3-D 10-node Tet10 elements and 2-D Serendipity 8-node S2 elements, are considered. For the displacements, the standard shape functions of these well-established elements are used.

3.4.2 Spaces for velocities

Since no derivatives of the velocity occur in the weak formulation, discontinuous velocity ansatz spaces may be chosen. For completeness, a purely constant ansatz function matrix is sufficient, i.e. with

$$\Psi_1^{1-D} = [1], \quad \Psi_1^{2-D} = \begin{bmatrix} 1 & 0 \\ 0 & 1 \end{bmatrix}, \quad \Psi_1^{3-D} = \begin{bmatrix} 1 & 0 & 0 \\ 0 & 1 & 0 \\ 0 & 0 & 1 \end{bmatrix} \quad (3.31)$$

in 1-D, 2-D and 3-D, respectively, consistency is guaranteed. Enriched choices for Ψ are discussed in Chapter 4 in the context of inertia customization. At first, the spaces for velocity depend only on the dimension, since the degrees of freedom are elemental and not nodal degrees of freedom. In Chapter 4, a recommendation for optimal velocity spaces and parameter choices in dependence of the customization goal and the element type are given. The usage of only discontinuous (i.e. C^{-1} -continuous) ansatz functions independent of the continuity of the displacement shape functions (i.e. also for B-spline and NURBS-based finite elements) allows the elimination of the velocity degrees of freedom from the system of equations by static condensation.

3.4.3 Spaces for linear momenta

Since also no derivatives of the linear momentum occur in the weak formulation, discontinuous linear momentum ansatz spaces are as well allowed. For completeness, the ansatz functions must be able to represent at least a constant value. These requirements were met by the proposed linear momentum ansatz functions in TKACHUK AND BISCHOFF (2015). There, it is suggested to use the standard dual basis from literature which satisfies the biorthogonality condition with

$$A_{ij} = \int_{\Omega} N_i \chi_j \, d\Omega = c_j \delta_{ij}. \quad (3.32)$$

The resulting diagonal projection matrix \mathbf{A} allows for a trivial solution in eq. (3.27) or (3.30). Finally, the standard dual basis is scaled with the so-called global support, which makes the diagonal matrix \mathbf{A} equal to the identity matrix and unitless so that \mathbf{A} can be simply omitted. The construction procedure to obtain these linear momentum ansatz functions reads the following: First, the displacement shape functions are multiplied with the inverted local metric, i.e.

$$\hat{\chi} = \mathbf{N}(\mathbf{m}_e^*)^{-1}, \quad (3.33)$$

where \mathbf{m}_e^* is the local metric

$$\mathbf{m}_e^* = \int_{\Omega_e} \mathbf{N}^T \mathbf{N} \, d\Omega_e. \quad (3.34)$$

Subsequently, each function $\hat{\chi}_i$ is scaled with the local support $\bar{t}_{e,i}$ of element e at the local degree of freedom i with

$$\tilde{\chi}_i = \hat{\chi}_i \bar{t}_{e,i} \quad \text{with} \quad \bar{t}_{e,i} = \int_{\Omega_e} N_i \, d\Omega_e. \quad (3.35)$$

This standard biorthogonal basis (cf. WOHLMUTH (2002)) satisfies partition of unity, i.e.

$$\sum_i \tilde{\chi}_i = 1 \quad (3.36)$$

and guarantees that a constant can be represented exactly for completeness. Then, to simplify eq. (3.27) with $\mathbf{A} = \mathbf{I}$, where \mathbf{I} is the identity matrix, the standard dual basis is scaled with the global support $\bar{\mathbf{T}}$ by

$$\chi_i = \frac{\tilde{\chi}_i}{\bar{T}_j} \quad \text{with} \quad \bar{\mathbf{T}} = \bigcup_e \bar{\mathbf{t}}_e, \quad (3.37)$$

where \bar{T}_j is the global support at the global degree of freedom j , which is obtained by assembly of the local support $\bar{\mathbf{t}}_e$ over all elements e . The local and global degrees of freedom i and j are mapped through the connectivity matrix $j = \text{ID}[i, e]$, which relates local and global node numbering. This scaling does not destroy the completeness achieved before, since it is carried out on the global degree of freedom level.

3.5 Limitations of the formulation

In the previous section, the ansatz spaces for constant density were provided. In this section, the ansatz spaces are first verified. Then, it is shown that the ansatz spaces proposed by TKACHUK AND BISCHOFF (2015) and described herein are not sufficient for non-constant density. This serves as justification for the proposal of improved ansatz spaces in the subsequent section.

3.5.1 Verification example for constant density in 1-D

At first, the example from Section 3.1 is again considered, but now in a variational setting. The rod is discretized with two linear finite elements with the shape functions for the displacement

$$N_1 = \frac{1}{2} - \frac{1}{2}\xi, \quad N_2 = \frac{1}{2} + \frac{1}{2}\xi. \quad (3.38)$$

The construction of the biorthogonal basis leads to the standard dual basis from literature

$$\tilde{\chi}_1 = \frac{1}{2} - \frac{3}{2}\xi, \quad \tilde{\chi}_2 = \frac{1}{2} + \frac{3}{2}\xi. \quad (3.39)$$

This standard dual basis is then again scaled by the global support to

$$\chi_1^{\text{el}=1} = \frac{1}{5} - \frac{3}{5}\xi, \quad \chi_2^{\text{el}=1} = \frac{1}{10} + \frac{3}{10}\xi, \quad (3.40)$$

$$\chi_1^{\text{el}=2} = \frac{1}{10} - \frac{3}{10}\xi, \quad \chi_2^{\text{el}=2} = \frac{1}{5} - \frac{3}{5}\xi \quad (3.41)$$

to satisfy $\mathbf{A} = \mathbf{I}$ on the global level. While the standard dual basis is the same for each element, scaling with the global support changes the shape function in dependence of the connectivity. The displacement shape functions N , the standard dual shape functions $\tilde{\chi}$ and the used linear momentum shape functions χ are visualized in Figure 3.3. For the velocity field, constant shape functions according to eq. (3.31) are used. With this choice of ansatz spaces, the following variationally scaled reciprocal mass matrices and projection matrices on the element level are obtained:

$$\mathbf{c}_1 = \begin{bmatrix} \frac{1}{1250} - \frac{3}{5000}C_2 & -\frac{1}{5000} + \frac{3}{10000}C_2 \\ -\frac{1}{5000} + \frac{3}{10000}C_2 & \frac{1}{5000} - \frac{3}{20000}C_2 \end{bmatrix}, \quad \mathbf{a}_1 = \begin{bmatrix} 1 & 0 \\ 0 & \frac{1}{2} \end{bmatrix}, \quad (3.42)$$

$$\mathbf{c}_2 = \begin{bmatrix} \frac{1}{5000} - \frac{3}{20000}C_2 & -\frac{1}{5000} + \frac{3}{10000}C_2 \\ -\frac{1}{5000} + \frac{3}{10000}C_2 & \frac{1}{1250} - \frac{3}{5000}C_2 \end{bmatrix}, \quad \mathbf{a}_2 = \begin{bmatrix} \frac{1}{2} & 0 \\ 0 & 1 \end{bmatrix}. \quad (3.43)$$

For $C_2 = 0$ the inverted mass matrix \mathbf{m}_e^{-1} and the projection matrix \mathbf{a}_e are linked with the reciprocal mass matrix \mathbf{c}_e by $\mathbf{a}_e \mathbf{m}_e^{-1} \mathbf{a}_e = \mathbf{c}_e$ on the element level. Assembly of the

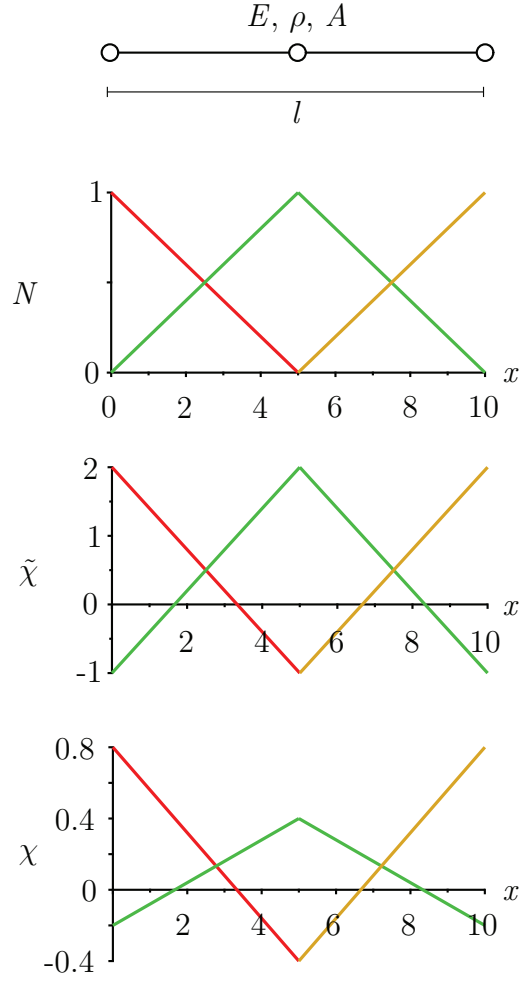


Figure 3.3: Shape functions for two linear finite elements of constant density.

elemental matrices leads to the variationally scaled reciprocal mass matrix

$$\mathbf{C}^\circ = \begin{bmatrix} \frac{1}{1250} - \frac{3}{5000}C_2 & -\frac{1}{5000} + \frac{3}{10000}C_2 & 0 \\ -\frac{1}{5000} + \frac{3}{10000}C_2 & \frac{1}{2500} - \frac{3}{10000}C_2 & -\frac{1}{5000} + \frac{3}{10000}C_2 \\ 0 & -\frac{1}{5000} + \frac{3}{10000}C_2 & \frac{1}{1250} - \frac{3}{5000}C_2 \end{bmatrix} \quad (3.44)$$

on the global level. All possible reciprocal mass matrices described by the template (3.44) preserve mass and linear momentum, independent of the choice for the free parameter C_2 . The variational setting is thus appropriate to develop families of variationally consistent reciprocal mass matrices for constant density. The special choice of $C_2 = \frac{2}{3}$ leads to a diagonal reciprocal mass matrix. This variationally obtained reciprocal mass matrix is

identical to the algebraically constructed one in Section 3.1, eq. (3.3, left). Next, the variational setting is tested for the assembly of elements with varying density.

3.5.2 Falsification example for non-constant density

In a second example, the same setup is considered, but the two linear finite elements are of different density, see Figure 3.4. Since the construction procedure of the linear

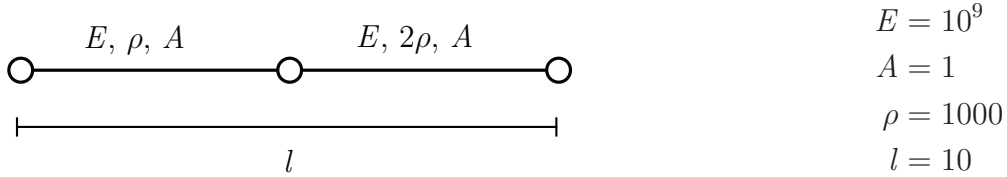


Figure 3.4: Assembly of two linear finite elements with constant, but different density.

momentum ansatz functions presented in eq. (3.33) to eq. (3.37) is independent of the density, the linear momentum ansatz functions remain unaltered, i.e. the ones presented in Figure 3.3 are still valid. The variationally scaled reciprocal mass matrix for piecewise constant density is then

$$\mathbf{C}^\circ = \begin{bmatrix} \frac{1}{1250} - \frac{3}{5000}C_2 & -\frac{1}{5000} + \frac{3}{10000}C_2 & 0 \\ -\frac{1}{5000} + \frac{3}{10000}C_2 & \frac{3}{10000} - \frac{9}{40000}C_2 & -\frac{1}{10000} + \frac{3}{20000}C_2 \\ 0 & -\frac{1}{10000} + \frac{3}{20000}C_2 & \frac{1}{2500} - \frac{3}{10000}C_2 \end{bmatrix}. \quad (3.45)$$

However, this template preserves mass only for the condition

$$(40000C_2 - 55000)/(-4 + 3C_2) = 15000, \quad (3.46)$$

i.e. only for $C_2 = 1$. The choice of $C_2 = 1$ violates the stability limit, i.e. the reciprocal mass matrix is singular in this case. The non-preservation of mass can also be easily

seen from the diagonal inverse mass matrix

$$\mathbf{C}^\circ = \begin{bmatrix} \frac{1}{2500} & 0 & 0 \\ 0 & \frac{3}{20000} & 0 \\ 0 & 0 & \frac{1}{5000} \end{bmatrix} \quad (3.47)$$

with $C_2 = \frac{2}{3}$, resulting in a total mass of 14166.67 instead of 15000. As a result, the shape functions proposed in TKACHUK AND BISCHOFF (2015) and provided in Section 3.4.3 are appropriate for constant density, but for non-constant density the formulation is not consistent.

3.6 Improved ansatz spaces for linear momenta

In order to provide appropriate ansatz spaces also for non-constant density, a generalized construction procedure is proposed. Then, the resulting ansatz spaces are evaluated for different density distributions in 1-D. The section closes with a verification for various density distributions in 2-D, performed with a patch of serendipity finite elements.

3.6.1 Generalized construction procedure

For mass preservation in case of non-constant density, the reciprocal mass matrices do not only need to contain information about the connectivity, but also about the material distribution in the neighboring element. This information is transferred by considering the density in the construction procedure of the biorthogonal basis. The density may vary in space, i.e. in a 1-D setting the density is $\rho = \rho(x)$.

Although it is clear that the density should be considered in the construction procedure, it is not obvious whether or not it should be taken into account in

- the metric,
- the local support and/or
- the global support.

To unify this variety of decision possibilities in one generalized construction procedure, the density is considered in the following with exponent 0 or 1 in each step. This allows

to take the density into account with $\rho^1 = \rho$ or neglect it with $\rho^0 = 1$. One class of biorthogonal shape functions is thus defined by

$$\hat{\chi} = \mathbf{N} \left(\int_{\Omega_e} \rho^{\bar{\alpha}} \mathbf{N}^T \mathbf{N} d\Omega_e \right)^{-1} \quad \text{with } \bar{\alpha} \in \{0,1\}, \quad (3.48)$$

$$\tilde{\chi}_i = \hat{\chi}_i \left(\int_{\Omega_e} \rho^{\bar{\beta}} N_i d\Omega_e \right) \quad \text{with } \bar{\beta} \in \{0,1\}, \quad (3.49)$$

$$\chi_i = \rho^{\bar{\delta}} \frac{\tilde{\chi}_i}{T_j} \quad \text{with } \bar{\mathbf{T}} = \bigcup_e \left(\int_{\Omega_e} \rho^{\bar{\gamma}} \mathbf{N} d\Omega_e \right) \quad \text{with } \bar{\gamma} \in \{0,1\}. \quad (3.50)$$

The usage of the density or not changes the units in each step. To guarantee consistent units and mass preservation for at least constant density, the shape functions need to be multiplied with a multiple of the density in step (3.50). The exponent $\bar{\delta}$ is thus dependent on the other parameters through the condition

$$-\bar{\beta} + \bar{\alpha} + \bar{\gamma} = \bar{\delta} \quad (3.51)$$

for the $\mathbf{u}\text{-}\mathbf{v}\text{-}\mathbf{p}$ -formulation.

All shape functions defined by this class satisfy the biorthogonality condition, i.e. \mathbf{A} is equal to a unitless identity matrix. The construction procedure (3.48) to (3.50) includes also the original construction procedure (eq. (3.33) to (3.37)) where the density was not taken into account with $\bar{\alpha} = \bar{\beta} = \bar{\gamma} = 0$. The proposed general construction procedure can as well be used for the $\mathbf{u}\text{-}\mathbf{v}\text{-}\mathbf{v}_p$ - formulation, where the condition

$$-\bar{\beta} + \bar{\alpha} + \bar{\gamma} - 1 = \bar{\delta} \quad (3.52)$$

need to be satisfied instead of eq. (3.51).

3.6.2 Validation for different density distributions in 1-D

Next, the different shape functions resulting from the generalized construction procedure are tested. The assembly of two linear finite elements is again considered. This time, the test is performed for different configurations of the spatial distribution of the density. The density in each element is defined by

$$\rho(\xi) = \rho_0 + \rho_1 P_1(\xi) + \rho_2 P_2(\xi), \quad (3.53)$$

Table 3.1: Check of mass preservation for different choices of $\bar{\alpha}$, $\bar{\beta}$, and $\bar{\gamma}$ for a constant, linear and quadratic spatial distribution of the density.

$\bar{\alpha}$	0	0	0	0	1	1	1	1
$\bar{\beta}$	0	0	1	1	0	0	1	1
$\bar{\gamma}$	0	1	0	1	0	1	0	1
$\rho = \text{const.}$	✓	✓	✓	✓	✓	✓	✓	✓
$\rho = \text{lin.}$	X	X	X	✓	X	X	X	✓
$\rho = \text{quad.}$	X	X	X	X	X	X	X	✓

where ρ_i are arbitrary density coefficients and $P_1(\xi)$ and $P_2(\xi)$ are Legendre polynomials of first and second order, respectively. The Legendre polynomials are orthogonal in the interval $-1 \leq \xi \leq 1$, i.e.

$$\int_{-1}^1 P_m(\xi)P_n(\xi) d\xi = \delta_{mn}. \quad (3.54)$$

Higher order terms are negligible in eq. (3.53) since they are ignored through orthogonality to the displacement shape functions by

$$\int_{-1}^1 \rho_2 P_2(\xi) \mathbf{N}(\xi) d\xi = \mathbf{0}, \quad (3.55)$$

$$\int_{-1}^1 \rho_3 P_3(\xi) \mathbf{N}(\xi)^T \mathbf{N}(\xi) d\xi = \mathbf{0}. \quad (3.56)$$

Thus, even if higher order terms occur in the density, they will be erased in the metric and the local and global support and therefore they will not show up in the biorthogonal basis.

First, the various construction possibilities are tested for mass preservation. Table 3.1 summarizes the results in dependence of various choices for the free parameters $\bar{\alpha}$, $\bar{\beta}$ and $\bar{\gamma}$. For all parameter choices, the mass is preserved for constant density. This is expected, since for constant density, the density can simply be canceled and the shape functions are independent of the parameters $\bar{\alpha}$, $\bar{\beta}$ and $\bar{\gamma}$. To satisfy mass preservation in the case of a linear density distribution, the density needs to be considered at least in the local and in the global support. The best result is obtained when the density is considered in the local support, the global support and additionally in the metric, i.e. $\bar{\alpha} = \bar{\beta} = \bar{\gamma} = 1$ holds. Then, the mass is preserved for a quadratic density distribution as well.

Thus, the improved construction procedure – which will be used in the rest of the present work – reads the following:

The displacement shape functions are multiplied with the density-weighted inverse metric

$$\hat{\boldsymbol{\chi}} = \mathbf{N}\mathbf{m}_e^{-1}, \quad (3.57)$$

with

$$\mathbf{m}_e = \int_{\Omega_e} \rho \mathbf{N}^T \mathbf{N} \, d\Omega_e. \quad (3.58)$$

Each function $\hat{\chi}_i$ is scaled with the local density-weighted support $t_{e,i}$ of element e at the local degree of freedom i with

$$\tilde{\chi}_i = \hat{\chi}_i \bar{t}_{e,i} \quad \text{with} \quad \bar{t}_{e,i} = \int_{\Omega_e} \rho N_i \, d\Omega_e. \quad (3.59)$$

For constant (or element-wise constant) density, these ansatz functions are equal to the standard biorthogonal basis. Independent of the density distribution, these ansatz functions satisfy partition of unity. Next, these functions are scaled with the density-weighted global support and multiplied with the density to satisfy mass preservation:

$$\chi_i = \rho \frac{\tilde{\chi}_i}{T_j} \quad \text{with} \quad \bar{\mathbf{T}} = \bigcup_e \bar{\mathbf{t}}_e. \quad (3.60)$$

The multiplication with the density is required to be consistent in terms of units. Remember that the biorthogonal basis has the unit $1/\text{m}^3$.

This novel construction procedure leads to the same ansatz spaces for constant density as the original procedure. For the earlier considered example of piecewise constant density, the shape functions are illustrated in Figure 3.5 in the left column. Only the shape function at the common degree of freedom is modified with respect to the original ones. The fact that some of the linear momentum and standard dual shape functions are continuous across element boundaries is only a coincidence. With these novel shape functions, the following variationally scaled reciprocal mass matrix is obtained for the

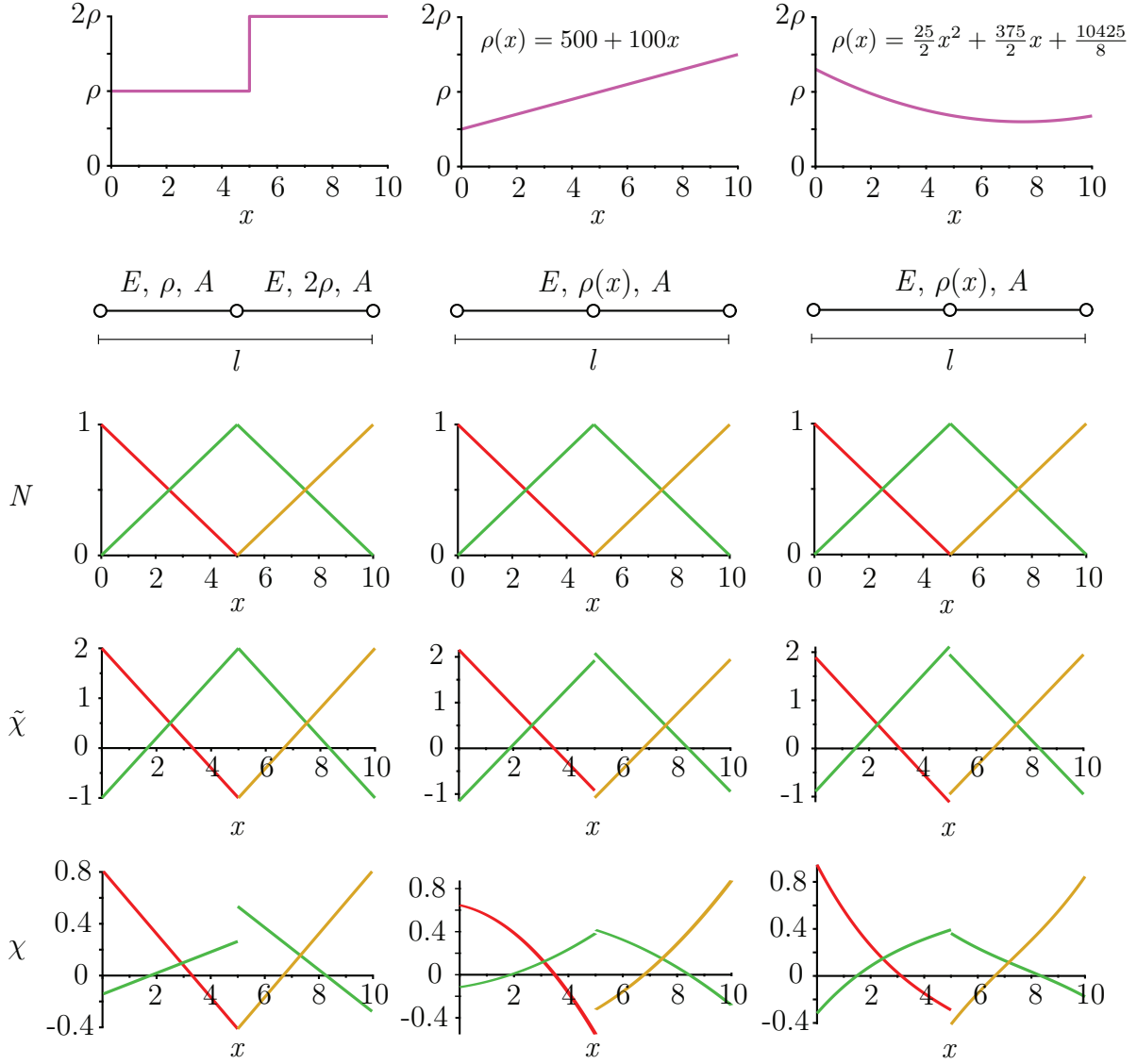


Figure 3.5: Shape functions for the $\mathbf{u-v-p}$ -formulation for two linear finite elements of piecewise constant (left), linear (middle) and quadratic (right) density distribution with $\bar{\alpha} = \bar{\beta} = \bar{\gamma} = 1$.

assembly of the two linear finite elements of piecewise constant density:

$$\mathbf{C}^\circ = \begin{bmatrix} \frac{1}{1250} - \frac{3}{5000}C_2 & -\frac{1}{7500} + \frac{1}{5000}C_2 & 0 \\ -\frac{1}{7500} + \frac{1}{5000}C_2 & \frac{1}{3750} - \frac{1}{5000}C_2 & -\frac{1}{7500} + \frac{1}{5000}C_2 \\ 0 & -\frac{1}{7500} + \frac{1}{5000}C_2 & \frac{1}{2500} - \frac{3}{10000}C_2 \end{bmatrix}. \quad (3.61)$$

This reciprocal mass template preserves mass and linear momentum for all values of C_2 in the stable range. The diagonal reciprocal mass matrix for $C_2 = 2/3$ is, as expected,

$$\mathbf{C}^\circ = \begin{bmatrix} \frac{1}{2500} & 0 & 0 \\ 0 & \frac{1}{7500} & 0 \\ 0 & 0 & \frac{1}{5000} \end{bmatrix}. \quad (3.62)$$

The shape functions for a linear and a quadratic spatial distribution of the density are as well illustrated in Figure 3.5 in the middle and right column, respectively. The shape functions before scaling with the global support $\tilde{\chi}$ are no longer equivalent to the standard biorthogonal basis from literature. Even though they look quite similar for the linear and the quadratic distribution, a second look shows that they are not. The final shape functions χ are quadratic and cubic in x for the linear and the quadratic distribution, respectively. By the improved ansatz spaces given in eq. (3.57) to (3.60) variationally consistent reciprocal mass templates for 1-D linear elements with up to quadratic density distribution in space are obtained. All templates preserve mass independent of the free parameter C_2 .

Unfortunately, the proposed construction scheme is not very intuitive. More obvious is the construction of the improved biorthogonal basis for the reparametrized formulation, where \mathbf{p} is replaced by $\mathbf{p} = \rho \mathbf{v}_p$ as described in Section 3.2.2. The reparametrization leads to reparametrized biorthogonal ansatz functions $\boldsymbol{\kappa} = \rho^{-1} \boldsymbol{\chi}$. The multiplication with the density in eq. (3.60) is thus omitted and therefore, the biorthogonal basis is of the same polynomial order as the displacement ansatz functions, independent of the spatial density distribution in the element. Nevertheless, the biorthogonal shape functions still depend on the density. The reparameterization has no influence on the formulation, i.e. the matrices

$$\mathbf{A} = \bigcup_e \mathbf{a}_e = \bigcup_e \left(\int_{\Omega_e} \rho \mathbf{N}^T \boldsymbol{\kappa} \, d\Omega_e \right), \quad \mathbf{W} = \bigcup_e \mathbf{w}_e = \bigcup_e \left(\int_{\Omega_e} \rho \boldsymbol{\kappa}^T \boldsymbol{\Psi} \, d\Omega_e \right), \quad (3.63)$$

$$\mathbf{C} = \bigcup_e \mathbf{c}_e = \bigcup_e \left(\int_{\Omega_e} \rho \boldsymbol{\kappa}^T \boldsymbol{\kappa} \, d\Omega_e \right). \quad (3.64)$$

are identical to the matrices given in eq. (3.17) and (3.18). The projection matrix \mathbf{A} is always unitless and the identity matrix.

3.6.3 Verification for various density distributions for a 2-D serendipity element

Although the proposed ansatz functions provide a consistent reciprocal mass template for the considered example, the question remains whether this improved construction procedure is valid for various solid finite element types.

In the following, the formulation is tested for a patch of 2-D serendipity finite elements. Serendipity elements are especially critical since the local support, i.e. the shape function integrated over the domain, is negative for the corner degrees of freedom. Due to this fact, the row-sum-lumping can not be applied to serendipity elements: it causes negative mass on the main diagonal.

Since the local support is used in density-weighted form in the construction procedure of the biorthogonal shape functions in eq. (3.59), it has to be checked whether it causes any artificial effects by performing inertia patch tests on a distorted patch.

Different versions of inertia patch tests (patch test A to E) were described in TKACHUK (2013) and they are similar to the well-known equivalent of element patch tests in static analysis (TAYLOR ET AL. 1986). Herein, inertia patch test C is used. Its scenario is the following: A stress-free structure ($\mathbf{F}^{\text{int}} = \mathbf{0}$) is subjected to a body load $\rho\hat{\mathbf{b}}$, where $\hat{\mathbf{b}}$ is a uniform acceleration. This body load results in an external force

$$\mathbf{F}^{\text{ext}} = \bigcup_e \mathbf{f}_e^{\text{ext}} = \bigcup_e \int_{\Omega_e} \rho \mathbf{N}^T \hat{\mathbf{b}} \, d\Omega_e, \quad (3.65)$$

where $\hat{\mathbf{b}}$ can for example be imagined as the gravitational acceleration. For simplicity it can in the following be assumed to be 1, acting in negative y -direction. The given problem setup can be interpreted as a real physical experiment and under this applied load, the structure is expected to move with a uniform acceleration, i.e. the vector

$$\ddot{\mathbf{U}} = \mathbf{C}^\circ \mathbf{P} = \mathbf{C}^\circ (\mathbf{F}^{\text{ext}} - \mathbf{F}^{\text{int}}) \quad (3.66)$$

contains -1 on all odd entries for the assumed gravitational acceleration of 1 in negative y -direction. This test can be performed with uniform gravitational acceleration – performing a so-called constant patch test or with linear or higher-order gravitational acceleration – performing a linear or higher-order patch test.

Beside the applied load, the density may be varied. In TKACHUK (2013), the patch test was always performed with constant density. In the last section, it was shown that it is important to validate the proposed formulation for different spatial distributions of the density. Therefore, patch tests with different distributions of the density are required.

Since the displacement shape functions of serendipity finite elements contain up to $\xi^2\eta$ -, $\xi\eta^2$ -terms and the product $\mathbf{N}^T\mathbf{N}$ contains up to bicubic terms, the highest polynomials in the density that can still be seen from the element are $\xi^3\eta^3$ -terms. Higher terms are canceled through orthogonality. The density is thus assumed to be of the form

$$\rho(\xi) = \rho_0 + \rho_1 P_1(\xi) + \rho_2 P_1(\eta) + \dots + \rho_{20} P_3(\xi) P_3(\eta), \quad (3.67)$$

where P_i are again Legendre polynomials of i^{th} order and ρ_j are arbitrary coefficients. Independent of its mass distribution, the structure is expected to move with uniform acceleration in the body, whereas the linear momentum varies in space.

In general, the patch test has to be performed with a patch, i.e. an assembly of various elements which are initially distorted to guarantee consistency not only for regular meshes, but for arbitrary ones.

For the validation a patch of three serendipity elements is considered, shown in Figure 3.6. Material and geometric parameters are provided next to the figure. The patch

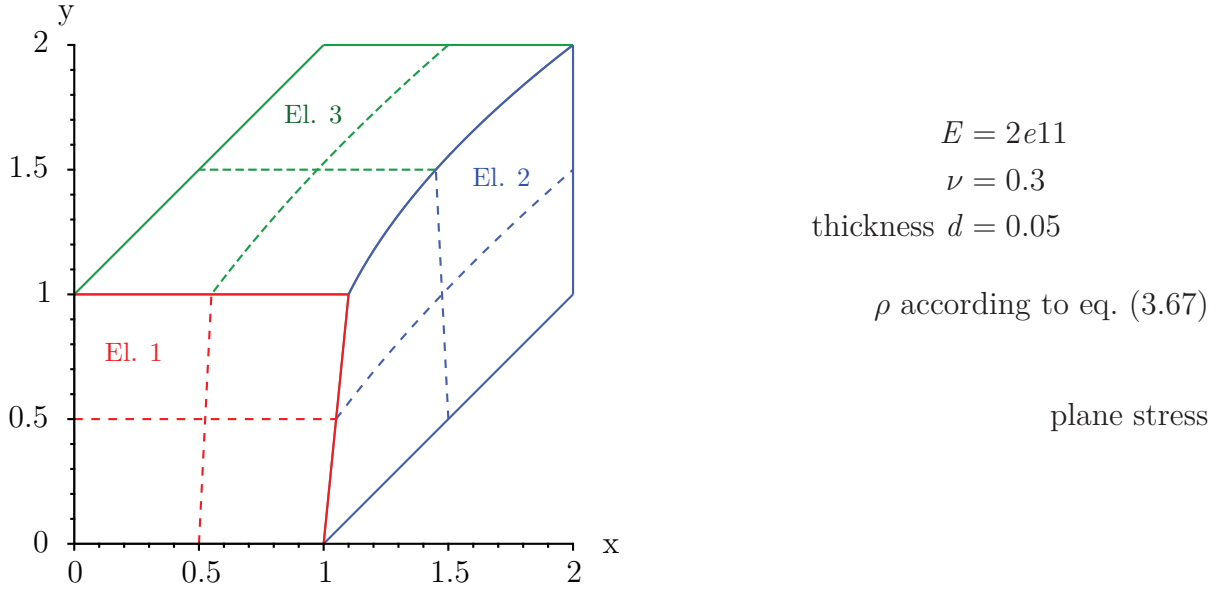


Figure 3.6: Patch consisting of three serendipity finite elements.

test is performed for a constant body load of 1 in x -direction. Both a constant density of $\rho = 1$ and a bicubic density distribution of $\rho = 1 + \xi\eta + \xi^3\eta^3$ in each element are considered. For constant density, any parameter choice of $\bar{\alpha}$, $\bar{\beta}$ and $\bar{\gamma}$ preserves the mass and passes the patch test. For the bicubic density distribution, only the formulation with $\bar{\alpha} = \bar{\beta} = \bar{\gamma} = 1$ preserves mass and passes the patch test, i.e. the uniform external body load results in a uniform rigid body motion. In Figure 3.7 the acceleration is visualized for a uniform body load of 1 in x -direction. The variationally scaled reciprocal mass matrix is used with scaling factor 0.5 and constant velocity ansatz space.

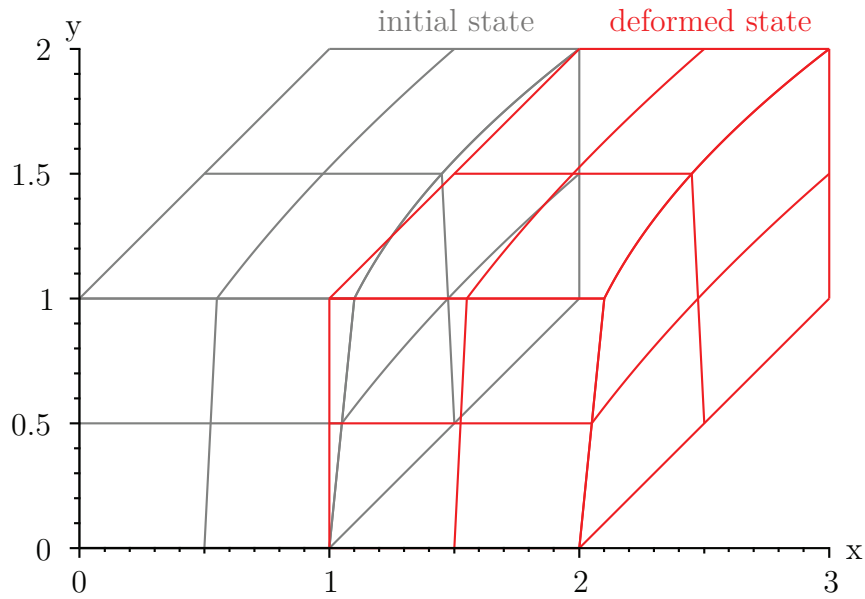


Figure 3.7: Result of patch test C, where a uniform external body load is applied. The result is a rigid body movement with uniform acceleration.

3.7 Treatment of boundary conditions and MPCs

In this section, the treatment of displacement boundary conditions and multi-point constraints for reciprocal mass matrices is discussed.

3.7.1 Homogeneous Dirichlet boundary conditions

When the boundary conditions are imposed by elimination, the linear momentum shape functions in the boundary element need to be modified to retain a purely explicit discretization scheme. Therefore, the number of linear momentum degrees of freedom has to be reduced to the number of unconstrained displacement degrees of freedom of the discretized system. This can be achieved by redistribution of the linear momentum ansatz functions of the constrained degree of freedom to the remaining degrees of freedom in the element. The procedure for the modification is the same for each element type: The linear momentum ansatz functions $\hat{\chi}_i$ constructed by the inverse metric (eq. (3.57)) are first scaled with the local support $t_{e,i}$ according to eq. (3.59) to obtain partition of unity. Then, the modification is performed under the condition of retaining partition of unity. This modification is unique only for simplex elements and it is described for a 1-D linear rod, a 3-node linear triangle and a 4-node tetrahedral finite element in TKACHUK AND BISCHOFF (2015). In SCHAEUBLE ET AL. (2017) different redistributions of the shape function of the constrained degree of freedom to the other degrees of freedom in the

element were studied for quadratic B-splines. A possible redistribution for a boundary element of a 1-D quadratic B-spline patch with open knot vector is illustrated in Figure 3.8. A homogeneous Dirichlet boundary condition is applied at the left end of a 1-D rod. Thus, the first shape function $\tilde{\chi}_1$ is erased and redistributed onto degree of freedom two and three in the first element. The shape function can be redistributed in the proportion 0.5/0.5 or with any other ratio. The investigation showed that a broad range

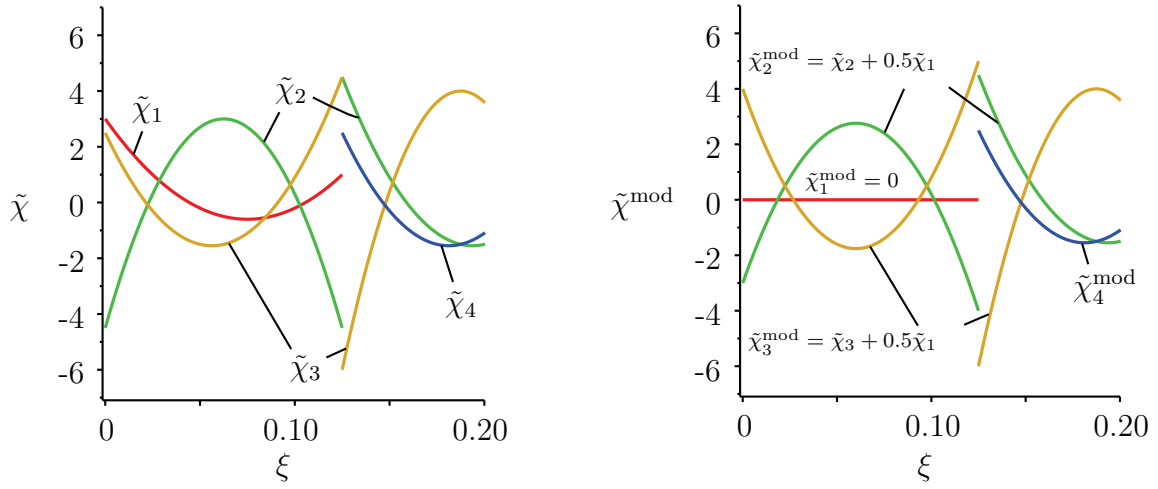


Figure 3.8: Linear momentum ansatz function in the boundary element without modification (left) and with modification (right) in the boundary element of a quadratic B-spline patch.

of variations in the redistribution resulted in the same maximum eigenfrequency and in the same convergence behaviour. Therefore, a uniform distribution with of the shape function onto the remaining degrees of freedom with 0.5/0.5 is recommended. All modifications led to a loss in the convergence order, for details it is referred to SCHAEUBLE ET AL. (2017).

That means for any solid finite element type with n non-zero shape functions per element (equal to the number of nodes for standard Lagrange finite elements), the modification on the shape function $\tilde{\chi}$ can be described as follows:

1. For each coordinate direction, the shape functions of all constrained degrees of freedom are added up to obtain the sum \mathcal{S} . The number of constrained degrees of freedom i in each direction is counted as c .
2. The shape functions of the constrained degrees of freedom are set to zero. The shape functions of the unconstrained degrees of freedom are modified by adding $\mathcal{S}/(n - c)$ to it.
3. Steps 1 and 2 are repeated for all coordinate directions.

Alternatively, the boundary conditions can be weakly satisfied, e.g. by the Lagrange multiplier, Nitsche or penalty method. With the Lagrange multiplier method, the number of degrees of freedom increases by the number of boundary conditions, but the convergence order can be preserved. Alternatively, the implementation can be carried out in an implicit-explicit scheme like described below for multi-point constraints.

Furthermore, the boundary conditions can be enforced by so-called localized Lagrange multipliers as done by GONZÁLEZ ET AL. (2018a).

3.7.2 Multi-point constraints

Any set of linear time-independent constraints can be written in the form

$$\mathbf{G}^T \mathbf{U} + \mathbf{g}_0 = \mathbf{0}, \quad (3.68)$$

where \mathbf{G} is the constraint matrix and \mathbf{g}_0 is a vector of constraint offsets. For n_c considered constraints, the matrix \mathbf{G} has n_c columns. The constraints given by eq. (3.68) can be transferred to a constraint on the acceleration by building the second derivative in time resulting in the constraint

$$\mathbf{G}^T \ddot{\mathbf{U}} = \mathbf{0}. \quad (3.69)$$

The total system of equations is then

$$\begin{cases} \ddot{\mathbf{U}} = \mathbf{C}^\circ (\mathbf{F}^{\text{ext}} - \mathbf{F}^{\text{int}} - \mathbf{G}\mathbf{Z}) \\ \mathbf{G}^T \ddot{\mathbf{U}} = \mathbf{0}, \end{cases} \quad (3.70)$$

where $\mathbf{G}\mathbf{Z}$ is the global vector of the reaction force and \mathbf{Z} is the vector of discrete reaction forces. Since the matrix \mathbf{G} is known in advance for multi-point constraints, the discrete

reaction forces \mathbf{Z} are first computed by solving the linear system of equations

$$(\mathbf{G}^T \mathbf{C}^\circ \mathbf{G}) \mathbf{Z} = \mathbf{G}^T \mathbf{C}^\circ (\mathbf{F}^{\text{ext}} - \mathbf{F}^{\text{int}}). \quad (3.71)$$

The linear system of equations to solve is of size n_c . Then, the acceleration is computed according to eq. (3.70)₁.

In case the matrix \mathbf{G} is not known in advance the solution can be carried out in two steps by an explicit-implicit algorithm as it is proposed in CARPENTER ET AL. (1991) for Lagrange-based contact resolution in explicit analyses.

3.8 A brief summary of Chapter 3

In the following, the advancements presented in Chapter 3 are shortly reviewed.

At the beginning of the chapter, the reader's attention was drawn to the specific properties of reciprocal mass matrices and the beauty of a variational scheme allowing the assembly of matrices that may typically not be assembled. After providing the variational formulation and presenting the originally proposed shape functions, this choice was critically questioned and improved ansatz spaces that allow mass preservation for arbitrary spatial density distributions were presented in eq. (3.57) to (3.60). The superiority of the proposed shape functions with respect to alternative ones was shown by considering examples of different density distribution, see Table 3.1. To test the provided ansatz spaces for arbitrary patches of different element types, a patch test for S2 serendipity elements is performed. At last, a general procedure to satisfy homogeneous boundary conditions by modification and a novel scheme to include multi-point constraints is proposed.

Inertia customization

In Chapter 3 the focus was on the appropriate formulation and appropriate ansatz spaces to obtain a consistent formulation. In this chapter, the focus is on enriched ansatz spaces for the velocity and tuning of the free parameters to the user's purpose to find optimal mass and inverse mass matrices with respect for specific customization goals. Customization goals could be, among others

- optimal low-frequency accuracy,
- highest speed-up with avoidance of negative dispersion,
- optimal accuracy for the same time step size as with the diagonal mass matrix,
- highest possible speed-up with at least i^{th} order low-frequency accuracy or
- highest possible speed-up (if limited by stability issues).

As the goal in mass scaling is to increase the speed-up (without deteriorating accuracy too much), especially the latter two customization goals describe what the mass scaling community is seeking for. Therefore, mass scaling can as well be understood as a special case of inertia customization (cf. FELIPPA ET AL. (2015)).

In the first section of this chapter, the enriched ansatz spaces proposed first in TKACHUK AND BISCHOFF (2013) for mass scaling are provided. In the subsequent section, a novel multi-parametric template is proposed allowing the combination of all these possible ansatz spaces by different scaling factors. Then, this multi-parametric template is systematically explored by grid dispersion analyses to tune the mass and reciprocal mass matrices for optimal low-frequency accuracy or other customization goals. Existing algebraic mass matrix formulations can as well be recovered with the provided template as shown in Section 4.3.5. Subsequently, the extension of the grid dispersion analysis to 2-D is discussed.

Note that throughout this chapter mostly B-spline finite elements are used to visualize the idea of inertia customization. The main reason is that, although improved spectral properties of B-spline and NURBS-based finite elements could be shown in COTTRELL ET AL. (2007, 2006), REALI (2006) and HUGHES ET AL. (2008), a sufficiently accurate (lumped) mass matrix for explicit dynamics for these elements is still focus of current research. The row-sum lumped mass, which is customary in standard finite element explicit analysis, is only 2nd order accurate, independent of the polynomial order p of the B-spline ansatz functions. Therefore, the multi-parametric template of Section 4.2 provides a powerful framework to rethink possible mass and inverse mass matrices also for B-spline and NURBS-based FEM and propose novel variationally consistent higher-order mass matrices and sparse reciprocal mass matrices. Moreover, algebraic higher order or scaled mass matrices from literature can be reproduced within the variational framework, confirming their theoretical soundness.

Herein, an introduction to B-splines, NURBS and the isogeometric approach is omitted. For readers who are not familiar with these topics it is referred to the paper of HUGHES ET AL. (2005) or the book of COTTRELL (2009).

4.1 Choice of ansatz spaces for speed-up and accuracy

In Section 3.2 a three-field formulation was presented that provides particularly more freedom than a standard displacement-based formulation. While the displacement ansatz spaces are determined from the chosen finite element type and the choice of the linear momentum ansatz space is restricted by the biorthogonality condition, the developer has the largest freedom in the choice of the velocity ansatz spaces. In order to guarantee consistency, at least constant velocity ansatz spaces as given in eq. (3.31) are required. With these ansatz spaces only translational inertia is preserved, but they guarantee satisfaction of the constant patch test, provided that the linear momentum ansatz spaces are chosen appropriately, as intensively discussed in the foregoing chapter and always assumed in the following.

For preservation of the translational and rotational inertia, the ansatz function matrix

$$\Psi_2^{2-D} = \begin{bmatrix} 1 & 0 & -Y^h \\ 0 & 1 & X^h \end{bmatrix} \quad \text{and} \quad \Psi_2^{3-D} = \begin{bmatrix} 1 & 0 & 0 & -Y^h & Z^h & 0 \\ 0 & 1 & 0 & X^h & 0 & -Z^h \\ 0 & 0 & 1 & 0 & -X^h & Y^h \end{bmatrix} \quad (4.1)$$

in 2-D and 3-D, respectively, is required. This ansatz function matrix includes all rigid body modes. X^h and Y^h are the approximation of the element geometry obtained from the isoparametric approach.

Alternatively, the linear terms from the rotation can be decoupled with

$$\Psi_3^{2-D} = \begin{bmatrix} 1 & 0 & Y^h & 0 \\ 0 & 1 & 0 & X^h \end{bmatrix} \quad \text{and} \quad (4.2)$$

$$\Psi_3^{3-D} = \begin{bmatrix} 1 & 0 & 0 & Y^h & Z^h & 0 & 0 & 0 & 0 \\ 0 & 1 & 0 & 0 & 0 & X^h & Z^h & 0 & 0 \\ 0 & 0 & 1 & 0 & 0 & 0 & 0 & X^h & Y^h \end{bmatrix} \quad (4.3)$$

in 2-D and 3-D, respectively. This reduces the fill-in in the inertia matrix compared to when eq. (4.1) is used.

Another option is to use the complete linear ansatz with

$$\Psi_4^{2-D} = \begin{bmatrix} 1 & 0 & X^h & 0 & Y^h & 0 \\ 0 & 1 & 0 & X^h & 0 & Y^h \end{bmatrix} \quad \text{and} \quad (4.4)$$

$$\Psi_4^{3-D} = \begin{bmatrix} 1 & 0 & 0 & X^h & Y^h & Z^h & 0 & 0 & 0 & 0 & 0 & 0 \\ 0 & 1 & 0 & 0 & 0 & 0 & X^h & Y^h & Z^h & 0 & 0 & 0 \\ 0 & 0 & 1 & 0 & 0 & 0 & 0 & 0 & 0 & X^h & Y^h & Z^h \end{bmatrix} \quad (4.5)$$

in 2-D and 3-D, respectively. So far, the matrices Ψ_i are assumed to be constant in time and the initial coordinates are used for X^h and Y^h . For large rotations, the matrices containing X^h and Y^h need to be updated during deformation. This will be experienced in Example 6.6.

The so far mentioned ansatz spaces are especially sufficient for displacement shape functions of up to quadratic polynomial order. For higher polynomial orders, higher order velocity ansatz functions may be advantageous, as it will be shown in Section 4.3.2. It is also worth mentioning that C^{-1} -continuous velocity ansatz functions are used for all finite element types and thus, also for B-spline- and NURBS-based finite elements. This allows static condensation of the velocity degrees of freedom from the system of equations.

4.2 Multi-parametric template

In the following, a novel template form is proposed, which allows the combination and systematic investigation of various ansatz spaces for the velocity to optimize accuracy and speed-up.

In the template form, the various ansatz spaces are considered with different free parameters in the construction of the augmented mass with

$$\boldsymbol{\lambda}^\circ = \sum_{\alpha} C_{3\alpha} (\mathbf{M} - \mathbf{B}_{\alpha} \mathbf{Y}_{\alpha}^{-1} \mathbf{B}_{\alpha}^T) \quad (4.6)$$

for the variational mass template, where

$$\mathbf{B}_{\alpha} = \bigcup_e \left(\int_{\Omega_e} \rho \mathbf{N}^T \boldsymbol{\Psi}_{\alpha} d\Omega_e \right), \quad \mathbf{Y}_{\alpha} = \bigcup_e \left(\int_{\Omega_e} \rho \boldsymbol{\Psi}_{\alpha}^T \boldsymbol{\Psi}_{\alpha} d\Omega_e \right) \quad (4.7)$$

for different choices of $\boldsymbol{\Psi}_{\alpha}$. Analogously, the augmented inverse mass for the variationally constructed reciprocal mass template is constructed by

$$\tilde{\boldsymbol{\lambda}}^\circ = \sum_{\alpha} C_{2\alpha} (\mathbf{W}_{\alpha} \mathbf{Y}_{\alpha}^{-1} \mathbf{W}_{\alpha}^T - \mathbf{C}), \quad (4.8)$$

where

$$\mathbf{W}_{\alpha} = \bigcup_e \left(\int_{\Omega_e} \rho \boldsymbol{\chi}^T \boldsymbol{\Psi}_{\alpha} d\Omega_e \right) \quad (4.9)$$

for different choices of $\boldsymbol{\Psi}_{\alpha}$. The different ansatz spaces are controlled by the free inertia template parameters $C_{3\alpha}$ and $C_{2\alpha}$. In contrast to previous works, where only one-parametric families were used, the multiple-parameter templates proposed herein allow more flexibility, especially to tune the mass and reciprocal mass matrices for higher-order accuracy.

Any mass or reciprocal mass matrix resulting from this multi-parametric template passes the constant patch test a priori, presupposing that stability is also not violated. This is guaranteed by including the translational rigid body modes in each velocity ansatz function matrix $\boldsymbol{\Psi}_{\alpha}$. If the constant modes are not included in each matrix, i.e. if instead of the matrix given in eq. (4.2), the matrix

$$\boldsymbol{\Psi}_{3^*}^{2-D} = \begin{bmatrix} Y^h & 0 \\ 0 & X^h \end{bmatrix} \quad (4.10)$$

is used, the patch test will not be passed. The result of such a patch test is illustrated in Figure 4.1 for the scaled reciprocal mass matrix. The serendipity element with bicubic density distribution as described in Section 3.6.3 is used. A uniform acceleration $\hat{\mathbf{b}}$ in horizontal direction is applied. The linear velocity ansatz function matrix from eq. (4.2) is replaced by the reduced linear velocity ansatz function matrix (4.10). The scaling factors are chosen with $C_{22} = 0.5$ and $C_{21} = C_{23} = C_{24} = 0$. It can be seen that the

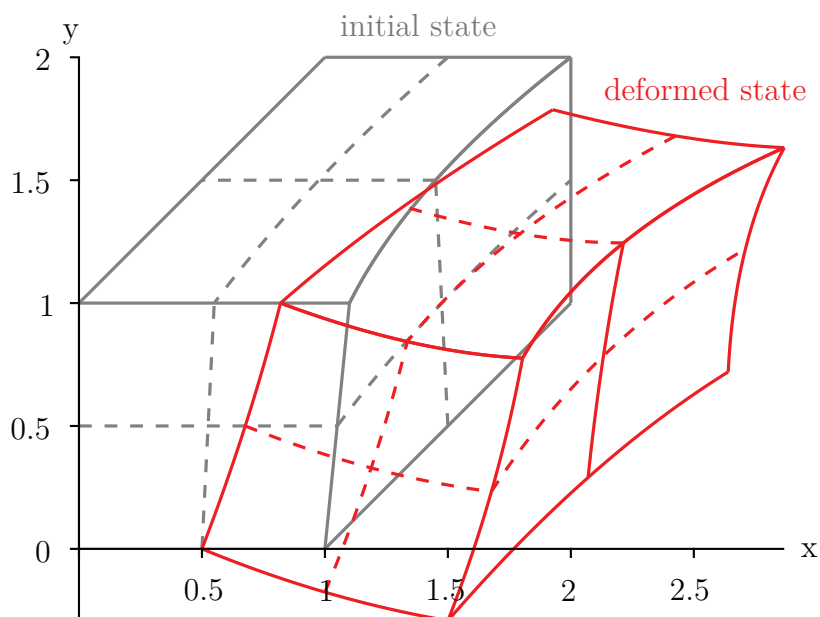


Figure 4.1: Result of patch test C, where a uniform external body load is applied. Since the result is not a rigid body motion, the patch test is not passed.

originally straight horizontal edges of the block do not remain straight in the patch test. Therefore, the test is not passed. The test is not even passed if the constant modes are already considered through a non-zero scaling factor C_{21} .

4.3 Systematic tuning by grid dispersion analysis (GDA) in 1-D

In the following, the systematic tuning of the proposed inertia templates by grid dispersion analysis is described. Grid dispersion analysis allows to study the propagation of waves in a structured, infinite mesh. The term “dispersion” denotes the dependence of the wave properties on the wave length. In a non-dispersive medium, like an infinite, continuous, elastic rod, the phase velocity, i.e. the quotient of angular frequency and wave number $c_0 = \omega/k$, is constant and a wave packet propagates without attenuation or dispersion. In a dispersive medium, waves with a larger wavelength may for example propagate faster than waves with a smaller one. Thus, a wave packet consisting of the superposition of many harmonic waves of different wave length disperses. This effect is illustrated in Figure 4.2. In red color, the original wave packet at time $t = 0$ is shown. The wave packet moves with a velocity of one. In blue, the wave packet without dispersion at $t = 2$ is shown. Without dispersion, the wave packet remains unaltered. With dispersion, some waves move faster whereas others move more slowly and therefore, the

wave packet disperses, as shown in green. The wave may also disperse with ripples as shown in grey. The effect of dispersion may have physical or numerical reasons. In the

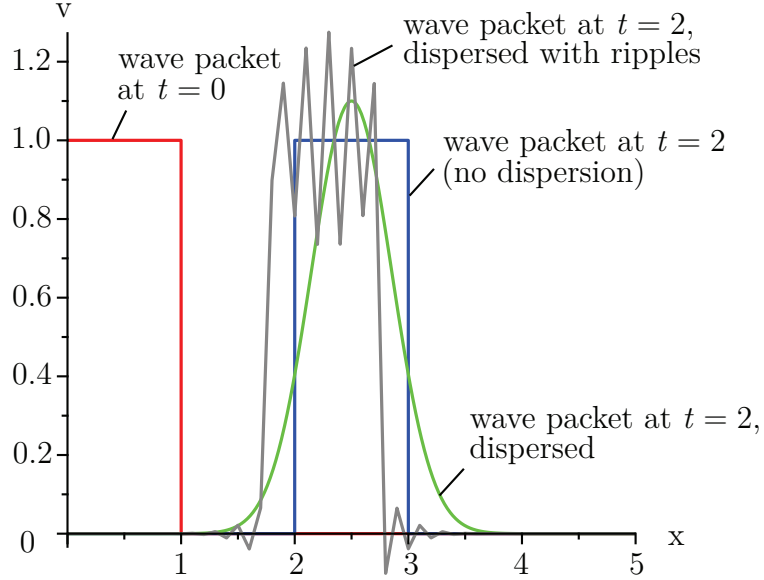


Figure 4.2: Schematic illustration of a wave packet with and without dispersion.

following, dispersion occurs due to the spatial discretization and the choice of different inertia templates.

In order to evaluate different choices of ansatz functions (i.e. different instances of the inertia template) regarding their potential for speed-up and optimal accuracy, analytical grid dispersion relations are obtained. By means of the grid dispersion relation, the following properties of the method can be examined: First, the maximum eigenfrequency and thus the speed-up, i.e. the ratio between the time step size of the novel approach and the lumped mass matrix can be determined. Second, the accuracy order of the dispersion relation and thus the convergence rate for the lowest eigenfrequencies can be obtained. Third, the appearance of negative dispersion can be studied. Negative dispersion denotes the numerical effect of negative group velocities, i.e. $v_g = \frac{\partial \omega}{\partial k} < 0$. This may lead to a change of the order of modes and is often tried to be avoided.

In the following, the tuning (i.e. the determination of optimal template parameters for a specific customization goal) by the analytical grid dispersion analysis is performed with an infinite, uniform, one-dimensional B-spline discretization. Later in Section 4.4 the extension to the two-dimensional case is discussed. The obtained results, i.e. obtained parameter sets, are as well valuable for bounded models discretized with moderately distorted NURBS discretizations as it will be shown in Example 6.2.

4.3.1 Grid dispersion analysis for reciprocal mass matrices

In the following, it is described how the grid dispersion relation is obtained by means of the Fourier method. For further information on this method see BELYTSCHKO AND MULLEN (1978), FELIPPA (2013c), HUGHES (2000) or KOLMAN ET AL. (2013). As stated earlier, in the Fourier method an infinite mesh is considered. Therefore, the representative structure of the finite element discretization, i.e. herein the repeating pattern of an infinite quadratic B-spline patch with equal-sized elements, is required. The consideration of an infinite patch allows the representation of the semi-discrete equation of motion with

$$\mathbf{M}_\infty^\circ \ddot{\mathbf{U}}_\infty + \mathbf{K}_\infty \mathbf{U}_\infty = \mathbf{0}, \quad (4.11)$$

for scaled mass matrices and with

$$\begin{cases} \dot{\mathbf{P}}_\infty + \mathbf{K}_\infty \mathbf{U}_\infty = \mathbf{0} \\ \dot{\mathbf{U}}_\infty = \mathbf{C}_\infty^\circ \mathbf{P}_\infty \end{cases} \quad (4.12)$$

for scaled reciprocal mass matrices. These equations describe the wave propagation in the lattice of a representative patch. Herein, \mathbf{M}_∞° , \mathbf{C}_∞° and \mathbf{K}_∞ are the scaled mass matrix, the scaled reciprocal mass matrix and the stiffness matrix of a representative patch. The projection matrix \mathbf{A}_∞ is omitted here, because it is the identity matrix for the scaled linear momentum ansatz functions introduced in the previous chapter. A representative element to determine a characteristic element matrix, as well as a representative patch to determine the characteristic structure of the global assembled matrices are marked in Figure 4.3 for the displacement and linear momentum shape functions of a quadratic B-spline element.

Local, element-wise supported biorthogonal ansatz functions, as proposed by SEITZ ET AL. (2016) and BRIVADIS ET AL. (2014), are used herein. In general, the density is again taken into consideration in the construction procedure as described in the previous chapter. However, for a constant density distribution, as considered in the following, the obtained bases are identical to the ones from literature. Alternatively to the local construction, the construction procedure can be applied on the global level resulting in globally supported, C^{p-1} -continuous ansatz functions according to WOŻNY (2013) or DORNISCH ET AL. (2017). These ansatz functions result in a dense global reciprocal mass matrix and the integration to compute the matrix needs to be performed over the whole patch. Due to the larger computational effort, locally constructed biorthogonal bases are used herein. A third possibility are biorthogonal ansatz functions with enlarged support and improved approximation properties, as described by OSWALD AND WOHLMUTH

(2001) for higher order Lagrange dual bases and mentioned in BRIVADIS ET AL. (2014) for B-splines.

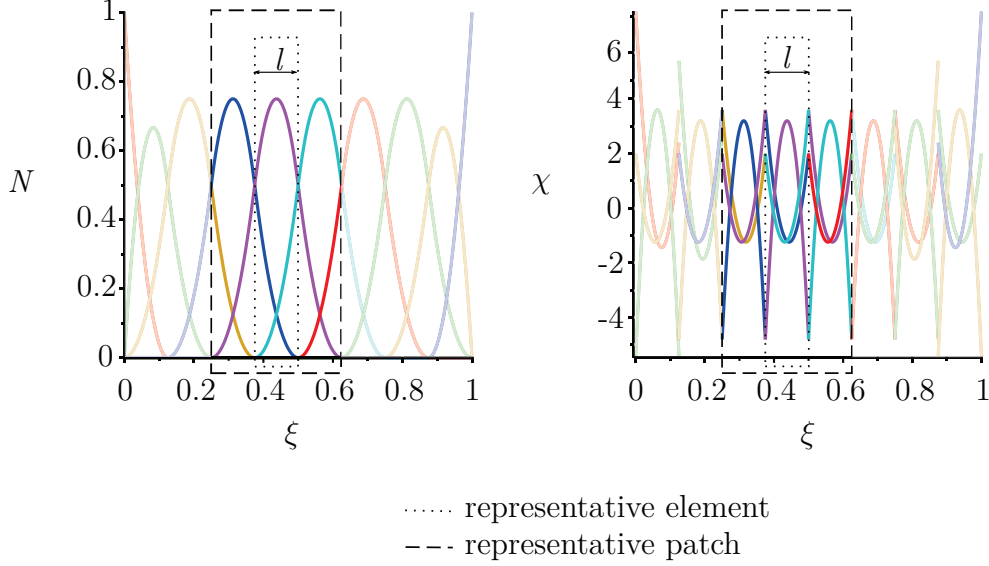


Figure 4.3: Representative patch and element (marked by dashed and dotted lines) considered in the grid dispersion analysis.

The representative global matrices of a quadratic B-spline patch take five degrees of freedom into consideration and can be written in form of a row vector – representing the characteristic band of the sparse symmetric representative matrix. In the following, the procedure to obtain the analytical grid dispersion relation by means of the Fourier method is exemplified by the reciprocal mass matrix (all template parameters are set to 0). The representative stiffness and reciprocal mass matrices are

$$\mathbf{K}_\infty = \frac{1}{6} \frac{EA}{l} \begin{bmatrix} -1 & -2 & 6 & -2 & -1 \end{bmatrix}, \quad (4.13)$$

$$\mathbf{C}_\infty = \frac{1}{12} \frac{1}{\rho A l} \begin{bmatrix} 23 & -104 & 174 & -104 & 23 \end{bmatrix} \quad (4.14)$$

with Young's modulus E , cross-sectional area A , density ρ and representative element length l . The material properties are assumed to be constant throughout this analysis. The discrete solution \mathbf{U}_∞ for the displacement and \mathbf{P}_∞ for the linear momentum of the representative semi-discrete equation is obtained by evaluating the continuous solutions for the displacement and the linear momentum with the ansatz

$$u(x, t) = \hat{U} e^{i(kx - \omega t)} = \hat{U} e^{i(\kappa x - \Omega c_0 t)/l} \quad \text{and} \quad (4.15)$$

$$p(x, t) = \hat{P} e^{i(kx - \omega t)} = \hat{P} e^{i(\kappa x - \Omega c_0 t)/l} \quad (4.16)$$

for traveling harmonic waves at different positions in space, namely at $x = x_{j-1} = x_j - l$, $x = x_j$ and $x = x_{j+1} = x_j + l$. In eq. (4.15) and (4.16), k is the wave number, ω is the angular frequency of the plane wave, $c_0 = \sqrt{E/\rho}$ is the phase velocity in continuum and $i = \sqrt{-1}$. The time t is retained as continuous variable in grid dispersion analyses. On the right hand side of eq. (4.15) and (4.16), the wave number k and the angular frequency ω are replaced by the dimensionless wave number

$$\kappa = kl \quad (4.17)$$

and the dimensionless angular frequency

$$\Omega = \frac{\omega l}{c_0}. \quad (4.18)$$

The discrete vectors of displacement and linear momentum are thus

$$\mathbf{U}_\infty = \hat{U} \begin{bmatrix} e^{-2i\kappa} \\ e^{-i\kappa} \\ 1 \\ e^{i\kappa} \\ e^{2i\kappa} \end{bmatrix}, \quad \dot{\mathbf{U}}_\infty = -\frac{i\Omega c_0}{l} \mathbf{U}_\infty, \quad (4.19)$$

$$\mathbf{P}_\infty = \hat{P} \begin{bmatrix} e^{-2i\kappa} \\ e^{-i\kappa} \\ 1 \\ e^{i\kappa} \\ e^{2i\kappa} \end{bmatrix}, \quad \dot{\mathbf{P}}_\infty = -\frac{i\Omega c_0}{l} \mathbf{P}_\infty. \quad (4.20)$$

Insertion of these vectors and the matrices (4.13) and (4.14) into eq. (4.12) leads to

$$\begin{bmatrix} -\frac{i\Omega c}{l} & -\frac{1}{3} \frac{23 \cos(\kappa)^2 + 32 - 52 \cos(\kappa)}{\rho Al} \\ -\frac{2}{3} \frac{EA(\cos(\kappa)^2 - 2 + \cos(\kappa))}{l} & -\frac{i\Omega c}{l} \end{bmatrix} \begin{bmatrix} \hat{U} \\ \hat{P} \end{bmatrix} = \mathbf{0} \quad (4.21)$$

for the reciprocal mass matrix. If eq. (4.21) is to be satisfied for any time t and any wave amplitude \hat{U} and \hat{P} , a characteristic equation can be obtained leading to the grid dispersion relation between the dimensionless frequency Ω and the wave number κ . The grid dispersion relation

$$\frac{\Omega}{\kappa} = \frac{\omega/k}{c_0} = \frac{c}{c_0} \quad (4.22)$$

describes the relation between the discretized lattice phase velocity $c = \omega/k$ and the continuous phase velocity c_0 . For the reciprocal mass matrix (RMM), the grid dispersion relation is

$$\frac{\Omega}{\kappa} = \frac{c}{c_0} = 1 + \frac{3}{8}\kappa^2 + \mathcal{O}(\kappa^4) \quad (4.23)$$

and the grid dispersion error is thus of second order. The dispersion relation is visualized in Figure 4.4. The dispersion relation of the consistent and lumped mass matrix and the continuous solution are added for comparison. It can be seen that for the reciprocal

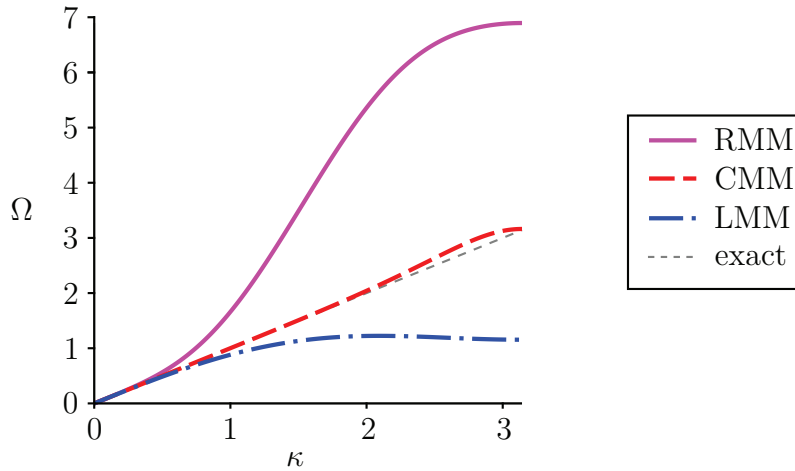


Figure 4.4: Dispersion graph for the consistent (CMM), the lumped mass matrix (LMM) and the reciprocal mass matrix (RMM, all scaling factors are set to zero) for an infinite 1-D quadratic B-spline patch.

mass matrix (RMM) the maximum eigenfrequency Ω_{\max} is much larger than for the other matrices. Therefore, very small time steps are required in an explicit analysis. The accuracy of the lowest modes (for small wave numbers κ) is similar as for the lumped mass matrix, whereas the accuracy of the consistent mass matrix is much higher (fourth order). For variationally scaled or customized reciprocal mass matrices, significantly larger critical time steps and higher order dispersion errors can be obtained as shown in the next section.

4.3.2 Tuning towards optimal low-frequency accuracy

At first, customization towards optimal low-frequency accuracy is performed, i.e. the order of the dispersion error is minimized for large wave lengths. The optimal free parameters for this purpose are obtained by performing a grid dispersion analysis, as

explained in the previous section for the unscaled reciprocal mass matrix, without specifying the free parameters. All results refer to a quadratic (according to Figure 4.3) or cubic B-spline patch.

For the variationally scaled mass matrix (VSMS) the dispersion relation for quadratic B-splines is

$$\frac{c}{c_0} = \frac{\Omega}{\kappa} = 1 - \frac{1}{24} C_{31} \kappa^2 + \left(\frac{1}{1440} + \frac{1}{360} C_{31} - \frac{1}{1440} C_{32} + \frac{1}{384} C_{31}^2 \right) \kappa^4 + \mathcal{O}(\kappa^6). \quad (4.24)$$

For the variationally scaled reciprocal mass matrix (VSRMS) the dispersion relation for quadratic B-splines is

$$\frac{c}{c_0} = \frac{\Omega}{\kappa} = 1 + \left(\frac{3}{8} - \frac{2}{3} C_{21} \right) \kappa^2 + \left(-\frac{17}{36} C_{21} - \frac{10}{9} C_{22} + \frac{4243}{5760} - \frac{2}{9} C_{21}^2 \right) \kappa^4 + \mathcal{O}(\kappa^6). \quad (4.25)$$

Then, the free parameters are chosen in a way to eliminate the highest error terms in the dispersion relation. The optimal free parameters for low-frequency accuracy are given in Table 4.1 and the dispersion errors are listed in Table 4.2 for quadratic, as well as for cubic, infinite, equally-spaced one-dimensional B-spline patches. In order to obtain

Table 4.1: Choice of free parameters for optimal low-frequency accuracy for the 1-D quadratic and cubic B-Spline patch.

	VSMS			VSRMS		
	C_{31}	C_{32}	C_{33}	C_{21}	C_{22}	C_{23}
$p=2$	0	1	0	9/16	577/1600	0
$p=3$	0	0	10/3	16/25	36/121	15238/266805

optimal accuracy for cubic B-splines, not only up to linear velocity ansatz spaces need to be used, but quadratic ones, i.e. the scaling factors $C_{3\alpha}$ and $C_{2\alpha}$ are related to the velocity ansatz function matrices

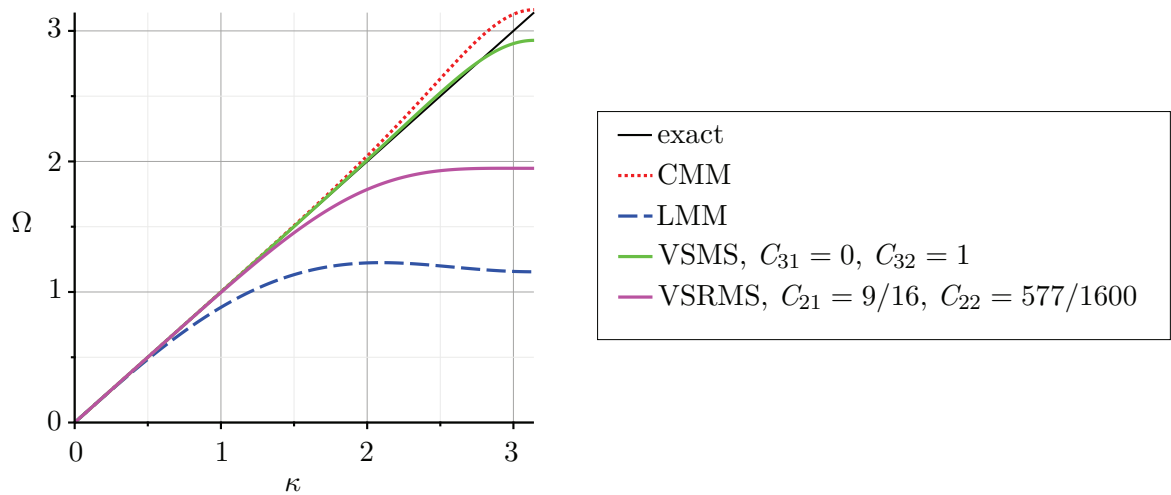
$$\Psi_{\alpha=1}^{1-D} = [1], \quad \Psi_{\alpha=2}^{1-D} = [1 \quad X^h] \quad \text{and} \quad \Psi_{\alpha=3}^{1-D} = [1 \quad X^h \quad (X^h)^2]. \quad (4.26)$$

As reference, the dispersion error of the consistent mass matrix, which is of fourth and sixth order for quadratic and cubic discretizations, as well as the dispersion error of the row-sum-lumped mass matrix, which is of second order independent of the polynomial order, are listed in Table 4.2 as well.

Table 4.2: Dispersion relation for different mass matrices for free parameters (if present), chosen according to Table 4.1.

	1-D quadratic c/c_0	1-D cubic c/c_0
consistent mass (CMM)	$1 + \frac{1}{1440}\kappa^4 + \mathcal{O}(\kappa^6)$	$1 + \frac{1}{60480}\kappa^6 + \mathcal{O}(\kappa^8)$
row-sum lumped mass (LMM)	$1 - \frac{1}{8}\kappa^2 + \mathcal{O}(\kappa^4)$	$1 - \frac{1}{6}\kappa^2 + \mathcal{O}(\kappa^4)$
variationally scaled mass (VSMS)	$1 + \frac{11}{120960}\kappa^6 + \mathcal{O}(\kappa^8)$	$1 + \frac{1}{145152}\kappa^8 + \mathcal{O}(\kappa^{10})$
var. scaled recipr. mass (VSRMS)	$1 - \frac{1}{189}\kappa^6 + \mathcal{O}(\kappa^8)$	$1 - \frac{409}{172800}\kappa^8 + \mathcal{O}(\kappa^{10})$

For both the variationally scaled mass and reciprocal mass matrix, a dispersion error of sixth order for quadratics and of eighth order for cubics can be obtained. Note that even though the dispersion order is the same for both methods, the error constant for the variationally scaled mass matrix is significantly smaller than for the reciprocal mass matrix. For quadratic B-splines it is by a factor of 60 and for cubic B-splines by a factor of 300 smaller. In the diagram in Figure 4.5 the dimensionless eigenfrequency is plotted versus the dimensionless wave number for quadratic B-splines. The parameters chosen for the variational inertia matrices are optimized for low-frequency accuracy (cf. Table 4.1). The scaled mass matrix shows almost ideal dispersion behaviour: Almost

**Figure 4.5:** Analytical grid dispersion curves for different mass and reciprocal mass matrices for optimized low-frequency accuracy for an infinite 1-D quadratic B-spline patch.

till $\kappa \rightarrow 3$ the curve coincides with the exact one. The required time step is very small, but still larger than for the consistent mass matrix. The reciprocal mass matrix has the same convergence order, but due to the larger error constant the curve diverges from the exact one for smaller wave numbers. The required time step is smaller than for the lumped mass matrix but significantly larger than for the variationally scaled mass matrix.

With the proposed formulation, where only the kinetic energy term is modified, an order of the dispersion error of at most $2p + 2$ can be reached for B-splines of polynomial order p , as the conventional stiffness matrix is used herein. To obtain the highest possible accuracy with dispersion errors of $4p$, both kinetic and internal energy need to be modified, leading to mass-stiffness templates (cf. algebraic construction from IDESMAN (2017)). These highly-optimized mass-stiffness templates may be quite sensitive to mesh distortion.

4.3.3 Tuning towards speed-up

An improvement of the speed-up, i.e. an increase of the critical time step size, is in general also accompanied by a deteriorated accuracy. Therefore, it is the user's choice, which reduction in the accuracy is tolerable for the desired speed-up.

Figure 4.6 and Figure 4.7 show the dispersion diagram for quadratic B-splines, where tuning towards speed-up with different side conditions for the inertia matrices is performed.

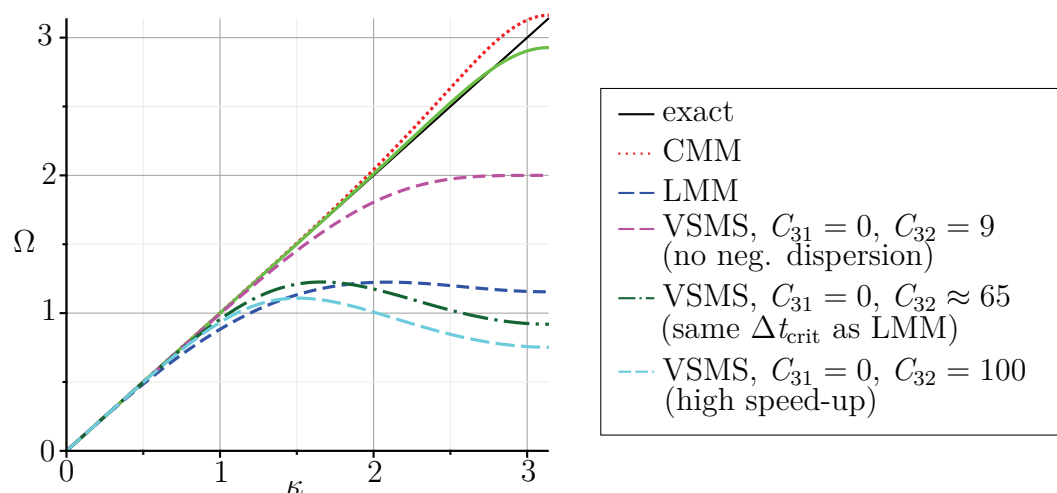


Figure 4.6: Analytical dispersion curves for the variationally scaled mass matrix (VSMS) for various choices of the free parameters for an infinite 1-D quadratic B-spline patch.

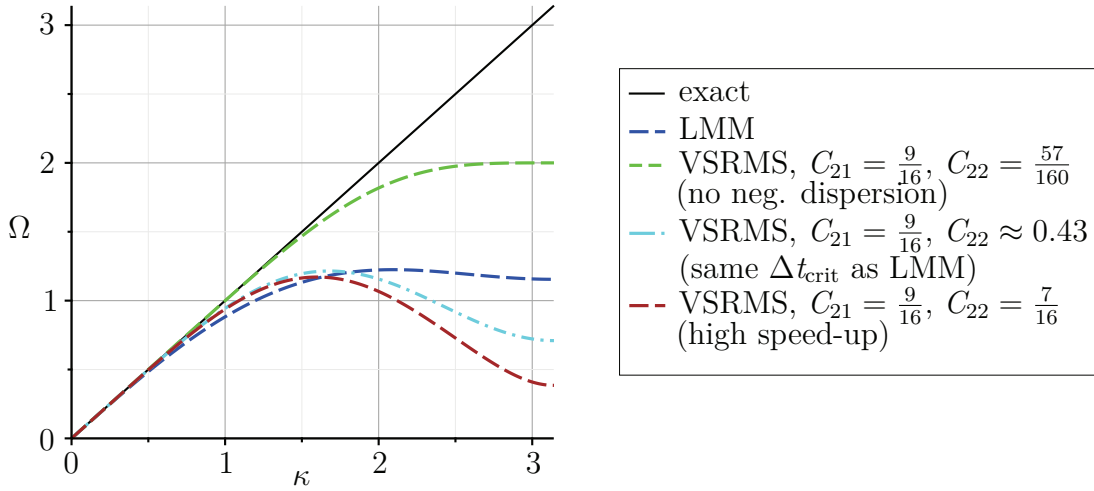


Figure 4.7: Analytical dispersion curves for the variationally scaled reciprocal mass matrix (VSRMS) for various choices of the free parameters for an infinite 1-D quadratic B-spline patch.

To retain at least the same convergence order as for the consistent mass matrix, only the second free parameter, namely C_{32} for the scaled mass matrix and C_{22} for the reciprocal mass matrix, is changed. With increasing C_{32} and C_{22} , the maximum eigenfrequency is reduced. The variationally scaled reciprocal mass matrix is observed to be only stable for $C_{21} + C_{22} \leq 1$. The stability is further analyzed in the next section. For values larger than $C_{32} = 9$ (VSMS) and $C_{22} = 57/160$ (VSRMS), negative dispersion occurs. This may have an influence on the order of the eigenmodes and may be undesirable for some applications.

For $C_{32} \approx 65$ (VSMS) and $C_{22} \approx 0.43$ (VSRMS) the maximum eigenfrequency is equal to the one of the lumped mass matrix, but higher accuracy is obtained in the lowest modes. For the scaled mass matrix, each time step is then still more expensive than for lumped mass due to the non-diagonal structure of the mass matrix, but for the reciprocal mass matrix, no extra expense is required. For larger values the critical time step size can be further increased, but additional negative dispersion occurs and accuracy deteriorates. Further decrease of the maximum eigenfrequency is possible by increasing C_{31} for the variationally scaled mass matrix and C_{21} for the reciprocal mass matrix, but then the convergence order reduces to two.

In general the analytical grid dispersion analysis shows, that novel consistent variationally scaled mass and reciprocal mass matrices can be customized for the user's purposes: by different choices of free parameters, higher accuracy in the low frequencies can be obtained than for the standard mass matrices and mass matrices with larger critical time step than the existing row-sum-lumped mass with at least the same accuracy can be developed.

4.3.4 Evaluation of stability

While for the variationally consistent mass matrix the time step can be arbitrarily increased, of course to the disadvantage of the accuracy and the condition number of the mass matrix, the time step of the variationally scaled reciprocal mass matrix is bounded by stability issues. So far, it was observed that the stability is violated if the scaling factor for the variationally scaled reciprocal mass matrix (or the sum of all scaling factors in a multi-parametric template) is larger than 1. By means the grid dispersion analysis, criteria for stability can be defined and the observation that the sum of the scaling factors should not exceed 1 can be examined. The formulation is unstable if $\Omega(\kappa) \leq 0$. Since mass scaling influences especially the highest modes, the condition can be further specified with $\Omega(\kappa = \Pi) \leq 0$. With this condition at hand the stability of the quadratic and cubic B-spline discretization, analyzed in the previous chapters, is studied. For the quadratic B-spline discretization, the stability is violated if the condition

$$\sqrt{963 - 960C_{31} - 960C_{32}} \leq 0 \quad (4.27)$$

holds. Thus, the condition on the scaling factors to guarantee stability is

$$C_{21} + C_{22} \leq \frac{321}{320}. \quad (4.28)$$

This means that for an infinite patch of quadratic B-splines a sum of scaling factors of 1 still leads to a stable solution. But with slightly larger scaling factors, the stability limit is reached. For the cubic B-spline discretization, the stability is violated if the condition

$$\sqrt{25450 - 25450C_{21} - 25410C_{23} - 25410C_{22}} \leq 0 \quad (4.29)$$

holds. The condition on the scaling factors to guarantee stability is then

$$C_{21} + \frac{2541}{2545}C_{22} + \frac{2541}{2545}C_{23} \leq 1. \quad (4.30)$$

With a sum of the three scaling factors of 1 (e.g. $C_{21} = C_{22} = C_{23} = 1/3$), the solution will still be stable for an infinite patch of cubic B-splines. Again, with slightly larger scaling factors, stability is violated. The general observation that the sum of all scaling factors should not exceed 1, i.e. $\sum_{\alpha} C_{2\alpha} \leq 1$, is confirmed by the grid dispersion analysis.

4.3.5 Recovery of existing mass matrices from literature

In earlier works, various algebraic approaches were proposed to provide improved mass matrices for B-spline-based FEM. The relation between different algebraic approaches and the variational framework is explained in the following.

For comparison the higher order mass matrix of WANG ET AL. (2013) and the algebraically scaled mass matrix according to OLOVSSON ET AL. (2004) are used. Wang suggested to algebraically construct a mixed mass matrix consisting of a linear combination of the consistent mass matrix and a matrix of reduced bandwidth, which also preserves mass and has the same approximation order than the consistent mass matrix. In the linear combination the highest error terms cancel and therefore a higher-order mass matrix is designed. For a comparison with standard matrices from mass scaling, algebraic mass scaling by Olovsson is transferred to B-spline finite elements. Herein, the transfer to B-splines is done in a rather naive way, where the diagonal mass is obtained by row-sum lumping and the augmented mass on the off-diagonal terms is equally distributed to all degrees of freedom. Better, non-intuitive constructions might be possible, but this question is not further pursued herein.

Table 4.3 can be understood as supplement to Table 4.2. The dispersion relations for Wang’s higher order mass matrix and the algebraically scaled mass matrix according to Olovsson are given for quadratic and cubic B-splines. The results obtained with the algebraically constructed higher order mass by WANG ET AL. (2013) are identical to the results obtained with the variationally scaled mass matrix, i.e. the algebraic mass matrices proposed by Wang can be reproduced in a variationally consistent form with the framework provided herein. The algebraically scaled mass results in a maximum fourth order dispersion error, independent of the polynomial order.

Table 4.3: Dispersion relation for different algebraic mass matrices for a 1-D quadratic and cubic B-Spline patch.

	1-D quadratic c/c_0	1-D cubic c/c_0
Wang’s higher order mass (see WANG ET AL. (2013))	$1 + \frac{11}{120960}\kappa^6 + \mathcal{O}(\kappa^8)$	$1 + \frac{1}{145152}\kappa^8 + \mathcal{O}(\kappa^{10})$
algebr. scaled mass (ASMS, see OLOVSSON ET AL. (2004))	$1 - \frac{23}{1440}\kappa^4 + \mathcal{O}(\kappa^6)$	$1 - \frac{13}{240}\kappa^4 + \mathcal{O}(\kappa^6)$

In Figure 4.8 the dispersion relation is illustrated for quadratic B-splines. Since the variational mass with optimal low-frequency error and Wang’s higher order mass are

identical, Wang’s mass matrix requires also quite small time steps. For $\beta = -\frac{1}{4}$, the optimal low-frequency accuracy for the algebraically scaled mass is obtained. Since the dispersion error is only of fourth order (in comparison to sixth order for Wang’s mass matrix), the dispersion curve diverges already for smaller wave numbers from the exact solution for continua. The size of the time step is moderate and can be further increased, accepting lower accuracy.

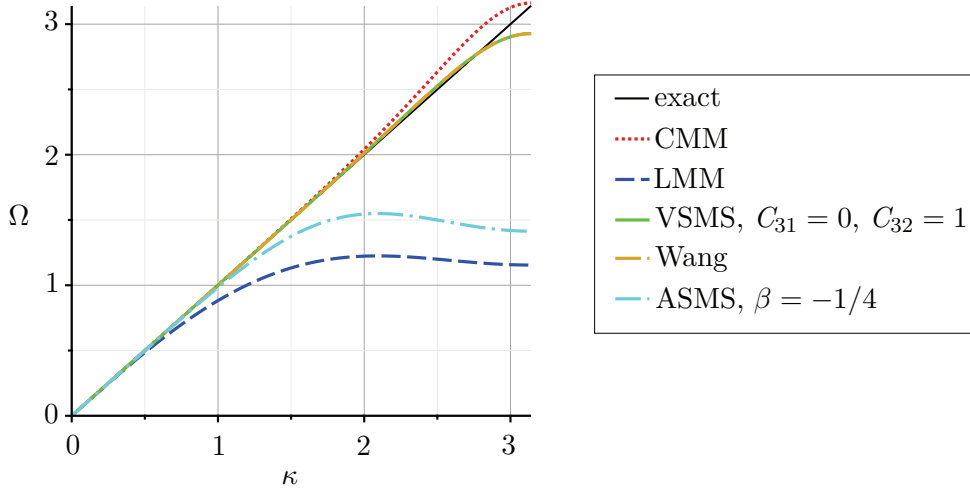


Figure 4.8: Analytical grid dispersion curves for different mass matrices for optimized low-frequency accuracy for an infinite 1-D quadratic B-spline patch.

With the proposed variational framework, the dispersion-corrected explicit integration scheme by KRENK (2001) can as well be reproduced with some tricks. Then, a relation between the free parameter γ of Krenk and the inertia scaling parameter C_{21} can be found with $C_{21} = \frac{2}{3} - \frac{2}{9}\gamma$ for constant density. A detailed description of the relation of the two methods is omitted here.

4.4 Grid dispersion analysis (GDA) in 2-D

In the multi-dimensional case, the dispersion relation is not only dependent on the wave number k (or the wave vector \mathbf{k} in multi-dimensions) and the free parameters $C_{2\alpha}$ and $C_{3\alpha}$ but also on the angle of inclination θ of the wave with respect to the mesh orientation, see Figure 4.9. This means that depending on the angle under which a wave propagates through a discretized body, the interrelation between the wave properties is different. Furthermore, two different wave types, namely dilatation and shear waves, need to be distinguished in 2-D wave propagation. The obtained result depends on the chosen dimensional reduction (plane strain or plane stress) and on Poisson’s ratio ν .

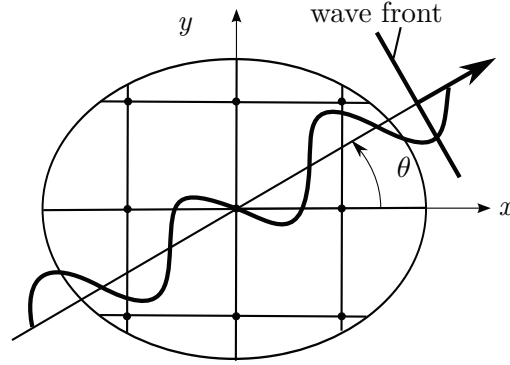


Figure 4.9: Plane wave propagating through a mesh under the angle of inclination θ .

The approach to obtain the grid dispersion relation is similar to 1-D. For reference on how to conduct a grid dispersion analysis in 2-D, the papers for the grid dispersion analysis of a serendipity finite element of KOLMAN ET AL. (2013) and for isogeometric finite elements with consistent mass of DEDÈ ET AL. (2015) are recommended. The ansatz for the solution of the displacement and the linear momentum in 2-D (cf. eq. (4.15) and (4.16) for 1-D) are

$$\mathbf{u}(\mathbf{x}, t) = \hat{\mathbf{U}} e^{[i(k \cos(\theta)x + k \sin(\theta)y - \omega t)]} \quad \text{and} \quad (4.31)$$

$$\mathbf{p}(\mathbf{x}, t) = \hat{\mathbf{P}} e^{[i(k \cos(\theta)x + k \sin(\theta)y - \omega t)]}, \quad (4.32)$$

where $k \cos(\theta)$ and $k \sin(\theta)$ are the x - and y -component of the wave vector \mathbf{k} . Note, that the displacement and linear momentum \mathbf{u} and \mathbf{p} , as well as the amplitudes $\hat{\mathbf{U}}$ and $\hat{\mathbf{P}}$ are now vectors with x - and y -component.

The continuous wave ansatz can then be evaluated at discrete points in space to obtain the discrete displacement and linear momentum vectors \mathbf{U}_∞ and \mathbf{P}_∞ . Subsequently, these vectors are inserted into the representative semi-discrete equation of motion, which allows to extract the characteristic equations describing the dispersion relation of the dilatation branch and of the shear branch, respectively.

In the following, first the dispersion relation for the dilatation and shear branches for different mass matrices in dependence of the inclination angle θ and its free parameters are given. Then, the special case of incoming waves aligned to the mesh ($\theta = 0$) are considered and optimal free parameters are found for this case. Subsequently, the dispersion behaviour for this specific parameter choice is as well studied in dependence of different inclination angles. In all studies, a 2-D infinite, uniform, quadratic B-spline patch is analyzed. Plane strain case with Poisson's ratio $\nu = 0$ is considered. For reference, the analytical dispersion relation for lumped and consistent mass matrices are as well obtained in dependence of different inclination angles and illustrated in

Appendix A. The dispersion relation of the variationally scaled mass matrix (VSMS) for the dilation branch in dependence of the scaling factors $C_{3\alpha}$ and the inclination angle θ is

$$\frac{c_d}{c_{d0}} = \frac{\omega_d}{k} = 1 - \frac{1}{24} \left(C_{31} + C_{32} + C_{33} \left(1 - 2 \cos(\theta)^2 + 2 \cos(\theta)^4 \right) \right) k^2 + \mathcal{O}(k^4). \quad (4.33)$$

The dispersion relation of the shear branch is

$$\frac{c_s}{c_{s0}} = \frac{\omega_s}{k/\sqrt{2}} = 1 - \frac{1}{48} \left(2C_{31} + C_{32} + 4C_{33} \left(\cos(\theta)^2 - \cos(\theta)^4 \right) \right) k^2 + \mathcal{O}(k^4). \quad (4.34)$$

For the 2-D analysis the results are given in dependence of ω and k instead of in terms of dimensionless quantities. This simplifies the algebraic analysis. Since the density, the elastic modulus and the mesh size are set to 1, there is no quantitative difference in the plotted dispersion graphs. While the dilatation wave speed in a continuum is 1 for the given parameters, the shear wave speed in a continuum is $1/\sqrt{2}$.

The dispersion relation of the dilatation branch of the variationally scaled reciprocal mass matrix in dependence of the free parameters $C_{3\alpha}$ and the inclination angle θ is

$$\frac{c_d}{c_{d0}} = \frac{\omega_d}{k} = 1 + \left(\frac{3}{8} - \frac{2}{3}C_{21} - \frac{2}{3}C_{22} - \frac{2}{3}C_{23} \left(1 - 2 \cos(\theta)^2 + 2 \cos(\theta)^4 \right) \right) k^2 + \mathcal{O}(k^4). \quad (4.35)$$

The dispersion relation of the shear branch of the variationally scaled reciprocal mass matrix is

$$\frac{c_s}{c_{s0}} = \frac{\omega_s}{k/\sqrt{2}} = 1 + \left(\frac{3}{8} - \frac{2}{3}C_{21} - \frac{1}{3}C_{22} - \frac{4}{3}C_{23} \left(\cos(\theta)^2 - \cos(\theta)^4 \right) \right) k^2 + \mathcal{O}(k^4). \quad (4.36)$$

The dispersion relations from eq. (4.33) and (4.34) for the scaled mass and from eq. (4.35) and (4.36) for the reciprocal mass allow to study either the dispersion behaviour for a given parameter set in dependence of the inclination angle θ or to find the optimal parameters for wave propagation under a defined inclination angle.

Next, the special case of waves travelling parallel to the mesh (i.e. $\theta = 0$) are considered. The dispersion relations for $\theta = 0$ are listed in Table 4.4 and 4.5 for the dilatation and shear branch, respectively. The results of the lumped and consistent mass matrix are listed for reference. The error of the dispersion relation is identical for the dilatation and the shear branch for the consistent and the lumped mass matrix as well. For the consistent mass matrix, the error is of fourth order. For the lumped mass matrix it is

4 Inertia customization

of second order. For the scaled mass matrix the error is of second order for both the

Table 4.4: Dispersion relation of the dilatation branch for different mass and inverse mass matrices for $\theta = 0$ for a 2-D quadratic B-spline patch.

	c_d/c_{d0}
consistent mass (CMM)	$1 + \frac{1}{1440}k^4 + \mathcal{O}(k^6)$
row-sum lumped mass (LMM)	$1 - \frac{1}{8}k^2 + \mathcal{O}(k^4)$
variationally scaled mass (VSMS)	$1 - \frac{1}{24}(C_{31} + C_{32} + C_{33})k^2 + \mathcal{O}(k^4)$
var. scaled recipr. mass (VSRMS)	$1 + \left(\frac{3}{8} - \frac{2}{3}C_{21} - \frac{2}{3}C_{22} - \frac{2}{3}C_{23}\right)k^2 + \mathcal{O}(k^4)$

Table 4.5: Dispersion relation of the shear branch for different mass and inverse mass matrices for $\theta = 0$ for a 2-D quadratic B-spline patch.

	c_s/c_{s0}
consistent mass (CMM)	$1 + \frac{1}{1440}k^4 + \mathcal{O}(k^6)$
row-sum lumped mass (LMM)	$1 - \frac{1}{8}k^2 + \mathcal{O}(k^4)$
variationally scaled mass (VSMS)	$1 - \frac{1}{48}(2C_{31} + C_{32})k^2 + \mathcal{O}(k^4)$
var. scaled recipr. mass (VSRMS)	$1 + \left(\frac{3}{8} - \frac{2}{3}C_{21} - \frac{1}{3}C_{22}\right)k^2 + \mathcal{O}(k^4)$

dilatation and the shear branch if the parameters are not further specified. However, for a parameter choice of $C_{31} = C_{33}$ and $C_{32} = -2C_{33}$ a fourth order dispersion error for both the dilatation and the shear branch are possible for $\theta = 0$. With the additional condition $C_{34} = 1$ even a sixth order dispersion error for both branches is achievable. The dispersion graph for the scaled mass matrix with $C_{31} = C_{32} = C_{33} = 0$ and $C_{34} = 1$ is illustrated in Figure 4.10 (left). Both the dilatation and the shear branch coincide very well with the exact solution for continua. The maximum eigenfrequency is approximately as large as for the consistent mass matrix, but the dispersion error is of sixth order in comparison to fourth order for the consistent mass matrix (cf. Appendix A). With a different parameter choice a larger time step for the variationally scaled mass can be reached, but then the order of the dispersion error is reduced and accuracy decreases.

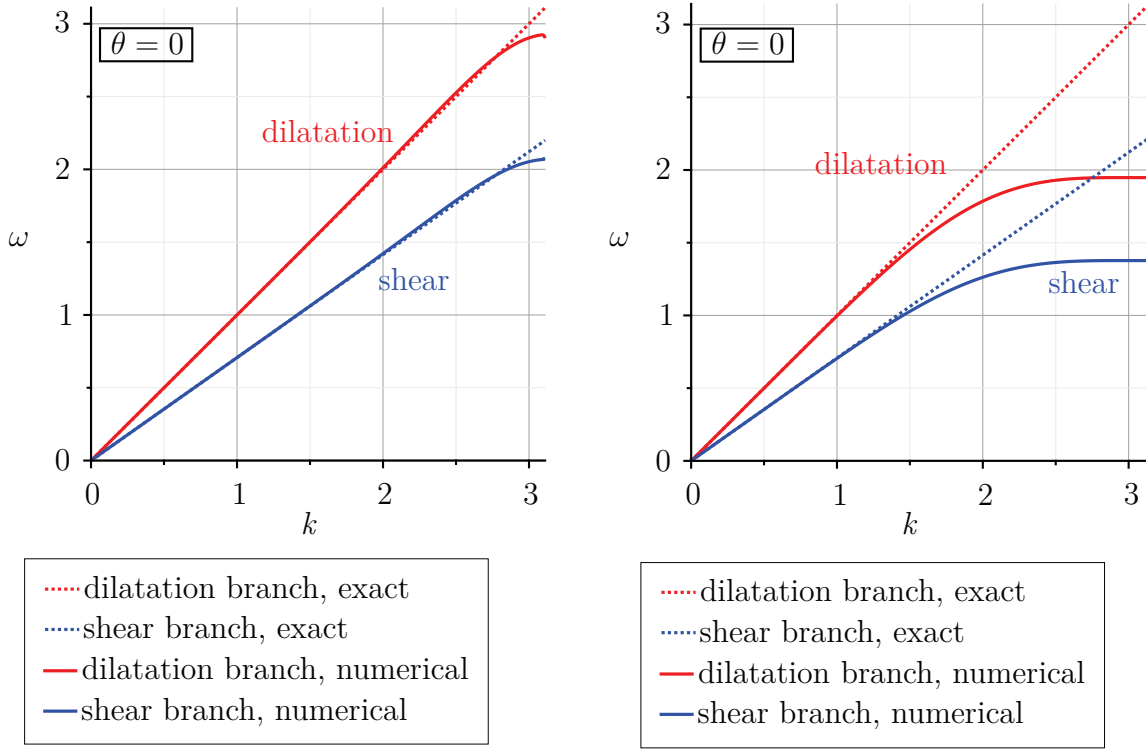


Figure 4.10: Dispersion relation for a 2-D quadratic B-spline patch for the variationally scaled mass (VSMS, left) and reciprocal mass matrix (VSRMS, right).

For the reciprocal mass matrix, the dispersion error for both the dilatation and the shear branch is as well of second order if the parameters are not further specified. With a parameter choice of $C_{21} = C_{23} + \frac{9}{16}$ and $C_{22} = -2C_{23}$ a dispersion error of fourth order for both the dilatation and the shear branch can be obtained. With the additional choice $C_{24} = \frac{577}{1600}$ a dispersion error of sixth order can be obtained for both branches. The dispersion graph for the reciprocal mass matrix with $C_{21} = \frac{9}{16}$, $C_{22} = C_{23} = 0$, $C_{24} = \frac{577}{1600}$ is shown in Figure 4.10 (right). For the reciprocal mass matrix the maximum eigenfrequency is significantly smaller than for the optimized variationally scaled mass matrix, that means computation with a significantly larger time step is possible. The dispersion error for both branches is again of sixth order, but due to the larger error constant of the remaining term in the dispersion relation, the curve diverges earlier from the exact solution than for the variationally scaled mass matrix. This was already observed in 1-D.

Next, the dispersion behaviour of the scaled mass and reciprocal mass matrix is studied for the chosen parameter set for the wave propagation under various inclination angles. For comparison similar analyses for the consistent and lumped mass matrix are listed in Appendix A. In Figure 4.11 the phase velocity error versus the wave number is shown

for dilatation waves (left) and shear waves (right) for different inclination angles for the variationally scaled mass matrix.

Waves propagating under an angle of 0° , 20° , 30° and 45° are studied and their results are illustrated by different colors. The influence of the inclination angle on the result for both dilatation and shear waves is rather small, comparable with the influence for the consistent mass matrix. From Figure 4.12 the behaviour of the reciprocal mass matrix can be studied. The error for both dilatation and shear waves shows a much stronger dependency on the inclination angle than the error of the variationally scaled mass matrix. Furthermore, the error is significantly larger. For small wave lengths ($k \rightarrow 3$) the phase velocity may be overestimated by a factor of 2. Furthermore, it is noticeable that the smallest error is obtained for waves propagating with an inclination angle larger than 0 and smaller than 20° .

In Sections 4.3 and 4.4, only grid dispersion analyses were performed. This type of analysis takes only the spatial discretization into account. To finally perform particularly accurate or fast transient analysis not only the spatial discretization but also the temporal discretization should be taken into account. This idea was initially proposed by KRIEG AND KEY (1973), who suggested that time and space discretization should be adjusted to each other. An extension of grid dispersion analysis that takes also the temporal discretization into account is the so-called full (or temporal-spatial) dispersion analysis. A full dispersion analysis is for example performed by KOLMAN ET AL. (2016) to study the dispersion behaviour of a serendipity element with the central difference time discretization method. A full dispersion analysis of the mass and reciprocal mass matrices proposed herein allows to tailor the mass or reciprocal mass matrix not only to the grid (i.e. spatial discretization), but also to the chosen time discretization method and time step. This could further improve the transient behaviour and is a possible direction for future work.

4.5 A brief summary of Chapter 4

In the following, the advancements presented in Chapter 4 are shortly reviewed.

At the beginning of the chapter, enriched ansatz spaces for the earlier proposed variationally scaled mass and reciprocal mass matrices were presented, which are especially suitable for inertia customization. Then, a novel multi-parametric template was introduced, which allows combination and systematic tuning of different ansatz spaces towards specific customization goals. Next, systematic tuning of the proposed mass and inverse mass matrices is performed for a 1-D infinite, uniform, quadratic B-spline patch. The tuning is performed e.g. with the goal of optimal low-frequency accuracy

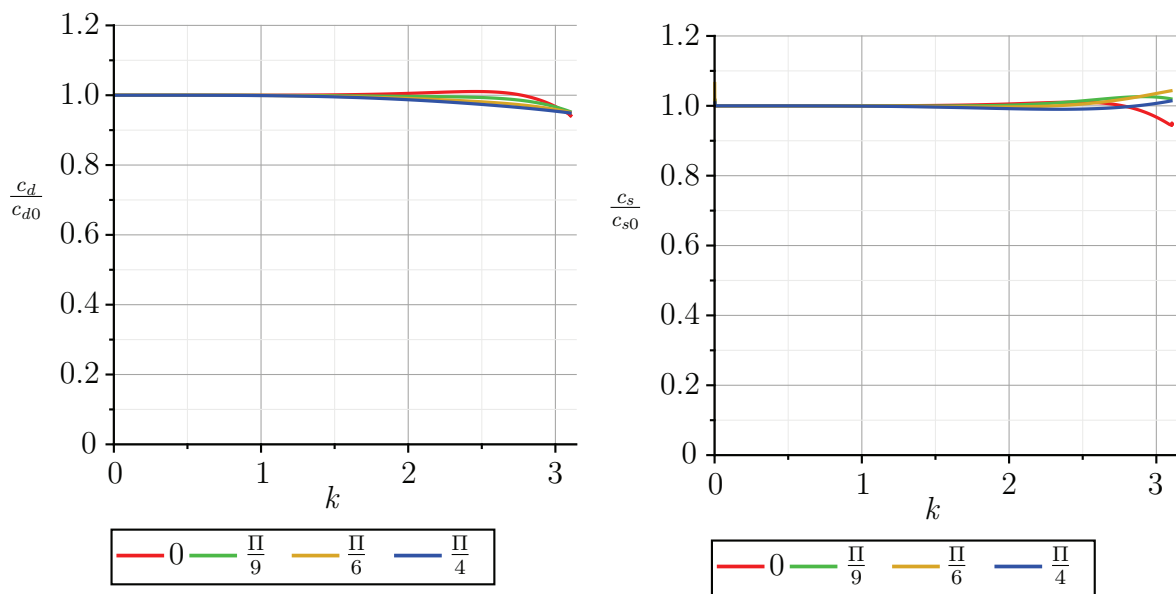


Figure 4.11: Dispersion error for different inclination angles θ for a 2-D quadratic B-spline patch for the variationally scaled mass matrix (VSMS) of the dilatation branch (left) and the shear branch (right).

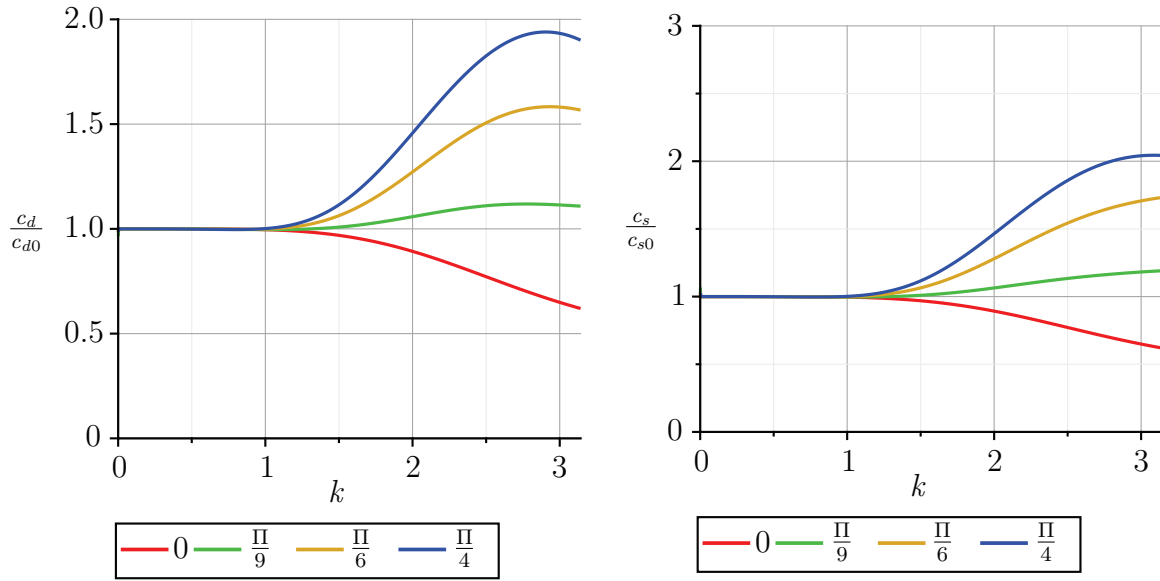


Figure 4.12: Dispersion error for different inclination angles θ for a 2-D quadratic B-spline patch for the variationally scaled reciprocal mass matrix (VSRMS) of the dilatation branch (left) and the shear branch (right).

or substantial speed-up. Subsequently, the extension of the performed analysis to 2-D is described and dispersion results in dependence of the wave inclination angle in a 2-D discretization are discussed. Therein, the free parameters are optimized with respect to dispersion behaviour for both dilatation and shear branches for waves travelling aligned to the mesh and finally, the dispersion behaviour for this parameter choice is studied under various inclination angles. For both variationally scaled mass and reciprocal mass matrices dispersion errors of at maximum sixth order are obtained in 1-D and in 2-D for both the dilatation and the shear branch. The variationally scaled reciprocal mass matrix has shown significant larger dependence of the results on the inclination angle.

Time-step estimates for reciprocal mass matrices and penalty contact

In order to exploit the full potential of the proposed reciprocal mass matrices, an efficient time step estimate to determine the allowable time step for explicit transient analyses is required.

Since, to the author's knowledge, efficient and conservative time step estimates for reciprocal mass matrices do not exist yet in literature (seeing that the idea of reciprocal mass matrices is also rather new), the critical time step is so far determined from the maximum global eigenfrequency, e.g. by performing a forward iteration on the global level. This procedure provides a very accurate estimate of the maximum eigenfrequency, but it is too expensive to be repeated frequently during the explicit simulation.

Therefore, a local and computationally cheaper time step estimate for reciprocal mass matrices was proposed in SCHAEUBLE ET AL. (2018) and it is described in the following. First, the requirements on the novel estimate and the potential applicability of existing local time step estimates for reciprocal mass matrices are discussed. Then, in Section 5.2, the novel estimate is developed from the existing nodal time step estimate for lumped mass matrices based on Gershgorin's theorem by KULAK (1989). Subsequently, possible penalty contact is taken into account. Finally, various rearrangements of the estimate to further increase the computational efficiency are discussed.

The time step estimate for reciprocal mass matrices proposed herein is not only valid for the reciprocal mass matrix from Chapter 3, but for reciprocal mass matrices in general, independent how they are obtained. Furthermore, the estimate works independently of the element type used in the finite element discretization.

5.1 Requirements on the novel estimate and limitations of existing ones

An overview of the classification of existing time step estimates was already provided in Section 2.3.2. Therein, it was distinguished between global and local estimates and local estimates were further split into node-based and element-based ones.

In general, regardless of the class of estimate considered, the requirements on the novel estimate can be summarized as follows: The novel estimate should be

- conservative,
- efficient and
- provide satisfactory results for irregular and distorted meshes.

Conservativeness presupposes that the obtained time step is smaller than the exact critical time step (see eq. (2.61)) so that stability is not violated. Efficiency implies both reasonable computational effort to compute the time step and an estimate that is not too conservative, i.e. the obtained time step is not too small compared to the exact critical time step. Due to the in general higher efficiency, local estimates are preferred over global ones. The applicability of the novel time step estimate for irregular and distorted meshes has to be confirmed by numerical examples.

Because a local estimate is preferred for the reason of efficiency, the question remains whether a node-based or an element-based estimate is desired for reciprocal mass matrices. Existing element-based estimates for lumped or consistent mass matrices are based on the element eigenvalue inequality, stating that the global eigenvalue λ (or eigenfrequency ω) is bounded by the element eigenvalues λ_i^e (or eigenfrequencies ω_i^e), see eq. (2.66). This inequality results from the inequality of the Rayleigh quotient on the local and global level with

$$\begin{aligned} \max_i \omega_i^2 &= \max_i \lambda_i = \max_i \frac{\phi_i^T \mathbf{K} \phi_i}{\phi_i^T \mathbf{M} \phi_i} \\ &\leq \max_{i,e} (\omega_i^e)^2 = \max_{i,e} \lambda_i^e = \max_{i,e} \frac{\phi_i^{eT} \mathbf{k}_e \phi_i^e}{\phi_i^{eT} \mathbf{m}_e \phi_i^e}, \end{aligned} \quad (5.1)$$

where ϕ_i^e , \mathbf{k}_e and \mathbf{m}_e are the i^{th} eigenvector, the stiffness matrix and the lumped or consistent mass matrix on the element level. ϕ_i , \mathbf{K} and \mathbf{M} are the respective quantities on the global level. This inequality is valid for the eigenvalues of a generalized eigenvalue problem of symmetric matrices. In the case of the reciprocal mass matrix, the eigenvalues

result from a product eigenvalue problem with

$$(\mathbf{C}^\circ \mathbf{K} - \lambda_i \mathbf{I}) \boldsymbol{\phi}_i = \mathbf{0} \quad \text{with} \quad \lambda_i = \omega_i^2, \quad (5.2)$$

where \mathbf{C}° is the reciprocal mass matrix. The eigenvector $\boldsymbol{\phi}_i$ in eq. (5.2) is actually a right eigenvector since the same eigenvalues λ_i can as well be obtained from the eigenvalue problem

$$(\boldsymbol{\phi}_i^L)^\top (\mathbf{C}^\circ \mathbf{K} - \lambda_i \mathbf{I}) = \mathbf{0} \quad \text{with} \quad \lambda_i = \omega_i^2, \quad (5.3)$$

where $\boldsymbol{\phi}_i^L$ is the left eigenvector, since the matrix $\mathbf{C}^\circ \mathbf{K}$ is not symmetric. The eigenvalues on the global and element level for the product eigenvalue problem can also be obtained from the Rayleigh quotient on the global and local level. For the product eigenvalue problem of an unsymmetric matrix, both the left and the right eigenvalue need to be used in the Rayleigh quotient (cf. LAMBERS (2010)). However, the inequality does not necessarily hold for the product eigenvalue problem, that means

$$\begin{aligned} \max_i \omega_i^2 &= \max_i \lambda_i = \max_i \frac{(\boldsymbol{\phi}_i^L)^\top \mathbf{C}^\circ \mathbf{K} \boldsymbol{\phi}_i}{(\boldsymbol{\phi}_i^L)^\top \boldsymbol{\phi}_i} \\ &\not\leq \max_{i,e} (\omega_i^e)^2 = \max_{i,e} \lambda_i^e = \max_{i,e} \frac{(\boldsymbol{\phi}_i^{L,e})^\top \mathbf{c}_e^\circ \mathbf{k}_e \boldsymbol{\phi}_i^e}{(\boldsymbol{\phi}_i^{L,e})^\top \boldsymbol{\phi}_i^e}. \end{aligned} \quad (5.4)$$

Consequently, the global eigenvalues are not necessarily smaller than the local ones. This statement is confirmed by a simple illustrative example in the following.

Verification example: Non-conservativeness of elemental estimates for reciprocal mass matrices

The rod consisting of two linear elements, which was already analysed in the thought experiment in Section 3.1, is considered. Material and geometric properties are given in Figure 3.1. The reciprocal mass matrix is computed according to Chapter 3. For simplicity, the special case of a diagonal reciprocal mass is again considered. The elemental lumped mass \mathbf{m}_e , the stiffness matrix \mathbf{k}_e and the reciprocal mass matrices of the left and right element $\mathbf{c}_e^{\circ,l}$ and $\mathbf{c}_e^{\circ,r}$ are

$$\mathbf{m}_e = \begin{bmatrix} 2500 & 0 \\ 0 & 2500 \end{bmatrix}, \quad \mathbf{k}_e = \begin{bmatrix} 2e8 & -2e8 \\ -2e8 & 2e8 \end{bmatrix}, \quad (5.5)$$

$$\mathbf{c}_e^{\circ,l} = \begin{bmatrix} 1/2500 & 0 \\ 0 & 1/10000 \end{bmatrix}, \quad \mathbf{c}_e^{\circ,r} = \begin{bmatrix} 1/10000 & 0 \\ 0 & 1/2500 \end{bmatrix}. \quad (5.6)$$

These elemental matrices result in the global matrices

$$\mathbf{M} = \begin{bmatrix} 2500 & 0 & 0 \\ 0 & 5000 & 0 \\ 0 & 0 & 2500 \end{bmatrix}, \quad \mathbf{K} = \begin{bmatrix} 2e8 & -2e8 & 0 \\ -2e8 & 4e8 & -2e8 \\ 0 & -2e8 & 2e8 \end{bmatrix}, \quad (5.7)$$

$$\mathbf{C}^\circ = \begin{bmatrix} 1/2500 & 0 & 0 \\ 0 & 1/5000 & 0 \\ 0 & 0 & 1/2500 \end{bmatrix}. \quad (5.8)$$

With these matrices at hand, different eigenvalue problems are evaluated. The result for the maximum eigenfrequency from the global and the element eigenvalue problem with the lumped mass matrix and the reciprocal mass matrix are compared. The maximum eigenfrequency ω_{\max} can either be obtained from solving the eigenvalue problem or from the Rayleigh quotient – the result is the same. The results for the different eigenvalue problems are listed in Table 5.1. From the table it can be seen that the maximum

Table 5.1: Comparison of the maximum eigenfrequency for different eigenvalue problems.

	ω_{\max}
$(\mathbf{K} - \lambda_i \mathbf{M})\phi_i = \mathbf{0}$	400.00
$(\mathbf{k}_e - \lambda_i \mathbf{m}_e)\phi_i^e = \mathbf{0}$	400.00
$(\mathbf{C}^\circ \mathbf{K} - \lambda_i \mathbf{I})\phi_i = \mathbf{0}$	400.00
$(\mathbf{c}_e^\circ \mathbf{k}_e - \lambda_i \mathbf{I})\phi_i^e = \mathbf{0}$	316.22

eigenfrequency on the element level is larger than or equal to the maximum eigenvalue on the global level for the generalized eigenvalue problem of stiffness and mass matrix. However, the maximum eigenvalue on the element level is smaller than the maximum eigenvalue on the global level for the product eigenvalue problem of stiffness and reciprocal mass matrix. This confirms eq. (5.4) and (5.1) and verifies the statement that the global eigenvalues are not necessarily smaller than the local ones for the product eigenvalue problem of the reciprocal mass matrix. Consequently, elemental estimates are not necessarily conservative for reciprocal mass matrices. Thus, the development of an efficient and conservative time step estimate focuses on a local node-based estimate.

5.2 Nodal time step estimate for reciprocal mass matrices

In this section, Gershgorin’s time step estimate for lumped mass matrices, as provided in eq. (2.73) without and in eq. (2.75) with penalty contact, is systematically extended

to reciprocal mass matrices. First, several variants of the time step estimate, namely a row-wise, a column-wise and a symmetric estimate, for problems without contact are considered. Secondly, the extension of the most promising one, namely the row-wise estimate, to penalty contact is developed. Thirdly, the time step estimate for penalty contact is rearranged. The rearrangements allow efficient recomputation of the time step in the case of contact where the active contact set varies in time.

5.2.1 Time step estimates for problems without contact

In eq. (2.73) the nodal time step estimate for lumped mass matrices by KULAK (1989) was given. His approach is a row-wise version, which is computationally cheaper than a column-wise estimate, as explained earlier. For the product eigenvalue problem of the reciprocal mass matrix from eq. (5.2) both a row-wise and a column-wise estimate are proposed in the following. With the usage of the row-wise Gershgorin's circles, the maximum eigenfrequency of eigenvalue problem (5.2) with reciprocal mass matrices is bounded by

$$\omega_{\max}^{\text{row-wise}} = \max_i \sqrt{\sum_{j=1}^n |(\mathbf{C}^\circ \mathbf{K})_{ij}|}. \quad (5.9)$$

Alternatively, column-wise Gershgorin's circles may be used leading to

$$\omega_{\max}^{\text{column-wise}} = \max_i \sqrt{\sum_{j=1}^n |(\mathbf{K} \mathbf{C}^\circ)_{ij}|} = \max_i \sqrt{\sum_{j=1}^n |(\mathbf{C}^\circ \mathbf{K})_{ji}|}. \quad (5.10)$$

Moreover, the unsymmetric eigenvalue problem can be transferred into a symmetric eigenvalue problem by a Cholesky decomposition of the reciprocal mass matrix with $\mathbf{C}^\circ = \mathbf{L} \mathbf{L}^T$, where \mathbf{L} is a lower triangular matrix. Then, Gershgorin's theorem is applied to the symmetric eigenvalue problem

$$(\mathbf{L}^T \mathbf{K} \mathbf{L} - \omega_i^2 \mathbf{I}) \boldsymbol{\varphi}_i = \mathbf{0} \quad (5.11)$$

which has different eigenvectors but the same eigenvalues as the EVP stated in eq. (5.2). The maximum eigenfrequency is then

$$\omega_{\max}^{\text{symm}} = \max_i \sqrt{\sum_{j=1}^n |(\mathbf{L}^T \mathbf{K} \mathbf{L})_{ij}|}. \quad (5.12)$$

Equations (5.9), (5.10) and (5.12) are thus three basic estimates of the maximum eigenfrequency. The time step estimates for the central difference method are then obtained

with eq. (2.61). For example for the row-wise estimate, the novel nodal time step estimate for reciprocal mass matrices resulting from eq. (5.9) is thus

$$\Delta t_{\text{crit}}^{\text{row-wise}} = \min_i \sqrt{\frac{4}{\sum_{j=1}^n |(\mathbf{C}^\circ \mathbf{K})_{ij}|}}. \quad (5.13)$$

In the denominator of eq. (5.13) only the row-sum of the absolute values of the product $\mathbf{C}^\circ \mathbf{K}$ for each row i is needed. To compute the i^{th} row of the matrix $\mathbf{C}^\circ \mathbf{K}$ all non-zero elements of the matrix \mathbf{K} , but only the i^{th} row of the matrix \mathbf{C}° is needed. Therefore, the computation can be rewritten as

$$\sum_{j=1}^n |(\mathbf{C}^\circ \mathbf{K})_{ij}| = \|\mathbf{C}_{i,:}^\circ \mathbf{K}\|_1, \quad (5.14)$$

where $\square_{i,:}$ denotes a row extraction operator which extracts the i^{th} row from a matrix and $\|\square\|_1$ is the ℓ_1 norm of a vector. The right-hand side of eq. (5.22) needs the same number of floating point operations (FLOPS), but less storage than the left-hand side, as the result is obtained by a sparse row extraction and a sparse vector-sparse matrix product. The memory for storage of the product is released after computing the sum of the absolute values in eq. (5.13).

In the following, a small example is introduced to compare the performance of the row-wise, column-wise and symmetric Gershgorin's estimates for reciprocal mass matrices.

Verification example: Row-wise, column-wise and symmetric nodal estimate

A 1-D linear truss with regular mesh with element length 2.5 and with irregular mesh with element lengths 5.0, 2.5, 1.25 and 1.25 are considered. Geometric and material properties are shown in Figure 5.1.

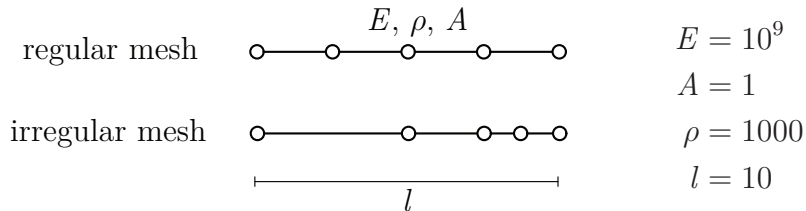


Figure 5.1: Problem setup for the example of the 1-D linear truss with regular and irregular mesh.

The reciprocal mass matrix as described in Chapter 3 with scaling parameter $C_{21} = 0.99$ is used.

The nodal time step estimates proposed in this section are compared to a reference value obtained with the global forward iteration method (with 10 to 12 iterations). The results are listed in Table 5.2. From the table it can be seen that all proposed nodal time step

Table 5.2: Comparison of different nodal time step estimates for the variationally scaled reciprocal mass matrix (VSRMS) for regular and irregular meshes.

	$\Delta t_{\text{crit}}^{\text{glob. it.}}$ (reference)	$\Delta t_{\text{crit}}^{\text{row-wise}}$	$\Delta t_{\text{crit}}^{\text{col-wise}}$	$\Delta t_{\text{crit}}^{\text{symm}}$
regular mesh	4.93e-3	4.79e-3	3.98e-3	4.52e-3
irregular mesh	2.95e-3	2.39e-3	2.27e-3	2.68e-3

estimates provide conservative estimates of the critical time step, since the nodal time steps are always smaller than the reference one. For the irregular discretization, the estimates provide slightly more conservative results than for the regular mesh, i.e. the difference between the nodal estimate and the reference is larger. For the regular mesh the row-wise Gershgorin estimate provides the closest result to the reference solution (i.e. allows the largest time step), for the distorted mesh the symmetric Gershgorin's estimate with Cholesky decomposition provides the closest result to the reference solution. The latter observation is only true for this specific example. The study of different examples turned out that there is no clear winner between the row-wise, column-wise and symmetric Gershgorin's estimate in terms of which one is more conservative.

5.2.2 Time step estimates for problems with penalty contact

Next, the estimate is extended for contact problems, where the contact constraint is introduced by the penalty method. An active penalty contact introduces additional stiffness at the associated degrees of freedom and this stiffness has an influence on the nodal time step. If the influence of the penalty stiffness is not taken into consideration, the critical time step may be overestimated and thus the explicit analysis may turn unstable. Therefore, a regular update of the time step during the explicit simulation of a contact problem is important. Herein, the derivation is restricted to a node-to-segment frictionless contact formulation. Due to contact, an additional force occurs in the system of equations, i.e. eq. (2.95) changes to

$$\ddot{\mathbf{U}} = \mathbf{C}^{\circ}(\mathbf{F}^{\text{ext}} - \mathbf{F}^{\text{int}} + \mathbf{F}^{\text{cont}}), \quad (5.15)$$

where the contact force \mathbf{F}^{cont} is obtained by gathering over the number of active constraints n_c with

$$\mathbf{F}^{\text{cont}} = \sum_{j=1}^{n_c} \varepsilon_j \mathbf{G}_j g_{Nj} \quad (5.16)$$

with ε_j being the penalty stiffness of contact pair j . The penalty stiffness is herein chosen according to the LS-DYNA Theory Manual (HALLQUIST 2006) to

$$\varepsilon_j = \frac{f_{si} K_j A_j^2}{V_j}, \quad (5.17)$$

where f_{si} is a scale factor for the interface stiffness. The default value is $f_{si} = 0.1$, larger values up to 10 can be chosen for hard contact. K_j , A_j and V_j are the bulk modulus, the face area and the volume of the element in contact. The contact constraint is only satisfied approximately in the penalty method and the gap g_{Nj} (or penetration in case of active penalty contact) at constraint j can be written in the form

$$g_{Nj} = \mathbf{G}_j^T \mathbf{U} + g_{N0j}, \quad (5.18)$$

where g_{N0j} is the initial gap and \mathbf{G}_j is the constraint matrix for normal contact with

$$\mathbf{G}_j^T = \frac{\partial g_{Nj}}{\partial \mathbf{U}}. \quad (5.19)$$

The penalty stiffness \mathbf{K}^P is, as well as the global stiffness matrix, not needed for the explicit solution. However, since active penalty contact decreases the critical time step, the penalty stiffness \mathbf{K}^P is to be added to the global stiffness matrix in the estimate of the critical time step. For the active constraints the penalty stiffness is

$$\mathbf{K}^P = \sum_{j=1}^{n_c} \mathbf{K}_j^P = \sum_{j=1}^{n_c} \varepsilon_j \mathbf{G}_j \mathbf{G}_j^T. \quad (5.20)$$

For problems including penalty contact, the novel row-wise time step estimate is thus

$$\Delta t_{\text{crit}}^{\text{row-wise, pen}} = \min_i \sqrt{\frac{4}{\sum_{j=1}^n |(\mathbf{C}^\circ(\mathbf{K} + \mathbf{K}^P))_{ij}|}}, \quad (5.21)$$

where the penalty stiffness matrix is simply added to the global stiffness matrix. Again, the denominator of eq. (5.21) can be rewritten with

$$\sum_{j=1}^n |(\mathbf{C}^\circ(\mathbf{K} + \mathbf{K}^P))_{ij}| = \|\mathbf{C}_{i,:}^\circ(\mathbf{K} + \mathbf{K}^P)\|_1, \quad (5.22)$$

since only the row-sum of the product $\mathbf{C}^\circ(\mathbf{K} + \mathbf{K}^p)$ for each row i is needed. Similarly as for the row-wise time step estimate, the column-wise and symmetric ones can be extended to penalty contact. This results in

$$\Delta t_{\text{crit}}^{\text{column-wise, pen}} = \min_i \sqrt{\frac{4}{\sum_{j=1}^n |(\mathbf{C}^\circ(\mathbf{K} + \mathbf{K}^p))_{ji}|}}, \quad (5.23)$$

$$\Delta t_{\text{crit}}^{\text{symm, pen}} = \min_i \sqrt{\frac{4}{\sum_{j=1}^n |(\mathcal{L}^T(\mathbf{K} + \mathbf{K}^p)\mathcal{L})_{ij}|}}. \quad (5.24)$$

In Figure 5.2 the required data for a row-wise and a column-wise estimate are schematically compared for a 2-D-penalty contact problem. Node i is in contact with the facing element. By the blue box in the left picture, all degrees of freedom with non-zero entries in row i of the reciprocal mass matrix are marked. If the vector $\mathbf{C}_{i,:}^\circ(\mathbf{K} + \mathbf{K}^p)$ is computed, all degrees of freedom marked by the green box have non-zero entries. Similarly, in the right figure, all non-zero entries of the i^{th} row of the stiffness matrix (consisting of the elastic and the penalty stiffness matrix) are marked by the blue box. If the vector $(\mathbf{K} + \mathbf{K}^p)_{i,:}\mathbf{C}^\circ$ is computed, all degrees of freedom with non-zero entries are again marked by the green box. From the picture, it can be seen that the row-wise estimate (left) requires less nodal information than the column-wise estimate (right). The row-wise estimate is thus pursued in the following.

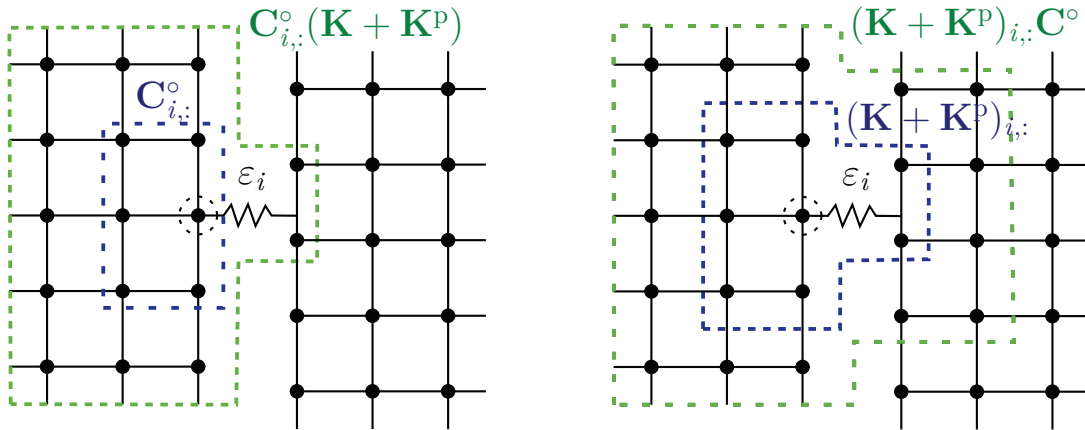


Figure 5.2: Visualization of the data required for row-wise (left) and column-wise (right) estimates for penalty contact.

In the following, the extension of the estimate to penalty contact is evaluated by a small numerical example.

Table 5.3: Results for different nodal time steps for different penalty stiffnesses ε_i for a 1-D linear truss in contact with a rigid wall with the reciprocal mass matrix (VSRMS, $C_{21} = 0.99$).

	$\varepsilon_i = 4.0e7$ ($f_{si} = 0.1$)		$\varepsilon_i = 8.0e8$ ($f_{si} = 2.0$)		$\varepsilon_i = 4.0e9$ ($f_{si} = 10.0$)	
	Δt_{crit}	ratio	Δt_{crit}	ratio	Δt_{crit}	ratio
reference (global estimate)	4.86e-3	1.00	3.08e-3	1.00	1.52e-3	1.00
row-wise Gershgorin, eq. (5.21)	4.58e-3	0.94	2.82e-3	0.92	1.48e-3	0.98
column-wise Gershgorin, eq. (5.23)	3.98e-3	0.82	2.57e-3	0.84	1.25e-3	0.83
symmetric Gershgorin, eq. (5.24)	4.52e-3	0.93	2.71e-3	0.88	1.39e-3	0.91

Verification example: Nodal estimate with penalty contact

The regularly meshed truss from the example of the previous chapter is again considered. This time it is in contact with a rigid wall, see Figure 5.3. The contact condition is taken into consideration by the penalty method. The variationally constructed reciprocal mass matrix (VSRMS, $C_{21} = 0.99$) is again used. In Table 5.3 the results are listed for the

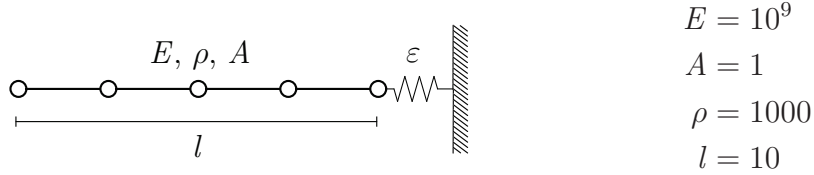


Figure 5.3: Problem setup for the example of the 1-D linear truss in contact with a rigid wall.

three different nodal time step estimates (and the global estimate for reference) and different penalty stiffnesses ε_i . Independent of the chosen penalty stiffness, all proposed time step estimates provide conservative results as expected. This can be seen from the fact that the ratio between the obtained time step and the reference time step is always smaller than 1. The nodal time step is 2 to 17% too conservative. The ratio between the estimated and the reference time step in dependence of the penalty scale factor for different nodal estimates is illustrated in Figure 5.4. For this example, the row-wise Gershgorin estimate provides the result closest to the reference solution (i.e. allows the largest time step).

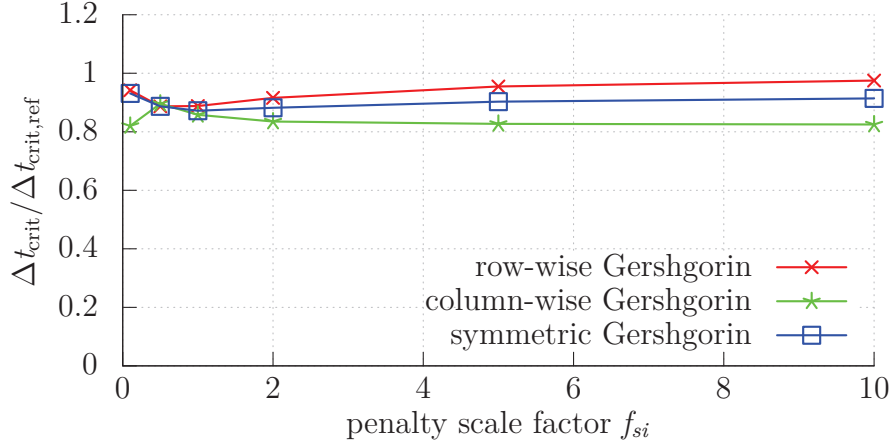


Figure 5.4: 1-D linear truss in contact with a rigid wall, ratio between estimated and reference time step in dependence of the penalty scale factor for different nodal estimates with the reciprocal mass matrix (VSRMS, $C_{21} = 0.99$).

The rearrangements discussed in the following are performed on the row-wise estimate.

5.2.3 Rearrangements for improved efficiency

The rearrangements presented in the following aim for an improved efficiency and are based on certain assumptions: In the case of contact, where the active contact set varies in time, the critical time step is mainly influenced by the changing penalty stiffness of the changing active contact set. Especially in case a geometrically linear problem is considered and non-linearities are only due to contact, the reciprocal mass matrix \mathbf{C}° and the stiffness matrix \mathbf{K} are constant throughout the analysis and we can benefit from the triangle inequality (or sub-additivity). The triangle inequality states that the norm of a sum of vectors is bound by the sum of the norm of the vectors. This leads to

$$\|\mathbf{C}_{i,:}^\circ (\mathbf{K} + \mathbf{K}^p)\|_1 \leq \|\mathbf{C}_{i,:}^\circ \mathbf{K}\|_1 + \|\mathbf{C}_{i,:}^\circ \mathbf{K}^p\|_1, \quad (5.25)$$

leading to a time step estimate with

$$\Delta t_{\text{crit}}^{\text{rw.}+\text{trngl., pen}} = \min_i \sqrt{\frac{4}{\|\mathbf{C}_{i,:}^\circ \mathbf{K}\|_1 + \|\mathbf{C}_{i,:}^\circ \mathbf{K}^p\|_1}}. \quad (5.26)$$

Then, the first summand in the denominator has to be computed only once. The second summand has to be updated with varying active contact set during simulation. It is

limited by an upper bound with

$$\|\mathbf{C}_{i,:}^{\circ}(\mathbf{K}^{\text{P}})\|_1 = \left\| \sum_{j=1}^{n_c} \mathbf{C}_{i,:}^{\circ} \mathbf{K}_j^{\text{P}} \right\|_1 \leq \sum_{j=1}^{n_c} \|\mathbf{C}_{i,:}^{\circ} \mathbf{K}_j^{\text{P}}\|_1. \quad (5.27)$$

In the first part of the equation, the penalty stiffness is obtained from the sum of the penalty stiffnesses of all active contact pairs. In the second part of the equation, the triangle inequality is again applied. As a next step, the right-hand side of eq. (5.27) can be expressed by

$$\sum_{j=1}^{n_c} \|\mathbf{C}_{i,:}^{\circ} \mathbf{K}_j^{\text{P}}\|_1 = \sum_{\substack{j=1 \\ \forall j \in (\mathcal{F}(\mathbf{G}_j) \cap \mathcal{F}(\mathbf{C}_{i,:}^{\circ}))}}^{n_c} \|\mathbf{K}_j^{\text{P}} \mathbf{C}_{:,i}^{\circ}\|_1. \quad (5.28)$$

Therein, \mathcal{F} denotes an operator returning indices of non-zero entries of a sparse vector. Thus, the penalty stiffnesses that do not contribute to the result are excluded. As a second modification, the factors in the norm are transposed in eq. (5.28). This is permitted since the penalty stiffness matrix and the reciprocal mass matrix are symmetric. Then, the L1 norm of a column vector instead of a row vector is computed which provides the same result. This modification allows further simplifications in the following. Next, the right-hand side of eq. (5.28) is again bounded by

$$\sum_{\substack{j=1 \\ \forall j \in (\mathcal{F}(\mathbf{G}_j) \cap \mathcal{F}(\mathbf{C}_{i,:}^{\circ}))}}^{n_c} \|\mathbf{K}_j^{\text{P}} \mathbf{C}_{:,i}^{\circ}\|_1 \leq \sum_{\substack{j=1 \\ \forall j \in (\mathcal{F}(\mathbf{G}_j) \cap \mathcal{F}(\mathbf{C}_{i,:}^{\circ}))}}^{n_c} \|\mathbf{K}_j^{\text{P}}\|_1 \|\mathbf{C}_{:,i}^{\circ}\|_1 \quad (5.29)$$

by means of the sub-multiplicativity property of vector norms. The sub-multiplicativity property states that the L1 norm of a matrix-vector product is bounded by the L1 norm of its factors. Last, the simplification

$$\sum_{\substack{j=1 \\ \forall j \in (\mathcal{F}(\mathbf{G}_j) \cap \mathcal{F}(\mathbf{C}_{i,:}^{\circ}))}}^{n_c} \|\mathbf{K}_j^{\text{P}}\|_1 \|\mathbf{C}_{:,i}^{\circ}\|_1 \leq k_{p,i}^{\text{scal}} \|\mathbf{C}_{:,i}^{\circ}\|_1, \quad (5.30)$$

is introduced. The scalar value of the penalty stiffness at each degree of freedom $k_{p,i}^{\text{scal}}$ is assembled from the subset of active constraints by

$$k_{p,i}^{\text{scal}} = \sum_{\substack{j=1 \\ \forall j \in (\mathcal{F}(\mathbf{G}_j) \cap \mathcal{F}(\mathbf{C}_{:,i}^{\circ}))}} \begin{cases} \varepsilon_j & \text{if single-body contact at d.o.f. } j \\ 2\varepsilon_j & \text{if multi-body contact at d.o.f. } j \\ 0 & \text{if no contact at node } j \end{cases} \quad (5.31)$$

where ε_j is the penalty stiffness factor defined above. For the special case of rigid wall contact with a strictly diagonal inverse mass, the usage of eq. (5.30) does not introduce

any additional approximation error, i.e. the equality holds exactly. Eq. (5.30) allows to split between the penalty stiffness and the norm of the i^{th} column $\mathbf{C}_{:,i}^{\circ}$. The latter is usually constant throughout the simulation and it must therefore also be computed only once. In the final result

$$\Delta t_{\text{crit}}^{\text{rw.}+\text{trngl.}+\text{pen.}, \text{pen}} = \min_i \sqrt{\frac{4}{\|\mathbf{C}_{i,:}^{\circ} \mathbf{K}\|_1 + k_{p,i}^{\text{scal}} \|\mathbf{C}_{:,i}^{\circ}\|_1}}, \quad (5.32)$$

only the changing penalty stiffness needs to be updated under the assumptions made. As in the whole rearrangement only upper bounds are used, the proposed time step estimate is guaranteed to be conservative.

Verification example: Rearrangements for the nodal estimate

To evaluate the approximation error introduced with different assumptions, the example from the previous section (see Figure 5.3) is again considered in the following. The original row-wise estimate from eq. (5.21) is compared with the rearranged ones proposed in eq. (5.26) and (5.32). The simplification from eq. (5.27) only makes a difference for several active contact pairs and does not need to be considered here. Similarly, the simplification from eq. (5.29) is not relevant for this example, since the penalty stiffness matrix is diagonal with only a single non-zero entry. Therefore, these two assumptions are not considered in the comparison. In Table 5.4 the results are listed for different penalty stiffnesses. Activation of the triangle inequality has no influence on the time step for 1-D problems. The assumption on the penalty stiffness from eq. (5.31) makes the result up to 16% more conservative. The ratio between the estimated time step and the reference time step (obtained by a global iterative estimate) for different penalty scale factors is illustrated in Figure 5.5 for the different assumptions. All nodal estimates provide a time step which is at least 80% of the reference time step.

In order to evaluate the savings in computational costs with respect to a global estimate and achieved by the rearrangements introduced in this section, a simple comparison of floating-point operation (FLOP) count can be performed. Of course, this FLOP count is not an accurate predictor for computation time on modern computers, but nevertheless allows a rough estimate of complexity and thus serves as a qualitative indicator for different approaches. Such a simple FLOP count is proposed in SCHAEUBLE ET AL. (2018). Alternatively, the computation time can be measured, requiring an efficient (or at least similarly efficient) implementation of all estimates.

Table 5.4: Results for different assumptions on the row-wise Gershgorin time step estimate for different penalty stiffnesses ε_i for a 1-D linear truss in contact with a rigid wall with the reciprocal mass matrix (VSRMS, $C_{21} = 0.99$).

	$\varepsilon_i = 4.0e7$ ($f_{si} = 0.1$)		$\varepsilon_i = 8.0e8$ ($f_{si} = 2.0$)		$\varepsilon_i = 4.0e9$ ($f_{si} = 10.0$)	
	Δt_{crit}	ratio	Δt_{crit}	ratio	Δt_{crit}	ratio
reference (global estimate)	4.86e-3	1.00	3.08e-3	1.00	1.52e-3	1.00
row-wise Gershgorin (eq. (5.21))	4.58e-3	0.94	2.82e-3	0.92	1.48e-3	0.98
row-wise Gershgorin + triangle inequality (eq. (5.26))	4.58e-3	0.94	2.82e-3	0.92	1.48e-3	0.98
row-wise Gershgorin + triangle inequality + penalty assumption (eq. (5.32))	4.49e-3	0.92	2.46e-3	0.80	1.24e-3	0.82

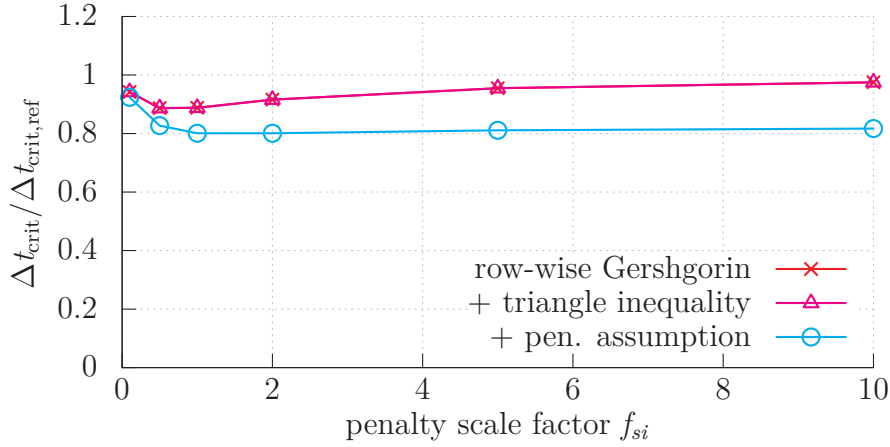


Figure 5.5: 1-D linear truss in contact with a rigid wall, ratio between estimated and reference time step in dependence of the penalty scale factor for different assumptions on the row-wise estimate with the reciprocal mass matrix (VSRMS, $C_{21} = 0.99$).

5.3 A brief summary of Chapter 5

In the following, the advancements presented in Chapter 5 are shortly reviewed. At the beginning of this chapter, the question whether a global, elemental or nodal estimate should be developed was studied. While a global estimate was excluded from the be-

ginning due to its large computational effort, the usability of an elemental estimate was refused since elemental estimates may provide non-conservative results for reciprocal mass matrices. Therefore, a novel nodal estimate was proposed. The proposed time step estimate is based on Gershgorin's theorem and works independently of the element type used in the finite element discretization. Furthermore, it is applicable to different reciprocal mass matrices proposed in literature, like the variationally constructed reciprocal mass matrices from Chapter 3 and the reciprocal mass matrices based on micro inertia assumptions by LOMBARDO AND ASKES (2013) (as shown in SCHAEUBLE ET AL. (2018)). Due to the unsymmetry of the matrix $\mathbf{C}^\circ\mathbf{K}$ in the EVP of reciprocal mass matrices, several estimates based on Gershgorin's estimate are possible, namely a row-wise (eq. (5.13)), a column-wise (eq. (5.10)) and a symmetric one (eq. (5.12)) were proposed. All provide conservative results for regular and irregular meshes. Subsequently, the estimates were extended for penalty contact. Finally, several rearrangements were proposed to improve the efficiency. The rearrangements are based on the idea that in case of an analysis where the non-linearity mainly results from the contact, main parts of the computation can be performed only once whereas the penalty stiffness resulting from a changing active contact set is regularly updated.

6

Numerical examples

In the following, the developments presented in Chapters 3 to 5 are supported by numerical examples. Both linear and nonlinear transient problems, modal analyses and an example for feasible time step estimates are considered. These examples cover Lagrange and NURBS-based finite elements with different instances of the proposed variationally consistent inertia templates.

In Example 6.1 a transient analysis of a 3-D-cantilever beam is performed. The example serves as introductory example and focuses on the comparison of speed-up and accuracy for different load cases, finite element discretizations, inertia matrices and choice of ansatz spaces.

Example 6.2 and 6.3 demonstrate the customization power of the proposed multi-parametric inertia template by means of an eigenvalue analysis and a transient analysis of a 2-D tapered structure discretized with quadratic NURBS finite elements.

Example 6.4 shows the improved behaviour of the formulation for non-constant material properties in comparison to the original formulation. The improvement is obtained by a modified construction of the biorthogonal ansatz spaces as proposed in Chapter 3.2. The tapered structure from Example 6.2 is again considered in form of a two-material model. First, the lowest eigenfrequencies are compared and evaluated for the original and novel formulation. Second, the convergence behaviour of both formulations is studied.

The development of the time step estimate for reciprocal mass matrices in Chapter 5 was accompanied by small verification examples in 1-D. In Example 6.5 the applicability of the proposed time step estimate is tested in 2-D for a highly irregular mesh with penalty contact.

The final Example 6.6 investigates the applicability of the proposed methods to problems including geometric and material nonlinearities.

6.1 Linear transient analysis of a 3-D cantilever beam

A 3-D cantilever beam discretized with 10-node tetrahedral elements is considered in a linear transient analysis. The results of the analysis are partly published in SCHÄUBLE ET AL. (2014). Geometry and material properties are given in Figure 6.1. A structured mesh is obtained by meshing first with $50 \times 3 \times 1$ hexahedral elements and splitting then each hexahedron into six tetrahedral finite elements. Four Gauss points are used for the internal force computation and 15 Gauss points are used for the inertia matrices. Two different load cases, namely a bending and a longitudinal load are considered.

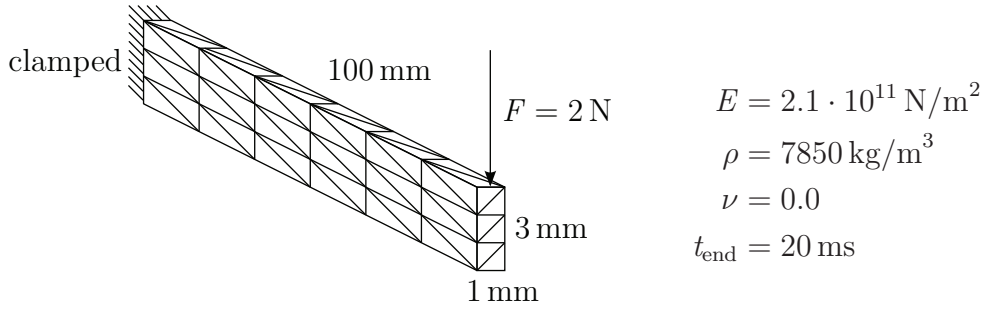


Figure 6.1: Setup of the 3-D-cantilever beam problem, bending load case.

First, the bending load case is analyzed. The initial velocity and the initial displacement are $\mathbf{u}_0 = \mathbf{v}_0 = \mathbf{0}$. An abrupt force of 2 N is applied at the tip of the clamped cantilever beam at time $t = 0$, as illustrated in Figure 6.1. Without taking damping into consideration, the beam is expected to oscillate around its equilibrium state without attenuation. An end time of $t_{\text{end}} = 20 \text{ ms}$ is selected to study the displacement over exactly five periods in order to observe possible period elongations due to different inertia matrices. The history of the tip displacement for the lumped mass matrix (HRZ-lumping) and different versions of the variationally scaled mass matrix are illustrated in Figure 6.2. The different versions of the variationally scaled mass matrix are obtained by the use of different scaling factors associated with different velocity ansatz function spaces. The scaling factors C_{31} , C_{32} and C_{33} are associated with constant (Ψ_1^{3D} , eq. (3.31)), coupled linear (Ψ_2^{3D} , eq. (4.1)) and decoupled linear (Ψ_3^{3D} , eq. (4.3)) velocity ansatz spaces, respectively. For the bending load case, an extreme speed-up of factor 22, i.e. a 22 times larger time step size than with the lumped mass matrix, is possible with the variationally scaled mass matrix without deteriorating the accuracy. While for linear finite elements the constant velocity ansatz (Ψ_1^{3D} , eq. (3.31)) provides already very accurate results, as shown in TKACHUK (2013), this choice leads to a significant phase error for quadratic finite elements. Therefore, linear ansatz functions (Ψ_2^{3D} , eq. (4.1)) are required. More elaborate ansatz spaces (Ψ_3^{3D} , eq. (4.3)) provide the same accuracy but require significantly more time steps and are therefore not recommended.

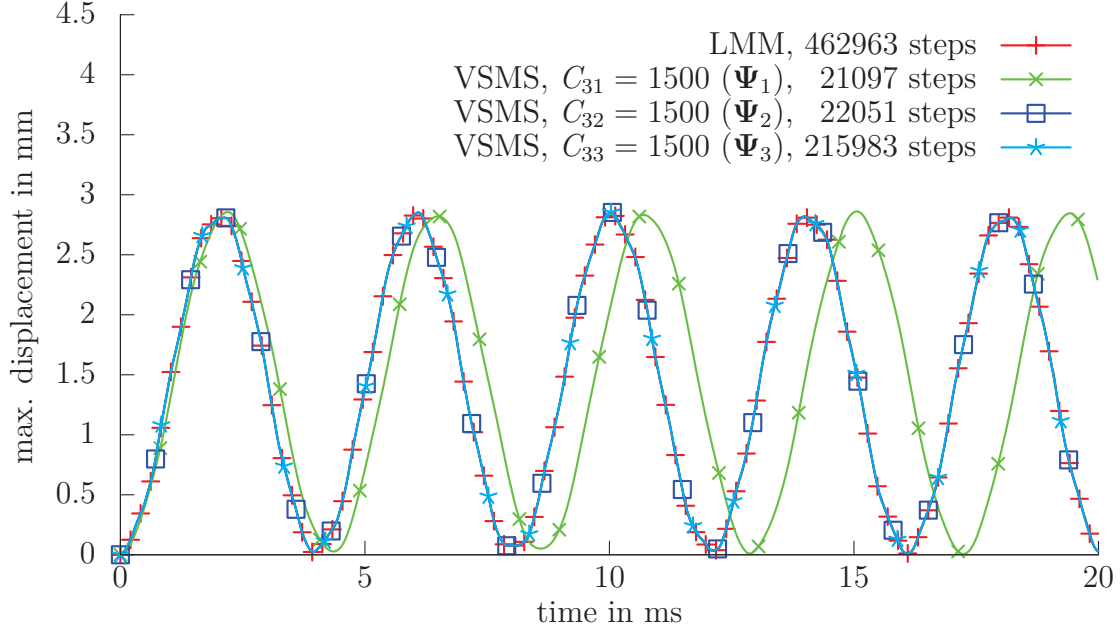


Figure 6.2: Tip displacement history for different variationally scaled mass matrices (VSMS) for the bending load case.

In Figure 6.3 the results are compared with the algebraic selectively scaled mass matrix. The comparison shows that the variationally scaled mass with linear velocity ansatz functions provides a more accurate result for the same number of time steps. The algebraically scaled mass matrix provides similarly accurate results as the variationally scaled mass matrix with constant velocity ansatz space.

Next, the reciprocal mass matrix is used. Due to the Dirichlet boundary conditions necessary modifications of the dual ansatz functions are required as described in Section 3.7.1. With the reciprocal mass matrix, the speed-up is limited to factor 2.7 due to stability issues ($\sum_{\alpha} C_{2\alpha} < 1$). Even with constant velocity ansatz functions a very accurate result is obtained for the reciprocal mass matrix as it can be seen from Figure 6.4.

Second, an axial load is applied as illustrated in Figure 6.5. The load is abruptly applied at $t = 0$. For such a load the axial displacement history at the tip shows a zig-zag shape. The maximum axial displacement can be predicted with $2Fl/EA = 0.645 \cdot 10^{-6}$ m and the period is $T = 2l/\sqrt{E/\rho} = 0.077$ ms. The end time is chosen with $t_{\text{end}} = 0.5$ ms, which contains approximately 6.5 periods. Again, a significant reduction of the number of time steps is possible. For the extreme speed-up of factor 22, less accurate results than for the longitudinal load case are obtained, as it can be seen from Figure 6.6. The reason is that the bending load case activates eigenmode 2, whereas the longitudinal load case excites mainly mode 13. Therefore, with very large speed-up, the second

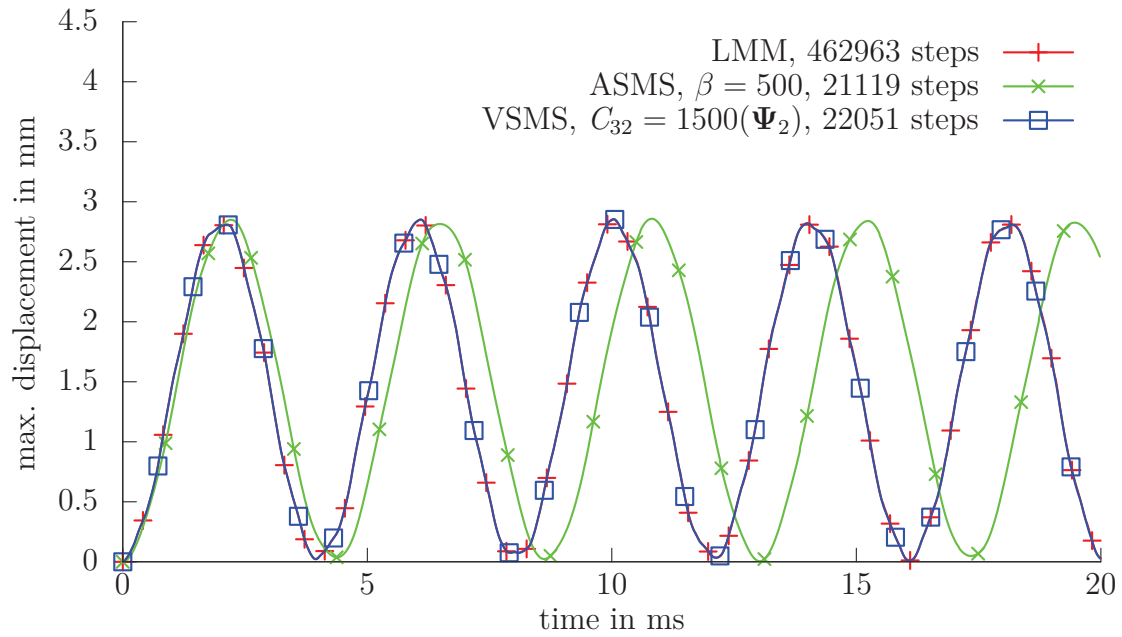


Figure 6.3: Tip displacement history for the variationally scaled mass matrix (VSMS) in comparison with the algebraically scaled mass matrix (ASMS) for the bending load case.

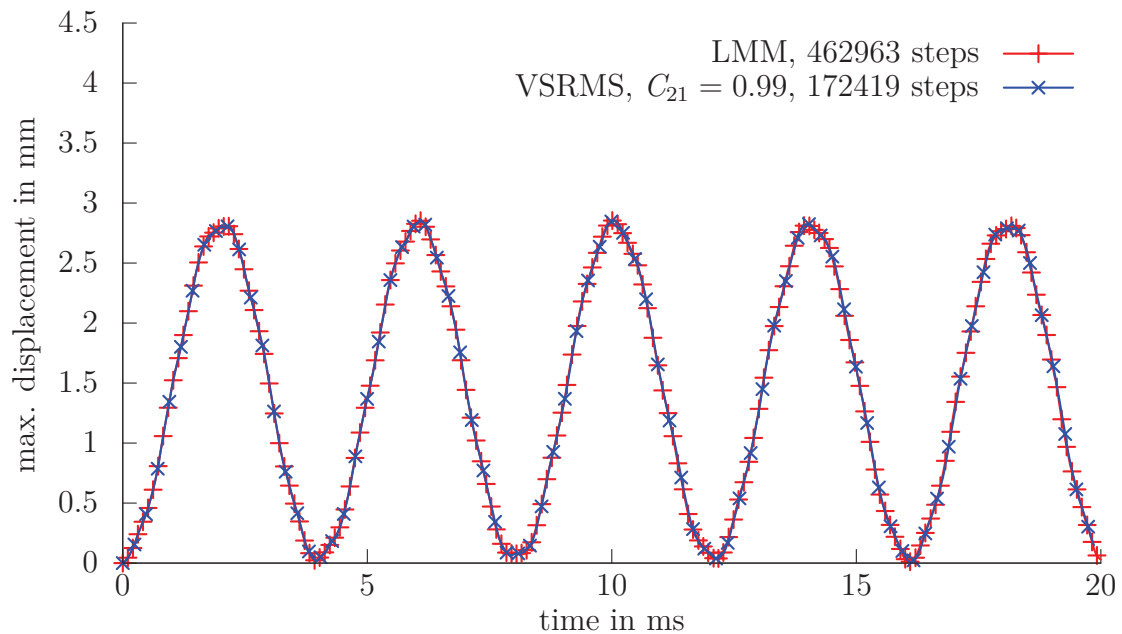


Figure 6.4: Tip displacement history for the variationally scaled reciprocal mass matrix (VSRMS) for the bending load case.

eigenmode is still exactly represented, whereas mode 13 shows already a deviation from the solution obtained with the lumped mass matrix. For the reciprocal mass matrix,

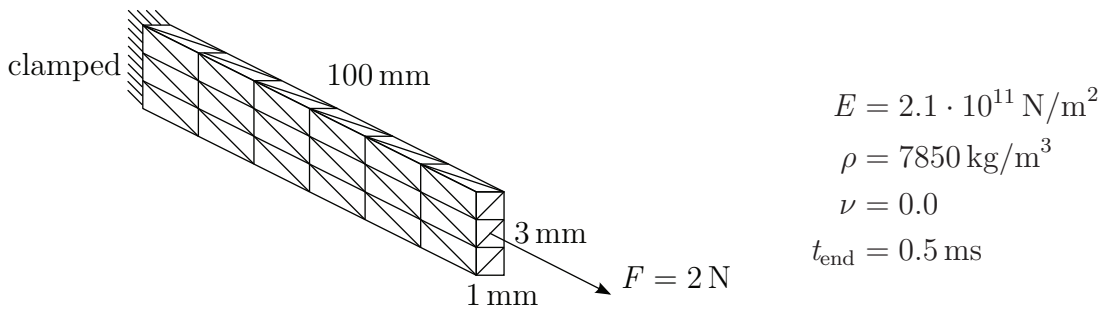


Figure 6.5: Setup of the 3D-cantilever beam problem, longitudinal load case.

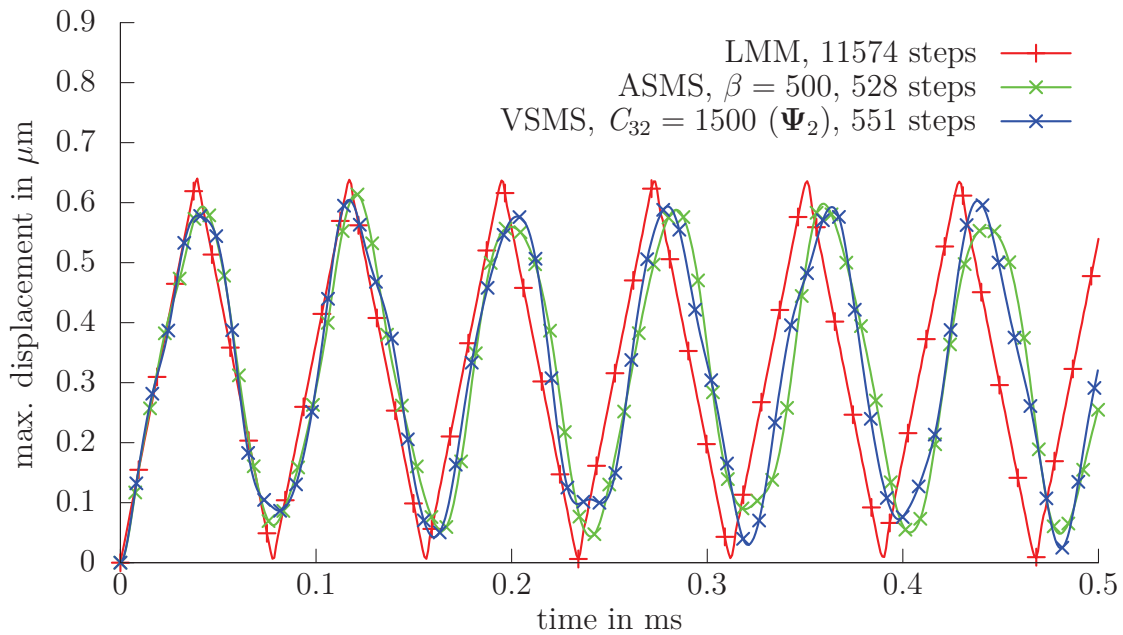


Figure 6.6: Tip displacement history for the variationally scaled mass matrix (VSMS) in comparison with the algebraically scaled mass matrix (ASMS) for the longitudinal load case

where the speed-up is limited to factor 2.7, the result is very accurate, as shown in Figure 6.7. The higher accuracy for the reciprocal mass matrix is mainly caused by less inertia scaling. Similar accuracy is obtained for the variationally scaled mass matrix for a similar speed-up.

An interesting observation is that with quadratic tetrahedral finite elements a speed-up in the time-step size of factor 2.7 with respect to the lumped mass matrix is obtained for reciprocal mass matrices, whereas for linear tetrahedral finite elements the speed-up is only 1.35. Therefore, one can conclude that a larger speed-up is possible for quadratic than for linear finite elements. However, the time step is smaller for quadratic than for linear finite elements for the same number of degrees of freedom for the lumped

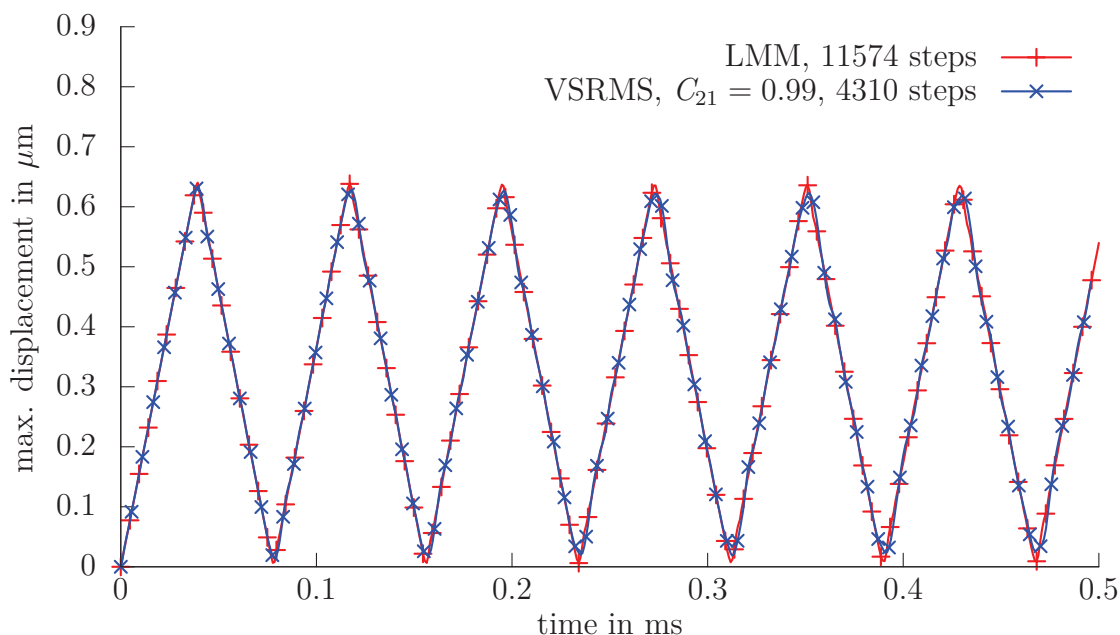


Figure 6.7: Tip displacement history for the variationally scaled reciprocal mass matrix (VSRMS) for the longitudinal load case.

mass matrix. In the following, a 1-D analogy is considered to study whether quadratic finite elements provide a larger possible time step size than linear finite elements in the context of reciprocal mass matrices.

Imagine a 1-D-rod is discretized either with linear or quadratic finite elements. For both discretizations the same number of degrees of freedom is used, therefore the same distance h between neighboring nodes exists. For the lumped mass matrix, the critical time step for linear finite elements is h/c . For quadratic finite elements the critical time step is less, namely $0.81 h/c$, cf. BELYTSCHKO ET AL. (2014). With the reciprocal mass matrix a speed-up with respect to the lumped mass matrix of 1.97 is obtained for linear finite elements, whereas for quadratic finite elements a speed-up of 3.16 with respect to lumped mass matrix is obtained. Therefore, although quadratic finite elements provide a smaller critical time step for the lumped mass matrix than linear finite elements, the critical time step is 60% larger for quadratic finite elements than for linear ones for the reciprocal mass matrix. This consideration is summarized in Table 6.1. However, since quadratic finite elements require more quadrature points for numerical integration, each time step is more expensive for quadratic than for linear finite elements in a nonlinear analysis.

Additionally, in some applications the numerical artifact of optical branches for higher order finite elements may pollute the solution. Then, NURBS or B-spline based finite

Table 6.1: Comparison of the critical time step for linear and quadratic 1-D discretizations with lumped and reciprocal mass matrix ($C_{21} = 0.99$). The distance between nodes is h , c is the wave speed.

	linear elements	quadratic elements
$\Delta t_{\text{crit,LMM}}$	h/c	$0.81 h/c$
$\Delta t_{\text{crit,VSRMS}, C_{21}=0.99}$	$1.97 \Delta t_{\text{crit,LMM}}^{\text{lin}} = 1.97 h/c$	$3.16 \Delta t_{\text{crit,LMM}}^{\text{quad}} = 2.57 h/c$

elements, which show improved spectral properties, may be of interest as an alternative in this context.

6.2 Eigenfrequency analysis of a 2-D tapered structure

The second example serves to test to what extent the results of the analytical grid dispersion analysis of infinite regular meshes from Chapter 4 are transferable to numerical analyses of bounded structures. The eigenfrequency benchmark FV32 of NAFEMS (1990) is considered, but with a specific discretization. First, the tapered structure is meshed with a regular 1x1 quadratic B-spline mesh. Then, the center control point is displaced by 2 in x -direction and the weight is changed from 1 to 2. Next, the mesh is refined by knot insertion to obtain 8x4 quadratic elements in a single patch. In this way, a distorted NURBS mesh is obtained as shown in Figure 6.8. It has to be tested whether the results from the dispersion analysis are beneficial for this example and whether more accurate results than with a lumped or consistent mass matrix can be obtained for the reciprocal mass matrix by inertia customization. For a good performance in transient analyses, a satisfactory accuracy of the first 30% of the modes is desired. The eigenfrequencies are compared with a reference solution obtained as an overkill-solution from ANSYS (400x200 S2-elements, consistent mass). The first five eigenfrequencies can as well be obtained from NAFEMS (1990). Since the reference eigenfrequency of the first 35 modes is required herein, the reference solution is created with ANSYS.

Geometry dimensions, mesh and material properties of the model are provided in Figure 6.8. Boundary conditions $u_x = u_y = 0$ are imposed on the left edge. Thus, 108 unconstrained degrees of freedom remain in the model. All element matrices are computed using $p + 1$ quadrature points per direction. Row-sum lumping is used for the lumped mass matrix. The reciprocal mass matrix is computed with dual ansatz functions with necessary modifications due to Dirichlet boundary conditions as described in Section 3.7.1.

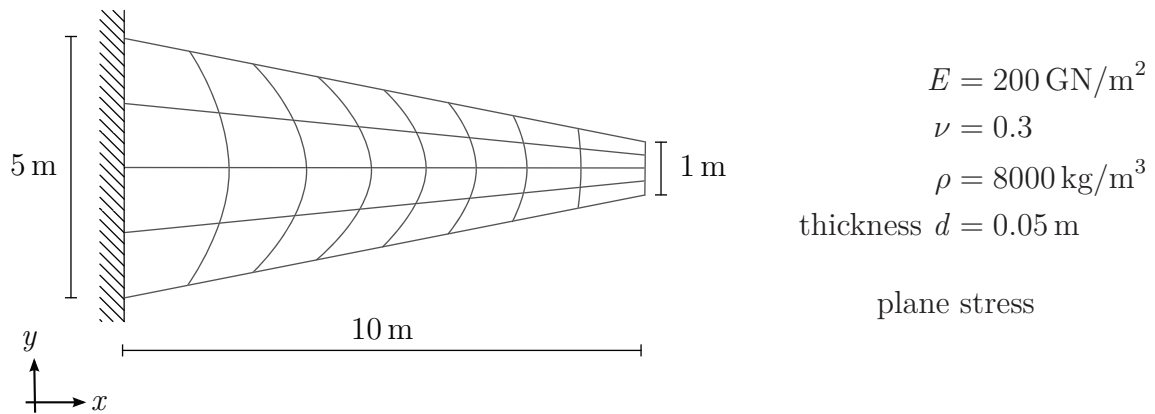


Figure 6.8: Setup of the 2-D tapered structure (similar to NAFEMS FV32 benchmark). The mesh is created by quadratic NURBS.

In Figure 6.9 the ratio between the eigenfrequency ω° for different mass or reciprocal mass matrices and the reference eigenfrequency ω_{ref} is plotted versus the mode number for the first 35 eigenfrequencies. While the consistent mass matrix provides a very accu-

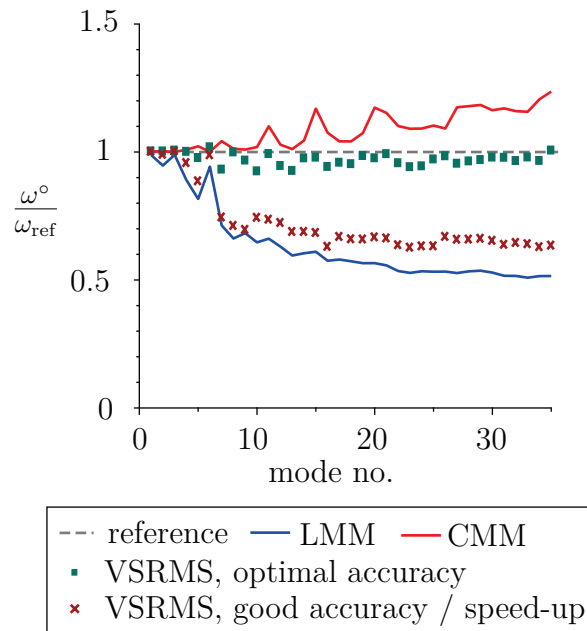


Figure 6.9: Relation between scaled and reference eigenfrequency versus mode number.

rate result for the first five eigenfrequencies the ratio between the eigenfrequency of the consistent mass matrix and the reference solution increases with increasing mode number. For the lumped mass matrix, the eigenfrequencies are significantly underestimated. With the optimal choice of scaling factors for the reciprocal mass matrix, as predicted by the 2-D analytical grid dispersion analysis, the error in the first 35 eigenfrequencies is very small. However, with this optimal choice of free parameters with $C_{21} = 9/16$,

$C_{24} = 577/1600$, $C_{22} = C_{23} = 0$ the maximum eigenfrequency is 65% larger than for the lumped mass matrix (but still smaller than for the consistent one).

In order to study whether the choice of scaling factors is really optimal with respect to accuracy, small perturbations of ± 0.02 are introduced for the free parameters C_{21} and C_{24} , respectively. As it can be seen from Figure 6.10, a small perturbation of the free parameter C_{21} (left) and C_{24} (right) leads to eigenfrequency ratios mainly above and below 1. Therefore, the results from the dispersion analysis can be evaluated as optimal.

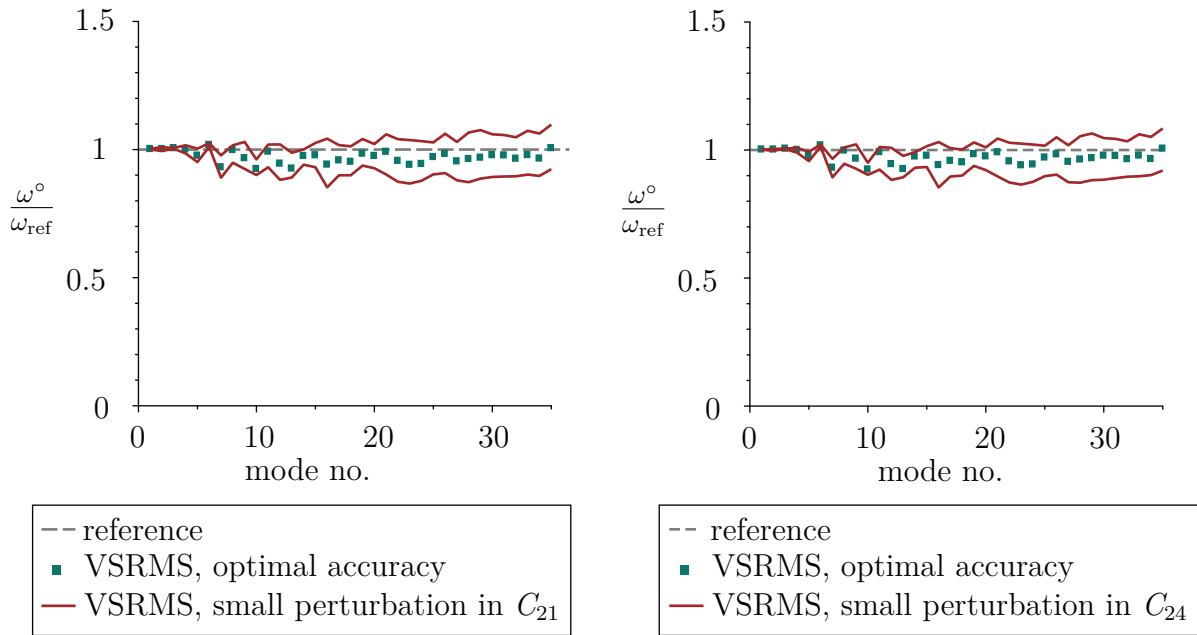


Figure 6.10: Relation between scaled and reference eigenfrequency versus mode number for the reciprocal mass matrix (VSRMS) with small perturbations of the free parameters C_{21} (left) and C_{24} (right), respectively.

In case a large speed-up in combination with high accuracy is desired, the second free parameter can be increased, e.g. to $C_{21} = 9/16$, $C_{24} = 27/64$, $C_{22} = C_{23} = 0$. The first parameter is kept with $C_{21} = 9/16$ in order to maintain the same convergence order as for the consistent mass matrix. The first eigenfrequencies are then only a little more accurate than with the lumped mass matrix as it can be seen from Figure 6.9, but the maximum eigenfrequency is reduced to 75 % of the eigenfrequency of the lumped mass matrix and therefore 25% less time steps are needed in a transient analysis.

A table with the exact numbers of the first six lowest eigenfrequencies for different variationally scaled mass and reciprocal mass matrices can be found in SCHAEUBLE ET AL. (2017).

6.3 Linear transient analysis of a tapered structure under an abrupt load

After the results from the 2-D analytical dispersion analysis have been confirmed in an eigenfrequency analysis, the same model is used to perform a linear transient analysis. The considered time interval is 0.1 s, i.e. ~ 4.5 periods of the first frequency of the structure are considered. Zero initial displacements and velocities are assumed. An abrupt distributed load of $F = 100$ MN/m is applied in vertical direction at the upper edge. Damping is not considered. The reference solution is again computed as an overkill solution with ANSYS (400x200 S2-elements, consistent mass matrix, implicit time integration with $\Delta t = 0.0001$ s). For all other computations, the time step is chosen with $0.9 \Delta t_{\text{crit}}$. Therefore, the consistent mass matrix requires 5312 steps, the lumped mass matrix 2072 steps and the reciprocal mass matrix 1560 steps. The reciprocal mass matrix thus allows a larger time step than the lumped mass matrix. This is reached with $C_{21} = 9/16$, $C_{24} = 27/64$, $C_{22} = C_{23} = 0$ for good accuracy / speed-up.

Evolution of the tip displacement in y -direction at the upper right node is compared in Figure 6.11 for the reciprocal mass matrix and standard mass matrices. From the time

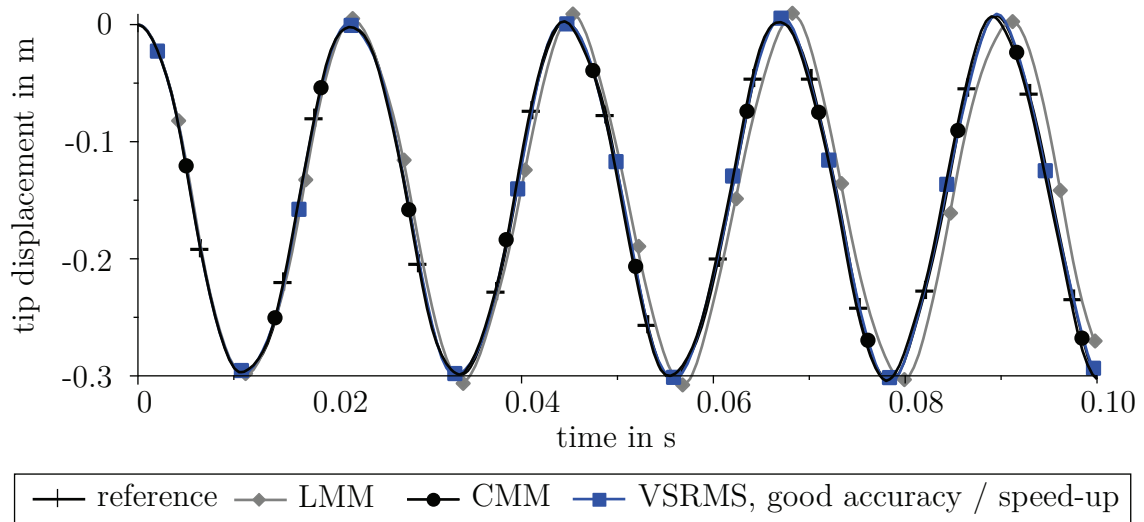


Figure 6.11: Displacement history at the upper right node for different mass matrices.

history of the tip displacement it can be seen that the lumped mass matrix shows some phase error, whereas the consistent mass matrix and the reciprocal mass matrix provide very accurate results. The reciprocal mass matrix requires 70 % less time steps than the consistent mass matrix (25% less than the lumped mass matrix) and every time step is significantly cheaper than for the consistent mass matrix.

In Figure 6.12 the relative error of the tip displacement between the solution of different mass and inverse mass matrices and the reference solution is illustrated. For the lumped

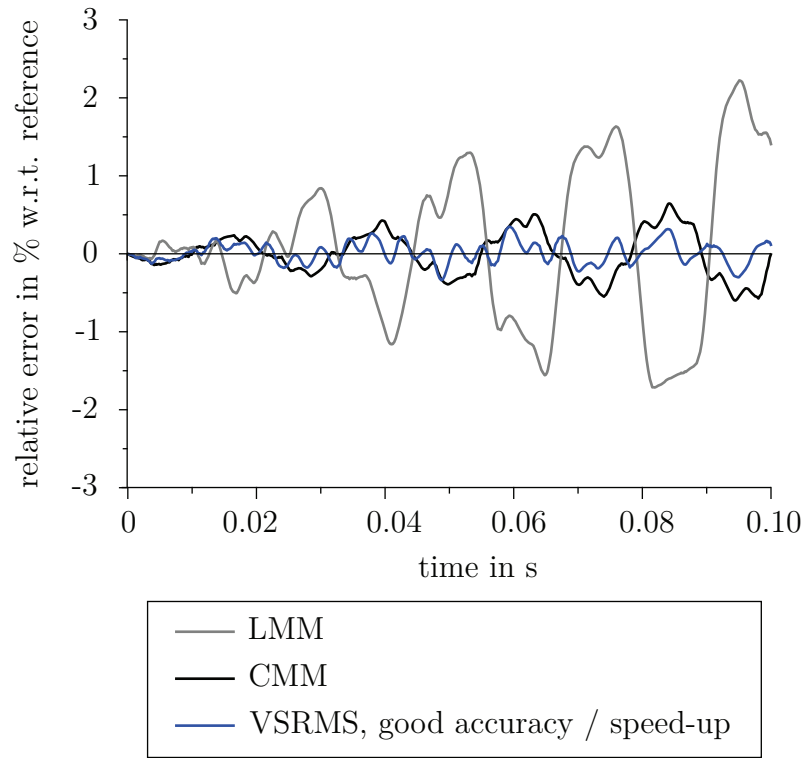


Figure 6.12: Relative error in the displacement at the upper right node with respect to the reference solution for different mass and reciprocal mass matrices

mass matrix the error is the largest, whereas for the reciprocal mass matrix it is even smaller than for the consistent mass matrix. The reason, why the reciprocal mass matrix provides even more accurate results than the consistent mass matrix for the considered transient problem is that the first mode, which is the most relevant one for this load case, is (despite the large speed-up) more accurately represented with the reciprocal mass matrix than with the consistent mass matrix.

6.4 Eigenvalue analysis and convergence study of a two-material 2-D tapered structure

In the following, a 2-D two-material problem is considered to evaluate the introduced modifications in the formulation for non-constant density from Chapter 3. The problem setup of the eigenvalue analysis from Example 6.2 is modified. While the geometric parameters and the boundary conditions remain unaltered, the density and the discretization are changed. The density is chosen to be piecewise constant in x-direction,

namely $\rho_1 = 8000 \text{ kg/m}^3$ in the left half and $\rho_2 = 4\rho_1 = 32000 \text{ kg/m}^3$ in the right half of the tapered structure, see Figure 6.13. Quadratic B-splines are used for the discretization.

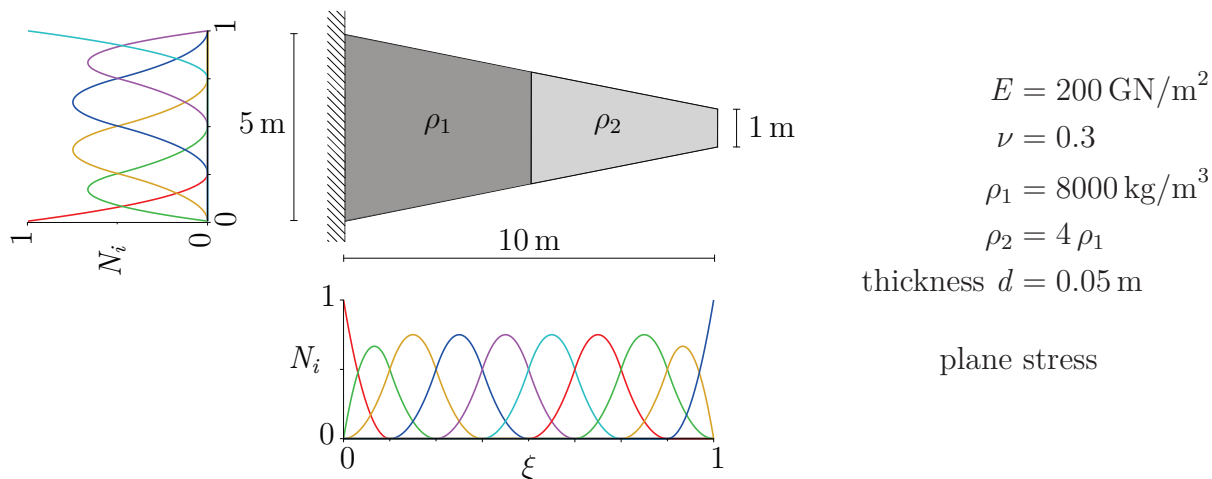


Figure 6.13: Setup of the FV32 NAFEMS benchmark, modelled with two different material densities. The mesh is created by quadratic NURBS.

First, the frequencies of the first six eigenmodes are compared for a discretization of 8×4 elements with a converged reference solution from ANSYS. Both the original formulation from TKACHUK AND BISCHOFF (2015) and the novel one proposed in Chapter 3 are considered. The results are listed in Table 6.2. While the first, second, third and sixth

Table 6.2: Comparison of the first eigenfrequencies (in s^{-1}) for a two-material problem. The relative error is given in brackets.

	reference	original	novel
f_1	23.010	24.858 (8.03%)	22.975 (0.13%)
f_2	78.138	87.090 (11.46%)	76.834 (1.67%)
f_3	89.339	97.997 (9.69%)	89.373 (0.04%)
f_4	169.502	176.304 (4.01%)	159.971 (5.62%)
f_5	255.339	266.864 (4.51%)	237.660 (6.92%)
f_6	258.891	287.767 (11.15%)	258.199 (0.27%)

frequency of the novel formulation show significantly smaller errors than the original formulation, the fourth and fifth frequency show a little larger deviations. In average, the relative error of the first six frequencies is 8.1 % for the original formulation, whereas for the novel formulation the error is only 2.4 %.

Second, a convergence study is performed to confirm that the improved ansatz spaces for non-constant density provide better results than the original ones. The convergence

plot for the original and the novel formulation are given in Figure 6.14. The relative error of the first six eigenfrequencies versus the number of elements in x -direction is studied. The vertical line marks 8 elements in x -direction. This discretization is used for the comparison of the first eigenfrequencies in Table 6.2. For refinement the number of elements in x -direction is increased by knot insertion. In y -direction always half as much elements are used than in x -direction. While the frequencies converge with third order for the novel formulation, the frequencies converge very poorly for the original formulation. The reason why they still converge although the formulation is not consistent is that the defect is reduced with decreasing element size.

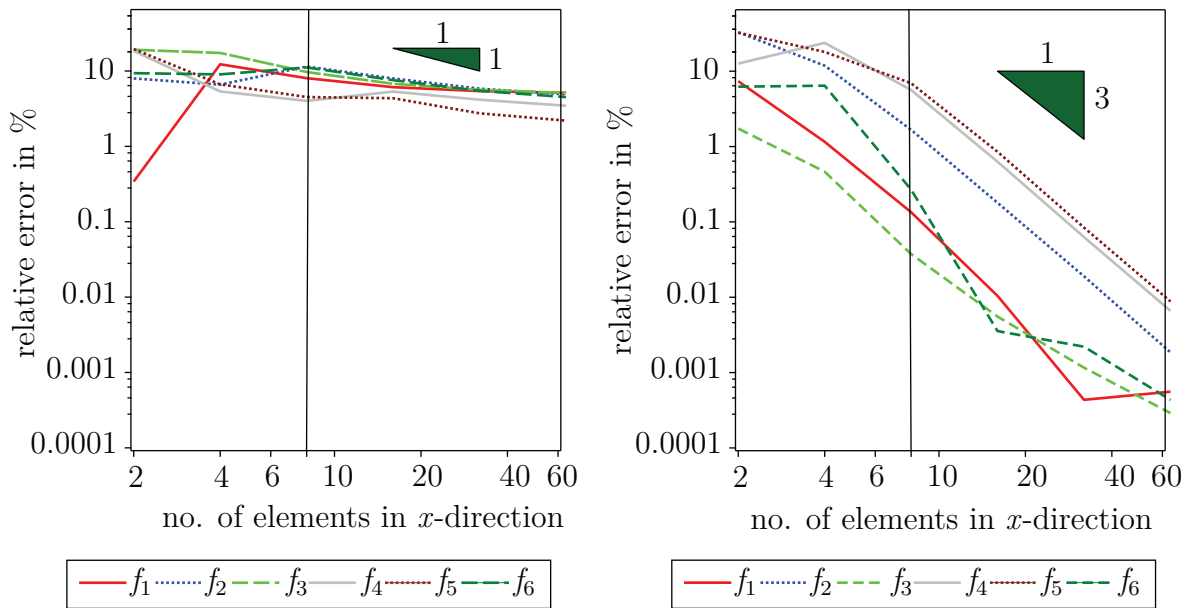


Figure 6.14: Convergence plot for a two-material problem for the original (left) and novel (right) formulation.

6.5 Time step estimation for a 2-D problem with penalty contact and highly distorted mesh

In this example, the time step estimates proposed in Chapter 5 are tested for the case of a highly distorted mesh in 2-D with contact. The example serves to test whether the proposed estimates work as well in 2-D as in 1-D and whether the obtained time step is still conservative for highly distorted discretizations and different penalty stiffnesses. Furthermore, the different proposed variants of the time step estimate are compared.

The problem setup is given in Figure 6.15. Fully integrated standard Q1 finite elements are used. At two nodes, penalty contact with a rigid obstacle is assumed. The reciprocal mass matrix with $C_{21} = 0.99$ is used.

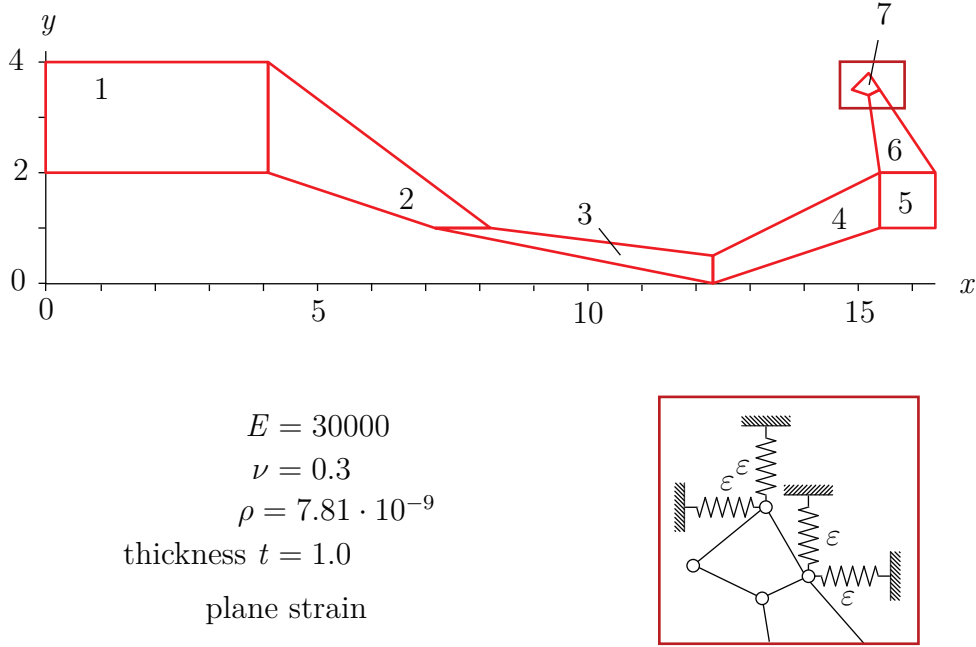


Figure 6.15: Setup for the example of a Q1 highly distorted mesh with penalty contact.

First, the critical time step is determined with different nodal estimates, namely

- the row-wise Gershgorin estimate (eq. (5.21))
- the column-wise Gershgorin estimate (eq. (5.23)) and
- the symmetric Gershgorin estimate with Cholesky decomposition (eq. (5.24)).

The nodal time step obtained with the row-wise Gershgorin estimate is exemplarily illustrated for different penalty scale factors $f_{si} = 10.0$ in Figure 6.16. The penalty scale factor f_{si} and the penalty stiffness ε_i are related through $\varepsilon_i = 4.04e3 \cdot f_{si}$. Note that although the Gershgorin estimate is called “nodal” in literature, the time step is determined at each degree of freedom. This means in 2-D that the Gershgorin estimate actually returns two values at each node which in general do not coincide. The conservative one, i.e. the smaller one is considered and illustrated in Figure 6.16. As expected, the critical time step of the structure is determined by the smallest element. The time step of this element is additionally reduced by the penalty contact.

In Table 6.3 the critical time step of the structure is listed for different Gershgorin estimates and different penalty stiffnesses. All estimates provide conservative results, even

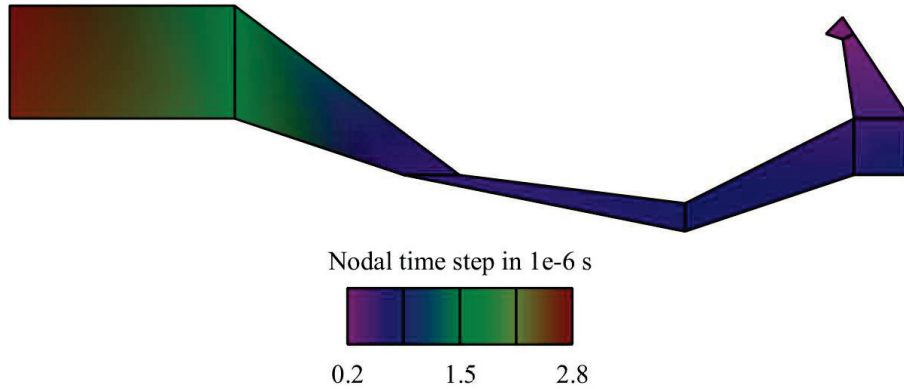


Figure 6.16: Contour plot of the nodal time step for $f_{si} = 10.0$ for the row-wise Gershgorin estimate, interpolated from the nodal values for visualization.

Table 6.3: Results for different nodal time step estimates for a highly distorted Q1 mesh for various penalty stiffnesses ε_i with the reciprocal mass matrix (VSRMS, $C_{21} = 0.99$).

	$\varepsilon_i = 4.04e2$ ($f_{si} = 0.1$)		$\varepsilon_i = 8.08e3$ ($f_{si} = 2.0$)		$\varepsilon_i = 4.04e4$ ($f_{si} = 10.0$)	
	Δt_{crit}	ratio	Δt_{crit}	ratio	Δt_{crit}	ratio
reference (global iterative)	$2.80e-7$	1.00	$2.57e-7$	1.00	$1.96e-7$	1.00
row-wise Gersh., eq. (5.21)	$1.89e-7$	0.68	$1.81e-7$	0.70	$1.53e-7$	0.78
column-wise Gersh., eq. (5.23)	$2.07e-7$	0.74	$1.96e-7$	0.76	$1.42e-7$	0.72
symmetric Gersh., eq. (5.24)	$2.31e-7$	0.83	$2.14e-7$	0.83	$1.69e-7$	0.86

for this highly distorted mesh. The estimates are on the safe side by 14 to 32 % compared to the reference solution obtained from an iterative global estimate. In this example, the symmetric estimate using Cholesky decomposition provides the least conservative result.

In Figure 6.17 the ratios between the estimated and the reference critical time step for reciprocal (left) and lumped mass matrices (right) are illustrated for different penalty scale factors. The nodal estimates for reciprocal mass matrices are shown to be not significantly more conservative than the nodal estimate for lumped mass matrices with penalty contact.

Next, the influence of different assumptions, namely

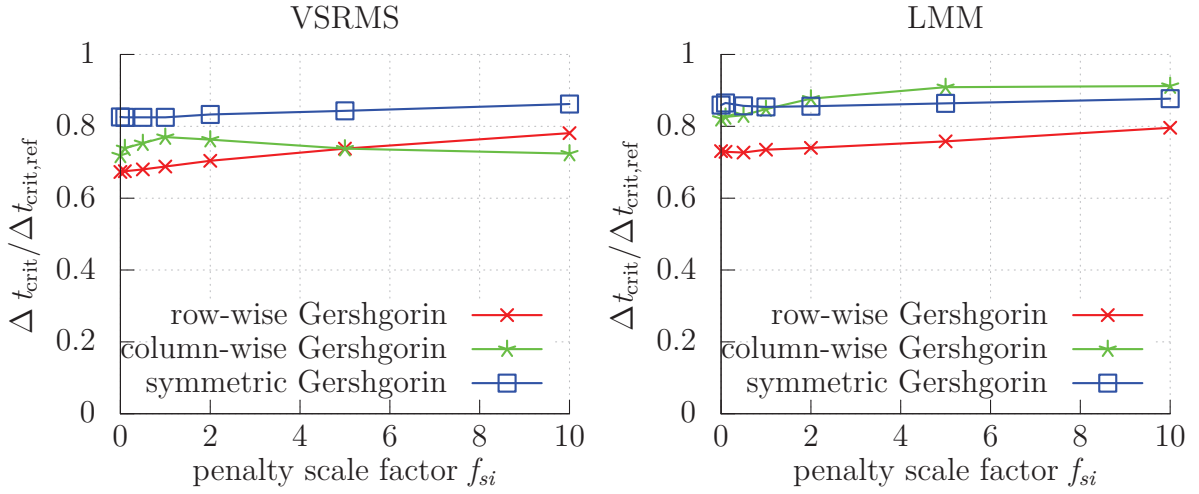


Figure 6.17: Ratio between estimated and reference time step in dependence of the penalty scale factor for different nodal estimates for the reciprocal mass matrix (VSRMS, left) and for the lumped mass matrix (LMM, right) for a highly distorted mesh.

- the sub-additivity to allow one-time stiffness computation (= triangle inequality, eq. (5.25) and (5.26))
- additionally, the sub-additivity to split between local penalty stiffnesses and the sub-multiplicativity to allow one-time inverse mass matrix computation (triangle inequality + penalty assumption, eq. (5.30) and (5.32))

introduced for the row-wise estimate to increase the efficiency in case of penalty contact is studied.

In Table 6.4, the result for the row-wise Gershgorin estimate is considered with the assumptions proposed in eq. (5.25) and (5.30). In 2-D, using the triangle inequality has a very small influence on the result for the reciprocal mass, whereas the assumption of a scalar penalty stiffness is more significant, especially for large penalty stiffness values. The assumptions have no influence on the time step for the lumped mass matrix, as it can be seen from Figure 6.18 (right).

Finally, in Figure 6.19, the critical time step for lumped and reciprocal mass matrices is plotted versus the penalty scale factor for various nodal estimates. From this graph, it can be seen that the time step obtained for the reciprocal mass (square symbol) is larger than the time steps obtained for the lumped mass (triangular symbol), independent of the chosen estimate. This guarantees that the increase of the time step by the scaled reciprocal mass matrix is not used up by the conservativeness of the estimate. For

Table 6.4: Results for different assumptions on the row-wise Gershgorin estimate for a highly distorted Q1 mesh for various penalty stiffnesses ε_i with the reciprocal mass matrix (VSRMS, $C_{21} = 0.99$)

	$\varepsilon_i = 4.04e2$ ($f_{si} = 0.1$)		$\varepsilon_i = 8.08e3$ ($f_{si} = 2.0$)		$\varepsilon_i = 4.04e4$ ($f_{si} = 10.0$)	
	Δt_{crit}	ratio	Δt_{crit}	ratio	Δt_{crit}	ratio
reference (forward iteration)	2.80e-7	1.00	2.57e-7	1.00	1.96e-7	1.00
row-wise Gersh., eq. (5.21)	1.89e-7	0.68	1.81e-7	0.70	1.53e-7	0.78
row-wise Gersh. + triangle inequality, eq. (5.26)	1.89e-7	0.68	1.79e-7	0.70	1.51e-7	0.77
row-wise Gersh. + triangle inequality + penalty assumption, eq. (5.32)	1.88e-7	0.67	1.72e-7	0.67	1.32e-7	0.67

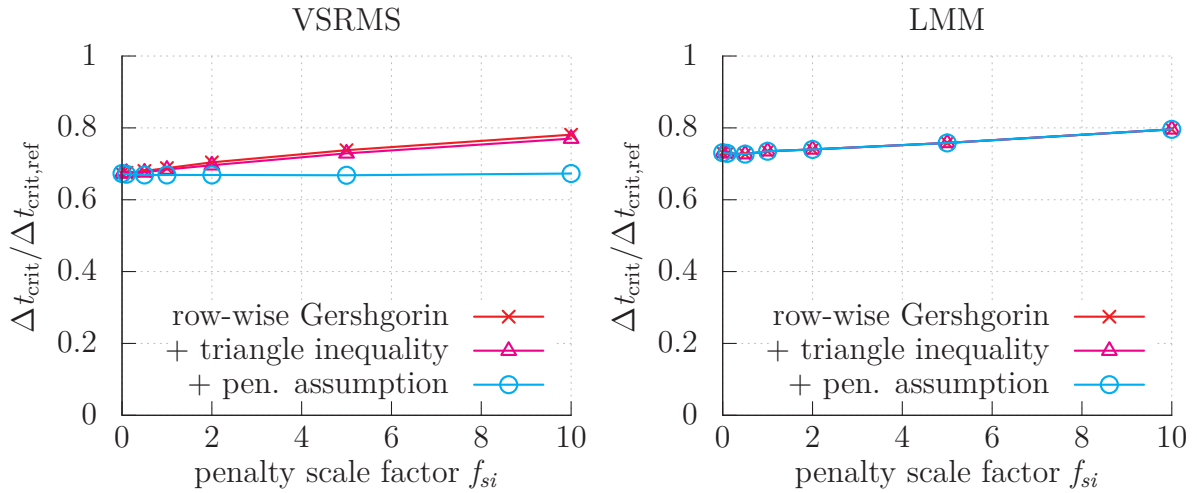


Figure 6.18: Ratio between estimated and reference time step in dependence of the penalty scale factor for different assumptions on the row-wise estimate for the reciprocal mass matrix (VSRMS, left) and for the lumped mass matrix (LMM, right) for a highly distorted mesh.

the same choice of estimate, the result is not significantly more conservative for the reciprocal mass matrix than for the lumped mass matrix.

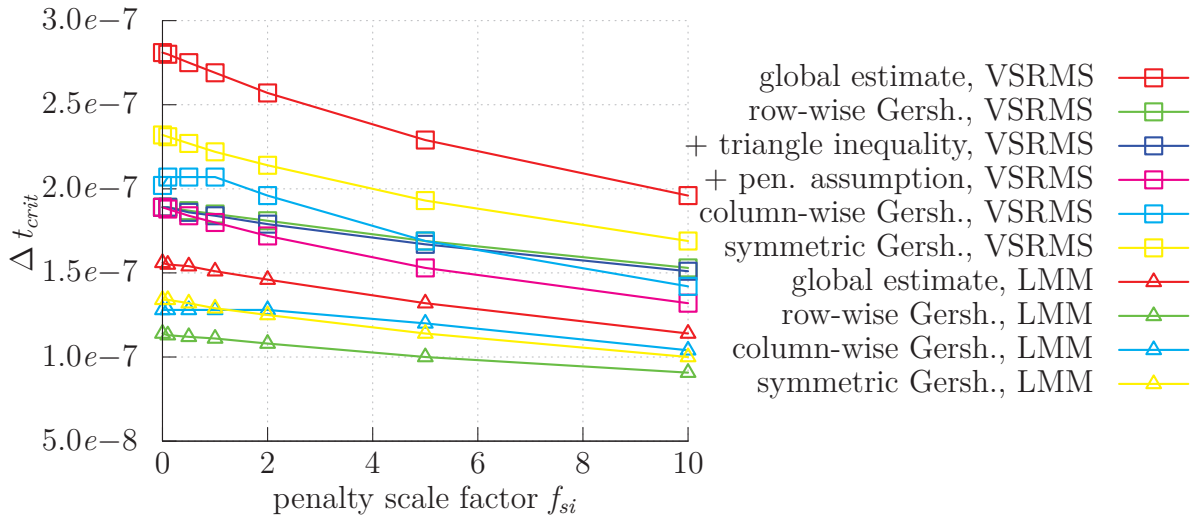
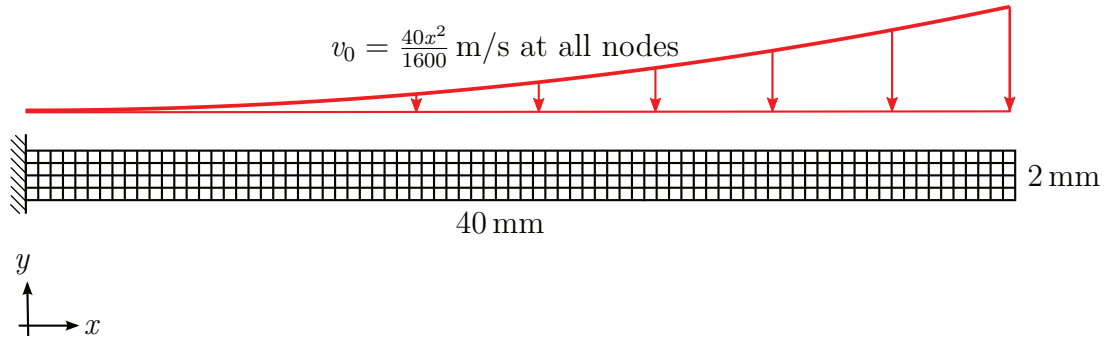


Figure 6.19: Critical time step in dependence of the penalty scale factor for different estimates for the reciprocal mass matrix and for the lumped mass matrix.

6.6 Transient analysis of a cantilever, taking material/geometric nonlinearities into account

In the foregoing examples, geometrically linear problems with linear elastic material behaviour were considered. Nonlinearities – if present – were only introduced through contact. The long-term goal is it to use variationally scaled mass and reciprocal mass matrices in highly nonlinear analyses as this is the typical application field of explicit dynamics. Therefore, a first outlook to nonlinear analyses is performed in the following, where a cantilever beam with elasto-plastic material behaviour under large rotations is considered.

The problem setup is illustrated in Figure 6.20. The beam is clamped on the left edge and modelled with 320 four-noded 1-point integrated Q1 elements with combined stiffness and viscous hourglass stabilization according to BELYTSCHKO AND BINDEMAN (1991). This element formulation is locking free, very efficient and the standard formulation in commercial explicit codes. All results are obtained with the hourglass stabilization factors $\alpha_s = 0.01$, $\zeta_D = 0.001$. The implemented formulation is summarized in Appendix B. Throughout the analysis, the energy history is observed to guarantee that the hourglass energy is smaller than 5% of the total energy.



$E = 1.14 \cdot 10^9 \text{ N/m}^2$ $\rho = 896.7 \text{ kg/m}^3$ $\nu = 0.4$ thickness $d = 1.0 \text{ m}$ plane strain	$J2$ -plasticity with combined kinematic and isotropic hardening $H_{\text{iso}} = H_{\text{kin}} = 0.1 \cdot 10^9 \text{ N/m}^2$ $\sigma_y = 0.025 \cdot 10^9 \text{ N/m}^2$ $\sigma_\infty = 0.05 \cdot 10^9 \text{ N/m}^2$ $\sigma_{\text{exp}} = 0.025$
--	--

Figure 6.20: Setup of the nonlinear cantilever beam problem.

A finite strain plasticity model from the universal material library Muesli (PORTILLO ET AL. (2017)) is used with $J2$ -plasticity with combined kinematic and isotropic hardening. The kinematic and isotropic hardening modulus are both set to $H_{\text{iso}} = H_{\text{kin}} = 0.1 \cdot 10^9 \text{ N/m}^2$. The hardening behaviour is nonlinear with a saturation hardening term for the isotropic hardening of exponential type of Voce as described in SIMO AND HUGHES (2006), defined by the initial yield stress σ_y , the saturation yield stress σ_∞ and the hardening exponent σ_{exp} .

The oscillation of the beam is induced by an initial velocity in y -direction applied at all nodes, which is a function of x with $v_0 = \frac{40x^2}{1600} \text{ m/s}$. The simulation time is 5 ms. The initial velocity increases thus quadratically from 0 at the left edge to a maximum initial velocity of 40 m/s at the right edge. The time history for different inertia matrices of the tip displacement of the upper left node is evaluated.

All computations are performed with $\Delta t = 0.9\Delta t_{\text{crit}}$. The critical time step is determined initially with an iterative estimate. Since the element geometry does not significantly change (the elements mainly rotate), the initially determined time step is kept constant throughout the analysis.

To evaluate the performance of different inertia matrices for this problem setup, the maximum possible time step size and the condition number of the sparse mass matrices is evaluated. The square root of the condition number is proportional to the required number of iterations in a preconditioned conjugate gradient method with Jacobi preconditioner to solve the linear system of equations, cf. BORRVALL (2011).

In Table 6.5 an overview of the compared mass matrices, the used scaling factors and the maximum possible time step sizes, as well as the condition number of the sparse matrices, is given. For the lumped mass matrix and the reciprocal mass matrix, no

Table 6.5: Time step size and condition number for different inertia matrices.

	parameter choice	no. of steps	condition no.
LMM	–	18453	–
ASMS	$\beta = 10$	5378	18.5
ASMS	$\beta = 100$	1904	167.0
ASMS	$\beta = 500$	875	790.6
VSMS (const.)	$C_{31} = 50$	5065	19.9
VSMS (const.)	$C_{31} = 500$	1719	188.9
VSMS (const.)	$C_{31} = 5000$	563	1652.1
VSMS (lin.)	$C_{32} = 50$	5208	30.7
VSMS (lin.)	$C_{32} = 500$	1767	221.7
VSMS (lin.)	$C_{32} = 1000$	1264	418.3
VSMS (lin.)	$C_{32} = 5000$	573	1942.8
VSRMS	$C_{21} = 0.99$	13051	–

condition number is provided since no linear system of equations needs to be solved. For the analysis with the lumped mass matrix (LMM) 18453 time steps are required. For the variationally scaled reciprocal mass matrix (VSRMS) a maximum speed-up is obtained with constant velocity ansatz functions with $C_{21} = 0.99$. Then, 13501 time steps are required. Thus, the number of time steps is reduced by 27% with approximately equal cost per time step as for the lumped mass matrix. The result of the time history of the tip displacement looks identical for both inertia matrices, see Figure 6.22.

The energy plot is exemplarily presented for the reciprocal mass matrix in Figure 6.21. The total energy is constant since no external force is applied. Initially, all energy is in the kinetic energy due to the initial condition. Then the energy is transferred to the internal energy and the velocity is reduced. When all energy is transferred into deformation, the beam is at its position of rest and the deformation decreases again. The second and third peak of the kinetic energy are reduced due to the plastic deformation. The hourglass energy is at maximum around 10^{-4} J and is thus less than 0.1% of the total energy. For moderate speed-ups the energy plot looks identical for

all inertia matrices. For larger speed-ups, the variationally or algebraically scaled mass

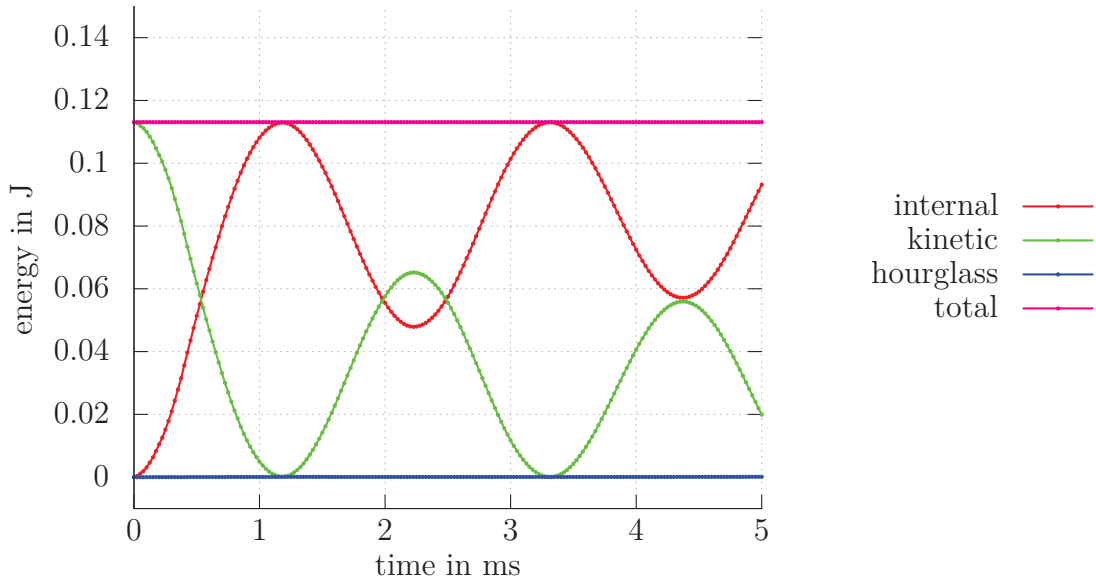


Figure 6.21: Energy history for the variationally scaled reciprocal mass matrix (VS-RMS).

matrices (VSMS or ASMS) need to be used. For these matrices, a linear system of equations has to be solved in every time step and therefore, each time step is more expensive than for the lumped mass matrix or the reciprocal mass matrix. In Figure 6.22, the results of the time history for different scaled mass matrices are compared with the results for the lumped and reciprocal mass matrix for a moderate speed-up. With around 5000 time steps, the scaled mass matrices show the same results as the lumped mass matrix and the reciprocal mass matrix. The condition number of the algebraically scaled mass matrix and the variationally scaled mass matrix with constant velocity ansatz functions are similar. For the variationally scaled mass matrix with linear velocity ansatz functions, the condition number is slightly larger. Next, the methods are compared for higher speed-ups. With increasing speed-up, the condition number of the mass matrices increases. Therefore a saturation may occur, which means that even though the time step size is further increased, the computation time is not reduced due to higher cost per time step. It is not possible to evaluate the actual computation time in the current form of the implementation, therefore only the required number of time steps and the condition numbers are analyzed. Higher scaling factors for the algebraically scaled mass matrix (ASMS) lead to significant deviations in the result, as it can be seen from Figure 6.23.

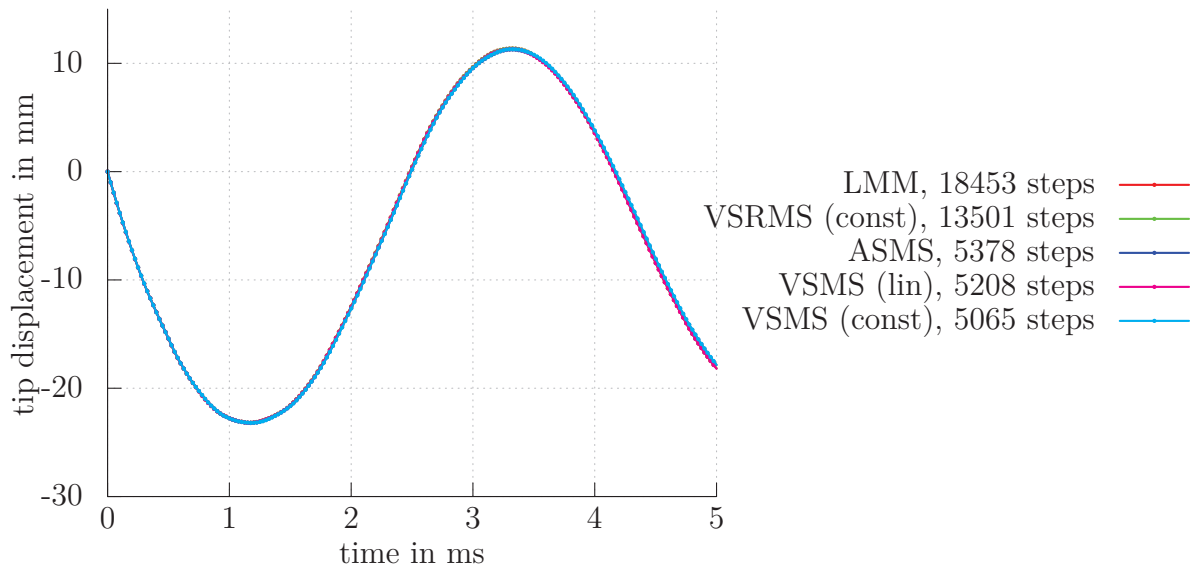


Figure 6.22: Tip displacement history for different methods for a moderate speed-up.

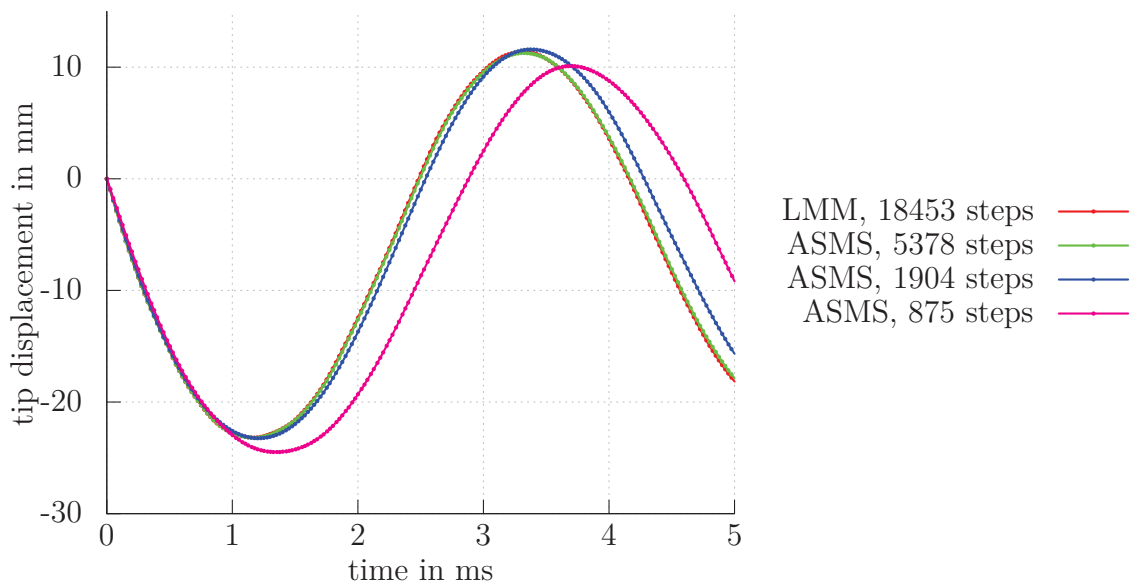


Figure 6.23: Tip displacement history for the algebraically scaled mass matrix (ASMS) for moderate to large speed-ups.

With 5378 steps a very accurate result is obtained. With a larger time step size and thus only 1904 steps, a significant phase error is observed. This phase error increases with increasing scaling factor (and increasing time step size).

Similar (or even worse) results are obtained with the variationally scaled mass matrix with constant velocity ansatz space (VSMS (const.)). With 563 time steps, both the phase error and the deviation in the amplitude are significant.

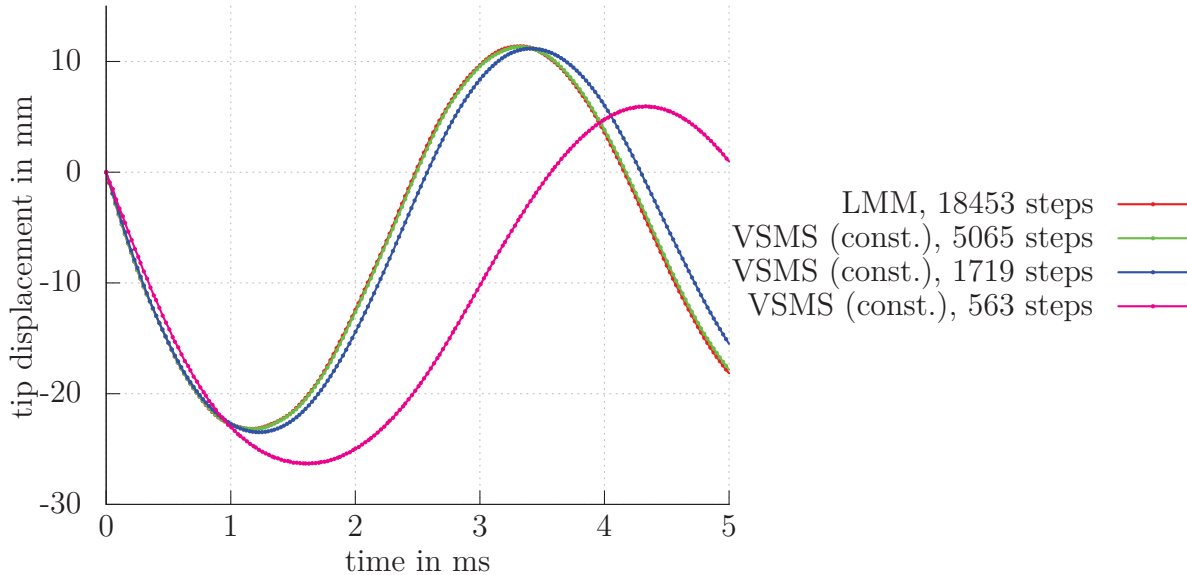


Figure 6.24: Tip displacement history for the variationally scaled mass matrix with constant velocity ansatz functions (VSMS, const.) for moderate to large speed-ups.

Last, the variationally scaled mass matrix with linear velocity ansatz space is investigated. Only with the variationally scaled mass matrix with linear velocity ansatz functions very accurate results can be obtained, even when the scaling factor is increased to 6.25 to compute with only 573 time steps. However, the computation with linear velocity ansatz space becomes unstable for large rotations, if the mass matrix is not updated during simulation. While in geometrically linear analyses the initial element geometry is used in the ansatz function matrix from eq. (4.1) to (4.5) and the matrix is constant, it needs to be updated for large rotations. Whether an update is necessary or not does not only depend on the rotation angle of the element, but also on the inertia scaling factor. The required time interval for the update of the mass matrix is documented in Table 6.6. It is observed that for larger scaling factors the update needs to be performed more often. While the variationally scaled mass matrix with constant velocity ansatz functions performs similar to the algebraically scaled mass matrix, the variationally scaled mass matrix with linear velocity ansatz functions performs significantly better for large speed-ups. For moderate speed-ups, all methods perform equally well. The main disadvantage of the reciprocal mass matrix is the limited speed-up for stability reasons.

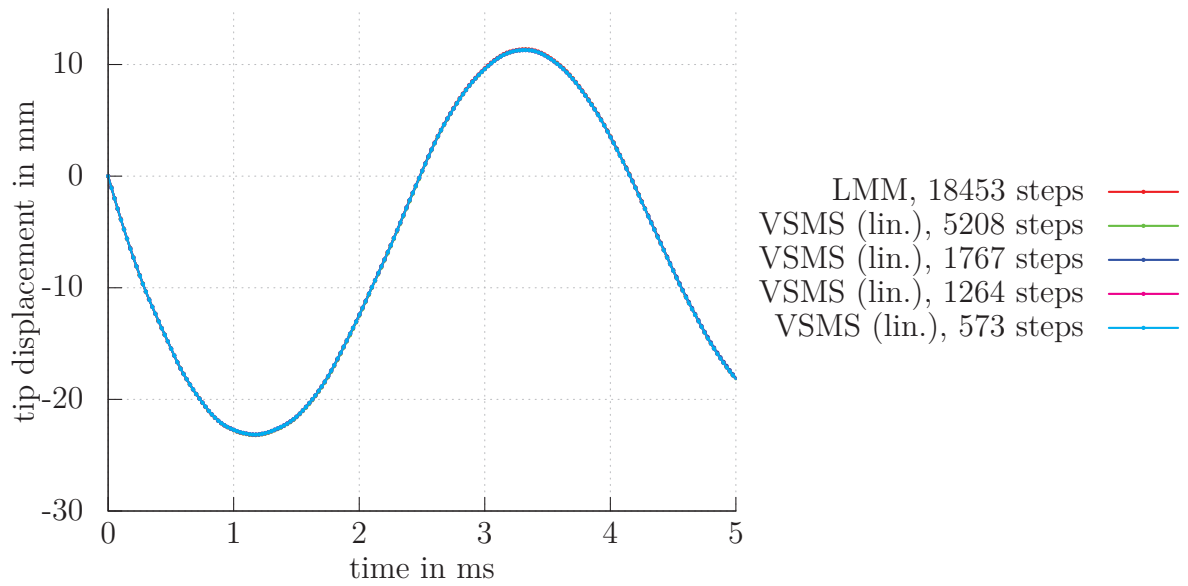


Figure 6.25: Tip displacement history for the variationally scaled mass matrix with linear velocity ansatz functions (VSMS, lin.) for moderate to large speed-ups.

Table 6.6: Required time interval for the mass update for the variationally scaled mass matrix with linear velocity ansatz space (VSMS,lin.).

	VSMS, $C_{21} = 50$	$C_{21} = 500$	$C_{21} = 1000$	$C_{21} = 5000$
time interval Δt_{update} for mass update in ms	0.1	0.1	0.1	0.01

It is worth noting that although the tip displacement for the variationally scaled mass matrix with large scaling factors looks identical to the tip displacement with lumped mass matrix, the energy history looks quite different to the original one presented in Figure 6.21. The energy history for the variationally scaled mass matrix with linear velocity ansatz functions (VSMS, lin.) with 573 steps is illustrated in Figure 6.26. Although the total energy is preserved with some oscillations, the total energy is different than in the original setup. This may be explained by the complicated initial condition. Since only the translational inertia is preserved with the linear velocity ansatz functions a quadratic initial velocity distribution may result in different initial kinetic energies for different inertia matrices. For moderate scaling factors, the introduced kinetic energy is similar, but for large scaling factors the difference is about 24%. However, this additional energy activates only very high modes leading to local oscillations, but does not influence the overall deformation of the beam. This artifact has to be further analyzed in future studies.

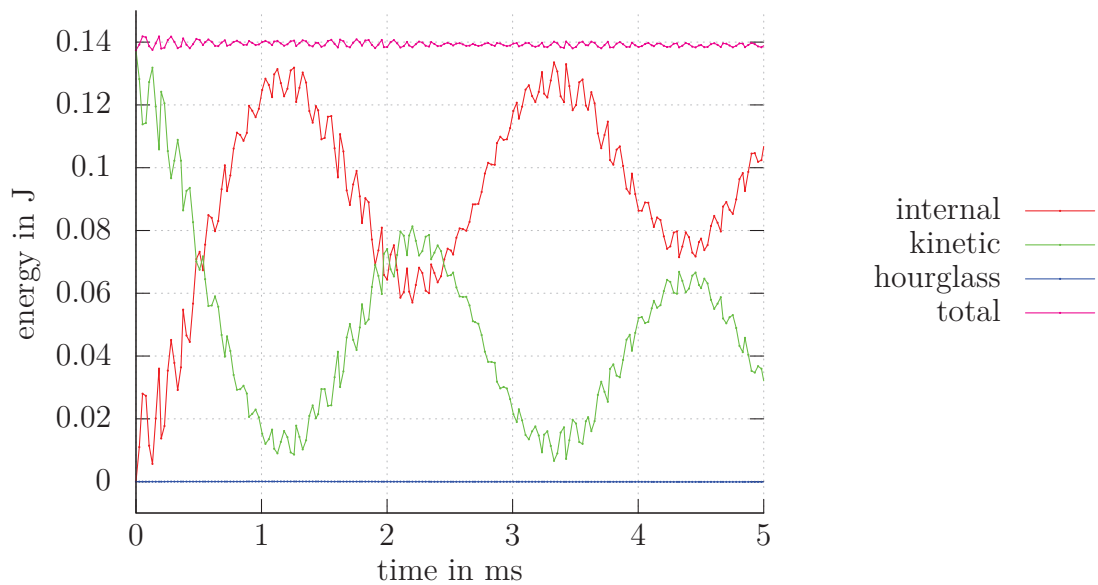


Figure 6.26: Energy history for the variationally scaled mass matrix (VSMS, lin.) with high speed-up (573 steps).

6.7 A brief summary of Chapter 6

In Chapter 6 various numerical examples were considered to support the findings from the previous chapters.

First, a linear transient analysis of a 3-D cantilever beam was considered as an introductory example. The speed-up and accuracy for different load cases, finite element discretizations, inertia matrices and different choice of ansatz spaces were compared. It is shown that for simple load cases very large speed-ups are possible with the variationally scaled mass matrix. For more complicated load cases where higher modes participate, very large speed-ups deteriorate the accuracy. Especially for higher order finite elements more accurate results can be obtained with the variationally scaled mass matrix than with algebraic approaches, but then higher order ansatz spaces for the velocity are required. The speed-up for the variationally scaled reciprocal mass matrix is limited by stability issues. Therefore, the sum of scaling factors needs to be chosen smaller than 1. For higher order finite elements larger speed-ups in the time step size are possible than for linear finite elements.

Second, an eigenfrequency analysis of a 2-D tapered structure was performed. Although a bounded structure, discretized with NURBS finite elements was considered, the determined scaling factors for optimal low-frequency accuracy from the 2-D grid dispersion analysis of an infinite quadratic B-Spline patch provided very good results. With the

optimal scaling factors higher accuracy than with the lumped mass matrix and higher accuracy than with the consistent mass matrix were obtained for the first 30% of the modes. The time step size is larger than for the consistent mass matrix (however, each time step is much cheaper), but smaller than for the lumped mass matrix. The accuracy in the lowest modes deteriorates rapidly with small changes on the optimal values of the scaling factors. This confirms the optimality of the result. With a parameter set for good accuracy and good speed-up a slightly higher accuracy in the lowest modes with a 25% larger time step size than for the lumped mass matrix is obtained.

Third, a linear transient analysis was performed with the tapered plate from the previous example. Although the free parameters were obtained from a grid dispersion analysis, which takes only the spatial and not the temporal discretization into account, very accurate results were obtained in the transient analysis. The relative error in the tip displacement is even smaller for the reciprocal mass matrix, with good accuracy and speed-up, than for the consistent mass matrix. The reason is that mainly the first mode is activated in this simple load case and for this mode the eigenfrequency is more precisely represented by the reciprocal mass matrix.

In the fourth example a two-material 2-D tapered structure was considered. Both an eigenvalue analysis and a convergence study were performed. While the original formulation leads to an average error in the first six eigenfrequencies of 8%, the error for the novel formulation is only 2%. In a convergence study it is shown that the first eigenfrequencies converge only very poorly with the original formulation. However, with the novel ansatz spaces, a convergence order of three is observed. Thus, the improved behaviour of the novel formulation for problems with non-constant density distribution is confirmed.

In the fifth example, the proposed time step estimates from Chapter 5 was tested for a 2-D highly distorted mesh with penalty contact. It is shown that the proposed estimate provides good results also in 2-D and for distorted meshes and that the obtained result is always conservative, independent of the penalty stiffness.

In the last example, a transient analysis of a cantilever beam was considered. Material and geometric nonlinearities were taken into account. With the reciprocal mass matrix a moderate speed-up of at most 27% is possible. For a moderate speed-up, all investigated inertia matrices show very accurate results. For larger speed-ups, the algebraically scaled mass matrix and the variationally scaled mass matrix with constant velocity ansatz functions show a significant phase error in the displacement history. Only with the variationally scaled mass matrix with linear velocity ansatz functions an accurate result is obtained for moderate to large speed-ups (up to factor 22). However, since the element geometry is taken into account in the linear ansatz function matrix, the mass matrix needs to be updated during the nonlinear analysis. The required time interval

for the update depends on the scaling factor. With larger scaling factors the update needs to be performed more often. Additionally, it is observed that for the complicated initial condition that is applied, the total energy in the system is significantly different for different inertia matrices for large speed-ups. The reason is that the matrices do not preserve inertia for the complicated prescribed initial velocity. However, the difference in the total energy has no influence on the overall deformation. It induces only small shock waves propagating in the structure which do not have an influence on the overall deformation.

Summary and Future Work

In this work, variationally consistent inertia templates for speed-up and customization in explicit dynamics were presented. The following two sections summarize the findings of this work and indicate open issues for further research.

7.1 Summary

In Chapter 3 the focus was on the variational consistency of the formulation. It was shown that the original formulation presented in TKACHUK AND BISCHOFF (2015) is only consistent for constant density throughout the domain. For non-constant density, a modification of the construction of the biorthogonal basis is necessary and was proposed herein. In contrast to the original construction scheme, the density is now taken into account in different steps of the construction of the biorthogonal basis (see eq. (3.48) to (3.50)). Only if the density is taken into account in all construction steps, the formulation is consistent for higher order density distributions and consequently passes the corresponding patch test. The investigated formulation and the proposed ansatz spaces for consistency are applicable and valid for a wide range of solid elements with translational degrees of freedom. The verification was performed for a patch of distorted serendipity finite elements with non-constant density distribution (Section 3.6.3). Additionally, the consideration of displacement boundary conditions by elimination and multi-point constraints was formulated in a general way for solid elements with reciprocal mass matrices. The improved behaviour of the formulation with the novel construction of the biorthogonal basis was confirmed in an eigenvalue analysis and a convergence study of a two-material 2-D tapered structure.

While Chapter 3 focused on the consistency of the formulation, Chapter 4 discussed a systematic enrichment of the ansatz space to tune the inertia template to user-specific

customization goals. The systematic enrichment is based on the introduction of a novel multi-parametric template, allowing to combine various possible velocity ansatz spaces with different customization parameters. By means of grid dispersion analyses the desired customization parameters of the formulation for optimal low frequency accuracy, high speed-up or other customization goals were determined. This systematic approach allows both the reconstruction of existing algebraic higher order mass matrices from literature in the context of a variational setup, as well as the development of novel accurate and efficient reciprocal mass matrices. The inertia customization was mainly performed on the example of 1-D and 2-D quadratic and cubic B-spline patches. Optimal parameters for higher order accurate variationally constructed mass and reciprocal mass matrices were determined. For quadratic B-splines sixth order accurate inertia matrices were constructed. For cubic B-splines 8th order accurate matrices were obtained. The variationally scaled mass matrix is identical to the higher order mass proposed algebraically by WANG ET AL. (2013). The novel reciprocal mass matrix is a promising alternative to the row-sum lumped mass matrix, which is only second order accurate independent of the polynomial order. The performance of the inertia matrices obtained by customization and the optimality of the determined parameter sets was confirmed in an eigenvalue analysis and a transient analysis of a 2-D tapered structure, discretized with quadratic NURBS finite elements.

Novel time step estimates for reciprocal mass matrices were proposed in Chapter 5. First, the characteristics of reciprocal mass matrices were highlighted and it was shown that the maximum eigenfrequency of the global system is not conservatively bound by the maximum eigenfrequency of all elements as it is the case for consistent and lumped mass matrices and stated by the eigenvalue inequality of FRIED (1972). Then, the nodal time step estimate of KULAK (1989) for lumped mass matrices, which is based on Gershgorin's theorem, was systematically extended for reciprocal mass matrices and penalty contact. Three different possible estimates were proposed, namely a row-wise, a column-wise and a symmetric Gershgorin estimate for reciprocal mass matrices. All three estimates provided conservative results for regular and distorted meshes, for problems with and without penalty contact. The performance of all three estimates regarding efficiency and conservativeness was observed to be similar, therefore there is no clear winner. However, the row-wise estimate showed small advantages in the amount of data to be stored for contact problems, therefore the possible rearrangements to improve efficiency were shown on the row-wise estimate. The rearrangements serve for problems where the nonlinearity results mainly from contact. Then, the reciprocal mass matrix and the stiffness matrix remain constant throughout the simulation and only the contact stiffness needs to be updated in case of a changing contact set. Exploitation of different upper bounds for matrix norms allows a reduction of the computational effort to obtain the critical time step. The novel time step estimate works independently of the element

type used in the finite element discretization and it is applicable to different reciprocal mass matrices.

7.2 Future Work

While for variationally selectively scaled mass matrices and algebraically scaled mass matrices from literature the critical time step can be increased arbitrarily (of course with decreasing accuracy), the increase of the time step for reciprocal mass matrices is limited for stability reasons. In order to shift this limit to higher values, a clustering of elements can be investigated in the future, so that the reciprocal mass matrices are not obtained by assembly from the element level but from the clustering level. In this way, the sparsity of the matrix is slightly deteriorated, but an increase of the speed-up is obtained. However, if a speed-up of factor 10 or more is desired, the scaled, non-diagonal mass matrices remain the only option.

In this work the possibilities of inertia customization were illustrated on the example of NURBS and B-spline finite elements. In order to obtain the optimal set of scaling factors for optimal low-frequency accuracy for different finite element types, each finite element type needs to be investigated in an analytical grid dispersion analysis of an infinite patch. Especially for 3-D finite elements, this procedure is cumbersome and analytical relations are not always possible to obtain. To what extent the obtained results are helpful for the analysis of more complicated geometries and load cases is as well questionable and needs to be further analyzed in the future. In this work only grid dispersion analyses were performed to tune the inertia templates for specific customization goals. Although customization was performed on a regular infinite grid, very accurate results were obtained for bounded and moderately distorted meshes with these parameter sets. However, a full dispersion analysis could be part of future research in order to find optimal inertia matrices with respect to space and time discretization.

The efficiency of the proposed time step estimate for reciprocal mass matrices can so far only be confirmed by a simple FLOP estimate. A comparison of the real computation time is desired, but requires an efficient (or at least similarly efficient) implementation of all estimates. Additionally, the conservativeness of the proposed nodal time step estimate was only compared with the conservativeness of a nodal estimate for the lumped mass matrix. Since mainly elemental estimates are used for the lumped mass matrix in practice, a nodal estimate for the reciprocal mass matrix and an elemental one for the lumped mass matrix should be compared. Furthermore, the evaluation of the physical speed-up in terms of computation time for the variationally scaled mass matrix is desired. For the reciprocal mass matrix one time step is computationally similarly expensive than

for the lumped mass matrix. Therefore, the ratio between the time step sizes is a direct indicator for the physical speed-up. For variationally scaled mass matrices the speed-up depends additionally on the overhead for the solution of a linear system of equations. Therefore, the condition number of the mass matrix, as well as the ratio of the time step sizes was provided herein in order to evaluate the speed-up. However, in order to determine the speed-up in terms of computation time the ratio between the element processing time and the time for the solution of a linear system of equations is required.

The proposed time step estimate for reciprocal mass matrices relies on the assembled stiffness matrix and may therefore not be attractive for a commercial implementation in its present form since the stiffness matrix is usually not required in an explicit analysis. However, the time step estimate requires actually only nodal information and can therefore as well be implemented on a local level. Moreover, using the initial stiffness matrix may be inadequate for problems involving large deformations. Then, a cheap and conservative approximation of the stiffness matrix at large deformations is required. Furthermore, the efficiency of the time step estimate may be increased by preselecting nodes that will drive the critical time step and computing the critical time step only at such nodes. These nodes are expected to belong to zones with a high penalty scale factor, fine mesh or stiff material.

In this work, the construction of the biorthogonal basis and the modification of the basis in case of Dirichlet boundary conditions for variationally scaled reciprocal mass matrices was discussed for various finite element types. However, the present work deals only with solid finite element formulations with translational degrees of freedom. An extension to shell finite element formulations is of high interest. Beside the extension to classical shell formulations, the transfer of selective mass scaling methods to hierarchical shell formulations of OESTERLE ET AL. (2017) is nearby and promising. In the locking-free hierarchic shell formulation the shear and bending deformation are totally decoupled. Thus, the formulation is an appropriate starting point for selective mass scaling with the aim to reduce the eigenfrequency of the shear modes without deteriorating the accuracy of the bending modes. Initial results on this topic were recently presented by KOOHI AND BISCHOFF (2018) and are to be pursued in the future.

With the present work, the idea of variationally scaled mass and reciprocal mass matrices was further developed towards practical applicability. The achieved advancements are the extension to contact problems, the proposal of a time step estimate for reciprocal mass matrices and the improvement of the formulation for heterogeneous material and reciprocal mass matrices. In the future, a more intensive analysis for geometrically nonlinear problems is required. The last example of the present work provided already preliminary results, but further studies are to be performed. Furthermore, all considered examples were rather academic with simple geometries and simple load cases to evaluate

individual effects. In the future, more complicated problem setups are to be studied in order to evaluate the applicability of the approach to practical problems and in order to compare the performance with existing approaches. Only if the novel matrices provide larger speed-ups than existing mass scaling methods or significantly more accurate results for various practically relevant problem setups, they will make their way into commercial codes and practical applications.

As a last recommendation, the author suggests to indicate open issues for future research in this field not only from methodological possibilities, but from practical problems where existing approaches reach their limits. These experiences can then be used for the determination of research goals which are pursued on a sound scientific and theoretical level. Otherwise the approach remains a nice methodological scientific idea with unexploited potential in practical applications.

Bibliography

ARGYRIS AND SCHARPF 1969

ARGYRIS, J. H. ; SCHARPF, D. W.: Finite elements in time and space. In: *The Aeronautical Journal* 73 (1969), No. 708, p. 1041–1044

BATHE 1982

BATHE, K.-J.: *Finite element procedures in engineering analysis*. Englewoods Cliffs, New Jersey : Prentice-Hall, 1982

BELYTSCHKO AND BINDEMAN 1991

BELYTSCHKO, T. ; BINDEMAN, L. P.: Assumed strain stabilization of the 4-node quadrilateral with 1-point quadrature for nonlinear problems. In: *Computer Methods in Applied Mechanics and Engineering* 88 (1991), No. 3, p. 311–340

BELYTSCHKO AND HUGHES 1983

BELYTSCHKO, T. (Editor) ; HUGHES, T. J. R. (Editor): *Computational methods for transient analysis*. Amsterdam : North-Holland, 1983

BELYTSCHKO ET AL. 2014

BELYTSCHKO, T. ; LIU, W. K. ; MORAN, B. ; ELKHODARY, K. I.: *Nonlinear finite elements for continua and structures*. 2nd ed. Chichester, West Sussex, United Kingdom : Wiley, 2014

BELYTSCHKO AND MULLEN 1978

BELYTSCHKO, T. ; MULLEN, R.: On dispersive properties of finite element solutions. In: *Modern problems in elastic wave propagation* (1978), p. 67–82

BELYTSCHKO AND NEAL 1991

BELYTSCHKO, T. ; NEAL, M. O.: Contact-impact by the pinball algorithm with penalty and Lagrangian methods. In: *International Journal for Numerical Methods in Engineering* 31 (1991), No. 3, p. 547–572

BERGAN 1980

BERGAN, P. G.: Finite elements based on energy orthogonal functions. In: *International Journal for Numerical Methods in Engineering* 15 (1980), No. 10, p. 1541–1555

BERGAN AND FELIPPA 1985

BERGAN, P. G. ; FELIPPA, C. A.: A triangular membrane element with rotational degrees of freedom. In: *Computer Methods in Applied Mechanics and Engineering* 50 (1985), No. 1, p. 25–69

BERGAN AND HANSSSEN 1975

BERGAN, P. G. ; HANSSSEN, L.: A new approach for deriving ‘good’ finite elements. In: *The Mathematics of Finite Elements and Applications 2* (1975), p. 483–498

BERGAN AND NYGÅRD 1984

BERGAN, P. G. ; NYGÅRD, M. K.: Finite elements with increased freedom in choosing shape functions. In: *International Journal for Numerical Methods in Engineering* 20 (1984), No. 4, p. 643–663

BONSIGNORE 2017

BONSIGNORE, licence: CC BY 2.0 (.: *Crimped Strain, Closeup, Simulation of a generic superelastic nitinol stent*. 2017. – URL <https://www.flickr.com/photos/confluent/32489704865>. – [Online; accessed June, 2018]

BORRVALL 2011

BORRVALL, T.: *Selective Mass Scaling (SMS), Theory and Practice*. presentation at LS-DYNA Entwicklerforum, October 12th 2011. 2011

BRIVADIS ET AL. 2014

BRIVADIS, E. ; BUFFA, A. ; WOHLMUTH, B. I. ; WUNDERLICH, L.: Isogeometric mortar methods. In: *Computer Methods in Applied Mechanics and Engineering* 284 (2014)

CANNAROZZI AND MANCUSO 1995

CANNAROZZI, M. ; MANCUSO, M.: Formulation and analysis of variational methods for time integration of linear elastodynamics. In: *Computer Methods in Applied Mechanics and Engineering* 127 (1995), No. 1-4, p. 241–257

CARPENTER ET AL. 1991

CARPENTER, N. J. ; TAYLOR, R. L. ; KATONA, M. G.: Lagrange constraints for transient finite element surface contact. In: *International Journal for Numerical Methods in Engineering* 32 (1991), No. 1, p. 103–128

CHAN AND EVANS 2018

CHAN, J. ; EVANS, J. A.: Multi-patch discontinuous Galerkin isogeometric analysis

for wave propagation: Explicit time-stepping and efficient mass matrix inversion. In: *Computer Methods in Applied Mechanics and Engineering* 333 (2018), p. 22–54

COCCHETTI ET AL. 2013

COCCHETTI, G. ; PAGANI, M. ; PEREGO, U.: Selective mass scaling and critical time-step estimate for explicit dynamics analyses with solid-shell elements. In: *Computers & Structures* 127 (2013), p. 39–52

COCCHETTI ET AL. 2015

COCCHETTI, G. ; PAGANI, M. ; PEREGO, U.: Selective mass scaling for distorted solid-shell elements in explicit dynamics: optimal scaling factor and stable time step estimate. In: *International Journal for Numerical Methods in Engineering* 101 (2015), No. 9, p. 700–731

CONFALONIERI ET AL. 2015

CONFALONIERI, F. ; GHISI, A. ; PEREGO, U.: 8-Node solid-shell elements selective mass scaling for explicit dynamic analysis of layered thin-walled structures. In: *Computational Mechanics* 56 (2015), No. 4, p. 585–599

CONFALONIERI ET AL. 2018

CONFALONIERI, F. ; GHISI, A. ; PEREGO, U.: Blade cutting of thin walled structures by explicit dynamics finite elements. In: *Meccanica* 53 (2018), No. 6, p. 1271–1289

COOK ET AL. 1989

COOK, R. D. ; MALKUS, D. S. ; PLESHA, M. E.: *Concepts and applications of finite element analysis*. 3. ed. New York : Wiley, 1989

COTTRELL ET AL. 2007

COTTRELL, J. A. ; HUGHES, T. J. R. ; REALI, A.: Studies of refinement and continuity in isogeometric structural analysis. In: *Computer Methods in Applied Mechanics and Engineering* 196 (2007), No. 41-44, p. 4160–4183

COTTRELL ET AL. 2006

COTTRELL, J. A. ; REALI, A. ; BAZILEVS, Y. ; HUGHES, T. J. R.: Isogeometric analysis of structural vibrations. In: *Computer Methods in Applied Mechanics and Engineering* 195 (2006), No. 41-43, p. 5257–5296

COTTRELL 2009

COTTRELL, J. A.: *Isogeometric analysis: toward integration of CAD and FEA*. Chichester, West Sussex, U.K. ; Hoboken, NJ : Wiley, 2009

COURANT ET AL. 1928

COURANT, R. ; FRIEDRICHS, K. ; LEWY, H.: Über die partiellen Differenzen-

gleichungen der mathematischen Physik. In: *Mathematische Annalen* 100 (1928), No. 1, p. 32–74

DEDÈ ET AL. 2015

DEDÈ, L. ; JÄGGLI, C. ; QUARTERONI, A.: Isogeometric numerical dispersion analysis for two-dimensional elastic wave propagation. In: *Computer Methods in Applied Mechanics and Engineering* 284 (2015), p. 320–348

DORNISCH ET AL. 2017

DORNISCH, W. ; STÖCKLER, J. ; MÜLLER, R.: Dual and approximate dual basis functions for B-splines and NURBS—Comparison and application for an efficient coupling of patches with the isogeometric mortar method. In: *Computer Methods in Applied Mechanics and Engineering* 316 (2017), p. 449–496

FELIPPA 1994

FELIPPA, C. A.: A survey of parametrized variational principles and applications to computational mechanics. In: *Computer Methods in Applied Mechanics and Engineering* 113 (1994), No. 1–2, p. 109–139

FELIPPA 2001A

FELIPPA, C. A.: Customizing high performance elements by Fourier methods. In: *Trends in computational mechanics, ed. by W. A. Wall et al.* (2001), p. 283–296

FELIPPA 2001B

FELIPPA, C. A.: Customizing the mass and geometric stiffness of plane beam elements by Fourier methods. In: *Engineering Computations* 18 (2001), No. 1/2, p. 286–303

FELIPPA 2004

FELIPPA, C. A.: A template tutorial. In: *Computational Mechanics: Theory and Practice, Chapter 3* (2004), p. 29–66

FELIPPA 2013A

FELIPPA, C. A.: *Mass Matrix Construction Overview, from Part V: Mass Matrices of Lecture Notes of the Course Matrix Finite Element Methods in Dynamics.* online. 2013

FELIPPA 2013B

FELIPPA, C. A.: *Mass Matrix Diagonalization, Appendix D of Lecture Notes of the Course Matrix Finite Element Methods in Dynamics.* online. 2013

FELIPPA 2013C

FELIPPA, C. A.: *Mass Templates for Bar2 Elements, Chapter 22 of Lecture Notes of the Course Matrix Finite Element Methods in Dynamics.* online. 2013

FELIPPA ET AL. 2015

FELIPPA, C. A. ; GUO, Q. ; PARK, K. C.: Mass matrix templates: general description and 1D examples. In: *Archives of Computational Methods in Engineering* 22 (2015), No. 1, p. 1–65

FELIPPA AND MILITELLO 1992

FELIPPA, C. A. ; MILITELLO, C.: Membrane triangles with corner drilling freedoms—II. The ANDES element. In: *Finite Elements in Analysis and Design* 12 (1992), No. 3-4, p. 189–201

FLANAGAN AND BELYTSCHKO 1984

FLANAGAN, D. P. ; BELYTSCHKO, T.: Eigenvalues and Stable Time Steps for the Uniform Strain Hexahedron and Quadrilateral. In: *Journal of Applied Mechanics* 51 (1984), No. 1, p. 35–40

FRIED 1969

FRIED, I.: Finite-element analysis of time-dependent phenomena. In: *AIAA Journal* 7 (1969), No. 6, p. 1170–1173

FRIED 1972

FRIED, I.: Bounds on the extremal eigenvalues of the finite element stiffness and mass matrices and their spectral condition number. In: *Journal of Sound and Vibration* 22 (1972), No. 4, p. 407–418

FRIED AND MALKUS 1975

FRIED, I. ; MALKUS, D. S.: Finite element mass matrix lumping by numerical integration with no convergence rate loss. In: *International Journal of Solids and Structures* 11 (1975), No. 4, p. 461–466

GAO AND CALO 2014

GAO, L. ; CALO, V. M.: Fast isogeometric solvers for explicit dynamics. In: *Computer Methods in Applied Mechanics and Engineering* 274 (2014), p. 19–41

GERŠGORIN 1931

GERŠGORIN, S.: Über die Abgrenzung der Eigenwerte einer Matrix. In: *Bulletin de l'Académie des Sciences de l'URSS. Classe des sciences mathématiques et na* no. 6 (1931), p. 749–754

GLEIM AND KUHL 2013

GLEIM, T. ; KUHL, D.: Higher order accurate discontinuous and continuous p-Galerkin methods for linear elastodynamics. In: *ZAMM-Journal of Applied Mathematics and Mechanics/Zeitschrift für Angewandte Mathematik und Mechanik* 93 (2013), No. 2-3, p. 177–194

GONZÁLEZ ET AL. 2018A

GONZÁLEZ, J. A. ; KOLMAN, R. ; CHO, S. S. ; FELIPPA, C. A. ; PARK, K. C.: Inverse mass matrix via the method of localized Lagrange multipliers. In: *International Journal for Numerical Methods in Engineering* 113 (2018), No. 2, p. 277–295

GONZÁLEZ ET AL. 2018B

GONZÁLEZ, J. A. ; KOPAČKA, J. ; KOLMAN, R. ; CHO, S. S. ; PARK, K. C.: *Variational Derivation of Reciprocal Mass Matrices for Isogeometrical Analysis via Localized Lagrange Multipliers*. WCCM XIII - The 13th World Congress on Computational Mechanics, NYC, July 22-27. 2018

GROSSEHOLZ ET AL. 2015

GROSSEHOLZ, G. ; SOARES, D. ; ESTORFF, O.: A stabilized central difference scheme for dynamic analysis. In: *International Journal for Numerical Methods in Engineering* 102 (2015), No. 11, p. 1750–1760

HALLQUIST 2006

HALLQUIST, J. O.: *LS-DYNA Theory Manual*. 2006

HANUKAH AND GIVLI 2018

HANUKAH, E. ; GIVLI, S.: Improving mass matrix and inverse mass matrix computations of hexahedral elements. In: *Finite Elements in Analysis and Design* 144 (2018), p. 1–14

HARTMANN AND BENSON 2014

HARTMANN, S. ; BENSON, D. J.: Mass scaling and stable time step estimates for isogeometric analysis. In: *International Journal for Numerical Methods in Engineering* (2014), p. 671–687

HILBER ET AL. 1977

HILBER, H. M. ; HUGHES, T. J. R. ; TAYLOR, R. L.: Improved numerical dissipation for time integration algorithms in structural dynamics. In: *Earthquake Engineering & Structural Dynamics* 5 (1977), No. 3, p. 283–292

HINTON ET AL. 1976

HINTON, E. ; ROCK, T. ; ZIENKIEWICZ, O. C.: A note on mass lumping and related processes in the finite element method. In: *Earthquake Engineering & Structural Dynamics* 4 (1976), No. 3, p. 245–249

HOLZAPFEL 2010

HOLZAPFEL, G. A.: *Nonlinear solid mechanics: a continuum approach for engineering*. Chichester, Weinheim : Wiley, 2010

HUGHES 2000

HUGHES, T. J. R.: *The finite element method: linear static and dynamic finite element analysis*. Mineola, NY : Dover Publications, 2000

HUGHES ET AL. 2005

HUGHES, T. J. R. ; COTTRELL, J. A. ; BAZILEVS, Y.: Isogeometric analysis: CAD, finite elements, NURBS, exact geometry and mesh refinement. In: *Computer Methods in Applied Mechanics and Engineering* 194 (2005), No. 39–41, p. 4135–4195

HUGHES ET AL. 1976

HUGHES, T. J. R. ; HILBER, H. M. ; TAYLOR, R. L.: A reduction scheme for problems of structural dynamics. In: *International Journal of Solids and Structures* 12 (1976), No. 11, p. 749–767

HUGHES ET AL. 2008

HUGHES, T. J. R. ; REALI, A. ; SANGALLI, G.: Duality and unified analysis of discrete approximations in structural dynamics and wave propagation: Comparison of p-method finite elements with k-method NURBS. In: *Computer Methods in Applied Mechanics and Engineering* 197 (2008), No. 49-50, p. 4104–4124

HULBERT 2017

HULBERT, G. M.: Computational structural dynamics. In: *Encyclopedia of Computational Mechanics, 2nd ed.* (2017), p. 1–25

IDESMAN 2017

IDESMAN, A.: Optimal reduction of numerical dispersion for wave propagation problems. Part 1: Application to 1-D isogeometric elements. In: *Computer Methods in Applied Mechanics and Engineering* 317 (2017), p. 970–992

JOHNSON ET AL. 1984

JOHNSON, C. ; NÄVERT, U. ; PITKÄRANTA, J.: Finite element methods for linear hyperbolic problems. In: *Computer Methods in Applied Mechanics and Engineering* 45 (1984), No. 1-3, p. 285–312

KOLMAN ET AL. 2016

KOLMAN, R. ; PLEŠEK, J. ; ČERV, J. ; OKROUHLÍK, M. ; PAŘÍK, P.: Temporal-spatial dispersion and stability analysis of finite element method in explicit elastodynamics. In: *International Journal for Numerical Methods in Engineering* 106 (2016), No. 2, p. 113–128

KOLMAN ET AL. 2013

KOLMAN, R. ; PLESEK, J. ; OKROUHLÍK, M. ; GABRIEL, D.: Grid dispersion

analysis of plane square biquadratic serendipity finite elements in transient elastodynamics. In: *International Journal for Numerical Methods in Engineering* 96 (2013), No. 1, p. 1–28

KOOHI AND BISCHOFF 2018

KOOHI, L. ; BISCHOFF, M.: *Mass scaling for hierarchic shear deformable, rotation-free Timoshenko beam elements*. ECCM 6, European Conference on Computational Mechanics. 2018

KRENK 2001

KRENK, S.: Dispersion-corrected explicit integration of the wave equation. In: *Computer Methods in Applied Mechanics and Engineering* 191 (2001), No. 8-10, p. 975–987

KRIEG AND KEY 1973

KRIEG, R. D. ; KEY, S. W.: Transient shell response by numerical time integration. In: *International Journal for Numerical Methods in Engineering* 7 (1973), No. 3, p. 273–286

KUHL AND CRISFIELD 1999

KUHL, D. ; CRISFIELD, M. A.: Energy-conserving and decaying algorithms in non-linear structural dynamics. In: *International journal for numerical methods in engineering* 45 (1999), No. 5, p. 569–599

KUHL AND RAMM 1996

KUHL, D. ; RAMM, E.: Constraint energy momentum algorithm and its application to non-linear dynamics of shells. In: *Computer Methods in Applied Mechanics and Engineering* 136 (1996), No. 3-4, p. 293–315

KUHL AND RAMM 1999

KUHL, D. ; RAMM, E.: Generalized energy–momentum method for non-linear adaptive shell dynamics. In: *Computer Methods in Applied Mechanics and Engineering* 178 (1999), No. 3-4, p. 343–366

KULAK 1989

KULAK, R. F.: Critical time step estimation for three-dimensional explicit analysis. In: BULSON, P. S. (Editor): *Structures under shock and impact*. Amsterdam : Elsevier, 1989, p. 155–163

LAMBERS 2010

LAMBERS, J.: *Lecture notes from Advanced Topics in Numerical Linear Algebra (CME 335)*. 2010

LOMBARDO AND ASKES 2013

LOMBARDO, M. ; ASKES, H.: Lumped mass finite element implementation of continuum theories with micro-inertia. In: *International Journal for Numerical Methods in Engineering* 96 (2013), No. 7, p. 448–466

MACEK AND AUBERT 1995

MACEK, R. W. ; AUBERT, B. H.: A mass penalty technique to control the critical time increment in explicit dynamic finite element analyses. In: *Earthquake engineering & structural dynamics* 24 (1995), No. 10, p. 1315–1331

MACNEAL 1970

MACNEAL, R. H.: *The NASTRAN Theoretical Manual, NASA Report SP-221.*, 1970

MATTERN ET AL. 2015

MATTERN, S. ; SCHMIED, C. ; SCHWEIZERHOF, K.: Highly efficient solid and solid-shell finite elements with mixed strain–displacement assumptions specifically set up for explicit dynamic simulations using symbolic programming. In: *Computers & Structures* 154 (2015), p. 210–225

MURA ET AL. 1992

MURA, T. ; KOYA, T. ; KOURIS, D.: *Variational Methods in Mechanics*. New York : Oxford Univ Pr, 1992

NAFEMS 1990

NAFEMS: *The Standard NAFEMS Benchmarks*. 1990

NEWMARK 1959

NEWMARK, N. M.: A method of computation for structural dynamics. In: *Journal of the engineering mechanics division* 85 (1959), No. 3, p. 67–94

OESTERLE ET AL. 2017

OESTERLE, B. ; SACHSE, R. ; RAMM, E. ; BISCHOFF, M.: Hierarchic isogeometric large rotation shell elements including linearized transverse shear parametrization. In: *Computer Methods in Applied Mechanics and Engineering* 321 (2017), p. 383–405

OLOVSSON AND SIMONSSON 2006

OLOVSSON, L. ; SIMONSSON, K.: Iterative solution technique in selective mass scaling. In: *Communications in Numerical Methods in Engineering* 22 (2006), No. 1, p. 77–82

OLOVSSON ET AL. 2005

OLOVSSON, L. ; SIMONSSON, K. ; UNOSSON, M.: Selective mass scaling for ex-

PLICIT finite element analyses. In: *International Journal for Numerical Methods in Engineering* 63 (2005), No. 10, p. 1436–1445

OLOVSSON ET AL. 2004

OLOVSSON, L. ; UNOSSON, M. ; SIMONSSON, K.: Selective mass scaling for thin walled structures modeled with tri-linear solid elements. In: *Computational Mechanics* 34 (2004), No. 2, p. 134–136

OSWALD AND WOHLMUTH 2001

OSWALD, P. ; WOHLMUTH, B. I.: On Polynomial Reproduction of Dual FE Bases. In: *Thirteenth international conference on domain decomposition methods*, 2001, p. 85–96

PAGANI ET AL. 2014

PAGANI, M. ; REESE, S. ; PEREGO, U.: Computationally efficient explicit nonlinear analyses using reduced integration-based solid-shell finite elements. In: *Computer Methods in Applied Mechanics and Engineering* 268 (2014), p. 141–159

PORTILLO ET AL. 2017

PORTILLO, D. ; POZO, D. del ; RODRÍGUEZ-GALÁN, D. ; SEGURADO, J. ; ROMERO, I.: MUESLI-a Material UnivErSal LIbrary. In: *Advances in Engineering Software* 105 (2017), p. 1–8

PSO 2006

PSO, licence: CC BY-SA 3.0 (<http://creativecommons.org/licenses/by-sa/3.0/>): *Numerical simulation of a vehicle crash*. 2006. – URL https://commons.wikimedia.org/wiki/File:FEM_car_crash1.jpg. – [Online; accessed June, 2018]

REALI 2006

REALI, A.: An isogeometric analysis approach for the study of structural vibrations. In: *Journal of Earthquake Engineering* 10 (2006), p. 1–30

ROBERTSSON ET AL. 2018

ROBERTSSON, K. ; BORGQVIST, E. ; WALLIN, M. ; RISTINMAA, M. ; TRYDING, J. ; GIAMPIERI, A. ; PEREGO, U.: Efficient and accurate simulation of the packaging forming process. In: *Packaging Technology and Science* (2018)

SCHAEUBLE ET AL. 2017

SCHAEUBLE, A.-K. ; TKACHUK, A. ; BISCHOFF, M.: Variationally consistent inertia templates for B-spline-and NURBS-based FEM: Inertia scaling and customization. In: *Computer Methods in Applied Mechanics and Engineering* 326 (2017), p. 596–621

SCHAEUBLE ET AL. 2018

SCHAEUBLE, A.-K. ; TKACHUK, A. ; BISCHOFF, M.: Time step estimates for

explicit dynamics with reciprocal mass matrices. In: *Computers & Structures* 202 (2018), p. 74–84

SCHÄUBLE ET AL. 2014

SCHÄUBLE, A.-K. ; TKACHUK, A. ; BISCHOFF, M.: Variationelle Methoden zur Massenskalierung für eine effizientere explizite Zeitintegration in der Dynamik. In: *Tagung Baustatik-Baupraxis 2014, TU München/Unibw München* (2014), p. 705–713

SCHUMAKER 2007

SCHUMAKER, L.: *Spline functions: basic theory*. Cambridge University Press, 2007

SEITZ ET AL. 2016

SEITZ, A. ; FARAH, P. ; KREMHELLER, J. ; WOHLMUTH, B. I. ; WALL, W. A. ; POPP, A.: Isogeometric dual mortar methods for computational contact mechanics. In: *Computer Methods in Applied Mechanics and Engineering* 301 (2016), p. 259–280

SIMO AND HUGHES 2006

SIMO, J. C. ; HUGHES, T. J. R.: *Computational inelasticity*. Volume 7. Springer Science & Business Media, 2006

SIMO AND TARNOW 1992

SIMO, J. C. ; TARNOW, N.: The discrete energy-momentum method. Conserving algorithms for nonlinear elastodynamics. In: *Zeitschrift für angewandte Mathematik und Physik ZAMP* 43 (1992), No. 5, p. 757–792

SIMO AND TARNOW 1994

SIMO, J. C. ; TARNOW, N.: A new energy and momentum conserving algorithm for the non-linear dynamics of shells. In: *International Journal for Numerical Methods in Engineering* 37 (1994), No. 15, p. 2527–2549

TAYLOR ET AL. 1986

TAYLOR, R. L. ; SIMO, J. C. ; ZIENKIEWICZ, O. C. ; CHAN, A. C. H.: The patch test – a condition for assessing FEM convergence. In: *International Journal for Numerical Methods in Engineering* 22 (1986), No. 1, p. 39–62

TKACHUK 2013

TKACHUK, A.: *Variational methods for consistent singular and scaled mass matrices*. Stuttgart, Institut für Baustatik und Baudynamik der Universität Stuttgart, Ph.D. thesis, 2013

TKACHUK AND BISCHOFF 2013

TKACHUK, A. ; BISCHOFF, M.: Variational methods for selective mass scaling. In: *Computational Mechanics* 52 (2013), No. 3, p. 563–570

TKACHUK AND BISCHOFF 2014

TKACHUK, A. ; BISCHOFF, M.: Local and global strategies for optimal selective mass scaling. In: *Computational Mechanics* 53 (2014), No. 6, p. 1197–1207

TKACHUK AND BISCHOFF 2015

TKACHUK, A. ; BISCHOFF, M.: Direct and sparse construction of consistent inverse mass matrices: general variational formulation and application to selective mass scaling. In: *International Journal for Numerical Methods in Engineering* 101 (2015), No. 6, p. 435–469

WANG ET AL. 2013

WANG, D. ; LIU, W. ; ZHANG, H.: Novel higher order mass matrices for isogeometric structural vibration analysis. In: *Computer Methods in Applied Mechanics and Engineering* 260 (2013), p. 92–108

WASHIZU 1982

WASHIZU, K.: *Variational Methods in Elasticity and Plasticity*. 1982

WOHLMUTH 2002

WOHLMUTH, B. I.: A Comparison of Dual Lagrange Multiplier Spaces for Mortar Finite Element Discretizations. In: *ESAIM: Mathematical Modelling and Numerical Analysis* 36 (2002), No. 06, p. 995–1012

WOŹNY 2013

WOŹNY, P.: Construction of dual bases. In: *Journal of Computational and Applied Mathematics* 245 (2013), p. 75–85

WRIGGERS 2001

WRIGGERS, P.: *Nichtlineare Finite-Element-Methoden*. Berlin, Heidelberg : Springer, 2001

WU AND QIU 2009

WU, S. R. ; QIU, W.: Nonlinear transient dynamic analysis by explicit finite element with iterative consistent mass matrix. In: *International Journal for Numerical Methods in Biomedical Engineering* 25 (2009), No. 3, p. 201–217

YANG ET AL. 2017

YANG, Y. ; ZHENG, H. ; SIVASELVAN, M. V.: A rigorous and unified mass lumping scheme for higher-order elements. In: *Computer Methods in Applied Mechanics and Engineering* 319 (2017), p. 491–514

YE ET AL. 2017

YE, W. ; BEL-BRUNON, A. ; CATHELIN, S. ; ROCHETTE, M. ; COMBESCURE, A.: A selective mass scaling method for shear wave propagation analyses in nearly

incompressible materials. In: *International Journal for Numerical Methods in Engineering* 109 (2017), No. 2, p. 155–173

ZIENKIEWICZ AND TAYLOR 2006

ZIENKIEWICZ, O. C. ; TAYLOR, R. L.: *The finite element method for solid and structural mechanics*. 6. ed. Amsterdam, Heidelberg : Elsevier Butterworth-Heinemann, 2006

Appendix

A Dispersion relation for standard mass matrices for an infinite, uniform 2-D B-spline discretization

The dispersion relation of an infinite, uniform, quadratic B-spline patch in 2-D is given in the following for the consistent mass matrix and the lumped mass matrix. The dispersion relation is given for the dilatation branch and the shear branch. The results serve as reference for the obtained results in Section 4.4 for the variationally scaled mass and reciprocal mass matrix.

A.1 Consistent mass matrix (CMM)

Dispersion relation of the dilatation branch:

$$\frac{c_d}{c_{d0}} = 1 + \left(\frac{1}{1440} - \frac{7}{2880} \cos(\theta)^2 + \frac{1}{320} \cos(\theta)^4 - \frac{1}{720} \cos(\theta)^6 + \frac{1}{1440} \cos(\theta)^8 \right) \kappa^4 + \mathcal{O}(k^6) \quad (\text{B.1})$$

Dispersion relation of the shear branch:

$$\frac{c_s}{c_{s0}} = 1 + \left(\frac{1}{1440} - \frac{1}{720} \cos(\theta)^2 + \frac{1}{360} \cos(\theta)^6 - \frac{1}{720} \cos(\theta)^8 \right) k^4 + \mathcal{O}(k^6) \quad (\text{B.2})$$

Both the dilatation and the shear branch of the consistent mass matrix are illustrated in Figure B.1 (left) for an inclination angle of 0° . In Figure B.2 the dispersion error is plotted over the wave number for different inclination angles for the dilatation (left) and shear branch (right) for the consistent mass matrix.

A.2 Lumped mass matrix (LMM)

Dispersion relation of the dilatation branch:

$$\frac{c_d}{c_{d0}} = 1 - \frac{1}{8}k^2 + \left(\frac{43}{5760} - \frac{1}{2880} \cos(\theta)^2 + \frac{1}{960} \cos(\theta)^4 - \frac{1}{720} \cos(\theta)^6 - \frac{1}{1440} \cos(\theta)^8 \right) k^4 + \mathcal{O}(k^6) \quad (\text{B.3})$$

Dispersion relation of the shear branch:

$$\frac{c_s}{c_{s0}} = 1 - \frac{1}{8}k^2 + \left(\frac{43}{5760} + \frac{1}{1440} \cos(\theta)^2 - \frac{1}{480} \cos(\theta)^4 + \frac{1}{360} \cos(\theta)^6 - \frac{1}{720} \cos(\theta)^8 \right) k^4 + \mathcal{O}(k^6) \quad (\text{B.4})$$

Both the dilatation and the shear branch of the consistent mass matrix are illustrated in Figure B.1 (right) for an inclination angle of 0° . In Figure B.3 the dispersion error is plotted over the wave number for different inclination angles for the dilatation (left) and shear branch (right) for the lumped mass matrix.

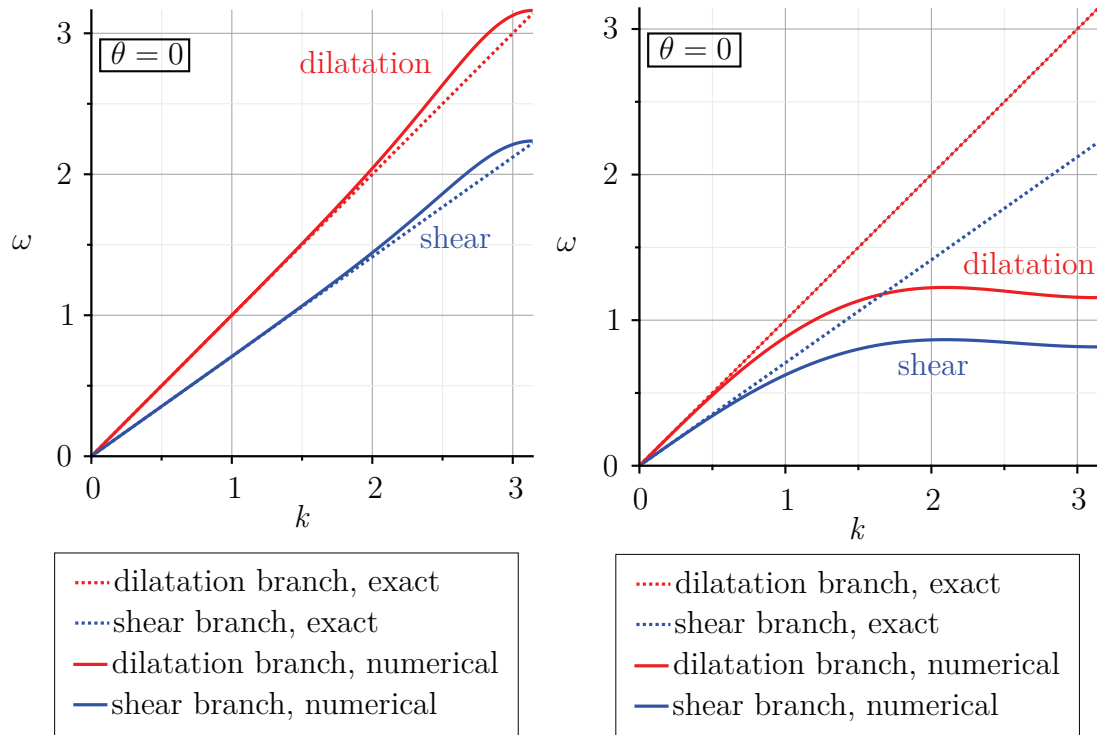


Figure B.1: Dispersion relation for a 2-D quadratic B-spline patch for CMM (left) and LMM (right).

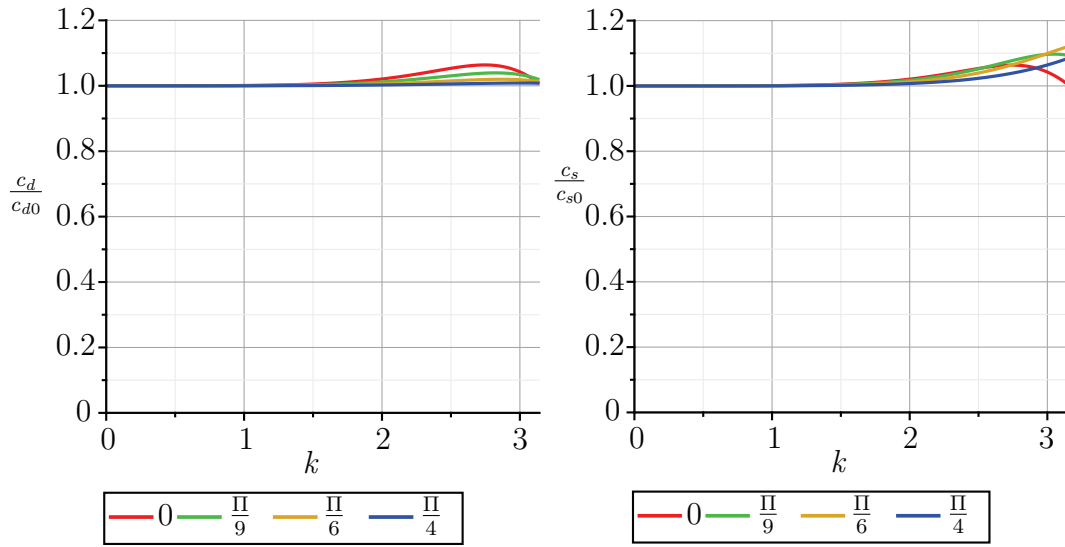


Figure B.2: Dispersion error for the consistent mass matrix (CMM) for different inclination angles θ for the dilatation branch (left) and the shear branch (right) for a 2-D quadratic B-spline patch.

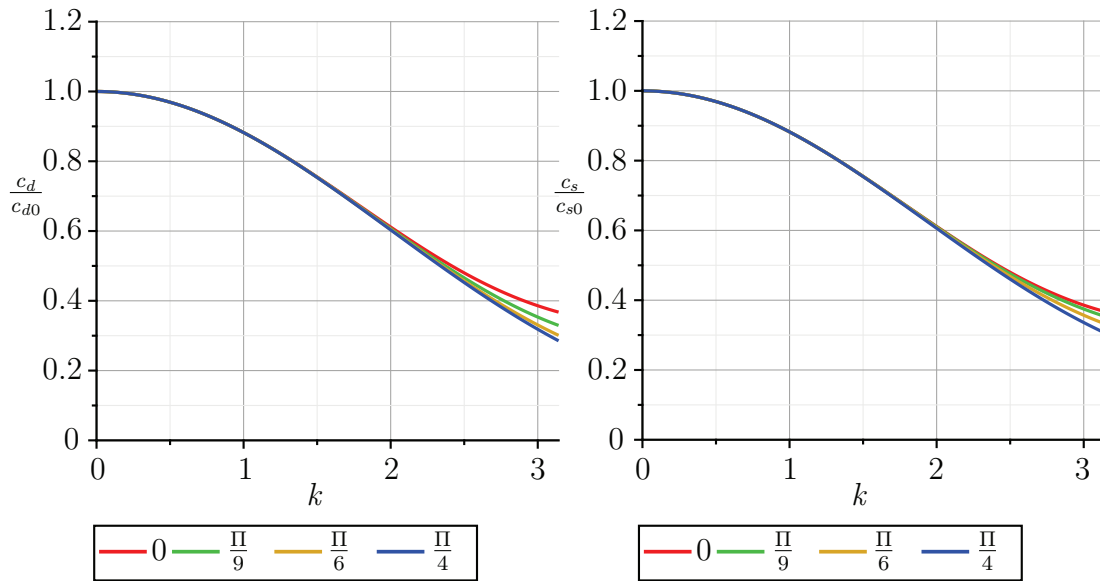


Figure B.3: Dispersion error for the lumped mass matrix (LMM) for different inclination angles θ for the dilatation branch (left) and the shear branch (right) for a 2-D quadratic B-spline patch.

B Reduced integrated Q1 element with stiffness/viscous hourglass control

In the following, the element formulation of a reduced integrated Q1 element with hourglass stabilization according to BELYTSCHKO AND BINDEMAN (1991) is provided. This element is used in Example 6.6.

The stiffness matrix (needed for the time step estimate) is obtained from the sum of the 1-point-integrated stiffness matrix and the stabilization stiffness matrix, i.e.

$$\mathbf{K}_e = \mathbf{K}_e^{1 \text{ pt}} + C^Q A \begin{bmatrix} \boldsymbol{\gamma} \boldsymbol{\gamma}^T & \mathbf{0} \\ \mathbf{0} & \boldsymbol{\gamma} \boldsymbol{\gamma}^T \end{bmatrix}. \quad (\text{C.5})$$

Therein, the element area is $A = 4 \det \mathbf{J}$, where \mathbf{J} is the element jacobian and the parameter

$$C^Q = \frac{1}{2} \alpha_s c_D^2 \rho A (\mathbf{b}_x^T \mathbf{b}_x + \mathbf{b}_y^T \mathbf{b}_y). \quad (\text{C.6})$$

\mathbf{b}_x and \mathbf{b}_y can be extracted from the nonlinear strain-displacement operator of the one-point integrated element with $\mathbf{b}_x = \mathbf{N}_{,x}$ and $\mathbf{b}_y = \mathbf{N}_{,y}$. Note that the derivative is taken with respect to the current coordinate in the case of a geometrically nonlinear problem setup. ρ is the material density and c_D is the dilatation wave speed which is

$$c_D^{\text{plane strain}} = \sqrt{\frac{(1-\nu)E}{(1+\nu)(1-2\nu)\rho}}, \quad c_D^{\text{plane stress}} = \sqrt{\frac{E}{(1-\nu^2)\rho}}, \quad (\text{C.7})$$

for plane strain and plane stress, respectively. α_s is a free parameter which is per default set to 0.1. The stabilization mode is

$$\boldsymbol{\gamma} = \frac{1}{4} \left(\mathbf{h} - (\mathbf{h}^T \mathbf{x}) \mathbf{b}_x - (\mathbf{h}^T \mathbf{y}) \mathbf{b}_y \right) \quad \text{with} \quad \mathbf{h} = \begin{bmatrix} 1 \\ -1 \\ 1 \\ -1 \end{bmatrix}. \quad (\text{C.8})$$

\mathbf{x} and \mathbf{y} are the current coordinate vectors in case of a nonlinear analysis. The internal force is computed with

$$\mathbf{f}^{\text{int}} = \mathbf{A} \mathbf{B}^T(0) \boldsymbol{\sigma}(0) + A \begin{bmatrix} Q_x \boldsymbol{\gamma} \\ Q_y \boldsymbol{\gamma} \end{bmatrix}, \quad (\text{C.9})$$

where the first summand is the internal force obtained by one-point quadrature ($\xi = 0$, $\eta = 0$). The second summand is the stabilization force \mathbf{f}^{stab} . For the computation of the internal force the generalized hourglass stress is needed with

$$Q_x = C^Q q_x + \zeta_D C^Q \dot{q}_x, \quad Q_y = C^Q q_y + \zeta_D C^Q \dot{q}_y, \quad (\text{C.10})$$

where ζ_D is the viscous hourglass stabilization parameter and chosen by the user. Usually it is chosen to be a fraction of the critical damping. The velocity strains are obtained by

$$q_x = q_x^{\text{old}} + \Delta t \dot{q}_x^{\text{old}}, \quad q_y = q_y^{\text{old}} + \Delta t \dot{q}_y^{\text{old}}, \quad (\text{C.11})$$

with

$$\dot{q}_x = \gamma^T \mathbf{v}_x, \quad \dot{q}_y = \gamma^T \mathbf{v}_y. \quad (\text{C.12})$$

The velocity in x - and y -direction is obtained from the current displacement and the displacement from the previous time step implicitly with

$$\mathbf{v}_x = \frac{\mathbf{d}_x - \mathbf{d}_x^{\text{old}}}{\Delta t}, \quad \mathbf{v}_y = \frac{\mathbf{d}_y - \mathbf{d}_y^{\text{old}}}{\Delta t}. \quad (\text{C.13})$$

Lebenslauf

Persönliche Angaben:

Name: Anne-Kathrin Schäuble
Geburtsdatum: 15. Dezember 1987
Geburtsort: Waldshut-Tiengen

Schulische Ausbildung:

1998 – 2007 Klettgau-Gymnasium, Waldshut-Tiengen

Universitäre Ausbildung:

2007 – 2011 Bachelor-Studium des Maschinenbaus an der Hochschule Esslingen

2011 – 2013 Master-Studium Computational Mechanics of Materials and Structures (COMMAS) an der Universität Stuttgart

08/2013 - 08/2018 Akademischer Mitarbeiterin am Institut für Baus-tatik und Baudynamik der Universität Stuttgart

Berichte des Instituts für Baustatik und Baudynamik der Universität Stuttgart

- 1 (1983) **P. Osterrieder:**
Traglastberechnung von räumlichen Stabwerken bei großen Verformungen mit finiten Elementen.
- 2 (1983) **T. A. Kompfner:**
Ein finites Elementmodell für die geometrisch und physikalisch nicht-lineare Berechnung von Stahlbetonschalen.
- 3 (1983) **A. Diack:**
Beitrag zur Stabilität diskret längsversteifter Kreiszyinderschalen unter Axialdruck.
- 4 (1984) **A. Burmeister, F.W. Bornscheuer, E. Ramm:**
Traglasten von Kugelbehältern mit Stützen und Formabweichungen unter Innendruck und Stützenlängskraft.
- 5 (1985) **H. Stegmüller:**
Grenzlastberechnungen flüssigkeitsgefüllter Schalen mit "degenerierten" Schalenelementen.
- 6 (1987) **A. Burmeister:**
Dynamische Stabilität nach der Methode der finiten Elemente mit Anwendungen auf Kugelschalen.
- 7 (1987) **G. Kammler:**
Ein finites Elementmodell zur Berechnung von Trägern und Stützen mit offenem, dünnwandigem Querschnitt unter Berücksichtigung der Interaktion zwischen globalem und lokalem Versagen.
- 8 (1988) **A. Matzenmiller:**
Ein rationales Lösungskonzept für geometrisch und physikalisch nicht-lineare Strukturberechnungen.
- 9 (1989) **D. Tao:**
Die Technik der reduzierten Basis bei nichtlinearen finiten Element-Berechnungen.

- 10 (1989) **K. M. Weimar:**
Ein nichtlineares Balkenelement mit Anwendung als Längssteifen axialbelasteter Kreiszyylinder.
- 11 (1990) **K.-U. Bletzinger:**
Formoptimierung von Flächentragwerken.
- 12 (1990) **S. Kimmich:**
Strukturoptimierung und Sensibilitätsanalyse mit finiten Elementen.
- 13 (1991) **U. Andelfinger:**
Untersuchungen zur Zuverlässigkeit hybrid"-gemischter Finiten Elemente für Flächentragwerke.
- 14 (1992) **N. Büchter:**
Zusammenführung von Degenerationskonzept und Schalentheorie bei endlichen Rotationen.
- 15 (1992) **T. J. Hofmann:**
Beitrag zur verfeinerten Balkentheorie.
- 16 (1994) **D. de Mesquita Roehl:**
Zur Berechnung von großen elastoplastischen Deformationen bei Flächentragwerken und Kontinua.
- 17 (1994) **R. Reitinger:**
Stabilität und Optimierung imperfektionsempfindlicher Tragwerke.
- 18 (1995) **R. L. M. Suanno:**
Ein dreidimensionales Simulationsmodell für Stahlbeton mit Plastizität und Schädigung.
- 19 (1995) **M. Braun:**
Nichtlineare Analysen von geschichteten, elastischen Flächentragwerken.
- 20 (1996) **N. Rehle:**
Adaptive Finite Element Verfahren bei der Analyse von Flächentragwerken.

-
- 21 (1996) **C. Hauber:**
Effiziente Dreieckselemente für Flächentragwerke.
- 22 (1996) **D. Kuhl:**
Stabile Zeitintegrationsalgorithmen in der nichtlinearen Elastodynamik dünnwandiger Tragwerke.
- 23 (1998) **H. Schmidts:**
Zur effizienten Modellierung und Analyse von Hochhaustragwerken.
- 24 (1998) **H. Wang:**
Interaktion des lokalen und globalen Stabilitätsverhaltens dünnwandiger Stäbe.
- 25 (1998) **K. Maute:**
Topologie- und Formoptimierung von dünnwandigen Tragwerken.
- 26 (1998) **B. Maurer:**
Karl Culmann und die graphische Statik.
- 27 (1998) **F. Cirak:**
Adaptive Finite-Element-Methoden bei der nichtlinearen Analyse von Flächentragwerken.
- 28 (1998) **M. Trautz:**
Zur Entwicklung von Form und Struktur historischer Gewölbe aus der Sicht der Statik.
- 29 (1999) **H. Menrath:**
Numerische Simulation des nichtlinearen Tragverhaltens von Stahlverbundträgern.
- 30 (1999) **M. Bischoff:**
Theorie und Numerik einer dreidimensionalen Schalenformulierung.
- 31 (1999) **W. A. Wall:**
Fluid-Struktur-Interaktion mit stabilisierten Finiten Elementen.
- 32 (2000) **E. Kuhl:**
Numerische Modelle für kohäsive Reibungsmaterialien.

- 33 (2001) A. Maute:**
Fehlerkontrolle bei Finite-Element-Methoden in der linearen Struktur-dynamik.
- 34 (2001) S. Schwarz:**
Sensitivitätsanalyse und Optimierung bei nichtlinearem Strukturverhalten.
- 35 (2001) A. Haufe:**
Dreidimensionale Simulation bewehrter Flächentragwerke aus Beton mit der Plastizitätstheorie.
- 36 (2001) D. P. Mok:**
Partitionierte Lösungsansätze in der Strukturmechanik und der Fluid-Struktur-Interaktion.
- 37 (2002) H. Steeb:**
Fehlerschätzer für FE-Berechnungen bei entfestigenden Materialien.
- 38 (2002) K. Krausz:**
Tragverhalten gemauerter Tonnengewölbe mit Stichkappen.
- 39 (2002) M. Hörmann:**
Nichtlineare Versagensanalyse von Faserverbundstrukturen.
- 40 (2003) V. Gravemeier:**
The Variational Multiscale Method for Laminar and Turbulent Incompressible Flow.
- 41 (2004) R. Kemmler:**
Stabilität und große Verschiebungen in der Topologie- und Formoptimierung.
- 42 (2004) G. A. D'Addetta:**
Discrete Models for Cohesive Frictional Materials.
- 43 (2004) M. Gee:**
Effiziente Lösungsstrategien in der nichtlinearen Schalenmechanik.

- 44 (2004) **T. Erhart:**
Strategien zur numerischen Modellierung transienter Impaktvorgänge bei nichtlinearem Materialverhalten.
- 45 (2005) **M. Leukart:**
Kombinierte anisotrope Schädigung und Plastizität bei kohäsiven Reibungsmaterialien.
- 46 (2006) **F. Huber:**
Nichtlineare dreidimensionale Modellierung von Beton- und Stahlbetontragwerken.
- 47 (2007) **A. Lipka:**
Verbesserter Materialeinsatz innovativer Werkstoffe durch die Topologieoptimierung.
- 48 (2007) **A. S. Hund:**
Hierarchische Mehrskalenmodellierung des Versagens von Werkstoffen mit Mikrostruktur.
- 49 (2007) **S. Hartmann:**
Kontaktanalyse dünnwandiger Strukturen bei großen Deformationen.
- 50 (2007) **T. M. Hettich:**
Diskontinuierliche Modellierung zur Versagensanalyse von Verbundmaterialien.
- 51 (2007) **C. Förster:**
Robust methods for fluid-structure interaction with stabilised finite elements.
- 52 (2009) **M. von Scheven:**
Effiziente Algorithmen für die Fluid-Struktur-Wechselwirkung.
- 53 (2010) **J. Kato:**
Material Optimization for Fiber Reinforced Composites applying a Damage Formulation.

- 54 (2010) **C. F. Hilchenbach:**
Optimierung von Mehrphasenstrukturen mit lokalem Schädigungsverhalten.
- 55 (2011) **I. Bruss:**
Dreidimensionale Schädigungsmodellierung heterogener Materialien.
- 56 (2012) **B. J. Schneider:**
Polygonale diskrete Elemente zur Modellierung heterogener Materialien.
- 57 (2012) **R. Etlender:**
Modellierung und Simulation der Wellenausbreitung in flexiblen hydraulischen Leitungen.
- 58 (2012) **T. Cichosz:**
Stabile und konsistente Kontaktmodellierung in Raum und Zeit.
- 59 (2013) **R. Echter:**
Isogeometric analysis of shells.
- 60 (2013) **A. Tkachuk:**
Variational methods for consistent singular and scaled mass matrices.
- 61 (2013) **J. Irslinger:**
Mechanische Grundlagen und Numerik dreidimensionaler Schalenelemente.
- 62 (2014) **T. E. Pohl:**
Adaptive Methoden zur Pfadverfolgung bei Entfestigung.
- 63 (2014) **A. Sorg:**
Adaptive diskret-kontinuierliche Modellierung von Materialien mit Mikrostruktur.
- 64 (2015) **M. E. Matzen:**
Isogeometrische Modellierung und Diskretisierung von Kontaktproblemen.

- 65 (2016) V. M. Effinger:**
Finite nichtlinear viskoelastische Modellierung offenzelliger Polymer-
schäume.
- 66 (2017) C. M. Wilking:**
Effiziente Integration und verbesserte Kontaktspannungen für duale
Mortar-Formulierungen.
- 67 (2018) B. Oesterle:**
Intrinsisch lockingfreie Schalenformulierungen.
- 68 (2018) F. Neukamm:**
Lokalisierung und Versagen von Blechstrukturen.



Anne-Kathrin Schäuble

The present work deals with innovative numerical methods for the computer simulation of dynamic problems with explicit time integration. The proposed methods aim to increase accuracy as well as reduce the calculation effort.

The basis for the development are variationally consistent inertia templates. The term 'inertia template' covers both alternatives to the commonly used diagonal mass matrices and novel reciprocal mass matrices. Reciprocal mass matrices result directly from the variational formulation and are sparse, assemblable, inverse mass matrices, which allow a trivial computation of the acceleration from Newton's second law.

In the first part of the work, the focus is on the variational consistency of reciprocal mass matrices and the therewith associated minimum requirements on the ansatz spaces. In the second part, the approach is systematically exploited not only to increase the critical time step but also to customize the inertia template to specific needs, like improved low-frequency accuracy. The third part aims at further development and investigation of reciprocal mass matrices to increase their usability for practical applications. The focus is therefore on the development of an efficient time step estimate and the treatment of contact.